A STUDY OF SUPERBUBBLES IN THE ISM : BREAK-OUT, ESCAPE OF LYC PHOTONS AND MOLECULE FORMATION

A Thesis
Submitted For The Degree Of
Doctor Of Philosophy
In The Faculty Of Science

by

Arpita Roy

Under the supervision of

Prof. Biman B. Nath (RRI)
Prof. Prateek Sharma (IISc)

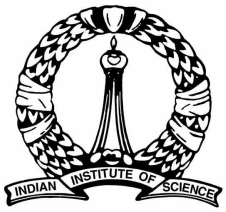

Joint Astronomy Programme (JAP)
Department of Physics
Indian Institute of Science
BANGALORE - 560012

August, 2016

Declaration

I, Arpita Roy, hereby declare that the work presented in this doctoral thesis titled 'A study of superbubbles in the ISM : break-out, escape of LyC photons, and molecule formation', is entirely original. This work has been carried out by me under the supervision of Prof. Biman B. Nath (RRI) and Prof. Prateek Sharma (IISc) at the Department of Astronomy and Astrophysics, Raman Research Institute under the Joint Astronomy Programme (JAP) of the Department of Physics, Indian Institute of Science.

I further declare that this has not formed the basis for the award of any degree, diploma, membership, associateship or similar title of any University or Institution.

Department of Physics
Indian Institute of Science
Bangalore, 560012
INDIA

Arpita Roy
Date :

Acknowledgements

First and foremost I would like to thank my supervisors Prof. Biman B. Nath (RRI) and Prof. Prateek Sharma (IISc). They have always spent substantial time whenever I've needed them for any academic discussions. I'm thankful for their inspirations and ideas to make my PhD experience productive and stimulating.

I'm equally grateful to our collaborator Prof. Yuri Shchekinov (P. N. Lebedev Physical Institute, Moscow, Russia). He has taught me as much as my supervisors did, and I'm thankful to him for his insightful comments not only for our publications but also for my thesis.

I would also like to thank all the faculties at RRI and IISc astrophysics group for all the fruitful discussions and critical comments in various occasions throughout my PhD career. A special mention goes to all the scientists who taught us in the first year course work of the JAP PhD programme.

Similar profound gratitude goes to all the administrative staffs of RRI and IISc physics department. Special thanks to Vidya at RRI Astro-floor for helping me out in anything and everything regarding any administrative issues. Her disciplined and motherly caring nature have made everything extremely swift in the department. I'm also hugely appreciative for all the discussions and comments I have received from all my fellow PhD students and post-docs at RRI and IISc astrophysics group.

Finally, but by no means least, thanks go to my mother, father, mom-in-law, dad-in-law for their immense support. They were always my strength in any emotional or spiritual matters. Special credit goes to my husband and fellow researcher Sourabh

Paul, who has supported me in anything and everything (academic, emotional, etc.), whenever and wherever I needed the most throughout my PhD days. A heartfelt gratitude also goes to my sisters, and sister-in-law Juhu.

Synopsis

Research Theme:

Multiple coherent supernova explosions (SNe) in an OB association can produce a strong shock that moves through the interstellar medium (ISM). These shocks fronts carve out hot and tenuous regions in the ISM known as superbubbles.

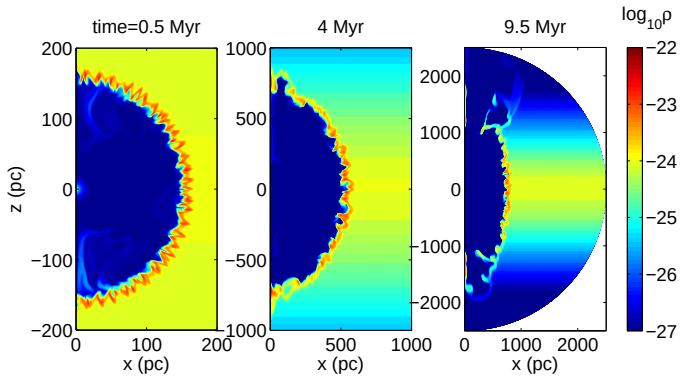

Figure 1: The density contour plot at three different times (0.5 Myr (left panel), 4 Myr (middle panel), 9.5 Myr (right panel)) showing different stages of superbubble evolution for $n_0 = 0.5$ cm^{-3}, $z_0 = 300$ pc, and for $N_{OB} = 10^4$. This density contour plot is produced using ZEUS-MP 2D hydrodynamic simulation with a resolution of 512×512 with a logarithmic grid extending from 2 pc to 2.5 kpc. For a detailed description of this figure, see Roy et. al., 2015.

The evolution of a superbubble is marked by different phases, as it moves through the ISM. Consider an OB association at the center of a disk galaxy. Initially the dis-

tance of the shock front is much smaller than the disk scale height. The superbubble shell sweeps up the ISM material, and once the amount of swept up material becomes comparable to the ejected material during SNe, the superbubble enters a self-similar phase (analogous to the Sedov-Taylor phase of individual SNe). As the superbubble shell sweeps up material, its velocity decreases, and thus the corresponding post-shock temperature drops. At a temperature of $\sim 2 \times 10^5$ K (where the cooling function peaks), the superbubble shell becomes radiative and starts losing energy via radiative cooling. This radiative phase is shown in the left panel of Figure 1. The superbubble shell starts fragmenting into clumps and channels due to Rayleigh-Taylor instabilities (RTI) (which is seeded by the thermal instability; for details see Roy et. al., 2013) when the superbubble shell crosses a few times the scale height. This is represented in the middle panel of the same figure. At a much later epoch, RTI has a strong effect on the shell fragmentation and the top of the bubble is completely blown off (the right panel).

In the first chapter of the thesis (reported in Sharma et. al., 2014), we show using ZEUS-MP hydrodynamic simulations that an isolated supernova loses almost all its mechanical energy within a Myr whereas superbubbles can retain up to $\sim$ 40% of the input energy over the lifetime of the starcluster ($\sim$ few tens of Myr), consistent with the analytic estimate of the second chapter. We also compare different recipes (constant luminosity driven model (LD model), kinetic energy driven model (KE model) to implement SNe feedback in numerical simulations. We determine the constraints on the injection radius (within which the SNe input energy is injected) so that the supernova explosion energy realistically couples to the interstellar medium (ISM). We show that all models produce similar results if the SNe energy is injected within a very small volume (typically 1–2 pc for typical disk parameters).

The second chapter concentrates on the conditions for galactic disks to produce superbubbles which can give rise to galactic winds after breaking out of the disk. The Kompaneets formalism provides an analytic expression for the adiabatic evolution

of a superbubble. In our calculation, we include radiative cooling, and implement the supernova explosion energy in terms of constant luminosity through out the lifetime of the OB stars in an exponentially stratified medium (Roy et. al., 2013). We use hydrodynamic simulations (ZEUS-MP) to determine the evolution of the superbubble shell. The main result of our calculation is a clear demarcation between the energy scales of sources causing two different astrophysical phenomenon: (i) An energy injection rate of $\sim 10^{-4}$ erg cm^{-2} s^{-1} (corresponding Mach number $\sim$ 2–3, produced by large OB associations) is relevant for disk galaxies with synchrotron emitting gas in the extra-planar regions. (ii) A larger energy injection scale $\sim 10^{-3}$ erg cm^{-2} s^{-1}, or equivalently a surface density of star formation rate ~ 0.1 M$_{\odot}$ yr^{-1} kpc^{-2} corresponding to superbubbles with high Mach number ($\sim$ 5–10) produces galactic-scale superwinds (requires super-starclusters to evolve coherently in space and time). The stronger energy injection case also satisfies the requirements to create and maintain a multiphase halo (matches with observations). Roy et. al., 2013 also points out that Rayleigh-Taylor instability (RTI) plays an important role in the fragmentation of superbubble shell when the shell reaches a distance approximately 2–3 times the scale-height; and before the initiation of RTI, thermal instability helps to corrugate the shell and seed the RTI. Another important finding of this chapter is the analytic estimation of the energetics of superbubble shell. The shell retains almost $\sim$ 30% of the thermal energy after the radiative losses at the end of the lifetime of OB associations.

The third chapter considers the escape of hydrogen ionizing (Lyc) photons arising from the central OB-association that depends on the superbubble shell dynamics. The escape fraction of Lyc photons is expected to decrease at an initial stage (when the superbubble is buried in the disk) as the dense shell absorbs most of the ionizing photons, whereas the subsequently formed channels (created by RTI and thermal instabilities) in the shell creates optically thin pathways at a later time ($\sim$ 2–3 dynamical times) which help the ionizing photons to escape. We determine an escape

fraction ($f_{\rm esc}$) of Lyc photons of $\sim 10 \pm 5\%$ from typical disk galaxies (within $0 \leq z$ (redshift) ≤ 2) with a weak variation with disk masses (reported in Roy et. al., 2015). This is consistent with observations of local galaxies as well as constraints from the epoch of reionization. Our work connects the $f_{\rm esc}$ with the fundamental disk parameters (mid-plane density (n_0), scale-height (z_0)) via a relation that $f_{\rm esc}^{\alpha} n_0^2 z_0^3$ (with $\alpha \approx 2.2$) is a constant.

In the fourth chapter, we have considered a simple model of molecule formation in the superbubble shells produced in starburst nuclei. We determine the threshold conditions on the disk parameters (gas density and scale height) for the formation of molecules in superbubble shells breaking out of disk galaxies. This threshold condition implies a gas surface density of ≥ 2000 M$_\odot$ pc^{-2}, which translates to a SFR of ≥ 5 M$_\odot$ yr^{-1} within the nuclear region of radius ~ 100 pc, consistent with the observed SFR of galaxies hosting molecular outflows. Consideration of molecule formation in these expanding superbubble shells predicts molecular outflows with velocities $\sim$ 30–40 km s^{-1} at distances $\sim$ 100–200 pc with a molecular mass $\sim$ 10^6–10^7 M$_\odot$, which tally with the recent ALMA observations of NGC 253. We also consider different combinations of disk parameters and predict velocities of molecule bearing shells in the range of $\sim$ 30–100 km s^{-1} with length scales of ≥ 100 pc, in rough agreement with the observations of molecules in NGC 3628 and M82 (Roy et. al., 2016, submitted to MNRAS).

Contents

List of Figures

List of Tables

Chapter 1

Introduction

Galaxies are the building blocks of the Universe. Gas inside galaxies gets converted into stars, and massive stars give rise to supernova explosions (SNe). Supernova explosions (SNe) inject mass, energy, and metals into the interstellar medium (ISM). The amount of metals and energy produced in SNe are proportional to the number of SNe. Multiple SNe within a small volume can overlap, and strongly affect the surrounding ISM and reduce the star-formation efficiency. The injected mass and metals aid the formation of next generation of stars. The injected energy heats up the ISM, on account of which a fraction of the hot gas may leave the galaxy. Since massive galaxies have deeper potential wells, metals produced in them are not easily transported to the IGM. Even in intermediate massive galaxies, these materials may not completely escape, and might stay in the galactic halo, or fall back onto the galactic disk as a galactic fountain. This whole process of recycling the galactic gas in the ISM, and the IGM (in some cases) is known as 'galactic feedback'. The process of enhancing star-formation (SF) is known as positive feedback, whereas the quenching of SF represents negative feedback to the ISM.

In massive galaxies (halo mass $M_h > 10^{12}$ $M_\odot$), SNe are not powerful enough to drive gas out of the galactic disks. These galaxies are believed to have a central black-hole, and the outflows and jets from the active galactic nuclei (AGN) help in sweeping away the baryons from the system, and therefore suppress the star-formation by reducing the total gas and metal content of the galaxies. AGN, and supernova driven outflows are the two important mechanisms in the evolution of galaxies.

Multiple coherent SNe shocks produce a superbubble (SB), which moves through the ISM. The evolution of the superbubble has different phases. Initially the shock front is at a much smaller radius compared to the scale height of the disk. The shocks produced by multiple SNe sweep up ISM material, and once the swept up material becomes comparable to the ejected supernova/wind material, the evolution enters the Weaver (analogous to Sedov-Taylor (ST) for blast waves) phase. As the superbubble shell sweeps up material, its velocity decreases, and thus the corresponding post-shock

temperature also drops. At a temperature of $\sim 2 \times 10^5$ K (where the cooling function peaks; see Sutherland & Dopita (1993) [197]), the superbubble shell starts losing its thermal energy via radiative cooling.

In section 1.1 we discuss various evolutionary aspects of superbubbles (geometric shapes, density jumps in the supershells), and their effects on the evolution of galaxies. Section 1.2 describes observations of SB breakout, production of galactic wind; and different theoretical models of SB evolution. In section 1.3, we introduce the three different phases (hot-ionized medium (HIM), warm neutral medium (WNM), and cold neutral medium (CNM)) associated with galactic outflows and the ISM in general. Section 1.4 discusses a few general aspects of superbubbles, and the motivation of the thesis. Section 1.5 contains the layout of the thesis.

1.1 Superbubbles and their evolution

Superbubbles are typically found in starburst galaxies, and in the active star-forming regions of galaxies with intermediate star-formation rate (SFR) (the Milky-Way type galaxies). As mentioned above, superbubbles evolve through different phases as they move through the ISM. At a later stage of their evolution, they blow out of the galactic disk if they are energetic enough to cross the scale-height of the disks. This breakout of the superbubbles often gives rise to galactic superwinds.

1.1.1 Shapes of the superbubbles

The shapes of superbubbles change as they evolve in different density structures of the ISM.

Uniform medium:

As the superbubble shock evolves, it is initially in freely expanding phase, and

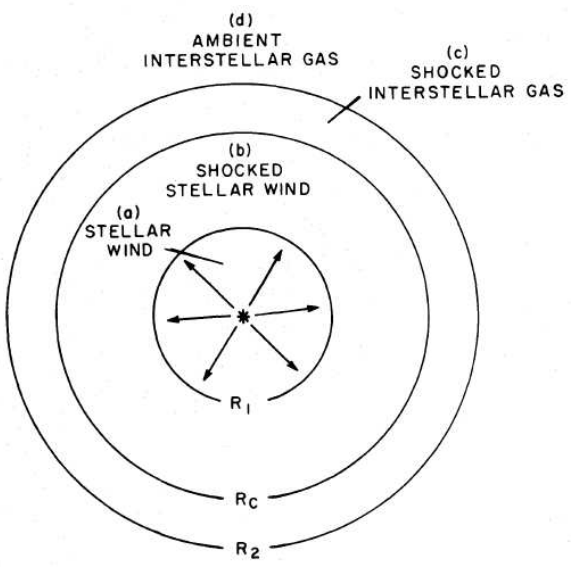

Figure 1.1: The schematic diagram of the different regions inside the wind driven bubble (Credit: Weaver et al. (1977) [224]).

supersonic with Mach number M ($\equiv v/c_s$) $\gg 1$, where v, c_s correspond to the shock velocity, and speed of sound respectively. In the subsequent ST phase the swept up mass is roughly $\sim$ 1000 times the ejected mass during SNe. However, ST phase is only valid for the blast wave cases. In a realistic case, the energy from SNe/wind is injected continuously in the form of constant mechanical luminosity, and the adiabatic evolution of superbubbles analogous to ST phase is described in detail in Weaver et al. (1977) [224].

The evolution of the bubble is self-similar with the expression for radius being given by Weaver et al. (1977) [224],

$$r = A \left(\frac{Lt^3}{\rho} \right)^{1/5} , \tag{1.1}$$

where L is the constant mechanical luminosity from the stellar winds, and SNe. Weaver et al. (1977) [224] estimated the energy distributions in the different regions of the bubbles to be $E_b = 5Lt/11$, and $E_c = 6Lt/11$; where "b", and "c" represent the shocked stellar wind (commonly known as hot bubble), and the shocked interstellar gas (dense shell) regions respectively.

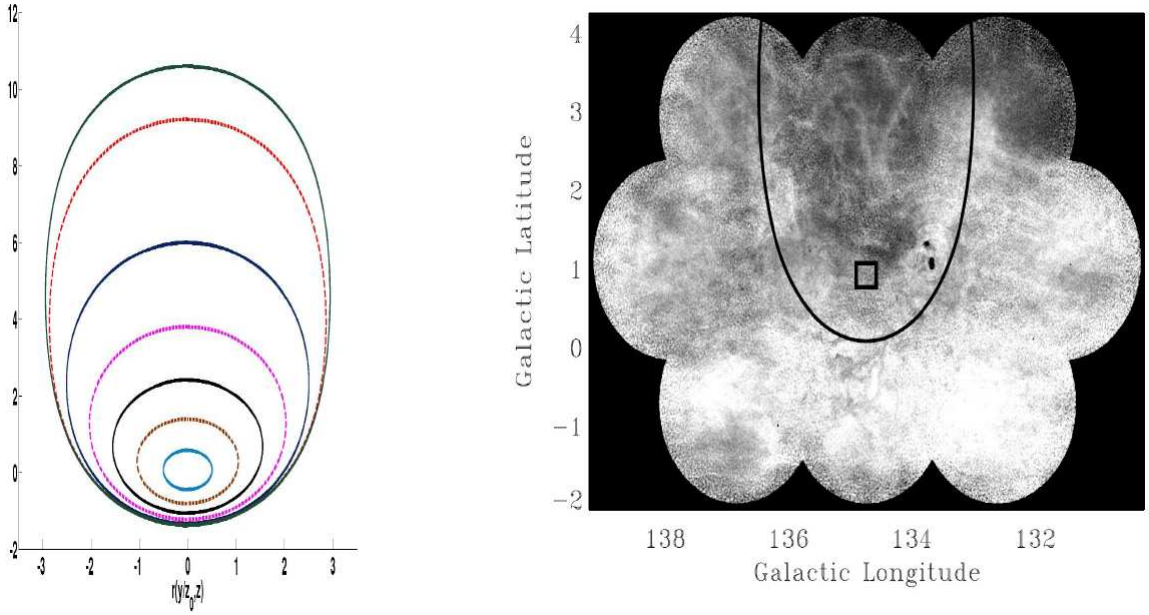

Figure 1.2: The left panel of the figure shows the analytic solution of the shock-front in an exponentially stratified medium. The right panel shows the HI map of the neutral gas associated with the W4 superbubble in the OCI 352 star-cluster (credit:Basu et al. (1999) [7]).

Density stratification:

In a more realistic density distributions of the ISM gas, an ambient medium has either exponential or sech^2 stratifications. In the exponentially ($n(z) = n_0 \exp(-z/z_0)$) stratified medium, the evolution of the shock-front as given by Kompaneets (1960) [107] is,

$$r = 2z_0 \arccos \frac{1}{2} \exp(z/2z_0)\big[1 - \frac{y^2}{4z_0^2} + \exp(-z/z_0)\big] \,, \tag{1.2}$$

where z_0 is the scale height of the ambient gas, and y denotes the scaled time parameter with a dimension of length :

$$y = \int_0^t \sqrt{\frac{(\gamma^2 - 1)Lt'}{2\rho_0 V(t')}}\, dt' \,. \tag{1.3}$$

The superbubble shock is initially spherical in shape as it should be for the Weaver bubble but it becomes oval shaped once it moves through the stratified ISM (elongated in positive z-direction as shown in the left panel of figure 1.2).

The Kompaneets solution is not only remarkable in the analytic modelling of superbubble evolution, but also equally important for observational purpose to study the bubble evolution (Basu et al. (1999) [7]). Using Kompaneets equation, Basu et al. (1999) [7] estimated the age and the scale-height of the local ISM, in the case of the W4-bubble in OCI 352 cluster. In the W4-bubble, the void in HI emission shows the presence of hot, low density bubble gas; Hα emission represents the dense shocked ambient gas (shell). Pidopryhora et al. (2007) [155] detected a superbubble (shown in figure 1.3) in both HI (using Green Bank Telescope (*GBT*)) and Hα (using Wisconsin H-Alpha Mapper (*WHAM*)) at a distance of $\sim$ 7 kpc and at $\sim$ 3.4 kpc above the Galactic plane. Using Kompaneets approximation they estimated the age of the superbubble to be $\sim$ 30 Myr, and the total energy of the supershells as $\sim 10^{53}$ erg.

However for realistic modelling of superbubble evolution, one needs to consider the symmetric density stratification, and include radiative cooling, and the disk gravity. The details of the realistic simulation set-ups are described in chapter 3.

1.1.2 HI holes & supershells

Many observations in the Milky-Way (e.g. Basu et al. (1999) [7], Pidopryhora et al. (2007) [155] as discussed above), and nearby galaxies show that superbubbles create holes in the HI distribution of host galaxies.

Milky-Way:

Pidopryhora et al. (2007) [155] measured 220,000 HI-emission spectra around a gigantic structure of the Ophiuchus superbubble using *GBT*. HI-plumes cover a region of 1.2×0.6 kpc in the top of the superbubble. Pidopryhora et al. (2007) [155] also found that the base of the structure has wide "whiskers" of HI covering $\sim$ a few 100s of pc, and extended till more than 1 kpc into the halo. They also found a vertical

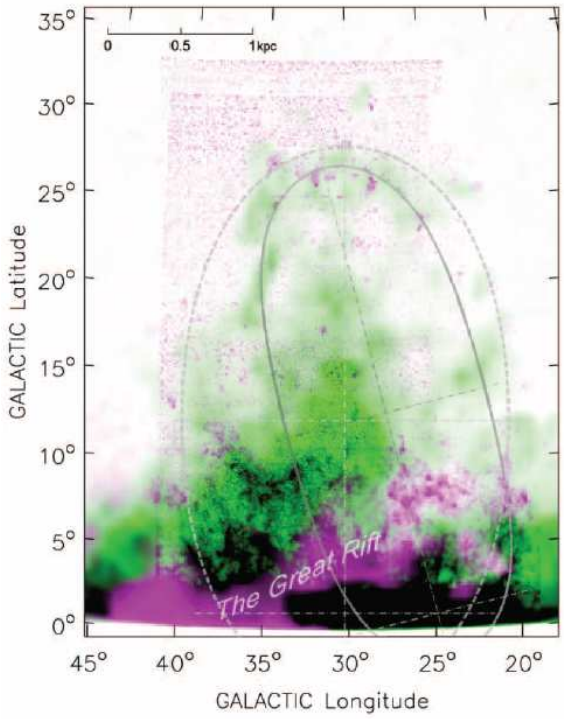

Figure 1.3: HI, and Hα emission in Ophiuchus superbubble are shown in purple, and green respectively. (credit:Pidopryhora et al. (2007) [155]). They fit two Kompaneets models to describe the structure. Both models produced similar results since the system is quite big to be reasonably robust to small changes in initial conditions. The striking similarities in the spatial extent of the HI, and Hα images indicate the presence of a gigantic superbubble.

density structure implementing the walls of the superbubble, similar to the vertical dust lanes observed in NGC 891. Other than these huge superbubbles, there are many shells and similar structures in the Milky-Way. A search for this shells at low galactic latitudes was undertaken by Heiles (1979) [81], Heiles (1984) [82]. These HI holes were named as "worms" by Heiles (Heiles (1979) [81], Heiles (1984) [82]). A similar task at high latitudes was done by Hu (1981) [90]. McClure-Griffiths et al. (2002) [129] performed a similar survey in the southern-hemisphere. Ehlerová et al. (2005) [51] discovered $\sim$ 300 such structures, and several of them were already catalogued by Heiles (1979) [81], Heiles (1984) [82], Hu (1981) [90].

These supershells can sometimes give rise to the second generation of star-formation. Oey et al. (2005) [151] observed one such star-formation driven superbubble, named as W3-superbubble in the star-cluster IC 1795 in the north-west edge of W4 superbubble.

Other galaxies:

Kamphuis et al. (1993) [97] observed an almost face-on galaxy NGC 6964 in 21-cm, and found HI emission at high velocities $\sim$ 100 km/s, primarily observed in the direction of the optical-disk. The emitting region is likely located in the halo with an associated HI mass of $\sim 5 \times 10^8$ $M_\odot$, and total kinetic energy $\sim 10^{55}$ erg. The high velocity HI has spatial correlation with holes in the HI-distribution suggesting the neutral gas to be swept up by stellar wind and SNe shocks. Later, Boomsma et al. (2008) [16] observed the same galaxy with the deep (192 hour) 21-cm HI observation, and detected HI high-velocity emissions associated with 121 HI-holes (shown in figure 1.4). Most of these holes are in the central regions of the galaxy where gas density and star-formation rate are high. They also concluded that fountains created by stellar outflows are the origin of these high velocity gas and HI holes. Other than NGC 6964, there are observations of shells and supershells in the nearby galaxies in the Local

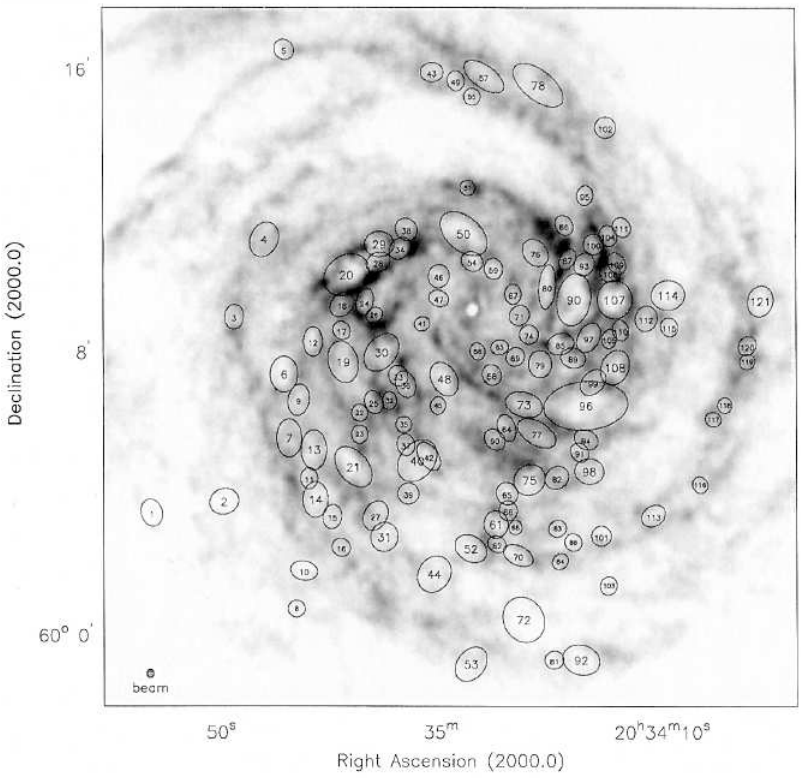

Figure 1.4: The figure shows HI-holes in the HI-map of NGC 6946. The ellipses show the sizes and orientations of the holes. The white spot at the centre is the HI absorption in the bright radio continuum nucleus, and not an HI hole (credit: Boomsma et al. (2008) [16]).

group such as the SMC, the LMC, and M31 (Brinks & Bajaja (1986) [19], Kim et al. (1999) [104], Walter et al. (1999) [221]).

'THINGS' ("The HI Nearby Galaxy Survey") survey has compiled a list of HI shells and supershells in nearby galaxies as these objects are important to understand the evolution of the ISM. The first paper by Walter et al. (2008) [223] obtained HI emission in 34 nearby ($2 \lesssim D \lesssim 15$ Mpc) galaxies with high spectral (≤ 5.2 km/s), and spatial (~ 6") resolution using *VLA*. Bagetakos et al. (2010) [5] analysed 20 of these 34 galaxies, and detected more than 1000 HI holes in total. These holes have sizes ranging from 100 pc (the resolution limit) to ~ 2 kpc, and expansion velocities ranging from $\sim$ 4–36 km/s, with the age range of 3–150 Myr, and they are located throughout the disks of the galaxies showing HI holes to be ubiquitous in the regions of star-formation activity.

Luminosity function of OB associations:

These HI holes and superbubbles have variety of sizes and luminosity. In order to understand the distribution, the first pioneering work was done by Kennicutt et al. (1988) [103]. They detected HII regions in 30 nearby spiral galaxies, and observed Hα emission-line fluxes to study the luminosity function (LF) of HII regions. They found that LF ($\phi(L)dL$) can well be represented by a power-law : $\phi_L dL \propto L^{-2\pm0.5}$ in most of the galaxies with systematic variation of normalization and the shape of the LF with Hubble type. Later on, Oey & Clark (1997) [150] obtained analytic expressions for the differential size distribution ($N(R)dR$) of superbubbles for uniform density ambient medium. Using the adiabatic expansion of superbubbles and LF of HII regions as described by Kennicutt et al. (1988) [103], and for constant SFR, they found that $N(R) \propto R^{1-2\beta}$ ($\equiv R^{-3}$) if $\phi_L \propto L^{-\beta}$ ($\beta \sim 2$). This estimation of $N(R)dR$ matches quite well with observations of HI shells in the SMC (Staveley-Smith et al. (1997) [187]). They also pointed that there are similar power law of $N(R)dR$ for the

momentum conserving phase of superbubble evolution.

1.1.3 Density structure of supershells

Besides the shape, it is instructive to study the density structure of superbubbles in different phases of evolution. All these shells and supershells are produced when the strong superbubble shock sweeps up ambient gas, and the swept up material is compressed in a dense, thin layer behind the shock-front. The shock then loses energy via adiabatic expansion. At a later epoch, the shell is compressed in a thinner and denser region due to radiative cooling as the post-shock temperature drops to $\sim 10^5$ K.

Adiabatic shocks:

The flow into and out of the shock can be considered as time independent (in the shock rest frame) as the shell thickness is a few times the mean free path of the particles. Suppose P_0, ρ_0, and u_0 are the upstream pressure, density, and velocity; and P_1, ρ_1, and u_1 are the downstream flow variables in the rest-frame of the shock-front. The mass flux (ϕ), momentum flux (ζ), and the specific total energy (η) are conserved across the shock-front :

$$\phi \equiv \rho u \tag{1.4}$$

$$\zeta \equiv P + \rho u^2 \tag{1.5}$$

$$\eta \equiv \frac{u^2}{2} + \frac{5}{2}\frac{P}{\rho}\,, \tag{1.6}$$

where P, ρ, and u are the flow pressure, density, and velocity respectively.

For the strong, adiabatic shock-wave for given ϕ, ζ, η; the velocity, and density of the post-shock gas are $u_1 = \frac{u_0}{4}$, and $\rho_1 = 4\rho_0$ respectively (known as Rankine-Hugoniot jump conditions). However, with the thermal conduction between the shell, and shocked stellar wind regions (denoted as "c", and "b" respectively as described before in section (Weaver et al. (1977) [224])), the density jump in the shell is less compared to the cases without conduction.

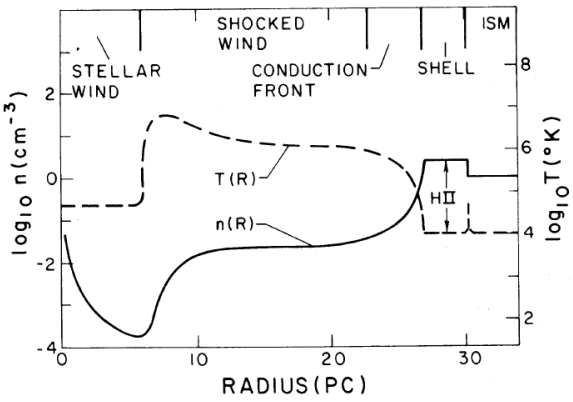

Figure 1.5: Figure shows density and temperature profiles in the wind-driven bubble with thermal conduction (Credit:Weaver et al. (1977) [224]).

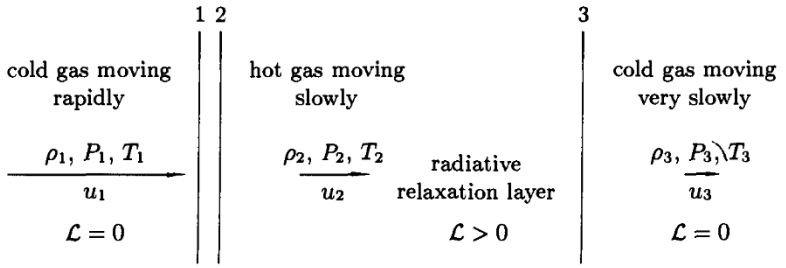

Figure 1.6: Schematic diagram of the radiative shock. (Credit:Shu [177]).

Radiative shocks:

For radiative shocks, the rapidly moving cold gas enters the radiative relaxation layer after crossing the viscous shock-front at 1 (shown is figure 1.6). The physical condition at 2 are determined by Rankine-Hugoniot jump conditions. At 2, the temperature increases rapidly with a maximum density jump of a factor of 4, making this region go out of thermal equilibrium. Therefore radiative cooling increases in the downstream gas of 2, thereby compressing the shell density by a large factor, and reducing the temperature and flow velocity for a given mass flux ρu. In 3, the shell is cooled enough to return to the equilibrium state again. A schematic diagram representing the density, temperature, and flow velocity profile at these three regions

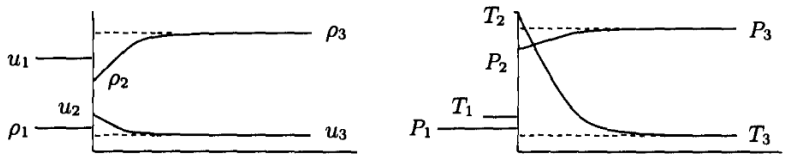

Figure 1.7: Schematic diagram of the density, temperature, and velocity profiles in regions 1, 2, and 3. (Credit:Shu [177]).

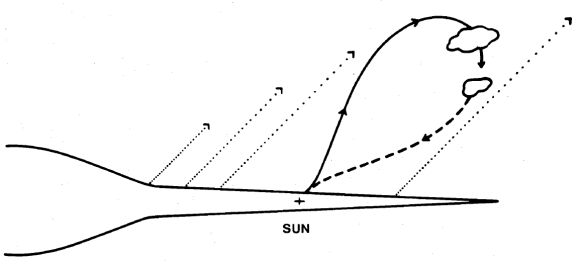

Figure 1.8: The dotted lines with arrows show the hot gas coming out of the galactic disk. The solid line shows the radial outflow of the hot flow, which cools via thermal instabilities, and falls back on the disk following the dashed line (credit:Bregman (1980) [18]).

is shown in figure 1.7.

In most of the cases, the gas in region 3 returns to the same temperature of the upstream gas via cooling in the thermally unstable region 2. For the isothermal case, the shock jump conditions are given by: $u_3 u_1 = a_T^2$, $\rho_3/\rho_1 = (u_1/a_T)^2$; where a_T is the isothermal sound speed ($a_T = \sqrt{(}kT/m)$, $T_3 = T_1 = T$). This relation is known as isothermal-shock-jump condition. We note that for radiative shocks, the shell density jump (ρ_3/ρ_1) can be as high as $\sim$ 100–1000 depending on the Mach number of the forward shock-front unlike adiabatic shocks.

1.1.4 Galactic fountains

The cooled supershells finally fragment in high density clumps and channels via Rayleigh-Taylor instabilities (RTI) (for details see Roy et al. (2013) [164]), and break out of the disk to enter the halo. The remnant of the dense supershells sometimes fall

back onto the galactic disks in the form of a "galactic fountain". Shapiro et al. (1976) [173] analysed the data from the hot ($\sim 10^6$ K) diffuse gas in the the galactic halo at ~ 1 kpc in soft X-ray (0.25 keV), and OVI absorption lines. They proposed that the hot gas in superbubbles can leak through the chimneys (similar to "fountain-like" structures) to the halo creating such hot halos, and may cool via convective-radiative cooling, and fall back onto the galactic disk with high velocities (~ 100 km/s) representing the origin of the high velocity clouds (HVC). This interpretation of HVC due to thermal-convective instability was first suggested by Suchkov & Shchekinov (1974) [195]. Also, Bregman (1980) [18] argued that the hot superbubble gas in a nearly hydrostatic corona travels further out conserving the angular momentum. This gas cools to form clouds, and these clouds move ballistically back towards the disk, and reach very high velocities similar to HVCs. However, recent studies by Wakker (2001) [217], Wakker et al. (2007) [218], Wakker et al. (2008) [219] confirm that at least some HVCs have sub-solar metallicities, and they may be formed by the intergalactic gas inflow; whereas these clouds originated by stellar activity have solar metallicities, and therefore they may be the origin of the intermediate velocity clouds (IVC).

1.2 Superbubble breakout and galactic winds

Superbubble breakouts create the large scale galactic winds (as mentioned above) with wide range of length scales starting from around a kpc to a few tens of kpc. There are many observations of these SB breakouts in the nearby starburst galaxies, and as well as in the Milky-Way. There are various theoretical models to understand the origin and evolution of these breakouts.

1.2.1 Observations of SB breakouts and galactic winds

Bland-Hawthorn & Cohen (2003) [11] observed bipolar structure at the galactic centre of the Milky-Way extending till ~ 8 kpc on both sides, perpendicular to the galactic

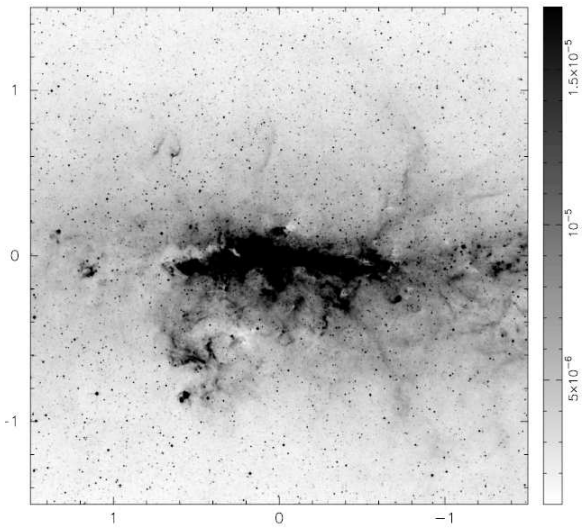

Figure 1.9: The figure shows the galactic centre of the Milky-Way at 8.3μm within a field of view of $\pm 1.5^{\circ}$ in latitude, and longitude. At the western side both above and below the galactic plane, bipolar dust shell is visible as an outflow signature (Credit:Bland-Hawthorn & Cohen (2003) [11]).

plane. This bipolar structure has filamentary emission at 8.3μm, and it is confined in an wide dome-shaped shell with the top as wide as $\sim$ 170 pc at $\sim$ 8 kpc. This is an evidence of a dust-entrained large-scale outflow powered by a central star-forming region. The energetics to drive such an outflow is $\sim 10^{55}$ erg, which requires $\gtrsim 10^4/\epsilon$ supernovae, ϵ being the thermalization efficiency of the ejected energy. They also found that the galactic centre drives such large-scale winds every $\sim$ 10–15 Myr.

Similar outflows have been observed in many nearby star-burst galaxies, and among them M82 is the nearest example ($\sim$ 3.5 Mpc) that has been observed in several wavebands in detail. It is interesting to study M82 among the many other star-forming galaxies as it shows grand outflows and galactic winds in different wavelengths. Figure 1.10 shows a composite image of M82.

A prominent outflowing HI gas has also been observed in NGC 253 (Boomsma et al. (2005) [15]). The 21-cm line observation reveals that the neutral hydrogen is extended till $\sim$ 12 kpc above the disk-plane in one direction. The HI emission is concentrated in a half-ring structure, and the HI-plumes seem to outline the boundaries

Figure 1.10: The composite image of M82 (credit:NASA/JPL-Caltech/STScI). The false colour codes represent the the image of M82 in different wavebands. The visible light of the stellar disk appears in yellow-green. The blue, red, and orange colours represent the X-ray image by Chandra, the Spitzer observation in molecular regime, and the HST image of the Hα emission respectively.

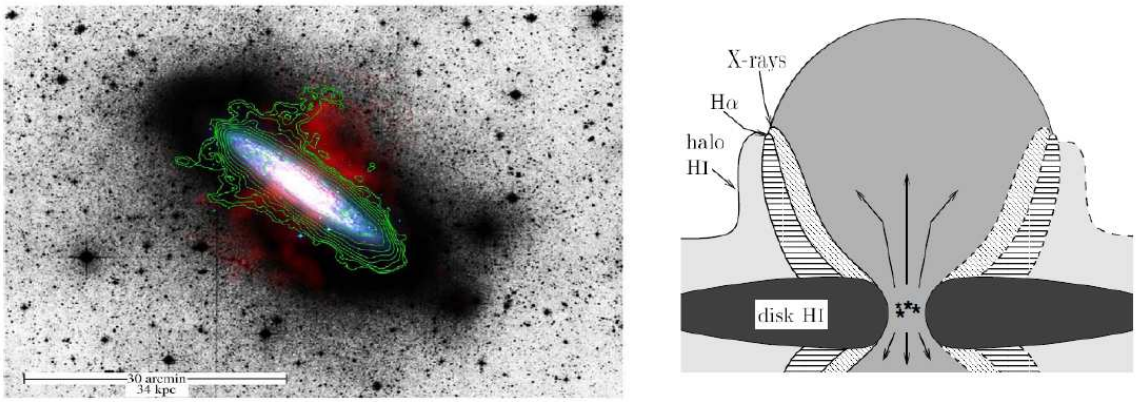

Figure 1.11: The left panel shows the multi-wavelength image of the star-burst galaxy NGC 253. The blue, and red colours represent the DSS optical disk, and soft X-ray (0.1–0.4 keV) emission respectively; and the green contours denote the HI-image. The right panel shows the schematic diagram of the different components of the outflow observed in various wavebands (X-ray, Hα, HI), and also the HI disk and the halo. The central region contains the driving source (O, B stars) of the outflows. The dashed line covered region at the extreme right is the undetected region. (Boomsma et al. (2005) [15]).

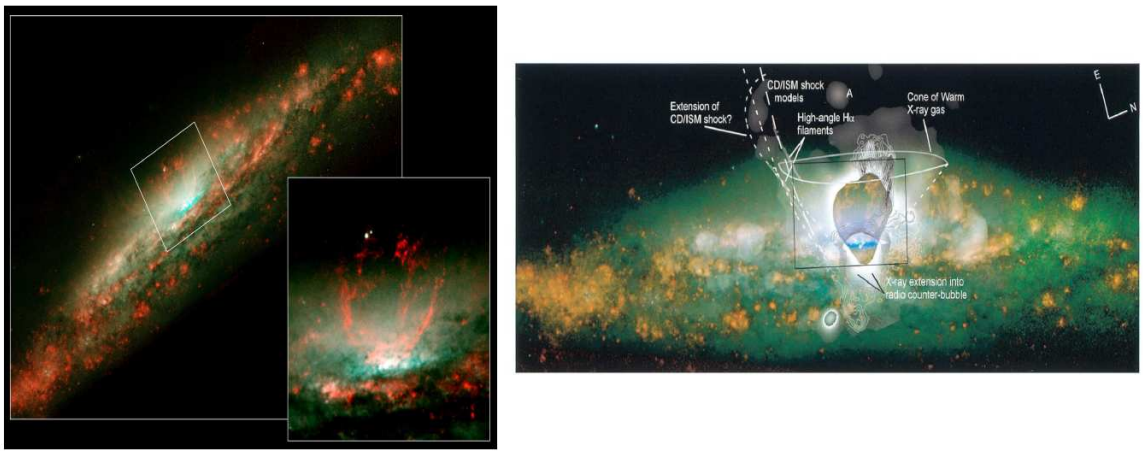

Figure 1.12: The left panel of the figure shows the optical HST image of NGC 3079 (credit: NASA HST site). The right panel shows the comparison between X-ray (gray scale), Hα+ NII lines (orange), radio (3.8 cm VLA image), and I-band continuum in green. The X-ray emission is from Cecil et al. (2002) [20] , and the rest of the images are taken from Cecil et al. (2001) [21] .

of the Hα and X-ray halo gas. Boomsma et al. (2005) [15] also pointed out that this extra-planar HI can be related to the active star-formation at the centre of the disk.

Cecil et al. (2002) [20] showed that the X-ray (*Chandra*), and Hα (*HST*) filaments in the superbubble of NGC 3079 have similar features. They also found that the soft X-ray gas has thermal energy $E_{TH} \sim 2 \times 10^{56} \eta_X^{0.5}$ ergs and kinetic energy $E_{KE} \sim 5 \times 10^{54} \eta_X^{0.5}$ ergs, which are similar to the energetics of the optical line-emitting gas if η_X (the volume filling factor of the X-ray emitting plasma) is large. The optical line seems to arise from the cool disk, or the cooled dense superbubble shell while the X-ray emission comes from the upstream bow shocks arising from the interaction of the hot bubble gas and the cold shell remnants (clumps), or from the conductive cooling at the clump/wind interfaces. This striking correlation (both spatial correlation, and energetics) of the optical, and X-ray emitting plasmas not only ensures the common origin of both of them, but also provides an observational evidence of a large scale galactic wind.

Heckman et. al. (1990) [79] have studied the optical spectroscopic data of the

ionized nebulae associated with 14 far-infrared galaxies (FIRG). Three of these 14 galaxies are nearby and also edge-on, which helps them to determine the kinematics of the outflowing gas. They found double emission lines with the line splitting of 200–600 km/s extended over kpc scales, away from the disk planes indicating a clear signature of outflows. They also found that the gas inside the nebulae is a few orders of magnitude overpressured compared to the Milky-Way ISM pressure, and the pressure drops systematically with the distance from the superbubble centre. The kinematics, morphology, and the pressure profile of the outflowing gas in their observations agree well with the numerical models of supernova driven bubbles.

1.2.2 Analytical modelling & Numerical simulations of SBs

Analytical modelling : There have been significant theoretical advance in the study of superbubbles. In this regard, McCray & Kafatos (1987) [130] found that stellar winds, and repeated SNe from OB associations, create cavities of sizes 100–300 pc in the ISM. They estimated that the interior pressure reduces in superbubble when it enters the snowplough phase, and within a few 10s of Myr it loses all its energy via radiative cooling, and stalls at a radius of $\sim$ 300 pc. At the same time the supershells become gravitationally unstable, and form giant molecular clouds to give rise to the second generation of SF. In association to the superbubble evolution, they also pointed it out that for a typical initial mass function (IMF), the energy injection rate via SNe is nearly constant for about $\sim$ 50 Myr.

These analytic estimates were taken forward by MacLow et al. (1988) [121] (see also Kovalenko & Shchekinov (1985) [111]). Using Kompaneets thin-shell approximation, they numerically modelled the superbubble evolution with various ISM density stratifications. They defined a dimensionless parameter $D \propto H^{-2} P_e^{-3/2} n_0^{1/2}$; where H, P_e, n_0 are the scale-height, thermal pressure, and the particle density of the ambient ISM gas respectively, as an indicator of whether the superbubble breaks out of the HI disk galaxies or collapses. They also pointed out that a superbubble blows

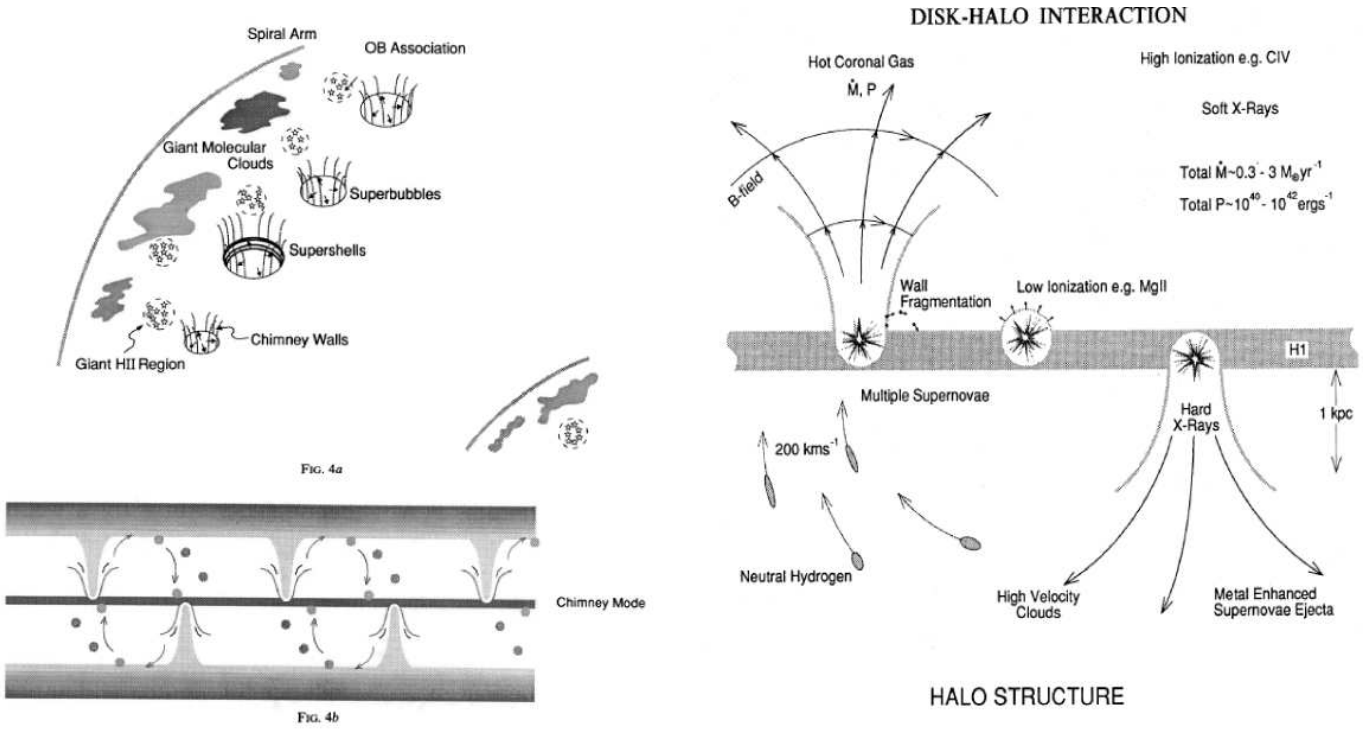

Figure 1.13: *Left panel*: Schematic diagrams of the superbubble formation from the OB-associations in the spiral arms (as shown in top marked as 4a), and the disk-halo interaction via superbubble evolution , and circulation of the disk gas via "disk-halo-disk" cycle (as shown in bottom marked as 4b). *Right panel*: A sketch of the halo structure in the chimney model (Credit:Norman & Ikeuchi (1989) [147]).

out symmetrically both above and below the plane of the disk if the star-formation takes place at the centre of the disk; the blow-out is one sided for the burst-centres at more than 50–60 pc above the plane for the typical Milky-Way density and scale height. Another important finding of MacLow et al. (1988) [121] is that when the superbubble shell crosses the dense clouds, finger-like structures of warm gas intrudes into the hot interior bubble, on account of "Rayleigh-Taylor" instabilities (RTI).

Norman & Ikeuchi (1989) [147] also supported the fact that spatially and temporally correlated SNe can drive superbubbles and supershells. They studied the disk-halo interaction by assuming that the gas flowing upward enters the halo via chimneys in the supershells created by RTI, and the gas carries mass, energy, mo-

mentum, and magnetic flux during its evolution into the halo. The cycle is completed by the downward fall of the cooled clouds onto the disk as the hot gas cools via radiative cooling and forms clumps. These clouds bring back the mass, and magnetic flux to the disk, and also a fraction of the momentum and energy as they strike the disks. This model is similar to the galactic fountain model as discussed earlier.

Numerical modelling : Using two-dimensional hydrodynamic simulations, Tomisaka & Ikeuchi (1988) [207] showed that the hot gas inside the bubble creates a hole in the HI image of the ISM, and vents through the chimneys in the superbubble shell during the later stage of its evolution, and percolates into the galactic halo. The cooled shell produced near the disk plane seems to be the origin of the CO spurs in the galactic halo of M82 (Tomisaka & Ikeuchi (1988) [207]).

MacLow et al. (1989) [122] studied the evolution of superbubble with ZEUS, a two-dimensional hydrodynamic simulations for the two different (exponential, and Gaussian) vertical density stratifications. Unlike earlier studies which found a large mass loading of the outflows, they found that only $\sim 5\%$ of the gas is accelerated upward. The density contours of the superbubble evolution for two density distributions at ~ 9 Myr when the bubble is blown out of the disk is shown in figure 1.15. The bubble evolution for both density stratifications agree well with Weaver et al. (1977) [224] at the early epoch, and with Kompaneets thin-shell approximation at a later epoch. For the two density stratifications, the morphologies of the dense shell are different only at a later epoch, and thus the dynamics also varies at late times (at or after the breakout). Depending on the different morphologies for different stratifications, the conditions for break-out also vary.

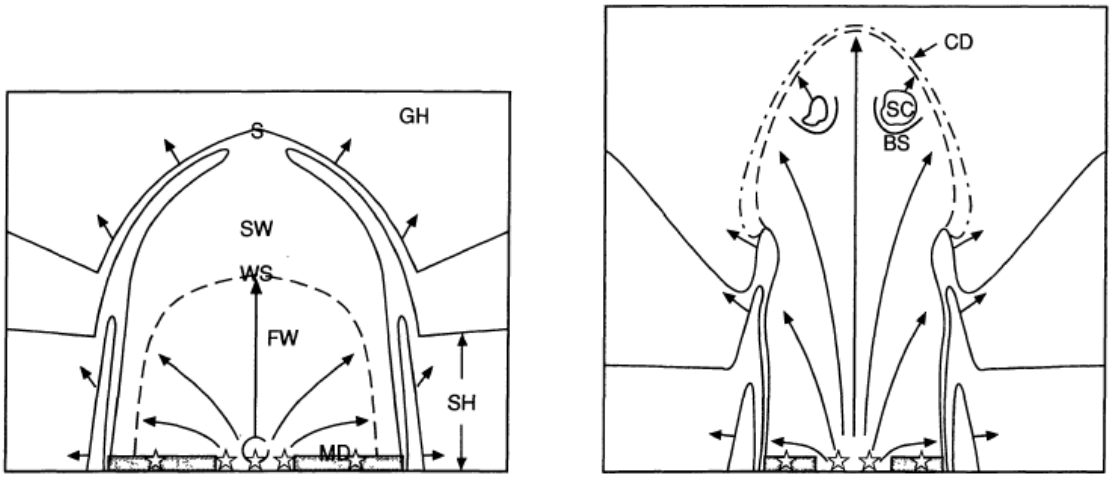

Figure 1.14: The figure shows the schematic diagram of the two evolutionary phases of the superbubble as described by the numerical model in Tomisaka & Ikeuchi (1988) [207] . The left panel shows the radiative phase before the bubble breaks out of the disk. "MD": molecular disk fueling the star-formation, "C" :central hot cavity, "FW" :Free wind region, "WS" : internal wind shock, "SW" : shocked wind gas, "S":thin shell, "GH": gaseous halo, isodensity contours of the gaseous halo are represented by the black solid contour-lines with the scale-height of "SH". The right panel shows the bubble when it reaches a few times the scale-height. "CD":contact discontinuity, "SC":shocked clouds, "BS" : bow shock (Heckman et. al. (1990) [79]). This figure is originally produced by Tomisaka & Ikeuchi (1988) [207]. Heckman et. al. (1990) [79] used this model to explain their observations.

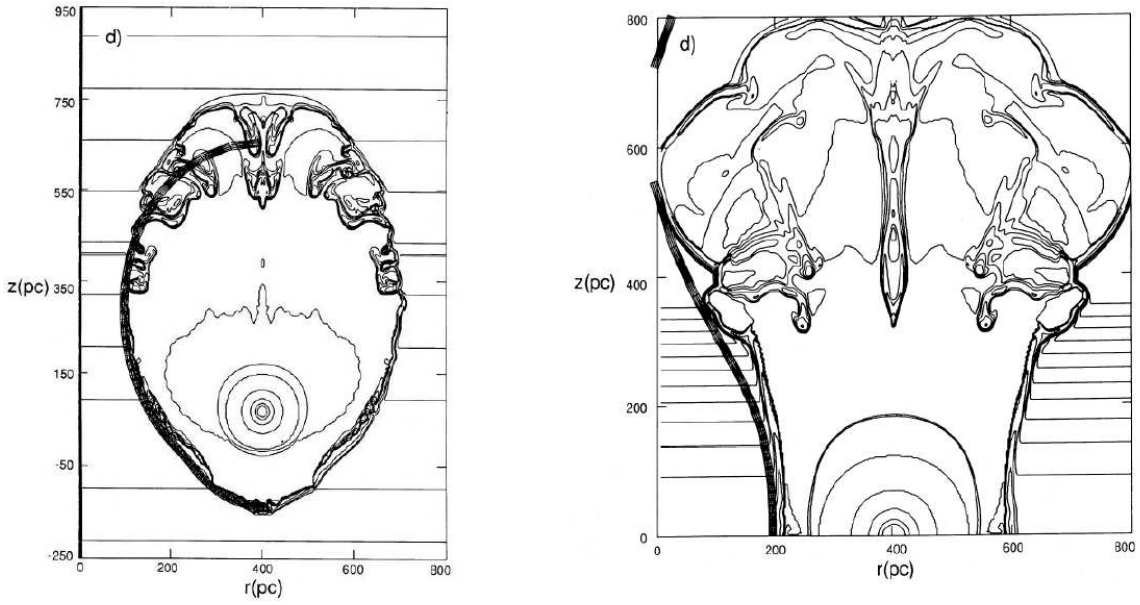

Figure 1.15: The figure shows the evolution of the superbubble at a later epoch ($\sim$ 9 Myr) for the exponential (left panel), and Gaussian (right panel) density stratifications. The density contours have logarithmic spacing of 0.5 dex from density of 10^{-28} (10^{-29}) gm cm^{-3} to 10^{-23} gm cm^{-3} for exponential (Gaussian) distribution (credit: MacLow et al. (1989) [122]).

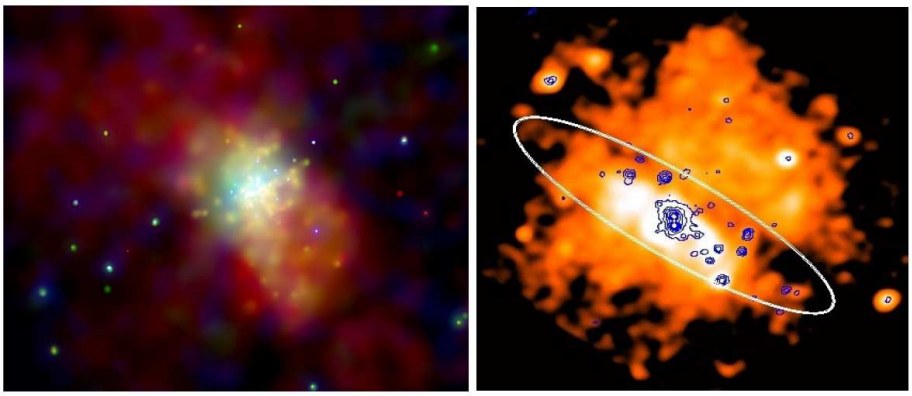

Figure 1.16: The left panel of the figure shows the X-ray image of M82 (Strickland & Heckman (2009) [191]). The soft X-ray (0.3–2.8keV), optical R-band (from starlight), and hard X-ray band (3–7 keV) emissions are shown in red, green, and blue respectively. The right panel shows the X-ray image of NGC 253 (credit: XMM official site). The low energy X-ray emission is shown in red, and the high energy emission in blue contours. The spiral disk is shown schematically by the ellipse.

1.3 Density/temperature structure of the superbubbles and ISM

Galactic outflows have a complex structure with different density/temperature phases of gas. There are three prominent density/temperature phases in the ISM : cold neutral medium (CNM) ($n \gtrsim 10$ cm^{-3}, $T \lesssim 100$ K), warm neutral medium (WNM)($n \sim 0.1$–1 cm^{-3}, $T \sim$ several 1000 K), and hot ionized medium (HIM) ($n \lesssim 0.01$ cm^{-3}, $T \gtrsim 10^5$ K).

Hot ionized phase:

The HIM is primarily detected in X-rays. Cox (2005) [35] claims that the HIM of the ISM can either be a part of the hot halo which is in hydrostatic equilibrium, or be produced by the thermal superwinds. In the thick disks of quiescent galaxies, the hot gas can be a part of the hot halo, whereas for the starburst galaxies the

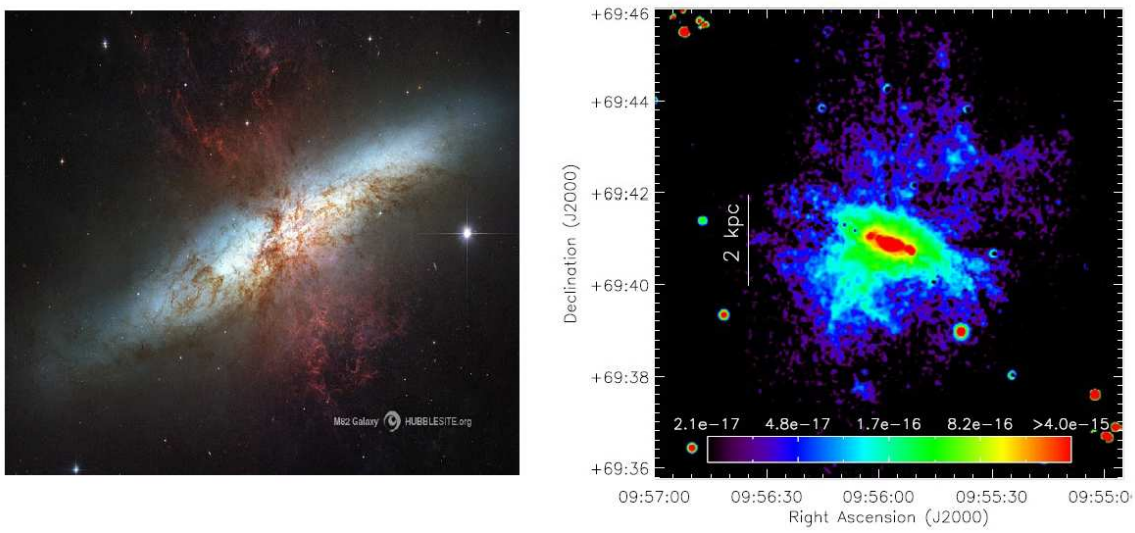

Figure 1.17: The red filaments in the left panel of the figure shows the filamentary, and clumpy Hα emission in the superwind of M82; the visible starlight is shown in blue. The right panel shows the 2.12μm H_2 emission upto $\sim$ 3 kpc on a false colour scale in M82 (Veilleux et al. (2009) [216]).

hot superbubble gas predominantly create the HIM. Diffuse thermal X-ray emission is observed at $\sim$ 5 to 10 kpc above the disk-plane in edge-on starburst galaxies (Strickland et al. (2004) [192], Heckman et. al. (1990) [79]). Figure 1.16 shows the X-ray emission from M82 and NGC253. The X-ray gas has a smooth distribution since the hot wind behaves as a free-wind as it enters the low density halo. We note that slightly cooler outflows ($T \sim 10^5$ K) cannot be detected in X-ray emission, and they are rather observed in the metal absorption lines (OVI, CIV, NV, etc.) (Jenkins & Meloy (1974) [94], Shapiro et al. (1976) [173]).

Warm and Cold neutral medium:

The WNM is primarily composed of neutral gas although it contains a some partially ionized gas; the CNM is completely neutral with mostly atomic hydrogen and sub-dominant diffuse molecular gas.

The CNM and WNM (cooled dense clumps, and inter-clump gas in the shells) are generally inseparable in galactic outflows. However, the detection mechanism for the two phases are different. The partially ionized portion of the WNM is primarily probed by Hα emission lines, and the neutral gas is observed by NaD (Heckman et al. (2000) [75]) and MgII lines. The filamentary Hα emission of M82 is shown in figure 1.17. The molecular H_2 knots are observed in 2.12 μm band at a vertical height of $\sim$ 3 kpc in the outflow of M82 (Veilleux et al. (2009) [216], shown in the right panel of figure 1.17). Interestingly, such difference also exists in the detection of CNM and WNM in the ISM. The CNM is primarily observed in 21-cm HI absorption lines while the Doppler broadened emission lines are dominantly due to dominantly WNM (Radhakrishnan et al. (1972) [158]). We note that the multiphase, clumpy ISM plays an important role in determining the escape of ionizing photons as discussed in detail in section 1.4.3, and chapter 4.

It is interesting to note that the extents of both the WNM/CNM are similar to the HIM (upto 1–2 kpc) although the morphologies of the two (WNM/CNM, and HIM) are quite different. The neutral medium is more clumpy (due to the thermal instabilities in the dense gas) compared to the smooth distribution of the hot gas.

It is however surprising that the cold gas survives at a height of $\sim$ 3–5 kpc surrounded by the hot wind gas, because the ram pressure of the hot gas drags the cold gas with it along its way, and therefore it is highly probable for the cold gas to evaporate. The survival of the cold clumps against the collapse due to its self-gravity is another stand-alone debatable issue on its own. It is possible that local thermal instabilities of the hot gas may produce the cold phase. Therefore, the mass exchange between the cold and hot phase is an important process both in the superbubbles and ISM (Cox (2005) [35]).

cold molecular phase:

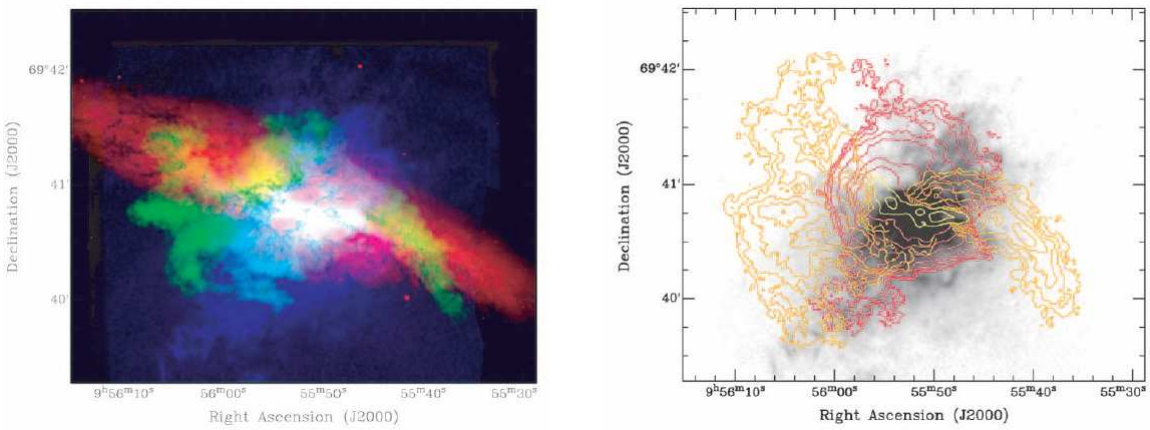

Figure 1.18: *Left panel :* The Red, and the blue colours reperesent the optical , and the Hα image of M82 respectively. The molecular CO map is shown in green. *Right panel :* The yellow contours represent the M82 disk, and the Hα image of M82 is shown in gray scale. The orange contours show the tidal streaming of the gas in M82. The red contours are molecular gas associated with the outflow in M82. The molecular gas is extended upto 1.2 kpc below the plane of the disk. (credit : Walter et al. (2002) [222]).

Galactic outflows also contain the dense molecular component. For example, Walter et al. (2002) [222] detected CO emission in M82 (shown in figure 1.18), extended upto 1.2 kpc in one side of the disk-plane. The detailed introduction of the molecular outflows in the central regions of starburst galaxies is discussed in section 1.4.4.

1.4 Overall aspects of SB evolution, and motivation of the thesis

We have so far discussed the importance of SBs, and various implications of its evolution on galaxies. For the purpose of the thesis, we intend to study a few aspects of SB evolution. We would like to introduce the motivations by laying out the problems we have attempted to study.

1.4.1 Threshold conditions for SB breakouts

The large scale global galactic winds as discussed above are termed "Superwinds" by Heckman et al. (2000) [75]. They studied the spectra of NaD absorption line for the sample of 32 FIRGs. In 18 of these galaxies, the absorption lines are produced by the interstellar gas, and in 12 of them the NaD lines are blueshifted by 100 km/s providing a direct observational evidence of outflows. It is generally believed that galaxies with a high star formation rate ($\gtrsim$ few tens of $M_\odot$ yr^{-1}) often show galactic winds although Heckman (2002) [77] pointed out that the surface density of the star-formation rate is more important in this regard rather than the total star-formation rate (SFR). He found that for exciting the galactic winds, the threshold SFR surface density is ~ 0.1 $M_\odot$ yr^{-1} kpc^{-2}.

There are studies of the existence of multiphase gas in the halos of the starburst galaxies, and their possible connection to the properties of the star-formation in the disks. Tüllmann et al. (2006) studied the luminosities in different bands (soft X-ray(0.3–2.0 keV), Hα, B-band, UV, radio continuum (1.4GHz), FIR) for the sample of 23 edge-on galaxies, and found a strong correlation (shown in figure 1.19) between their strength, morphology, and spatial extent. They also inferred that the halo contains gas of different densities and temperatures (multiphase halo), if the threshold condition for the surface density of the energy injection rate is $\sim 10^{-3}$ erg s^{-1} cm^{-2}. Another study by Dahlem et al. (1995) [40] on a sample of 5 edge-on galaxies shows that the halo gas exhibits radio-continuum emission, and the strength of the emission correlates with SFR. The existence of the filamentary structures in radio-emission of the halo requires cosmic-ray electrons to be convected to the halo along ISM magnetic fields. They also pointed out that the radio-emission is exhibited only if the energy injection rate due to star-formation exceeds a threshold of $\sim 10^{-4}$ erg s^{-1} cm^{-2}, which is an order of magnitude lower than the estimate for multiphase halo (Tüllmann et al. (2006) [211]).

The hierarchy of the threshold values of SNe energy input rates for these phenom-

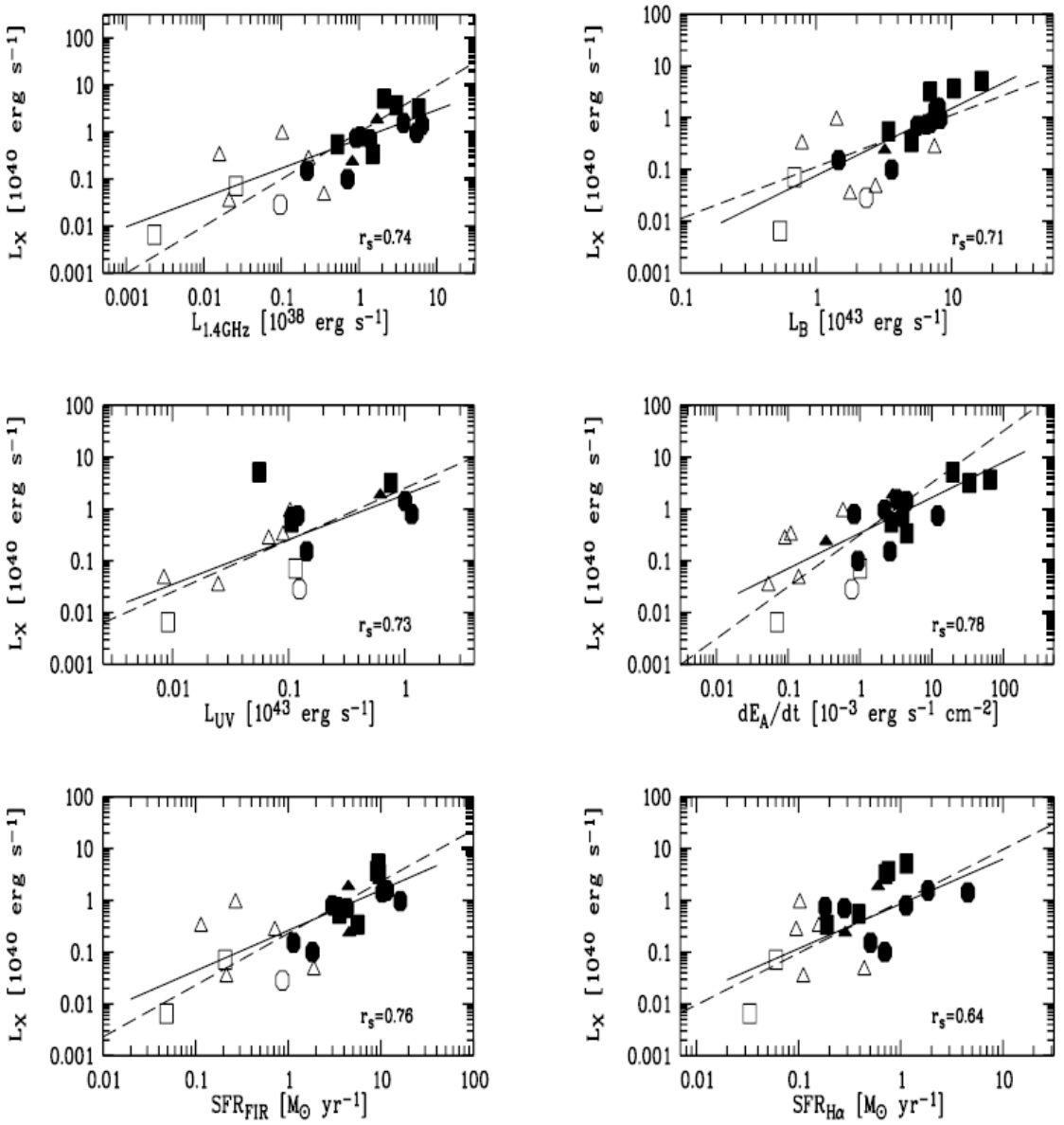

Figure 1.19: The figure shows the correlation of the luminosities obtained from different bands with the X-ray luminosity (Tüllmann et al. (2006) [211]). The circles, squares, and the triangles represent the data from Tüllmann et al. (2006) [211], Strickland et al. (2004) [192], and from the literature as mentioned in Table 1 of Tüllmann et al. (2006) [211] respectively. Filled and open symbols refer to the undetected and detected gaseous halos of galaxies respectively (credit:Tüllmann et al. (2006) [211]).

ena motivated us to investigate the connections between all these energy scales and galactic outflow properties. We also explore whether or not these energy scales can be explained by a single physical process.

1.4.2 Numerical implementation of SB feedback

The effective numerical implementation of SNe energy input into the ISM is a long-standing important issue to resolve. The structure of the universe at large scales is governed largely by gravity and dark energy, while at the galactic scales, various baryonic processes such as heating, cooling, self-gravity, and star-formation play important roles (Springel et al. (2005) [186]). These complex physical processes require different numerical recipes and high resolution (varying according to the scale of the problem) over an wide range of length scales starting from scales of stellar clusters (a few 10s of pc) to the galactic scales (a few 10s of Mpc). Therefore these numerical prescriptions are computationally expensive and may not show converged results (discussed in detail in the introduction of chapter 2).

For large scale outflows leading to superwinds, superbubbles are more effective feedback mechanism compared to single supernova explosions. In this regard, Cox (1972) [33], Thornton et al. (1998) [204] found that single supernova explosions lose most of their input energy soon after the initiation of the radiative phase, and retain only a fraction ~ 0.1 of the total energy within $\lesssim 0.1$ Myr. In contrast, a fraction of $\gtrsim 0.3$ of the total explosion energy is retained in the case of multiple SNe (Strickland & Heckman (2009) [191]). Recently, Vasiliev et al. (2015) [215], and Nath & Shchekinov (2013) [139] have argued that to create a more effective superbubble strong shock, supernova explosions have to be spatially and temporally coherent. Assuming that all the supernova explosions take place within a small volume so that they are coherent in space and time to maintain a strong shock even after radiative losses. Roy et al. (2013) [164] estimated the threshold condition for the surface density of SFR to be 0.3 $M_\odot$ yr^{-1} kpc^{-2}, close to the threshold condition for the superwinds

as calculated by Heckman (2002) [77].

SNe feedback is an important topic to discuss in detail among many other feedback processes such as radiation pressure, photoionization, and cosmic rays. There have also been discussions whether one should inject the supernova explosion energy in a cold, dense medium (which is the origin of massive stars) or the injection should take place in a hot dilute medium (as the medium has been diluted by the stellar wind feedback much before the supernovae explode). There are two important feedback models : (i) thermal feedback (Katz (1992) [100]), and (ii) kinetic feedback model (Navarro et al. (1994) [142], Navarro et al. (1997) [143], Navarro et al. (2000) [144]). If the energy is injected in a larger volume, then the cooling time becomes shorter than the thermalization time, and therefore the feedback mechanism is suppressed. This is the so called numerical "over-cooling" problem in numerical cosmology (in both Eulerian (e.g., Dubois & Teyssier (2008) [49], Tasker & Bryan (2006) [200]), and Lagrangian (Springel & Hernquist (2003) [185], Stinson et al. (2006) [188]) simulations). In order to thermalize the feedback energy to couple to the ISM effectively, these cosmological simulations (Dubois & Teyssier (2008) [49], Gerritsen (1997) [63], Springel & Hernquist (2003) [185]) resort to either artificially switching off the cooling for an uncertain period of time (which can be as long as the life-time of the star-clusters) or depositing the injected energy in a hot, less dense medium so that the cooling time is longer.

The overcooling problem in cosmological simulations due to the lack of the resolutions motivated us to study the numerical recipes of SNe feedback in detail. Our objective is to find out the scale at which SNe energy should be deposited in various injection prescriptions for the energy to couple effectively to the ISM.

1.4.3 Escape of ionizing photons

Massive stars are not only the source of the mechanical or thermal energy, they are also the source of highly energetic ionizing photons. The hydrogen ionizing photons

(Lyc photons) influence galaxy evolutions. The 'chimneys' in the dense supershells not only transport the hot, metal enriched gas to the halo, but also create optically thin pathways for Lyc photons to escape the disk and enter the diffuse ionized medium aka "Reynolds layer" in Milky-Way (Dove & Shull (1994) [44], Reynolds (1991) [161]). However, for the escape of substantial fraction of Lyc photons, the superbubble shells have to fragment before the main sequence life-time of O stars, as they are the primary contributors to the ionizing photons from stellar sources (Dove et al. (2000) [45], Zastrow et al. (2013) [231]). Therefore the fragmentation time-scale should be of $\sim$ 3–5 Myr, consistent with the dynamical timescale ($t_d \propto H^{5/3}(n_0/L_{SN})^{1/3}$) when the number of SNe $\sim$ 200 for typical disk parameters (n_0, z_0). In order to fragment within this short time, thermal instabilities have to play an equally important role as RTI (Roy et al. (2013) [164]).

The escape of Lyc photons from galaxies, or in other words, the total contribution to the UV background radiations from all the galaxies at high redshifts (z) cause the re-ionization of the universe at $z \gtrsim 6$. However, it is unclear whether the main contribution to the ionizing photons arises from starburst galaxies or AGNs because we do not have a solid knowledge of the formation mechanism of local UV background in individual galaxies. There is a lot of work done in this regard both observationally, and theoretically to estimate the value of the fraction of Lyc photos that escapes galactic disks (escape fraction $f_{\rm esc}$).

We mention here a few observational methods to estimate $f_{\rm esc}$. Bland-Hawthorn & Maloney (1999) [10] modelled the production and transport of ionizing photons in an optically thick ISM, and with the help of Hα observations in the Magellanic stream they have estimated $f_{\rm esc}$ for our Galaxy ($f_{\rm esc} \leq 6\%$). A recent observation by Zastrow et al. (2013) [231] obtained the emission line ratio maps of [SIII]/[SII] (an effective tool to study the radiative transfer) for six dwarf starbursts in order to calculate $f_{\rm esc}$, and found that the ionizing photons escape through a narrow opening angle ($\sim 40 \pm 5^\circ$ in most of the galaxies in their observations). Borthakur et al.

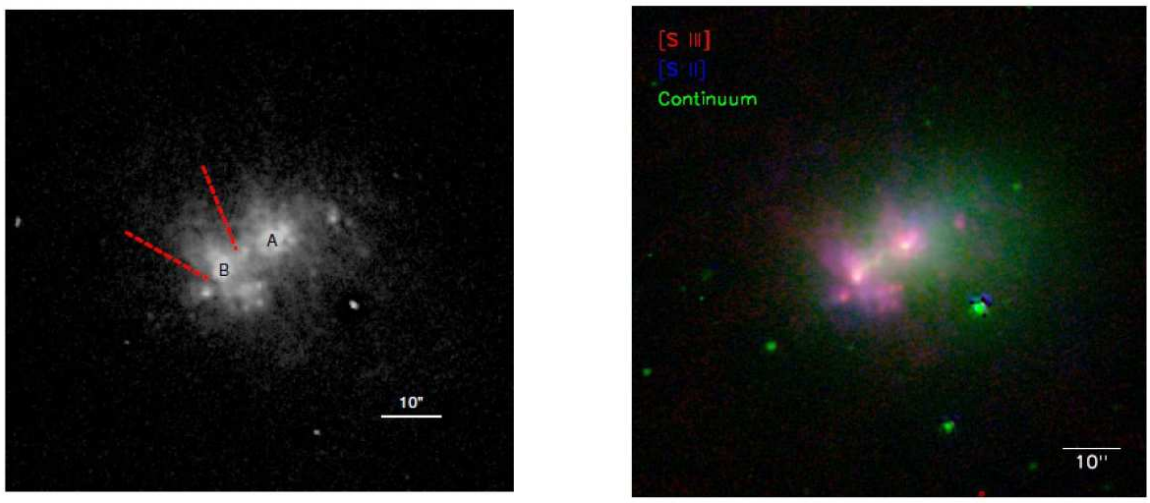

Figure 1.20: The left panel shows the Hα image of NGC 3125, indicating the opening angle of the cone by the two red-dashed lines. In the right panel, the red, blue, and green colours represent the emission lines of SIII, SII, and λ6680 continuum respectively (Zastrow et al. (2013) [231]).

(2014) [17] have also recently observed UV emission from the galaxy J0921+4509, and estimated $f_{\rm esc}$ by adopting the production rate of ionizing photons from stellar population model. They concluded that the "picket-fence" structure of the supershells due to the fragmentation has a substantial effect on the leaking of the Lyc photons.

There also exist various analytical and numerical prescriptions for the estimation of $f_{\rm esc}$. However, *the dependences of escape fraction on the disk parameters* (mid-plane density (n_0), and scale-height (z_0), or the disk mass and radius in the cosmological terms) are yet unknown (e.g. as mentioned in Zastrow et al. (2013) [231]). The quest for the understanding of this dependence is the motivation behind the study of $f_{\rm esc}$ in the framework of superbubble evolutions.

1.4.4 Observations of molecular outflows

The nuclear regions of nearby starburst galaxies show molecular outflows. In general, dense molecular clouds are observed in CO. To observe and understand the dynamics of these molecular outflows in the centrally located dense region, one requires to

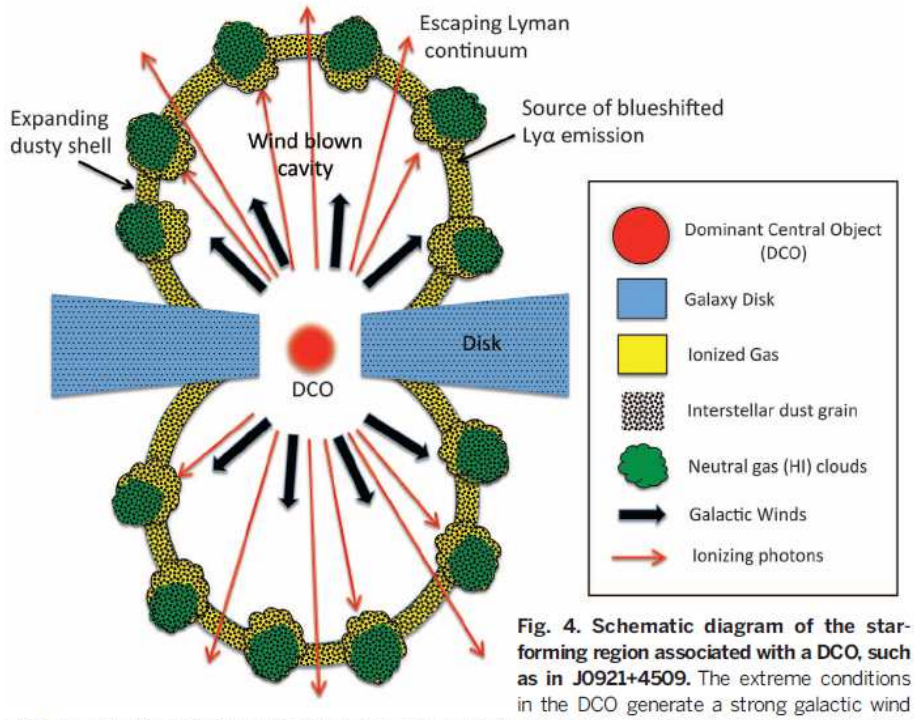

Fig. 4. Schematic diagram of the star-forming region associated with a DCO, such as in J0921+4509. The extreme conditions in the DCO generate a strong galactic wind and large quantities of ionizing flux that clear out a cavity (windblown cavity in the figure) and parts of the neutral gas cover. However, the entire region is covered by dust. The neutral gas cover contains gaps, where the gas becomes completely ionized and consequently has negligible optical depth due to photoelectric absorption of Lyman continuum photons by hydrogen. Thus, these gaps facilitate the escape of Lyman continuum and Lyman-α photons.

Figure 1.21: The details of the figure are mentioned in the figure itself (credit:Borthakur et al. (2014) [17]).

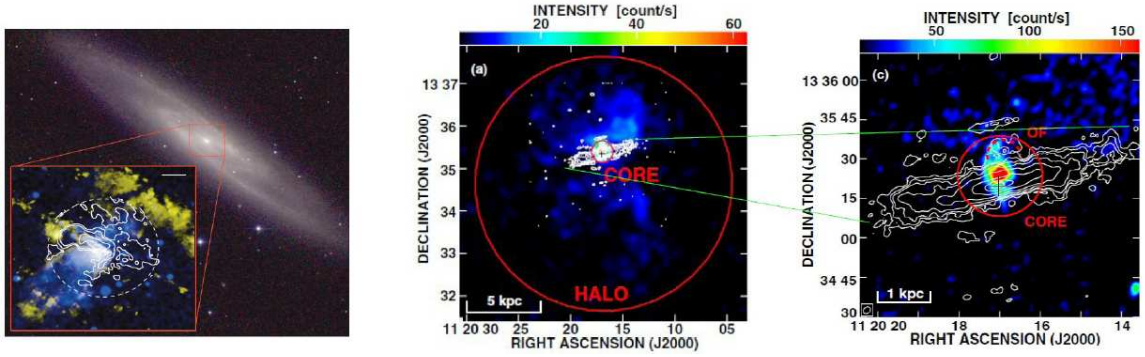

Figure 1.22: The left panel (credit: Bolatto et al. (2013) [13]) shows the stellar disk of NGC 253 in the JHK composite image with an inset of central $\sim$ 2 kpc with a scale-bar of 250 pc as shown in the top right. In the inset, the false colours show X-ray (in blue), and Hα (in yellow) image of the central region with a white dashed circle indicating the central zone observed by *ALMA*. The white contours show the *ALMA* CO(1–0) observations. The middle panel shows the Chandra soft X-ray data (0.3–2.0 keV, shown in the colour scale) with the CO(1–0) contours in the central region of NGC 3628, which is zoomed in the right panel (central $2' \times 2'$). One can notice that X-ray image, and the CO-contours have nice spatial correlation (Tsai et al. (2012) [210]).

have an instrument with both good sensitivity, covering a wide range of length scales starting from a few 10s of pc to $\sim$ 500 pc, and high resolution with a resolving power of structures less than $\sim$ 100 pc as well. In this regard, *ALMA* (Atacama Large Millimeter/submillimeter Array) is a powerful instrument, and in light of recent observations of molecular components with the advent of *ALMA*, this topic has become interesting to study in detail.

Molecular CO features associated with the outflow in the central region of NGC 253, have been observed by Bolatto et. al. 2013 with *ALMA*. NGC 253 has a star formation rate ~ 3 $M_\odot$ yr^{-1}, which can be as large as ~ 9 $M_\odot$ yr^{-1}. Four expanding shells have been observed with radii 60–90 pc with expansion velocities of $\simeq$ 23–42 km s^{-1}, indicating a dynamical age of $\sim$ 1.4–4 Myr. The CO-luminosities totalling the four expanding shells is estimated to be $\sim 2 \times 10^7$ K km s^{-1} pc^2, equally split on both sides of the disks. Assuming an optically thin CO-to-H_2 conversion factor $\alpha_{CO} \sim 0.34$ $M_\odot$ K^{-1} km^{-1} s pc^{-2}, they have estimated the total molecular mass to

be $(0.3-1)\times10^7$ $M_\odot$. They also calculated the kinetic energy associated with this outflow to be $\sim(2-20)\times10^{52}$ erg. These shells are likely to outline a larger shell around the central starburst region.

Tsai et al. (2012) [210] detected molecular outflow in the central region of NGC 3628 with the length-scale of 370–450 pc through CO(1–0) observations. They found that the outflow gas has a velocity $\sim 90\pm10$ km/s, inferring an expansion time-scale $\sim$ 3.3–6.8 Myr. The molecular gas outflow rate is 4.1–8.5 $M_\odot$ yr^{-1}, and the total mass is $\sim 2.8\times10^7$ $M_\odot$. In order to eject this molecular mass with the aforementioned velocity, one requires a mechanical energy to be $\sim(1.8\text{–}2.8)\times10^{54}$ ergs. The outflow is dominated by the northern part of the central region with a weak bubble breaking out (shown in the right panel of figure 1.22).

M82 also has a molecular component, which has the similar mass, size, and velocity as the two other galaxies discussed here. The detailed morphology of the molecular outflow in M82 is quite complicated, and is discussed in detail in the introduction of chapter 5.

Other than the starburst galaxies in the local universe, recent observation at higher redshift indicates that molecules can also be observed in an outflow at much larger radii driven by the radiation pressure of the stellar sources if the SFR is high. This study by Geach et al. (2014) [62] in CO (2–1) show molecular outflows at a radius $\sim$ 10 kpc in SDSS J0905+57 at redshift $z\sim0.7$. This galaxy has a compact structure (with effective radius $r_e\sim100$ pc), and high SFR ~ 260 $M_\odot$ yr^{-1}. They found that $\sim 35\%$ of the total molecular mass is extended at $\sim$ 10 kpc with one-third of this gas moving with velocities of as high as $\sim$ 1000 km/s. It has a molecular mass outflow rate of $\sim 80\pm20$ $M_\odot$ yr^{-1}, and a SFR surface density of ~ 4700 $M_\odot$ yr^{-1} kpc^{-2} within the effective radius. This ejection of high molecular mass of total $\sim 10^8$–10^9 $M_\odot$ (both wings, and the central emitting region) with such a high velocity requires an associated kinetic energy as high as $\sim 10^{56}$–10^{57} erg, which is consistent with the available momentum flux from the stellar radiation pressure.

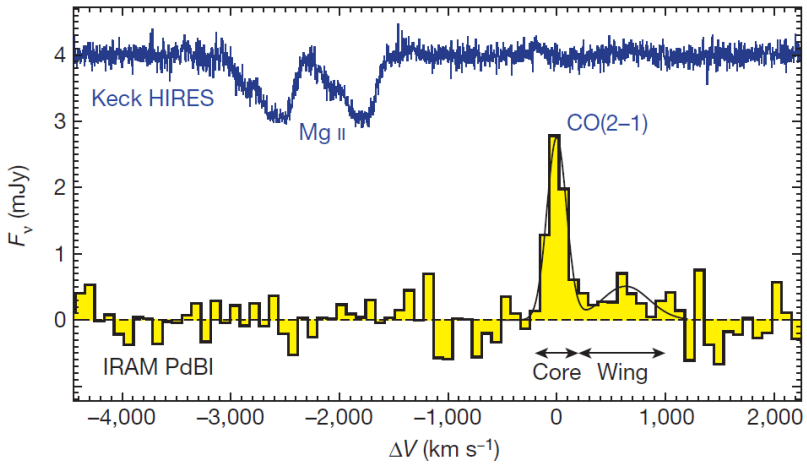

Figure 1.23: This figure shows the 2 mm spectrum of SDSS J0905+57. A Gaussian profile is fitted to the observed CO (2–1) flux density, with a width of 200 km/s (FWHM). A significant amount of CO emission is in the high-velocity range (known as wing) upto $\sim$ 1000 km/s. This galaxy is also known to have outflows of ionized gas, as shown by the strongly blue-shifted, high velocity ($\sim$ 2500 km/s, higher than the velocity of CO gas) MgII doublet (at wavelengths λ = 2796 and 2803 A° in the absorption features (Credit:Geach et al. (2014) [62]).

The striking similarities of the mass, size, and the speed of the molecular outflows for the three aforementioned star-burst galaxies (NGC 253, NGC 3628, M82) in *local universe* motivated us to study the formation and destruction mechanisms of molecules in the expanding superbubble shells in order to understand the generic features of molecular outflows in star-forming galaxies.

1.5 Structure of the thesis

The thesis is comprised of four chapters based on our four publications. The thesis structure is following :

- In chapter 2, we calculate analytic expressions for the injection radius within which we input the SNe energy for different feedback prescriptions for effective SNe feedback. We also discuss the differences, and similarities between the

different SNe feedback models using 1-dimensional hydrodynamic (HD) simulations in a uniform density ISM.

- We investigate the connections and origins of the three different energy scales to create galactic superwinds, synchrotron radio, and multiphase halos with the aid of Kompaneets solution and 2-dimensional HD simulations (ZEUS-MP) of superbubble evolution in an exponentially stratified medium in chapter 3. We also include the effects of radiative cooling and disk gravity.

- In order to understand the connection of escape fraction ($f_{\rm esc}$) with disk-parameters, we study the effects of superbubble evolution on the estimation of $f_{\rm esc}$, and scan a large region in the parameter space and calculate the average $f_{\rm esc}$ for each set of n_0–z_0 combinations. This work is described in chapter 4.

- Chapter 5 studies the formation and destruction mechanisms of molecules in the superbubble outflows in nuclear regions of star-burst galaxies. We use 1 dimensional HD simulations (ZEUS-MP) in a ambient medium with uniform density in order to obtain superbubble shell position and velocity.

Chapter 2

Feedback to the ISM : numerical implementation

Based on : "In a hot bubble: why does superbubble feedback work, but isolated supernovae do not?"
Sharma, P., Roy, A., Nath, B. B., Shchekinov, Y., 2014, MNRAS, 443, 3463

Numerical prescriptions of the supernova explosion feedback mechanism is one of the longstanding, "not-yet-completely-resolved" issues in the field of galaxy evolution. A single supernova loses most of its energy as it enters the radiative phase during its evolution in the ISM, and becomes a sound wave over 10s of Myr. On the contrary, multiple, collocated supernovae retain most of the injected thermal energy over this timescale. The coherent supernovae are also known to produce the steady thermal winds. There are many numerical models to implement SNe feedback. We study the different feedback models in order to understand their benefits and drawbacks. Our interest is also to obtain an effective feedback model that couples to the ISM. We also study the condition to drive a steady thermal wind. We use an idealised 1-D Eulerian hydrodynamic simulation to address the aforementioned questions.

Primary results

- Isolated supernova loses almost all its injected energy via radiative cooling within $\lesssim 0.1$ Myr and stalls at scales $\lesssim 100$ pc. On the other hand, superbubbles can retain up to $\sim 40\%$ of the input energy over the lifetime of the star cluster (few 10s of Myr). These conclusions hold even in the presence of realistic magnetic fields and thermal conduction.

- We derive analytic expressions for the injection radius ($r_{\rm in}$) in order to produce, and maintain the strong shocks for various numerical prescriptions. We also find that the explosion energy needs to be deposited within a small volume ($r_{\rm in} \lesssim$ 10–20 pc, less than the size of the star-clusters) depending on the density of the ambient medium, and the number of SNe going off at the centre) in all these different models in order to effectively couple to the ISM.

- We show that a steady thermal wind within the superbubble appears only for a large number ($\gtrsim 10^4$) of supernovae. For smaller clusters we expect multiple

internal shocks instead of a smooth, dense thermalized wind.

2.1 Introduction

Gravity and dark energy govern the structure in the universe at the largest scales but complex baryonic processes like cooling, heating, self-gravity and star formation are important at galactic scales (e.g., Springel et al. (2005) [186]). Numerical simulations have made tremendous progress in understanding galaxy formation, starting from pure gravitational N-body simulations to the current models which try to model the aforementioned complex processes. Modeling the gravitationally-interacting dark matter is straightforward in principle, and only limited by the available computing power. But the modeling of baryonic processes is rather involved. In particular, there is no consensus on which baryonic processes are important and how they should be implemented numerically. Given the dynamic range of scales, from large scale structure (10s of Mpc) to an individual star forming cloud (∼pc), simulations have to resort to unresolved 'subgrid' models for star formation and feedback due to star formation (e.g., Gerritsen (1997) [63], Guedes et al. (2011) [69], Hopkins, Quataert, & Murray (2012) [89], Navarro & White (1993) [140], Springel & Hernquist (2003) [185] and references therein). While different star formation recipes seem to give similar star formation histories and stellar mass distributions, provided molecular clouds are resolved (e.g., Hopkins, Quataert, & Murray (2011) [88]), simulations are quite sensitive to the various feedback prescriptions (e.g., thermal feedback due to supernovae, momentum injection via dust absorbing/scattering photons produced by massive stars and supernovae) even with high resolution.

Stars form in clusters and super-star-clusters (100s to 10^6 stars) of various sizes and in different environments, ranging from low density galactic outskirts to dense galactic centers (see Portegies Zwart et al. (2010) [156] for a review). These clusters are observed to disrupt the dense molecular clouds in which they are born (e.g., see Leisawitz et al. (1989) [114], Zhang et al. (2001) [233]). This stellar feedback (due to strong radiation, stellar winds and supernovae) disperses cold gas and suppresses further star formation. Because of the stellar initial mass function (IMF) and the main

sequence lifetimes, the energy input is roughly constant per unit time over the life time of stars more massive than 8 $M_\odot$ ($\sim$ 50 Myr; McCray & Kafatos (1987) [130]). Therefore, stellar feedback is sometimes modeled as a constant luminosity driven blast wave (Gerritsen (1997) [63], MacLow et al. (1989) [122], Weaver et al. (1977) [224]). A superbubble (SB) expands faster than an isolated supernova remnant (SNR) because of continuous energy injection, and suffers smaller cooling losses because most supernovae (SNe) go off in a low density bubble.

The hot bubble breaks out through the gas disk if the outer shock driven by overlapping SNe crosses the scale height with a sufficient Mach number within the starburst lifetime (e.g., see section 2 of Roy et al. (2013) [164]). After breakout the hot, metal-rich stellar ejecta is spread out into the galactic halo via the Rayleigh-Taylor instability. Spreading of metals over large scales is required to explain the high metallicity observed in the intergalactic medium (IGM), far away from the stellar disk (Tumlinson et al. (2011) [212]). While this fact, that the formation of low density bubble is important so that the explosions can occur in a medium where radiative cooling is negligible in order to create the SNe feedback to be effective (as discussed in chapter 1), has been appreciated (e.g., Gnedin (1998) [65], Joung & Mac Low (2006) [95]), we present *quantitative* conditions for the formation of a strong shock and a hot, dilute bubble for different thermal feedback prescriptions.

The continuous injection of mass and energy by SNe deep within the hot SB is expected to launch a steady wind (as first calculated by Chevalier & Clegg (1985) [25]; hereafter CC85). CC85 obtained analytic solutions for a superwind assuming a constant thermal energy and mass input rate with an injection radius. By modeling realistic SNe as fast moving ejecta within SBs we show that a steady CC85 wind is obtained only if a large number of SNe ($\gtrsim 10^4$) go off within the star cluster. For a smaller number of SNe, an individual SN's kinetic energy is not thermalized within a small injection radius and there is an unsteady outflow. This should have implications for works that simply assume a CC85 wind within the SB.

This chapter presents the analytic results that can be readily used for the numerical implementation of thermal feedback using various recipes. These analytic criteria are verified and extended using idealized numerical simulations. The fundamental difference between isolated supernovae and superbubbles – that the former is ineffective on galactic scales – is highlighted. By modeling realistic SNe as fast moving ejecta within SBs we also show that a steady CC85 wind is obtained only if a large number of SNe ($\gtrsim 10^4$) go off within the star cluster. For a smaller number of SNe, an individual SN's kinetic energy is not thermalized within a small injection radius and there is an unsteady outflow. This should have implications for works that simply assume a CC85 wind within the SB.

This chapter is organized as follows. In section 2.2 we describe various ways of implementing thermal feedback due to SNe. Section 2.3 describes the numerical setup used to study SNe and SBs. In section 2.4 we present different analytic criteria for feedback to work with a range of feedback prescriptions. We also derive the conditions for obtaining a thermalized CC85 wind within a SB. In section 4.4 we present 1-D numerical simulations of different feedback recipes with and without cooling, and compare the results with our analytic estimates. We also briefly discuss the effects of magnetic fields and thermal conduction.

2.2 ISM & SN feedback prescriptions

Although ISM is multiphase and extremely complex, for simplicity we consider a uniform, static model with a given density (typically $n = 1$ cm^{-3}) and temperature (10^4 K corresponding to the warm ISM). We do not consider stratification because the disk scale height is typically a few 100 pc and the fizzling of SN feedback is essentially a small scale problem. Moreover, the scales of interest (100s of pc; few Myr) are much bigger than the cluster size and the local ISM/circumstellar inhomogeneities. For simplicity we also assume that all SNe explode at $r = 0$. This is a good approximation

because the size of a typical (super) star-cluster is smaller than the bubble size at the beginning of the radiative phase.

The SN prescriptions that we consider in our analytic estimates and numerical simulations cover the full range of methods used in the literature. These are:

1. *Kinetic Explosion Models* (KE): In these models the SN energy ($E_{\rm ej}$, chosen to be 1 Bethe $\equiv 10^{51}$ erg) is given to a specified ejecta mass ($M_{\rm ej}$, chosen to be 1 $M_\odot$) distributed uniformly with an ejecta density $\rho_{\rm ej} = 3M_{\rm ej}/[4\pi r_{\rm ej}^3]$ within an ejecta radius $r_{\rm ej}$. The ejecta velocity is homologous with $v_{\rm ej}(r) = v_0(r/r_{\rm ej})$ within the ejecta; the normalization is such that the kinetic energy of the ejecta is $E_{\rm ej}$; i.e., $v_0 = (10E_{\rm ej}/3M_{\rm ej})^{1/2}$. The ejecta temperature is taken to be small ($T_{\rm ej} = 10^4$ K). After every (fixed) SN injection time $t_{\rm SN}$ the innermost $r_{\rm ej}$ of the volume is *overwritten* by the ejecta density and velocity, thereby pumping SN energy into the ISM. After the reverse shock propagates toward the bubble center, once the swept-up mass is comparable to the ejecta mass, the bubble density structure is fairly insensitive to the ejecta density distribution (Truelove & McKee (1999) [209]). This model most closely resembles a physical SNR in early stages at small ($\ll 1$ pc) scales when the SN 'piston' at large speed rams into the ISM. This prescription is not widely used in galaxy formation simulations (there are some exceptions, e.g., Tang & Wang (2005) [199]).

2. *Thermal Explosion Models* (TE): In these models the energy is deposited within the ejecta radius in form of thermal energy at an interval of $t_{\rm SN}$. There are two variants of this model. In one class, the mass and internal energy densities are *overwritten* within the ejecta radius ($r_{\rm ej}$) such that the *uniformly distributed* ejecta thermal energy is $E_{\rm ej}$ (1 Bethe) and the *uniformly distributed* ejecta mass is $M_{\rm ej}$ ($1M_\odot$). We abbreviate these models as TEo and they behave like KE models. The second class of models is where we *add* (in contrast to overwrite) the ejecta mass (with uniform density) to the preexisting mass and the ejecta thermal energy (distributed uniformly) to the preexisting internal energy within

$r_{\rm ej}$. We refer to these models as TEa. There are significant differences between the TEa and TEo/KE models in presence of cooling because TEa ejecta can become radiative if thermal energy is added to a dense ISM. Most models in the literature are analogous to TEa models with some variations (e.g., Katz (1992) [100], Joung & Mac Low (2006) [95], Creasey, Theuns, & Bower (2013) [37]; some works such as Stinson et al. (2006) [188] , Thacker & Couchman (2000) [203], Agertz, Teyssier, & Moore (2011) [2] unphysically turn off cooling for some time for SN feedback to have an impact). Sometimes all the SN energy is deposited in a single grid cell (e.g., Tasker & Bryan (2006) [200]) or in a single particle (e.g., SN particle method in section 3.2.4 of Gerritsen (1997) [63]).

3. *Luminosity Driven Models* (LD): As discussed earlier, for typical IMFs, the mechanical energy input due to OB stars per unit time is roughly constant. This motivates a model in which internal energy and mass within an injection radius (denoted by $r_{\rm ej}$) increase at a constant rate corresponding to internal energy $E_{\rm ej}$ and mass $M_{\rm ej}$ for each SN. Some of the works that use this prescription are Chevalier & Clegg (1985) [25], Cooper et al. (2008) [32], MacLow et al. (1989) [122], Mac Low & Ferrara (1999) [123], Palouš et al. (2013) [153], Recchi & Hensler (2013) [160], Roy et al. (2013) [164], Strickland & Stevens (2000) [190], Suchkov et al. (1994) [193].

All our models are identified with the number of OB stars $N_{\rm OB}$ (which equals the number of SNe in the star cluster) or luminosity $L_{\rm ej} = E_{\rm ej}/t_{\rm SN} = N_{\rm OB}E_{\rm ej}/t_{\rm OB}$, where $t_{\rm OB}$ is the lifetime of the OB association (taken to be 30 Myr) and $t_{\rm SN} = t_{\rm OB}/N_{\rm OB}$ is the time interval between SNe. We note that the overwrite models do not strictly conserve mass and energy. While the supernova energy is much larger than the overwritten thermal energy, one needs to choose a small enough ejecta radius such that the overwritten mass is subdominant relative to the ejecta mass. The explosion models are substantially slower compared to the smooth luminosity driven models

because of very high temperatures created due to sudden energy injection in the former.

2.3 Numerical setup

In this section we describe the numerical setup corresponding to our one-dimensional simulations discussed in section 4.4. Our numerical simulations use the ISM setup and the various feedback prescriptions described in section 2.2. The ISM density and temperature are chosen to 1 cm^{-3} and 10^4 K, respectively, unless specified otherwise. The mean mass per particle is $\mu = 0.62$ and per electron is $\mu_e = 1.17$. The initial density and temperature are uniform, and the velocity is zero.

We use the grid-based `ZEUS-MP` code in spherical, one-dimensional geometry (Hayes et al. (2006) [73]) to solve the standard Euler equations with source terms mimicking SN energy/momentum/mass injection for the chosen feedback model, and a sink term in the internal energy equation representing radiative cooling. Our equations are similar but not identical to Eqs. 20-22 in Roy et al. (2013) [164].[1] We note that the `ZEUS` code does not conserve energy to the machine precision. However, we have confirmed that energy conservation holds to better than 90% in most of our runs. In fact, the Sedov-Taylor blast wave in 1-D spherical coordinates is one of the standard test problems presented in Hayes et al. (2006) [73]; the numerical results match analytic solutions very closely. While most of our runs are hydro, in section 2.5.4 we briefly discuss runs with simple models of magnetic fields and thermal conduction; various parameters for these runs are discussed there.

The radial velocity is set to zero at the inner radial boundary and other fluid variables are copied in the ghost cells. Outflow boundary conditions are applied at the outer radial boundary. Note that the outer boundary is out of causal contact.

[1] The difference from Roy et al. (2013) [164] is that the mass and energy source terms are not uniform in time. Moreover, different feedback heating prescriptions use different source terms; e.g., KE models use a momentum source term rather than a source term in the internal energy equation.

Since the setup produces strong shocks, we use the standard ZEUS artificial viscosity to prevent unphysical oscillations at shocks (Stone & Norman (1992) [189]). The CFL number of 0.2 is found to be more robust compared to the standard value of 0.5, and is used in all the simulations.

The cooling function that we use is the collisional-ionization-equilibrium based solar metallicity table of Sutherland & Dopita (1993) [197], with the cooling function set to zero below 10^4 K. The cooling step is implemented via operator splitting using the semi-implicit method of Sharma, Parrish, & Quataert (2010) [176]. Cooling is subcycled and the number of subcycles is limited to be less than 100.

Most of our runs use a 1024 resolution grid extending from 1 pc to 2 kpc. A logarithmically spaced grid is used to better resolve smaller radii; there are equal number of grid points covering 1 pc to $\sqrt{2000}$ pc and $\sqrt{2000}$ pc to 2 kpc. Some runs with stronger SN feedback use a larger spatial extent (c.f. $N_{\rm OB} = 10^6$ runs in Fig. 2.3), and some uniform very high resolution runs (16384 grid points; c.f. Fig. 2.5) use a smaller extent (1 to 200 pc). All our simulations (except the very high resolution ones that are run for 3 Myr) are run for 30 Myr, typical age of a young star cluster.

2.4 Analytic criteria

In this section we present the analytic criteria that need to be satisfied for various feedback models discussed in section 2.2 to work. These analytic estimates help us understand the results of numerical simulations discussed in section 4.4. While radiative cooling is the most discussed phenomenon in the context of fizzling SN feedback, the feedback prescription should satisfy additional constraints for the energy input to couple realistically with the ISM. A recurring concept in what follows is that of thermalization; i.e., in order to be effective the input energy should have time to couple to the ISM before it is radiated or is overwritten. In section 2.4.3 we show that a steady superwind within a superbubble, as envisaged by Chevalier & Clegg

(1985) [25], occurs only if the number of SNe is sufficiently large.

In the following sections we derive upper limits on the ejecta radius within which the feedback energy must be deposited for it to be effective. We can easily convert this radius limit into a critical mass resolution needed in smooth-particle-hydrodynamics (SPH) simulations; namely, $n_{\rm nbr} m_{\rm crit} \approx (4\pi/3)\rho r_{\rm crit}^3$, where ρ is the ISM density, $n_{\rm nbr}$ is the number of neighbors used in the SPH smoothing kernel and $m_{\rm crit}$ is the maximum SPH gas particle mass required for feedback to work.

2.4.1 Energy coupling without cooling

Ejecta radius constraint for overwrite models

In models where energy within the ejecta radius is overwritten (KE, TEo) the ejecta radius should be smaller than a critical radius ($r_{\rm ej} \lesssim r_{\rm crit}$) for the input energy to get coupled to the ISM. The critical radius equals the Sedov-Taylor shock radius at $t_{\rm SN}$,[2] the time lag between SNe,

$$r_{\rm crit} \equiv \left(\frac{E_{\rm ej} t_{\rm SN}^2}{\rho}\right)^{1/5} \approx 50 \text{ pc } n^{-1/5} E_{\rm ej,51}^{1/5} t_{\rm SN,0.3}^{2/5}, \tag{2.1}$$

where ρ (n) is the ISM (number) density (assuming $\mu = 0.62$), $E_{\rm ej,51}$ is the ejecta energy in units of 10^{51} erg, and $t_{\rm SN,0.3}$ is the time between consecutive SNe in units of 0.3 Myr. If the ejecta radius is larger than this value the ejecta energy is overwritten before it can push the outer shock. Thus, in such a case, the input SN energy is overwritten without much affecting the ISM.

[2] We use the Sedov-Taylor expression for the bubble radius in Eq. 2.1 because the shock quickly transitions from a free-expanding to a Sedov-Taylor state; the Sedov-Taylor radius (when the swept up ISM mass equals the ejecta mass) is $r_{\rm ST} \equiv (3M_{\rm ej}/4\pi\rho)^{1/3} \approx 2.5$ pc $M_{\rm ej,\odot}^{1/3} n^{-1/3}$, much smaller than the estimate in Eq. 2.1, where $M_{\rm ej,\odot}$ is the ejecta mass in solar units.

Sonic constraint

For thermal SN feedback to launch a strong shock the energy should be deposited over a small enough volume, such that the post-shock pressure is much larger than the ISM pressure. This is equivalent to demanding the outer shock velocity to be much larger than the sound speed in the ISM. The shock velocity ($v_{\rm OS} \equiv dr_{\rm OS}/dt$; $r_{\rm OS}$ is the outer shock radius), expressed in terms of the shock radius in Sedov-Taylor stage, is $v_{\rm OS} \approx 0.4 E_{\rm ej}^{1/2} \rho^{-1/2} r_{\rm OS}^{-3/2}$ for an isolated SN and $v_{\rm OS} \approx 0.6 L_{\rm ej}^{1/3} \rho^{-1/3} r_{\rm OS}^{-2/3}$ for a luminosity driven SB (Weaver et al. (1977) [224]). The condition for a strong shock for an isolated SN is ($v_{\rm OS} \lesssim a_T$; a_T is the ISM isothermal sound speed)

$$r_{\rm ej} \lesssim 174 \text{ pc } E_{\rm ej,51}^{1/3} n^{-1/3} T_4^{-1/3} \tag{2.2}$$

and for a SB is (see Eq. 3 in Silich et al. (2009) [181])

$$r_{\rm ej} \lesssim 1.5 \text{ kpc } L_{\rm ej,38}^{1/2} n^{-1/2} T_4^{-3/4}, \tag{2.3}$$

where $L_{\rm ej,38}$ is the ejecta luminosity ($L_{\rm ej} = E_{\rm ej}/t_{\rm SN}$ for explosion models) in units of 10^{38} erg s^{-1} (this corresponds to $N_{\rm OB} = 100$ over $t_{\rm OB} = 30$ Myr) and T_4 is the ISM temperature in units of 10^4 K.

The sonic constraint ($v_{\rm OS} \lesssim a_T$) is typically less restrictive than the compactness requirements due to cooling in a dense ISM (see next section). Tang & Wang (2005) [199], who considered supernova feedback in the hot ISM ($\sim 10^7$ K) of galaxy clusters and elliptical galaxies, found that the shock can quickly (when outer radius is only ≈ 20 pc; see Eq. 2.2) decelerate to attain the sound speed in the hot ISM. After this the outer shock propagates as a sound wave. While the sound wave can spread the SN energy over a larger radius ($\propto t$ for a sound wave, unlike a strong blast wave in which $r_{\rm OS} \propto t^{2/5}$), energy dissipation is not as efficient as in shocks.

2.4.2 Energy coupling with cooling

Luminosity driven model

In luminosity driven models (LD), SN feedback does not fizzle out (in fact, the shock can get started) only if the cooling rate is smaller than the energy deposition rate, i.e., $3L_{\rm ej}/4\pi r_{\rm ej}^3 \gtrsim n^2\Lambda$ ($\Lambda[T]$ is the cooling function), or

$$r_{\rm ej} \lesssim 20 \text{ pc } L_{\rm ej,38}^{1/3} n^{-2/3} \Lambda_{-22}^{-1/3}, \tag{2.4}$$

where Λ_{-22} is the cooling function in units of 10^{-22} erg cm^3 s^{-1}.

Thermal explosion addition model

The above criterion (Eq. 2.4) for the luminosity driven models is quite different from the criterion that we now derive for the widely used thermal explosion models with energy and mass addition (TEa model in section 2.2). Since energy is *added* to the (possibly dense) pre-existing medium, cooling in this model can be substantial. In contrast, since the ejecta density is low, cooling losses are smaller in the overwriting models (KE, TEo). For TEa models to launch a shock, radiative losses over the timescale in which the shock from a point explosion reaches the ejecta radius,

$$t_{\rm ej} = E_{\rm ej}^{-1/2} r_{\rm ej}^{5/2} \rho^{1/2}, \tag{2.5}$$

should be smaller than the energy deposited (here ρ is the density of the medium in which energy is injected, not necessarily the ISM density); i.e.,

$$n^2 \Lambda t_{\rm ej} \lesssim 3E_{\rm ej}/4\pi r_{\rm ej}^3. \tag{2.6}$$

Plugging in the expression for $t_{\rm ej}$, we get

$$r_{\rm ej} \lesssim 31 \text{ pc } E_{\rm ej,51}^{3/11} \Lambda_{-22}^{-2/11} n^{-5/11}. \tag{2.7}$$

This condition is much more restrictive than the one obtained by replacing $t_{\rm ej}$ in Eq. 2.6 by the CFL stability timestep. Moreover, this is the appropriate timescale to use

because the relevant timescale for the injected energy to couple to the ISM is the thermalization time ($t_{\rm ej}$).

Creasey et al. (2011) [36] and Dalla Vecchia & Schaye (2012) [39] have used similar arguments and derived results not too different from ours for the thermal explosion addition models. A slight difference from our work is that they consider energy deposition over a resolution element (a necessity because of a larger range of scales in cosmological galaxy simulations), but we allow for energy deposition over a resolved region. Creasey et al. (2011) [36] have expressed their resolution limit in terms of the cooling rate per unit mass and Dalla Vecchia & Schaye (2012) [39] in terms of the post-shock temperature; we use the cooling function (Λ) to express the critical radius within which the energy needs to be deposited.

Overwrite models

In models where the energy and mass densities are overwritten within $r_{\rm ej}$, the condition for overcoming cooling losses and launching a shock is

$$n_{\rm ej}^2 \Lambda t_{\rm ej} \lesssim \frac{3E_{\rm ej}}{4\pi r_{\rm ej}^3},$$

where ejecta number density $n_{\rm ej} = \rho_{\rm ej}/\mu m_p$ and $\rho_{\rm ej} = 3M_{\rm ej}/4\pi r_{\rm ej}^3$; note that this expression is different from Eq. 2.6 in that the ejecta density is used instead of the ISM density. The overwrite models (KE, TEo) behave quite differently from addition (TEa, LD) models because a larger ejecta radius means a smaller density ejecta to which energy is added. Replacing the ISM density by the ejecta density in Eq. 2.5 gives $t_{\rm ej} = E_{\rm ej}^{-1/2} r_{\rm ej}^{5/2} \rho_{\rm ej}^{1/2}$, and the condition for energy thermalization is

$$r_{\rm ej} \gtrsim 0.003 \text{ pc } M_{\rm ej,\odot}^{5/4} \Lambda_{-22}^{1/2} E_{\rm ej,51}^{-3/4}. \tag{2.8}$$

In order to avoid radiative losses the ejecta radius should be *larger* than above. This early cooling of the mass loaded SN ejecta, responsible for creating cold filaments in young SNe (e.g., Chevalier & Blondin (1995) [26]), is physical (unlike fizzling out of

the energy addition models) and should reduce the energy available to drive the SN. All our simulations use an ejecta radius much greater than this limit.

2.4.3 Conditions for CC85 wind

Chevalier & Clegg (1985) [25] (hereafter CC85) found analytic solutions for a luminosity driven wind with a fixed injection radius. Luminosity injection is expected to drive both an outer shock bounding the bubble and a wind that shocks within the hot bubble at the termination shock (see Fig. 1 in Weaver et al. (1977) [224]; see also LD run in Fig. 2.3). In this section we show that for a small number of SNe (c.f. Eq. 2.11) the SN ejecta does not thermalize within the termination shock. In that case, the density inside the bubble is much lower than the CC85 wind because most SNe occur in the dilute bubble created by earlier SNe and the thermalization radius is comparable to the outer shock radius. This has important implications on cooling and luminosity of SN ejecta.

Following Weaver et al. (1977) [224], the outer shock radius of a luminosity driven bubble is given by $r_{\rm OS} \approx (L_{\rm ej} t^3/\rho)^{1/5}$, velocity by $v_{\rm OS} \approx 0.6 r_{\rm OS}/t \propto t^{-2/5}$, and the post-shock pressure by $p_{OS} \approx 0.75 \rho v_{\rm OS}^2 \approx 0.27 L_{\rm ej}^{2/5} \rho^{3/5} t^{-4/5}$. Assuming a steady superwind, the ram pressure at the termination shock ($r_{\rm TS}$; the wind is assumed to be supersonic at this radius) is $\rho_{\rm TS} v_{\rm TS}^2 = \dot{M}_{\rm ej} v_{\rm TS}/(4\pi r_{\rm TS}^2)$, where $v_{\rm TS} = (2L_{\rm ej}/\dot{M}_{\rm ej})^{1/2}$ is the wind velocity, $\rho_{\rm TS}$ is the density upstream of the termination shock, and $\dot{M}_{\rm ej}$ is the mass injection rate. The wind termination shock ($r_{\rm TS}$) is located where the wind ram pressure balances the bubble pressure; i.e.,

$$\frac{\dot{M}_{\rm ej} v_{\rm TS}}{4\pi r_{\rm TS}^2} \approx 0.75 \rho v_{\rm OS}^2.$$

Using $v_{\rm OS} \approx 0.6 L_{\rm ej}^{1/3} \rho^{-1/3} r_{\rm OS}^{-2/3}$ and $\dot{M}_{\rm ej} = 2L_{\rm ej}/v_{\rm TS}^2$ gives,

$$\frac{r_{\rm TS}}{r_{\rm OS}} \approx \left(\frac{v_{\rm OS}}{v_{\rm TS}}\right)^{1/2} \approx 0.08 E_{\rm ej,51}^{-1/12} M_{\rm ej,\odot}^{1/4} n^{-1/6} r_{\rm OS,2}^{-1/3} t_{\rm SN,0.3}^{-1/6}, \tag{2.9}$$

where $r_{\rm OS,2}$ is the outer shock radius in units of 100 pc, $t_{\rm SN,0.3}$ is the time between SNe normalized to 0.3 Myr (corresponding to $N_{\rm OB} = 100$); we have used $L_{\rm ej} = E_{\rm ej}/t_{\rm SN}$

and $\dot{M}_{\rm ej} = M_{\rm ej}/t_{\rm SN}$. The ratio $r_{\rm TS}/r_{\rm OS}$ depends very weakly on time ($\propto t^{-1/5}$); this comes from the time dependence of $r_{\rm OS}$ in Eq. 2.9. The reverse shock for an isolated SN very quickly (at the beginning of Sedov-Taylor stage) collapses to a point but the termination shock for a SB is present at all times. Thus the non-radiative termination shock can power a SB long after the outer shock becomes radiative, unlike a SN which dies off shortly after the outer shock becomes radiative (see section 2.5.4 for our results from simulations).

The condition for the existence of a smooth CC85 wind is that the ejecta thermalization radius should be smaller than the termination shock radius. The superwind is mass loaded by previous SNe (the bubble density in the absence of mass loading is quite small because most of the mass is swept up in the outer shell). The swept up mass till radius r in a CC85 wind is

$$M_{\rm sw} = \int_0^r 4\pi r'^2 \rho_w(r') dr' \approx \frac{\dot{M}_{\rm ej} r}{v_{\rm TS}} = \frac{M_{\rm ej} r}{t_{\rm SN} v_{\rm TS}},$$

where $\rho_w(r')$ is the wind density profile; here we have assumed that the swept up mass is dominated by the supersonic portion of the wind. Now the thermalization radius (the radius within which the deposited energy is thermalized and which should correspond to CC85's injection radius) of the ejecta is where the swept up mass roughly equals the ejecta mass, or

$$r_{\rm th} \approx v_{\rm TS} t_{\rm SN} \approx 3 \text{ kpc } E_{\rm ej,51}^{1/2} M_{\rm ej,\odot}^{-1/2} t_{\rm SN,0.3}. \tag{2.10}$$

Since the thermalization radius is quite large, a thermalized CC85 solution will only occur for large clusters (with shorter $t_{\rm SN}$, the time lag between SNe); for modest star clusters the ejecta will only thermalize beyond the termination shock. Of course, the thermalization radius cannot be smaller than the size of the star cluster launching the energetic ejecta. Using Eq. 2.9 and $r_{\rm OS} \approx (L_{\rm ej} t^3/\rho)^{1/5}$, the termination shock radius can be expressed as

$$r_{\rm TS} \approx 5 \text{ pc } E_{\rm ej,51}^{1/20} M_{\rm ej,\odot}^{1/4} n^{-3/10} t_{\rm SN,0.3}^{-3/10} t_{0.3}^{2/5},$$

where $t_{0.3}$ is time in units of 0.3 Myr. A CC85 solution will appear only if this termination shock radius is larger than the thermalization radius (Eq. 2.10); i.e., if

$$t_{\rm SN,0.3} \lesssim 0.007 E_{\rm ej,51}^{-9/26} t_{0.3}^{4/13} n^{-3/13} M_{\rm ej,\odot}^{15/26}. \tag{2.11}$$

This means that $N_{\rm OB} \gtrsim 3500$ (recall that $t_{\rm SN} = t_{\rm OB}/N_{\rm OB}$, where $t_{\rm OB} = 30$ Myr is the cluster lifetime and $N_{\rm OB}$ is the number of SNe) is required for a CC85 wind to appear by 30 Myr. Thus, a thermally driven CC85 wind occurs only for a sufficiently big starburst, with a large mass loading, and at late times.

2.5 Simulation Results

In this section we present the results from our one-dimensional numerical simulations. We vary the ISM density and SN injection parameters to assess when SN energy can significantly affect the ISM, both with and without cooling. We also numerically verify the various analytic constraints presented in section 2.4. We discuss the structure of a radiative SB and compare the energetics of isolated SNe and SBs. While isolated SNe lose most of their mechanical energy by a few Myr, SBs can retain up to $\sim 40\%$ of the input energy long after the outer shock becomes radiative. Thus, SBs, and not isolated SNe, are the viable energy sources for global, galactic-scale feedback. In section 2.5.4 we briefly discuss the impact of magnetic fields and thermal conduction on SBs.

2.5.1 Realistic SN shock (KE models)

The SN shock is launched once a protoneutron star forms at the center of a massive evolved star (with size $\sim 10^{14}$ cm). In the ejecta dominated state (when the swept up ISM mass is less than the ejecta mass) the cold ejecta is dominated by kinetic energy (e.g., Truelove & McKee (1999) [209]). In our 'realistic' simulations (KE models; see section 2) we choose the ejecta to have a constant density and a velocity

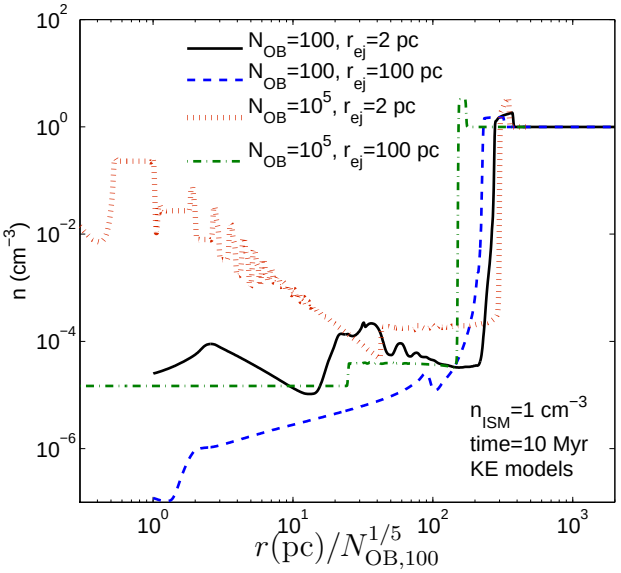

Figure 2.1: Number density as a function of radius (scaled to the self-similar scaling) for different parameters of realistic KE runs at 10 Myr. The outer shock is closer in for models using a larger ejecta radius because energy is overwritten before it can couple to the ISM.

proportional to the radius (homologous expansion; this is a similarity solution for the freely expanding ejecta) within the ejecta. The SN shock develops a reverse shock after sweeping up its own mass in the ISM; this slows down the ejecta and communicates the presence of the ISM to the supersonic ejecta. In this section we compare the evolution of *adiabatic* (cooling is turned off) KE models with different parameters, highlighting the importance of having a small ejecta radius ($r_{\rm ej}$) even in absence of cooling for overwrite (KE, TEo) models. We have verified that kinetic explosion (KE) and thermal explosion overwrite (TEo) models behave in a similar fashion.

Figure 2.1 shows the density profile as a function of radius (normalized to the self similar scaling, $r_{\rm OS} \approx [L_{\rm ej} t^3/\rho]^{1/5}$, where $L_{\rm ej} = E_{\rm ej}/t_{\rm SN} = E_{\rm ej} N_{\rm OB}/t_{\rm OB}$) for different realistic runs (results are similar for TEo models) with $N_{\rm OB} = 100,\ 10^5$ at 10 Myr. The runs with a large ejecta radius (100 pc) give a smaller outer shock radius because

most of the energy is overwritten without being thermalized (see section 2.4.1 for a discussion). The problem is worse for larger $N_{\rm OB}$ (shorter $t_{\rm SN}$), as expected from Eq. 2.1. The normalized location of the outer shock falls almost on top of each other for a small ejecta radius ($r_{\rm ej}$ = 2 pc). As expected, the shock is weaker, broader, and with a modest density jump for a smaller number of SNe.

2.5.2 Comparison of adiabatic models

While the KE model is most realistic, we expect other models in section 2.2 to give a similar location for the outer shock after the swept-up ISM mass equals the ejecta mass and the shock is in the Sedov-Taylor regime. The structure within the bubble depends on SN prescription, as we show in section 2.5.3.

Figure 2.2 shows the location of the outer shock (measured by its peak density) as a function of time for various models (KE, LD, TEa) and SN parameters in absence of cooling. The solid line at the bottom shows the transition from a single blast wave (outer shock radius, $r_{\rm OS} \propto t^{2/5}$) to a continuously driven bubble ($r_{\rm OS} \propto t^{3/5}$; Weaver et al. (1977) [224]) for $N_{\rm OB}$ = 100 run. The runs with more SNe show such a transition very early on. The dot-dashed line shows the outer shock radius for the KE run using a large ejecta radius violating the criterion in Eq. 2.1; the outer shock radius is much smaller than expected because energy is overwritten before it energizes the hot bubble (see section 2.4.1). The luminosity driven (LD) and kinetic explosion (KE) models agree only if the ejecta radius satisfies Eq. 2.1 for KE models (we have verified that this constraint also applies to the thermal explosion overwrite [TEo] models). TEa (thermal explosion addition) runs and LD runs fall on top of each other for both choices of $r_{\rm ej}$ (2, 100 pc). The outer shock radii for the runs with $r_{\rm ej}$ = 100 pc increase only after a thermalization time (Eq. 2.5; although in this case ρ is not the ISM density but the much lower density of the bubble within which energy is added).

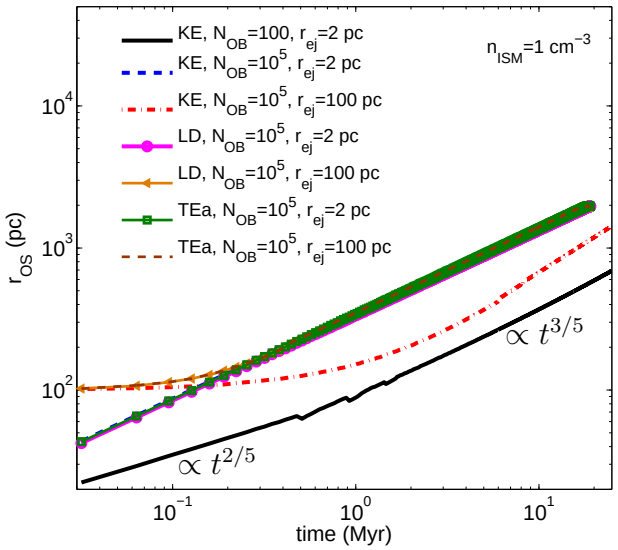

Figure 2.2: The outer shock radius as a function of time for various runs using kinetic explosion (KE), luminosity driven (LD) and thermal explosion addition (TEa) models. The KE models give correct results only if the ejecta radius ($r_{\rm ej}$) is sufficiently small; otherwise energy is overwritten before getting coupled to the ISM. There is no such problem for energy addition and luminosity driven models. At early times the outer shock radius scales with the Sedov-Taylor scaling ($r_{\rm OS} \propto t^{2/5}$) and later on, after many SNe go off, it steepens ($r_{\rm OS} \propto t^{3/5}$).

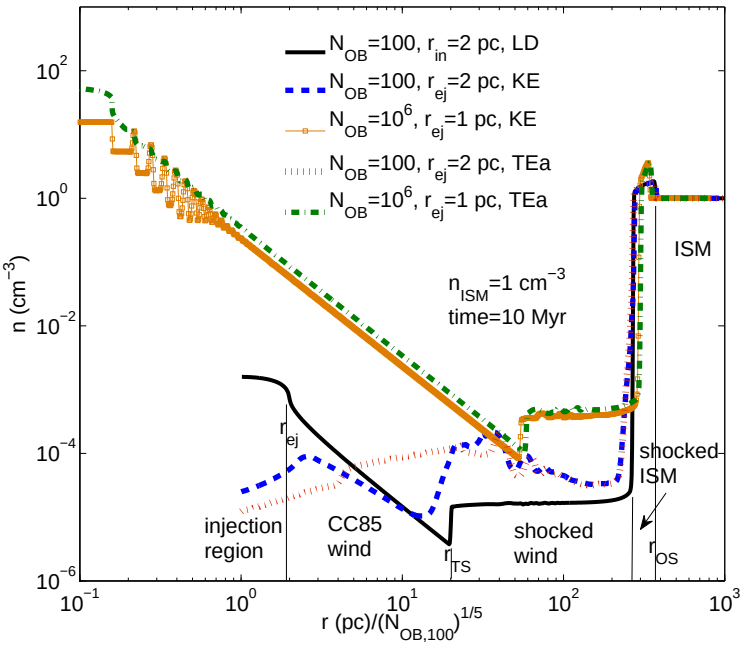

Figure 2.3: Density profile as a function of normalized radius for luminosity driven (LD), kinetic explosion (KE), and thermal explosion addition (TEa) models. The standard CC85 wind within the bubble appears for the LD model, and for KE and TEa models with $N_{\rm OB} = 10^6$, but not for KE/TEa models with $N_{\rm OB} = 100$; the smooth CC85 wind is identified by the density profile varying $\propto r^{-2}$ between the ejecta radius and the termination shock (various regions have been marked for the LD run). The CC85 wind density using $N_{\rm OB} = 10^6$ is slightly smaller for the KE model compared to the TEa model because density is overwritten (and hence mass is lost) in KE models.

2.5.3 CC85 wind within the bubble

In this section we show that a simple steady wind, as predicted by CC85, exists within the bubble only if the number of SNe is sufficiently large (see section 2.4.3). Figure 2.3 shows the density profile as a function of the scaled radius for various models. The solid line shows density for a luminosity driven (LD) model with $N_{\rm OB} = 100$ and $r_{\rm ej} = 2$ pc; various regions for the smooth CC85 wind within the bubble are marked. The superwind has a structure identical to the CC85 wind; the sonic point is just beyond the energy injection radius (2 pc). The wind shocks at the termination shock

($r_{\rm TS}$) where the wind ram pressure balances the bubble pressure. The ratio of the termination shock and the outer shock ($r_{\rm OS}$) is ≈ 0.07, in good agreement with Eq. 2.9. For comparison, Figure 2.3 also shows the density profiles for the kinetic explosion (KE) and thermal explosion addition (TEa) models with the same parameters. While the outer shock radius agree for these runs, the density profiles within the bubble are quite different. The most blatant difference, for runs with $N_{\rm OB} = 100$, is the absence of a CC85 wind in KE and TEa models. In accordance with the discussion in section 2.4.3, SN shocks do not thermalize within the termination shock for a small number of SNe (see Eqs. 2.10 & 2.11); therefore a smooth CC85 wind is not expected in any model with small $N_{\rm OB}$ except LD.

Only for a large enough $N_{\rm OB}$ and late enough times does a CC85 wind start to appear within the hot bubble. Figure 2.3 includes the density profiles for kinetic explosion (KE) and TEa models using $N_{\rm OB} = 10^6$ (the inner [outer] radius of the computational domain for these runs is 0.5 pc [5 kpc]; $r_{\rm ej} = 1$ pc is chosen to satisfy the constraint in Eq. 2.1). Clearly, in these cases we see the appearance of the CC85 wind solution within the termination shock because the injected energy is thermalized. For the KE run with $N_{\rm OB} = 10^6$ one can still see the internal shocks due to isolated SNe interacting with the superwind. The density profile for the KE model using $N_{\rm OB} = 10^5$ is shown by the dotted line in Figure 2.1. In agreement with Eq. 2.9, the ratio $r_{\rm TS}/r_{\rm OS}$ increases with an increasing $N_{\rm OB}$. For $N_{\rm OB} = 10^5$ thermalization is less complete as compared to $N_{\rm OB} = 10^6$, but happens within the termination shock. In comparison, a clear termination shock is absent for $N_{\rm OB} = 100$ because the thermalization radius is larger than the termination shock radius (see Eq. 2.11).

2.5.4 Effects of radiative cooling

In this section we study the effects of radiative cooling on SNe and SBs. We focus on a few aspects: the fizzling out of thermal feedback in some models in which energy is not injected over a sufficiently small scale; comparison of cooling losses and

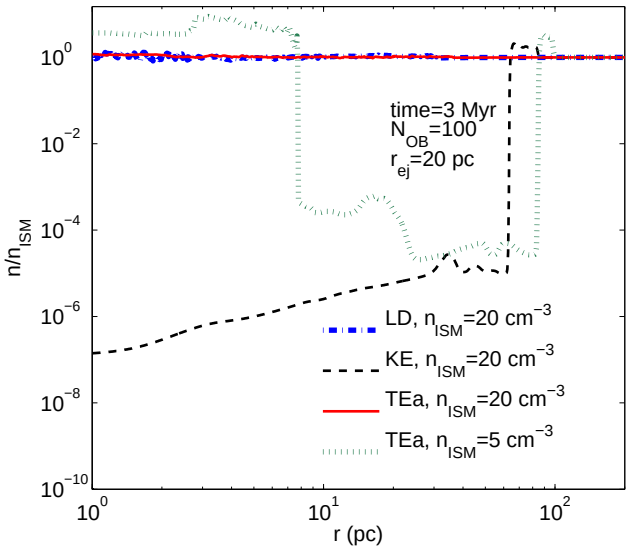

Figure 2.4: Density as a function of radius for different runs at 3 Myr to show that energy addition totally fizzles out for a high ISM density. While TEa and LD models do not show the formation of a hot, dilute bubble for ISM density of 20 cm^{-3}, KE model indeed shows a bubble and a forward shock. Also shown is the density profile for TEa model with a lower density (5 cm^{-3}) ISM; at later times it shows a bubble which pushes the shell outwards. The outer shock radius is larger for a lower density ISM because $r_{\rm OS} \propto \rho^{-1/5}$.

mechanical energy retained by radiative SNRs and SBs; the influence of magnetic fields and thermal conduction.

Unphysical cooling losses with thermal energy addition

As we mentioned in section 2.4.2, some models (TEa, LD) in which we *add* SN thermal energy in a dense ISM, over a large radius, can suffer unphysical catastrophic radiative cooling. In such cases a hot bubble is not even created and SN feedback has no effect, whatsoever. Early SN feedback simulations suffered from this problem because of low resolution.

Figure 2.4 shows the density profiles at 3 Myr for three of our energy injection models (KE, LD, TEa) with $N_{\rm OB} = 100$ and the ISM density of 20 cm^{-3}. The ejecta

radius is chosen to be large such that it violates conditions in Eqs. 2.4 & 2.7. The figure shows a comparison of the luminosity driven (LD) and thermal explosion addition (TEa) models that fizzle out, and kinetic explosion (KE) model which shows a hot, dilute bubble. Thus, our results are in agreement with the analytical considerations of section 2.4.2. The outer shock location for the KE model roughly agrees with the self similar scaling of Weaver et al. (1977) [224] if the luminosity is reduced by a factor ≈ 0.35; this is comparable to the fraction of mechanical energy retained by SBs after the outer shock becomes radiative (see section 2.5.4 and the right panel of Fig. 2.8).

For most runs in Figure 2.4 we have chosen a rather high density ($n = 20$ cm^{-3}) compared to the critical values in Eqs. 2.4 & 2.7. For lower densities (e.g., 5 cm^{-3} for TEa model in Fig. 2.4) we find that the energy does not couple at early times. Energy injection excites large amplitude sound waves and associated density perturbations, such that at late times the lowest density regions no longer violate Eqs. 2.4 & 2.7. After this, a hot bubble starts to grow because of energy injection in a dilute medium (see dotted line in Fig. 2.4), and eventually the outer shock radius starts to agree with analytic estimates.

SB evolution with cooling

This and later sections, which study the influence of radiative cooling on SBs and SNRs, use the realistic kinetic explosion (KE) model for supernova energy injection with ejecta radius $r_{\rm ej} = 2$ pc. However, we have verified that other models discussed in section 2.2 give similar results, as long as the conditions in section 2.4 are satisfied.

Spherical adiabatic blast waves, both SNRs and SBs, have shells with finite thickness. An estimate for the shell thickness is obtained by assuming that all the swept-up ISM mass lies in a shell and that the post shock density is 4 times the ISM density for a strong shock; this gives $\Delta r/r_{\rm OS} \approx 1/12$. Of course, the shock transition layer is unresolved in simulations, and in reality is of order the mean free path. The structure of an adiabatic blast waves is fairly simple. The density jump at the shock is 4 for

a strong shock, and as the shock becomes weaker the density jump decreases and the shell becomes broader. Eventually, the outer shock is so weak that it no longer compresses gas irreversibly, but instead becomes a sound wave with compressions and rarefactions (see Fig. 2 in Tang & Wang (2005) [199]).

Since the evolution of isolated SNRs with cooling has been thoroughly studied in past (e.g., Thornton et al. (1998) [204]; hereafter T98), we only highlight the differences between isolated SNRs and SBs. The fundamental difference between the two is that SNRs suffer catastrophic losses just after they become radiative because, unlike in SBs, there is no energy injection after this stage. In SBs, the cool (yet dilute), fast SN ejecta periodically thermalizes within the bubble and powers it long after the forward shock becomes radiative. This keeps the radiative forward shock moving (like a pressure-driven snowplow), as long as SNe go off within the hot bubble.

The structure of a radiative shell is quite complex. The shell become radiative when the cooling time of the post-shock gas is shorter than its expansion time (which is of order the age of the blast wave). Moving inward from the upstream ISM, the outer shock transition happens over a mean free path, which is followed by a thin radiative relaxation layer of order the cooling length (see, for example, pp. 226-229 of Shu [177] and the top-right panel of Fig. 2.5). The radiative relaxation layer is followed by a dense shell, which is separated by a contact discontinuity from the dilute hot bubble. In steady state, radiative cooling is concentrated at two unresolved boundary layers, the outer radiative relaxation layer and the inner contact discontinuity. Here the density is high and the temperature is conducive to radiative cooling.

Figure 2.5 shows the zoomed-in density and temperature structure of the radiative shell for a SB (with $N_{\rm OB} = 10^5$; upper panels) and a SNR ($N_{\rm OB} = 1$; lower panels) using high resolution (with 16384 grid-points) runs. It clearly shows an outer radiative shock and an inner contact discontinuity. Within the contact discontinuity of the SB ($N_{\rm OB} = 10^5$) is the shocked SN ejecta; Figure 2.3 shows the full structure of a superwind within the SB. Just when the outer shock becomes radiative the

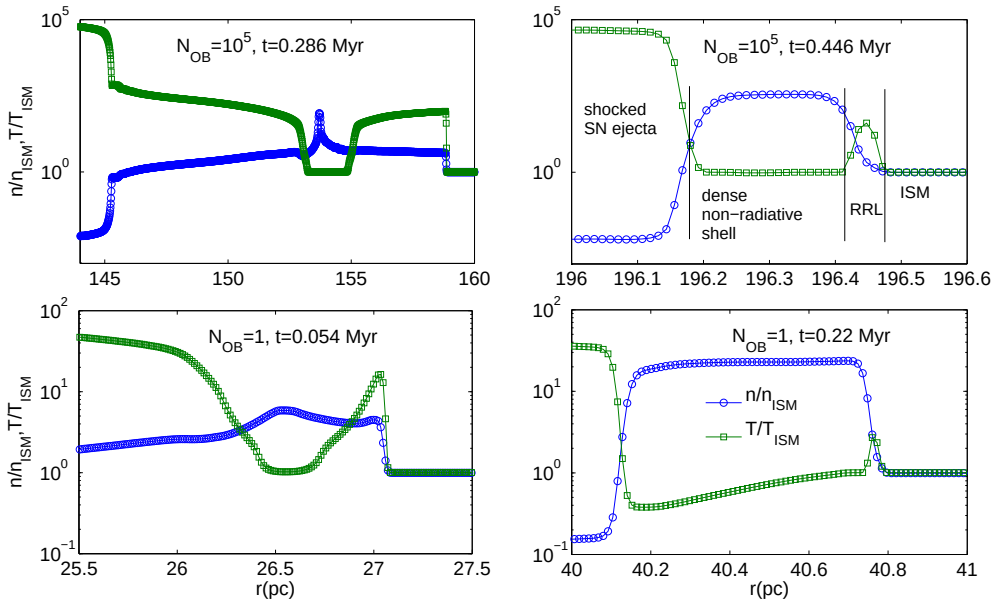

Figure 2.5: The normalized (with respect to the ISM) density and temperature profiles zoomed-in on the outer shock as a function of radius for the high resolution (16384 grid points uniformly spaced from 1 to 200 pc) runs. Top panel: $N_{\rm OB} = 10^5$ run; bottom panel: a single SNR ($N_{\rm OB} = 1$) run. Left panels correspond to a time when the outer shocks just become radiative and the right panels are for later times. Markers represent the grid centers. For a single SNR the temperature in the dense shell is lower than the temperature floor (ISM temperature) because of weakening of the shock and the resultant adiabatic losses. Different regions (unshocked ISM, radiative relaxation layer, dense non-radiative shell, and shocked SN ejecta) are marked in the top-right panel.

coolest/densest part is compressed by high pressure regions sandwiching it (left panels of Fig. 2.5). After a sound crossing time the post-shock region is roughly isobaric and in the pressure-driven snowplow phase (right panels of Fig. 2.5).

Unlike SBs, for isolated SNRs there is no energy injection at later times; the pressure in the bubble falls precipitously after the outer shock becomes radiative at ≈0.05 Myr. By $\sim$ 0.5 Myr the bubble pressure becomes comparable to the ISM pressure, the shell density falls and it becomes momentum conserving with a velocity comparable to the sound speed in the ISM. At even later times ($\sim$ few Myr) the hot bubble just oscillates as a weak acoustic wave.

Figure 2.6 shows the distribution of radiative losses in the shell and in the bubble (shell is defined as the outermost region where density is above 1.01 times the ISM density; bubble comprises of all the grid points with radius smaller than the inner shell radius) for a superbubble with $N_{\rm OB} = 10^5$; results from runs with and without thermal conduction are shown. Here we only discuss the run without conduction; the run with conduction is highlighted in section 2.5.4. Unlike Figure 2.5, here we use our standard resolution runs (1024 grid points) because we are running for a much longer time. Results from the higher resolution runs match our standard runs, highlighting the fact that the volume integrated cooling is the same even if the radiative relaxation layer and the contact discontinuity are unresolved. The time and volume integrated losses ($\int\int n^2 \Lambda 4\pi r^2 dr dt$) in bubble and shell are sampled appropriately and differentiated in time to obtain their respective cooling rates. As already discussed, cooling is concentrated at the radiative relaxation layer, which is included in the shell, and at the contact discontinuity, part of which is included in the bubble. Consistent with our previous discussion, most radiative losses are concentrated in the shell. Fractional radiative losses in the bubble (concentrated at the contact discontinuity) are $\sim 10^{-4} - 0.3$, which increase with time as the outer shock becomes weaker.

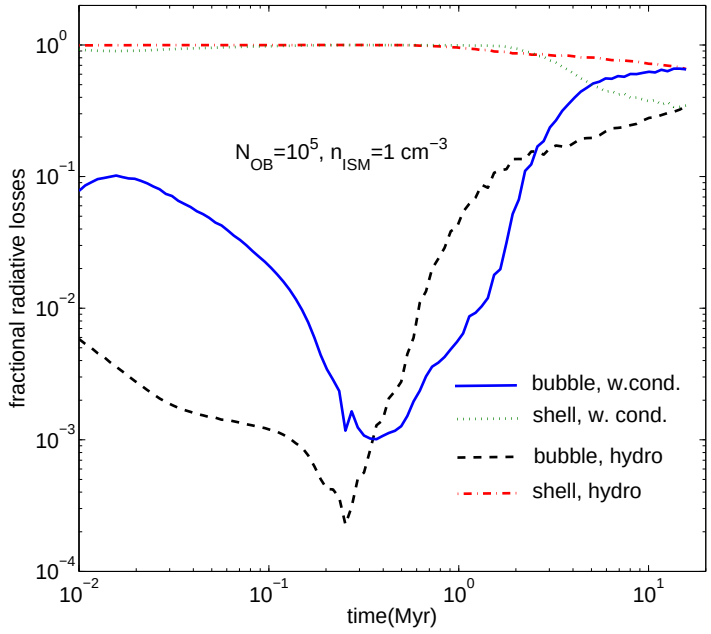

Figure 2.6: Fractional radiative losses in shell ([shell cooling rate]/[total cooling rate]) and bubble ([bubble cooling rate]/[total cooling rate]) for KE models ($N_{\rm OB} = 10^5$) with and without conduction (the run with thermal conduction is discussed in section 2.5.4). Most radiative energy losses happen at the radiative relaxation layer ahead of the dense shell. At late times, as the outer shock weakens, radiative losses in the bubble become more dominant. Bubble is comparatively more radiative (in fact, bubble losses exceed shell losses after 5 Myr) with conduction because of mass loading of the bubble by evaporation from the dense shell. Results from the high resolution run and the luminosity driven (LD) model are similar. The minimum in fractional radiative losses corresponds to the time when the outer shock becomes radiative.

Scales in radiative shocks

The structure of a radiative shock is well known (see, e.g., pp. 226-229 in Shu [177]). Applying mass and momentum conservation across the radiative relaxation layer in the shock frame, and assuming the same temperature upstream/downstream of it (see the top-right panel of Fig. 2.5 for different regions of the outer shock) gives $\rho_3/\rho_1 = (u_1/u_3) = (u_1/a_T)^2$ (Eq. 16.36 in Shu [177]), where ρ_3 (ρ_1) is the density downstream (upstream) of the radiative relaxation layer, u_1 (u_3) is the upstream (downstream) velocity in the shock rest frame, and a_T is the isothermal sound speed of upstream ISM (at $T = 10^4$ K below which radiative cooling vanishes). Thus, we expect larger density jump across stronger shocks ($u_1 \gg a_T$). This is evident from the shell density for the two cases ($N_{\rm OB} = 10^5,\ 1$) in Figure 2.5.

The thickness of the cold, dense shell can be estimated by equating the swept-up ISM mass with the mass in the constant density shell; $\Delta r/r_{\rm OS} \approx (a_T/u_1)^2/3$. This thickness is quite small, with $\Delta r/r_{\rm OS} \approx 0.003$ for a 100 km s^{-1} shock. This estimate agrees with our results in Figure 2.5, and as predicted, the shell is thicker for a smaller $N_{\rm OB}$ and becomes thicker with time as the shock becomes weaker.

The thickness of the radiative relaxation layer can also be estimated. The size of the radiative relaxation layer is $L_{\rm cool}$ ($L_{\rm cool}$ is the distance behind the outer shock after which the advection time becomes longer than the cooling time), such that

$$\int_0^{L_{\rm cool}} \frac{dx}{u} = \int_0^{t_{\rm cool}} dt = t_{\rm cool}, \tag{2.12}$$

where $u(x)$ is the velocity in the relaxation layer in the shock rest frame. While this equation can only be solved after numerically solving for the structure of the relaxation layer, we can make an order of magnitude estimate. The integral on the LHS of Eq. 2.12 can be estimated as $L_{\rm cool}/\langle u\rangle$, where $\langle u\rangle = a_T/2$ is the geometric mean of the velocity at the front of the relaxation layer ($u_1/4$ for a strong shock) and just downstream of it ($u_3 = a_T^2/u_1$). Similarly, the cooling time $t_{\rm cool}$ in Eq. 2.12 can be estimated by using a geometric mean of densities across the relaxation layer; i.e.,

$t_{\rm cool} \approx 1.5kT/(\langle n \rangle \Lambda)$, where $\langle n \rangle = 2(u_1/a_T)n_1$ and we can use the peak of the cooling function for T and Λ. Putting this all together gives,

$$L_{\rm cool} \sim a_T \left(\frac{a_T}{u_1}\right) \frac{kT_0}{n_1 \Lambda_0}, \tag{2.13}$$

which is $\sim 10^{-4}$ pc for fiducial numbers, far from being resolved even in our highest resolution runs. While the transition layers (contact discontinuity and radiative relaxation layer) where all our cooling is concentrated are unresolved, we find that the volume integrated quantities such as radiative losses, kinetic/thermal energy in shell/bubble are converged even at our modest (1024 grid points; results are similar even for 256 grid points) resolution.

Energetics of radiative SBs & isolated SNRs

In this section we focus on the energetics of SB shell/bubble and compare it with the results from isolated SNRs. We define the shell to be the outermost region where the density is larger than 1.01 times the ISM density. All gas at radii smaller than the shell inner radius is included in the bubble (this definition is convenient but not very precise as it includes small contribution from the unshocked SN ejecta). Figure 2.7 shows a comparison of kinetic and thermal energies in bubble and shell as a function of time for a SB driven by 10^5 SNe. The bubble kinetic energy is not included because it is much smaller. Also included is a comparison of the same quantities for the same frequency of SNe that go off independently. The results for multiple isolated SNe are obtained by combining the single SN run at different times. We simply use the data at an interval of $t_{\rm SN}$ (time between individual SNe) and add them to obtain total kinetic/thermal energy in the shell and bubble at a given time. For instance, the thermal energy in bubbles of all independent SNe at time $10t_{\rm SN}$ is obtained by summing up the bubble thermal energy from a single SN ($N_{\rm OB} = 1$) run at $t = 0$, $t_{\rm SN}$, $2t_{\rm SN}$, ..., till $10t_{\rm SN}$. This is equivalent to a cumulative sum over time for a single

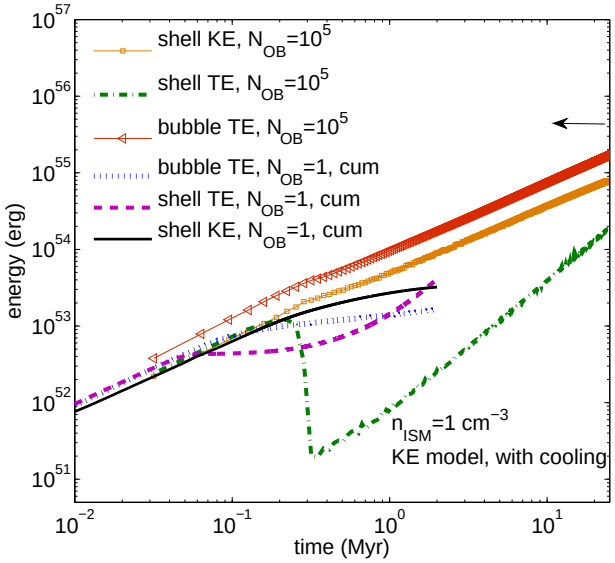

Figure 2.7: Comparison of kinetic and thermal energies in the shell and thermal energy in the bubble as a function of time for SBs and an equal number of isolated SNe. Results from an isolated SN run ($N_{\rm OB} = 1$) have been combined cumulatively (see Eq. 2.14), assuming that SNe go off independently in the ISM. Pre-radiative phase energetics are similar but isolated SNRs are extremely deficient in mechanical energy (after 1 Myr) as compared to a SB with the same energy input. The arrow on top right shows the bubble thermal energy at the end for an adiabatic SB run. Isolated SN results are only shown till 2 Myr because SNRs become weak sound waves by then.

SN run,

$$E_{\rm cum}(t) = \sum_{i=0}^{i<N} E(it_{\rm SN}) = \frac{1}{t_{\rm SN}} \int_0^t E(t')dt', \tag{2.14}$$

where E stands for, say, bubble thermal energy and N is the number of SNe till time t.

Weaver et al. (1977) [224] have given analytic predictions for energy in different components of SBs: the total energy of the shell is $(6/11)L_{\rm ej}t$ (40% of this is kinetic energy and 60% is thermal) and the thermal energy of the bubble is $(5/11)L_{\rm ej}t$ (kinetic energy of the bubble is negligible). These analytic predictions agree well with our numerical results in the early adiabatic (non-radiative) SB phase in Figure 2.7.

Figure 2.7 shows that the SB shell loses most of its thermal energy catastrophically at ≈ 0.25 Myr; the trough in shell thermal energy can be estimated by assuming that all the swept-up mass till then cools to the stable temperature (10^4 K). The thermal energy of the cold shell increases after that as it sweeps up mass from the ISM; this is not a real increase in the thermal energy because the newly added material, which was previously part of the ISM, simply becomes a part of the dense shell at the same temperature. The bubble thermal energy and the shell kinetic energy show only a slight decrease in slope after the radiative phase because they are energized by the non-radiative termination (internal) shock(s) driven by SN ejecta. However, there are some losses because of cooling at the contact discontinuity (see Figs. 2.5 & 2.6).

The shell kinetic energy and the bubble thermal energy in radiative SB simulations at 20 Myr are roughly half of the values obtained in adiabatic simulations (which agree with analytic predictions). Thus, the mechanical energy retained in the SB is $\approx 0.34L_{\rm ej}t$. This should be contrasted with the energy evolution in isolated SNRs. The isolated SNR becomes radiative much earlier (≈ 0.05 Myr; when the shell thermal energy shown by dashed line flattens suddenly in Fig. 2.7) because of a weaker shock compared to a SB. Note that the energies for isolated SNe in Figure 2.7 are *cumulative sums* over time of a single SN run (see Eq. 2.14). The bubble thermal energy and shell kinetic energy also drop for an individual SNR after it becomes radiative (albeit not

catastrophically, unlike the shell thermal energy; see Fig. 3 in T98; this is the pressure-driven snowplow stage) because of cooling at the contact discontinuity and adiabatic losses, and because there is no new energy source (unlike the termination/internal shocks in a SB). The total mechanical energy in the bubble and shell of a single SNR at the beginning of the momentum conserving phase (1 Myr; when bubble pressure is comparable to the ISM pressure) is 10^{50} erg, which is only 10% of the input energy (see Fig. 3 in T98). This agrees with the energy fraction available as mechanical energy of the SNR, as quoted by T98. After a few Myr the SNR should be considered a non-energetic part of the ISM, as the thermal energy of the swept up ISM becomes larger than the SNR's mechanical energy, and the bubble becomes a weak acoustic wave.

In order to compare isolated SNRs and superbubbles over the cluster lifetime we must extrapolate our cumulative SN energies to 30 Myr. This is also the relevant timescale for preventing large-scale galactic inflows from efficiently forming stars (the free-fall timescale at ~ 10 kpc for galactic halos is few 10s of Myr). For isolated SNRs the shell kinetic energy + bubble thermal energy is $\sim$7% of the input energy by 2 Myr, and only 0.7% when extrapolated to 30 Myr. We should not extrapolate the shell thermal energy because its rise at late times in Figure 2.7 is due to the sweeping up of the ISM into the shell, without an increase in the temperature. To conclude, isolated SN feedback is much weaker (by a factor ~ 50) as compared to the feedback due to SBs over the cluster lifetime.

The left panel of Figure 2.8 shows the total radiated energy over the whole computational domain as a function of time for an isolated SNR ($N_{\rm OB} = 1$; solid line) and for SBs (dashed lines). The results are qualitatively different for SBs (even for $N_{\rm OB} = 10$) and isolated SNe. While an isolated SN radiates almost all of the input energy (10^{51} erg) over a Myr timescale, SBs radiate a smaller fraction ($0.6 - 0.8$) of their energy even till late times. The runs with smaller $N_{\rm OB}$ and larger density become radiative at an early time as the shock is weaker, but SB runs are qualitatively

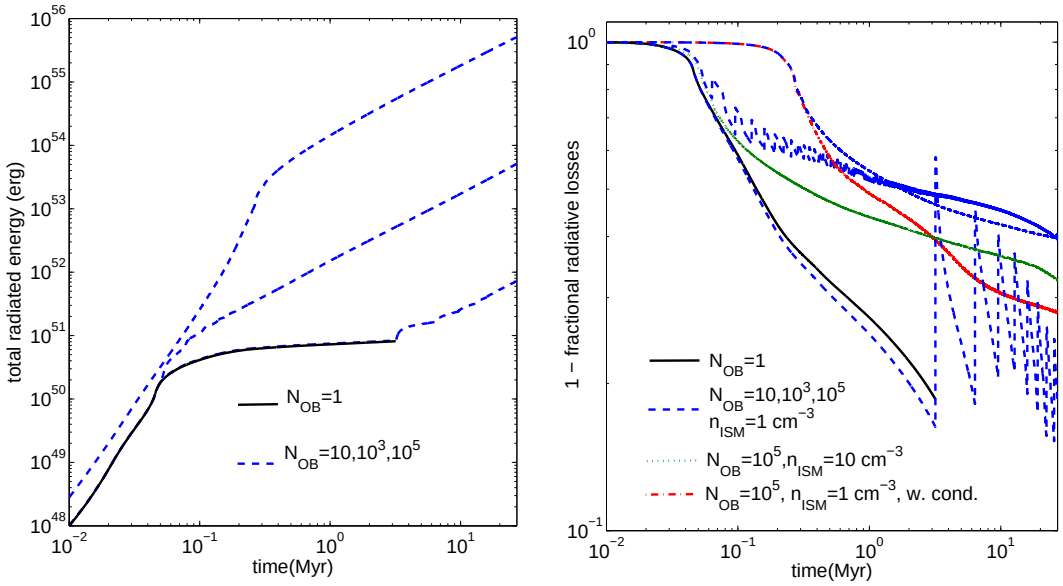

Figure 2.8: Radiative losses as a function of time for SBs and isolated SNe. Left panel shows the total radiated energy as a function of time for an isolated SN run (solid line) and for SB runs (dashed lines) with $N_{\rm OB} = 10,\ 1000,\ 10^5$; larger $N_{\rm OB}$ leads to larger radiative losses because of a higher density and temperature in the radiative relaxation layer (see Fig. 2.5). The right panel shows fractional cooling losses (1 - [energy radiated]/[input energy]) as a function of time; the total energy input at some time equals the number of SNe put in by that time multiplied by 10^{51} erg (the spikes for $N_{\rm OB} = 10,\ 10^3$ in the right panel reflect the discreteness of SN energy input within SBs). All SB runs, including those with conduction and with higher density, show that only a factor of $0.6 - 0.8$ is radiated by 20 Myr (and a factor of $0.2 - 0.4$ is retained as mechanical energy). In contrast, the isolated SN run (solid line) loses 80% of its energy by 3 Myr, after which it is no longer over-pressured with respect to the ISM.

similar. Unlike in isolated SNe, a significant fraction of the input energy in SBs is retained in the bubble thermal energy and the shell kinetic energy ($0.2 - 0.4$; see Fig. 2.7). The key reason for the difference between isolated SNe and SBs is that in SBs the non-radiative termination/internal shocks keep the bubble overpressured but isolated SNe, which do not have further energy input after the initial explosion, simply fizzle out soon after they become radiative.

The right panel of Figure 2.8 shows the fraction of energy retained (1-the fraction radiated) as a function of time for several runs. All SB runs, including a higher density run ($n_{\rm ISM} = 10$ cm^{-3}) and the run with conduction (see section 2.5.4), show the asymptotic fraction of energy retained to be $\gtrsim 0.25$. In contrast, an isolated SN loses 90% of the input energy by few Myr (and almost all of it by 10 Myr; see also Fig. 2.7). Radiative losses for an isolated SNR at late times ($\gtrsim$ few Myr) are more than the energy input (10^{51} erg); these come at the expense of the thermal energy of the swept-up ISM.

We can compare our results of coincident SNe with the case of multiple SNe distributed over space in a random manner. The two cases presented in Figure 2.7 represent two extreme limits: spatially coincident SNe in a SB and totally independent SNe. For spatially distributed SNe we expect results somewhere in between these two extremes. Vasiliev et al. (2015) [215] compare the total explosion energy that remains as the thermal energy of hot gas in the case of spatially distributed SN explosions. They study the effects of coherent explosions, as defined in Roy et al. (2013) [164], which implies that SNe overlap before they become radiative. If the shell radius of a SNR when it becomes radiative is R_a and the corresponding time scale is t_a, then for a SN rate density of $\nu_{\rm SN}$, the coherency condition is that $(4\pi/3)\, R_a^3\, t_a\, \nu_{\rm SN} > 1$. Vasiliev et al. (2015) [215] compare the cases in which explosions occur coherently with those in which they do not. They find that a fraction ~ 0.3 of the explosion energy is retained in the gas with temperature $T \geq 3 \times 10^6$ K if the explosions occur coherently, and the fraction is $0.02 - 0.2$ if the explosions are incoherent. Our results

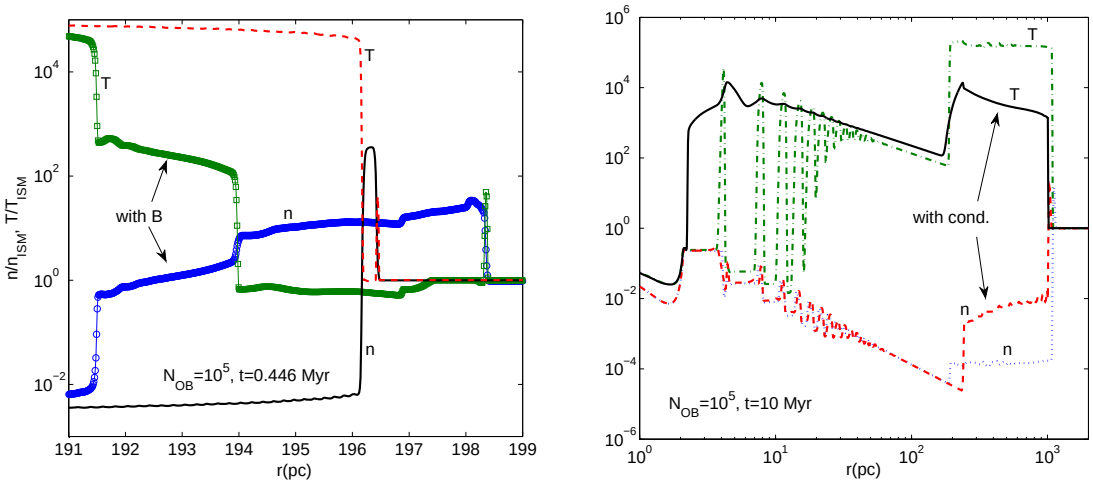

Figure 2.9: The normalized density and temperature profiles to show the effects of magnetic fields and thermal conduction on SB evolution with cooling. The left panel shows the profiles zoomed in on the outer shock for MHD (initial $\beta = 1$) and hydro runs with 16384 grid points. Magnetic field is enhanced in the shell and the shell is thicker. The right panel shows the profiles for radiative hydro runs with and without thermal conduction (1024 grid points); unlike in the left panel, we show the whole computational domain and the dense shell is barely visible. Thermal conduction evaporates mass from the dense shell and spreads it into the bubble, thereby making it denser and less hot compared to the hydro run. The temperature structure in the internal shocks (within the superwind) is also smoothened out by thermal conduction.

here for SBs correspond to the coherent case, since $t_{\rm SN}$ is always shorter than the cooling time of the gas in the bubble. Therefore, our result of a fraction ~ 0.35 being retained as SB's mechanical energy is consistent with Vasiliev et al. (2015) [215].

Effects of magnetic fields and thermal conduction

Since the ISM is magnetized, we try to assess the qualitative effects of magnetic fields using an idealized high resolution (16384 grid points) MHD simulation. We assume an azimuthal (ϕ) component of the magnetic field so that only magnetic pressure forces (and no tension) are present. We choose a plasma β (ratio of gas pressure and magnetic pressure) of unity in the ISM, and our SN ejecta is also magnetized with

the same value of β. Since the ejecta is dominated by kinetic energy and the bubble is expanding, we do not expect magnetic fields to affect the bubble and the ejecta structure. However, the radiative shell is compressed because of cooling, and due to flux-freezing magnetic pressure is expected to build up in the dense shell. This is indeed what we find in our simulations with magnetic fields. The left panel of Figure 2.9 shows the zoomed-in density and temperature structure of the radiative outer shock with and without magnetic fields. The key difference between the hydro and MHD runs is that the dense shell in MHD has a lower density and is much broader. This is because magnetic pressure prevents the collapse of the dense shell.[3] The dense shell (194 pc $< r <$ 198 pc in the left panel of Fig. 2.9) is magnetically dominated with plasma $\beta \sim 0.01$. The MHD run has two contact discontinuities; one at the boundary of the hot bubble ($r \approx 191.5$ pc), and another at $r \approx 194$ pc left (right) of which the plasma is dominated by thermal (magnetic) pressure.

Another important physical effect, especially in the hot bubble is thermal conduction. We carry out a 1024 resolution hydro run with thermal conduction to study its qualitative influence. However, it is difficult to determine the ISM conductivity in a magnetized (presumably turbulent) plasma. Therefore, we use the Spitzer value with a suppression factor of 0.2 (see Eq. 11 in Sharma, Parrish, & Quataert (2010) [176]). Moreover, since the bubble can become very hot such that the diffusion approximation breaks down, we limit the conductivity to an estimate of the free streaming diffusivity (chosen to be 2.6 $v_t r$ where v_t is the local isothermal sound speed and r is the radius). Thermal conduction is operator split, and implemented fully implicitly through a tridiagonal solver using the code's hydro time step.

Conduction is expected to evaporate matter from the dense shell and deposit it into a conductive layer in the bubble; in steady state the rate of conductive transport

[3]The photon mean-free-path for a dense shell can become smaller than the shell thickness. When this happens, the assumption of optically thin cooling breaks down, and the shell can become thicker because of radiation pressure.

of energy from bubble to the shell is balanced by the rate of heat advection from shell to the bubble (Weaver et al. (1977) [224]). The outer and termination shock locations are not affected much by conduction. However, the density and temperature structure in the hot bubble is affected significantly. Without conduction the bubble is very hot ($\sim 10^9$ K), but with conduction the temperature drops into the X-ray range ($10^7 - 10^8$ K) and density is higher. This can enhance the X-ray emissivity of SBs; a rough estimate of hard X-ray luminosity ($\int 4\pi r^2 n^2 \Lambda dr$ over the hot bubble) at 10 Myr from the right panel of Figure 2.9 is few 10^{38} erg s^{-1} (which is ~ 0.003 the energy put in by SNe by that time). Since galactic superwinds are copious X-ray emitters, we expect thermal conduction to be a very important ingredient for explaining observations. Figure 2.6 confirms that the fraction of radiative losses from the bubble is much higher with conduction than without conduction because of a higher density. However, the right panel of Figure 2.8 shows that the total fractional radiative losses with thermal conduction are only slightly higher compared to the non-conductive $N_{\rm OB} = 10^5$ SB run.

We emphasize that our treatment of magnetic fields and thermal conduction is extremely simplified. Realistic calculations must be done in three dimensions with tangled magnetic fields and with anisotropic thermal conduction along fields lines. However, we expect the qualitative effects of realistic magnetic fields and thermal conduction to have some semblance with our simplified treatment.

2.6 Conclusions & astrophysical implications

We have obtained several important results in this paper, on both numerical implementation of SN/SB feedback and on differences between isolated SNe and SBs. SBs are a result of spatially and temporally correlated SNe. Since most massive stars are expected to be born in star clusters few 10s of pc in extent (e.g., Larsen (1999) 113), pre-SN stellar winds and first SNe are expected to carve out a low density bubble,

which by a fraction of Myr encloses the whole star cluster (see Fig. 2.5). Therefore, subsequent SNe happen in the low density bubble and we are in the SB regime of coherent SNe (see Vasiliev et al. (2015) 215**?**).

Magnificent galactic outflows, such as M82, are powered by multiple super-star-clusters and the problem of understanding coalescing SBs is important. Star clusters more massive than $10^5 M_\odot$ (and hence with > 1000 SNe) are rare (e.g., see Portegies Zwart et al. (2010) 156); therefore, the superbubbles in M82 and in our $N_{\rm OB} = 10^5$ SB model should be considered as giant bubbles driven by 100s of overlapping superbubbles due to individual star clusters. Indeed, 100s of star clusters have been observed in the central few 100 pc of M82 (O'Connell et al. (1995) 148). We note that vertical stratification is important for the acceleration and assimilation of the metal-rich bubble into the halo. In this paper we consider the idealized smaller-scale problem of the behavior of isolated SNRs and multiple coincident SNe within a SB in a uniform ISM. Some of our most important results are:

- Our most realistic kinetic explosion (KE) models (and other models in which SN energy is *overwritten*), in which the SN energy in kinetic form is overwritten in a small volume, give correct results only if the energy is deposited within a small length scale (see section 2.4.1); otherwise, energy is overwritten without coupling to the ISM. This is true even without considering any radiative losses.

- With cooling, if feedback energy is deposited within a length scale $r_{\rm ej}$ larger than the critical values mentioned in section 2.4.2, such that the input energy is radiated before it is thermalized, a hot bubble is not formed in the widely used luminosity driven and thermal explosion addition (LD, TEa) models. Thus SN fizzles out at early stages due to artificially large cooling losses.

- With insufficient resolution and large ISM densities the bubble fizzles out completely in the luminosity driven (LD) and thermal explosion addition (TEa) models (in which energy is *added* to the ISM; see section 2.2) and cannot have

any effect on the ISM (see Fig. 2.4). As also pointed out previously (e.g., by Creasey et al. (2011) 36, Dalla Vecchia & Schaye (2012) 39), early galactic-scale SN feedback simulations failed mainly because of this. However, for a realistic SN (as mimicked by our KE model) a bubble is formed and subsequent SNe occuring within the non-radiative bubble power the radiative outer shock. Another, probably more serious, problem faced by numerical simulations is that the SN energy is not typically put in coherently over a small volume in space and within a short interval. Feedback due to SNe in young star clusters is expected to be coherent and much more effective than a similar number of isolated SNe (see Figs. 2.7, 2.8). For correlated SNe, isolated SN bubbles overlap to form a superbubble which is powered by the non-radiative termination/internal shocks, long after the outer shock becomes radiative. In contrast, an isolated supernova becomes powerless a bit after ($\sim$ 1 Myr) the outer shock becomes radiative.

- A smooth CC85 wind within the superbubble is possible only if the number of SNe ($N_{\rm OB}$) over the cluster lifetime is large (i.e., $N_{\rm OB} \gtrsim 10^4$). Only in these cases, individual SNe going off inside the superbubble are able to thermalize within the termination shock. This result has implications for modeling the X-ray output, for example, in individual bubbles blown by star clusters and in the inner regions of galactic outflows, since the CC85 wind structure is often assumed where it may not be valid.

- Most of the radiative losses come from the unresolved radiative relaxation layer at the outer shock. The fractional radiative losses from the interior region, concentrated at the contact discontinuity between the shocked ISM and the shocked ejecta, varies between $\sim 0.001 - 0.3$, with larger losses occurring at later times. While these radiative layers are unresolved even in our highest resolution simulations, the volume integrated radiative losses in them converge

even for a modest resolution.

- As compared to isolated SNe, superbubbles can retain a larger fraction of the initial energy of explosions as thermal/kinetic energy of the gas. Isolated SNe are mixed with the ISM soon after they become radiative; by few Myr they are incapable of affecting the ISM at all. While most energy is radiative away (close to 100%, and not $\sim 90\%$, as is often assumed) for isolated SNe over 10 Myr, a SB can retain a fraction ~ 0.35 (for $n = 1$ cm^{-3}) as the bubble thermal energy + the shell kinetic energy. This fraction is only weakly affected by a higher ISM density and by thermal conduction (see the right panel of Fig. 2.8). Thus, SBs are expected to significantly affect even a dense ISM. Substantial radiative losses can partly explain the smaller observed bubble sizes compared to what is expected by modeling the stellar populations (see Oey (2009) 149 for a summary).

- The temperature profile of SBs strongly depend on thermal conduction, whose inclusion can decrease (increase) the temperature (density) and thereby enhance the X-ray luminosity. Thermal conduction (and other sources of mass loading of the hot bubble, such as turbulent mixing) plays an important role in explaining the X-ray emission from galactic superbubbles because very little gas is expected to be in the X-ray emitting regime ($10^6 - 10^8$ K) in its absence (see the right panel of Fig. 2.9).

Our simple one-dimensional simulations show that isolated supernova remnants, owing to large radiative losses, are much weaker feedback agents compared to superbubbles driven by coherently overlapping supernovae. However, detailed three-dimensional calculations, particularly with a realistic distribution of stars in a cluster, and magnetic fields and thermal conduction, are required in order to make quantitative comparisons with observations. This will be done in future.

Chapter 3

Superbubble breakout in disk galaxies

Based on : "Superbubble breakout and galactic winds from disc galaxies"
Roy, A., Nath, B. B., Sharma, P., Shchekinov, Y., 2013, MNRAS, 434, 3572

Multiple supernovae not retain most of their thermal energy as discussed in the previous chapter, and they produce superbubbles that eventually create galactic superwinds. Superbubble shells are known to undergo various instabilities such as thermal, and Rayleigh-Taylor (RT) instabilities, and are therefore prone to 'corrugations'. The corrugations in the shell help to fragment it into clumps and channels. At a later epoch, the top of the shell is blown off, and the fragmented dense shell remnants move in the hot, dilute gas creating a multiphase halo. The highly energetic electrons accelerated at shocks generate synchotron emission as they follow the magnetic field lines. There are various threshold energy input rates for different observational manifestations of SNe feedback such as superwinds, multiphase halo, and radio halo. In addition to the effective feedback model (as described in chapter 2), we incorporate density stratification of the ambient gas, and perform 2D simulations to address the following questions : (i) what are the threshold conditions, energy input rates, and Mach numbers, etc., to create galactic superwinds, mutiphase halo and radio halo, (ii) is there any connection between the three different energy input rates, and (iii) can they all be produced from the same physical processes? We are also interested in determining the epochs and the nature of instabilities that play a dominant role in corrugating the supershells.

Primary results

- By including radiative cooling in the Kompaneets solution, we analytically estimate that $\sim 30\%$ of the input energy is retained in the superbubble. This result matches well with our estimate from numerical simulations as discussed in chapter 2.

- Using hydrodynamic simulations in stratified discs we find that superbubbles can break out of the discs with a clear demarcation between the two energy input

rates : (i) with Mach number of $\sim$ 2–3 corresponding to an energy input rate of $\sim 10^{-4}$ erg cm^{-2} s^{-1}, which is the threshold energy input rate for synchotron emitting galaxies, (ii) A larger energy injection threshold $\sim 10^{-3}$ erg cm^{-2} s^{-1} corresponding to the threshold condition for the multiphase halo gas in the disc galaxies. This is equivalent to the threshold surface density of SFR of ~ 0.1 M$_{\odot}$ yr^{-1} kpc^{-2} corresponding to the threshold condition for the galactic superwinds. The final energy input rate corresponds to a Mach number $\sim$ 5–10, which can only be produced by super-starclusters evolving coherently in space and time. The former energy scales can be obtained by the milder superbubbles driven by large OB-associations.

- We find that RT-instability becomes dominant after the shell reaches a few scale-heights, contrary to the general belief that RT-instability occurs right when the shell reaches a scale-height.

3.1 Introduction

Observations of nearby and high-redshift galaxies have shown that star formation in them often leads to galactic winds. Starburst galaxies, with star formation rate (SFR) in excess of a few tens of $M_\odot$ yr^{-1} are known to excite such outflows. However, Heckman (2002) pointed out that it is not the average SFR, but the SFR surface density which is a deciding factor for the existence of outflows. He found a threshold SFR surface density of ~ 0.1 M$_\odot$ kpc^{-2} yr^{-1} as a prerequisite for starbursts to be able to produce galactic winds.

The standard scenario of star formation leading to the wind phenomena posits that super-starclusters give rise to a large number of supenovae (SN) in a relative small region, which can produce a superbubble in the disk and can break out of the disk with enough momentum to produce a wind. Such super-star clusters, or young globular clusters, have been observed to have masses in the range of few $\times 10^5$–6×10^7 M$_\odot$ within a typical radius of $\sim$ 3–10 pc (Ho 1997; Martín-Hernández et al. 2005, Walcher et al. 2005). The large amount of energy deposited into the interstellar medium (ISM) by these objects in the form of UV radiation and mechanical energy is believed to be an important feedback process. The mechanical energy from these super-starclusters has been shown to be important for the superbubble produced by the combined SNe to break out of the disk and produce a large scale wind (e.g., Tenorio-Tagle, Silich, Muñoz-Tuñón 2003).

There have been a number of calculations, both analytical and numerical, dealing with the breakout of superbubbles from disk galaxies. The conditions for breakout depend strongly on the assumption of the stratification of gas in the disk. Consider an exponentially stratified disk with mid-plane ambient gas pressure P_0, gas density ρ_0, scale height z_0, and a bubble being blown by mechanical luminosity $\mathcal{L}$. Mac Low & McCray (1988) defined a dimensionless parameter $D \equiv \mathcal{L}\rho_0^{1/2}/(P_0^{3/2} z_0^2)$, and noticed in their numerical simulations that breakout of bubbles occurred when $D \geq 100$. The importance of this parameter can be understood by considering the self-similar evolu-

tion of a superbubble driven by an energy injection rate of $\mathcal{L}$, given by $r \sim (\mathcal{L}t^3/\rho_0)^{1/5}$, and $\dot{r} \sim (3/5)(\mathcal{L}/\rho_0)^{1/5}t^{-2/5}$. This implies a speed of $\sim (3/5)(\mathcal{L}/\rho_0 z_0^2)^{1/3} \propto D^{1/3}$ when the superbubble reaches a distance of the scale height, for an ambient gas at a given temperature. According to this criterion, for a scale height $z_0 = 200$ pc, and mid-plane gas density $\mu_H n_0 \sim 2.3 \times 10^{-24}$ g cm^{-3}, $P_0/k_b \sim n_0 10^4$ K cm^{-3}, a bubble with total mechanical luminosity of $\mathcal{L} \sim 3.8 \times 10^{37}$ erg s^{-1} will be able to breakout of the ISM.

Basu et al. (1999) defined a dimensionless parameter $b \equiv (27/154\pi)^{1/2}\mathcal{L}^{1/2}\rho_0^{1/4}P_0^{-3/4}z_0^{-1}$ which is a ratio of the radius where the Mach number of the superbubble becomes unity, to the scale height. This is motivated by the self-similar solution of a stellar wind, $r \sim (125/154\pi)^{1/5}\mathcal{L}^{1/5}\rho_0^{-1/5}t^{3/5}$. They showed that this parameter is related to the above mentioned D parameter as $D = 17.9b^2$. In other words, a superbubble with $b < 1$ is likely to be confined where as blowout will occur for $b \geq 1$.

Koo & McKee (1992) analytically determined a condition for the breakout. Since the bubbles accelerate after reaching a distance of order the scale height, owing to the rapidly decreasing density, it becomes liable to fragment due to Rayleigh-Taylor instability. If the Mach number of the bubble at scale height is ≥ 3, then they argued that the bubble would be able to breakout. They used radiative bubble model of Weaver et al (1977) for a uniform density atmosphere in order to derive a critical mechanical luminosity for which the Mach number is unity, $\mathcal{L}_{cr} \sim 17.9\rho_0 z_0^2 c_s^3$, where c_s is the isothermal sound speed of the ambient gas. The Mac Low & McCray condition of $D \geq 100$ translates to $\mathcal{L}/\mathcal{L}_{cr} \geq 5$. As we will find in our simulations, the Mach number of a bubble after breakout is of order $(1/5c_s)(\mathcal{L}/\rho_0 z_0^2)^{1/3}$. Therefore, the Mac Low-McCray condition of $D \geq 100$ translates to the condition that the Mach number at breakout is of order unity. We also note that they considered superbubbles that originated at a height from the mid-plane, which made it easier for bubbles to break out. Our simulations show that the critical luminosity for Mach number at a distance of the scale height to be unity is $\mathcal{L}_{cr} \sim 125\rho_0 z_0^2 c_s^3$, larger than the estimate of Koo &

McKee (1992).

Koo & McKee (1992) then considered an additional strata of HII gas with a scale height of 1 kpc and mid-plane number density 0.025 cm^{-3}, and found the breakout condition to be of order $N_{OB} \sim 800$, or equivalently, $\mathcal{L} \geq 4.1 \times 10^{38}$ erg s^{-1}. Silich & Tenorio-Tagle (2001) considered the effect of halo gas pressure and determined a minimum energy for the superbubble to blow out of the galaxies (with both disk and spherical ISM distribution) with ISM gas mass in the range of 10^6–10^9 $\mathrm{M}_\odot$. For a disk galaxy with $M_{ISM} \sim 10^9$ $\mathrm{M}_\odot$, they found a minimum energy of $\sim 10^{38}$ erg s^{-1}, corresponding to $N_{OB} \sim 1000$.

As Heckman (2002) has emphasized, it is the surface density of SFR that determines the condition for the existence of galactic winds, and not the total luminosity. To translate the above energy conditions into a surface density, we need to estimate the surface area of such bubbles at the breakout epoch. In this chapter, we re-visit this issue in order to understand the empirical threshold SFR surface density for galactic winds. Murray, Ménard, Thompson (2011) have recently argued that radiation pressure from UV radiation from a disk with a SFR surface density larger than 0.1 $\mathrm{M}_\odot$ kpc^{-2} yr^{-1} can produce a large scale wind. This estimate however crucially depends on the assumption of the grain opacity, and as Sharma & Nath (2012) have shown the relevant opacity at UV may fall short of the requirements.

There have also been studies on the existence of multiphase gas in the halos of spiral galaxies, and their connection to the star formation properties in the disk. Dahlem, Lisenfeld, Golla (1995) considered nine edge-on galaxies with extended synchrotron emitting halo gas, and derived a minimum value of surface density of energy injection for superbubble breakout, as $\sim 10^{-4}$ erg s^{-1} cm^{-2}. Tüllmann et al. (2006) further considered X-ray, radio and far-infrared (FIR) emission from the extended halo gas in a sample of 23 edge-on spiral galaxies, and found that the halo contained gas at low and high temperatures (multiphase) if the surface density of energy injection in the disk exceeds $\sim 10^{-3}$ erg s^{-1} cm^{-2}. If the existence of multiphase halo gas depends on

the process of superbubbles breaking out of the disk and depositing hot interior gas (as suggested by Tomisaka & Ikeuchi 1986; Tenorio-Tagle, Rozyczka, Bodenheimer 1990), as well as cold gas in the shell, then it would be interesting to compare the energetics of such superbubbles and the observed threshold energy injection rate.

In this chapter, we study the standard scenario of thermal pressure of the gas interior to superbubbles being the driving mechanism for the wind, and derive a threshold condition for the superwind. We find that radiative loss of energy is important for the dynamics of shocks, and the inclusion of radiation loss increases the energy budget for the bubbles to breakout of the disk and produce a wind. We also find that our estimate of the threshold energy requirement can explain the observed threshold SFR surface density for galactic outflows.

The chapter is organized as follows. In §2 we derive an order-of-magnitude estimate of the threshold based on the key idea that the superbubble energetics needs to balance radiative cooling. Then we present the analytical formalism in §3 and discuss the results in §4. We then present the results from numerical simulations in §5, and discuss the effect of thermal and RT instability in §6.

3.2 Analytic Estimates

To begin with, we derive a threshold rate of SNe for a superbubble to continue to grow and ultimately breakout of the disk from simple arguments. We can first consider the condition that the superbubble is able to drive a strong shock in the disk. This requires the volume energy injection time scale to be shorter than the sound crossing time. In other words, if we consider a region of radius R in the disk and an energy injection rate of $\mathcal{L}$, then one needs

$$\frac{1.5nkT}{\mathcal{L}/(4\pi R^3/3)} \ll R/c_s\,, \tag{3.1}$$

where c_s is the sound speed. This gives a lower limit of $\mathcal{L}/(\pi R^2) \gg 3\times10^{-6} n T_4^{3/2}$ erg s^{-1} cm^{-2}, where n is the ambient gas particle density in cm^{-3}, and $T = T_4\, 10^4$ K.

A second, and more stringent, constraint on SNe luminosity comes from accounting for radiative losses. Let us assume that when a SN remnant enters the radiative stage it quickly loses its energy and does not contribute to the energy input of the superbubble. Assume then that the radiative stage begins when the post-shock temperature is $T_s \simeq 2 \times 10^5$ K such that the radiation loss function is maximum and much larger than the minimum at $\sim 10^6$ K. We therefore define the time when a SN remnant loses its energy at time when the shock velocity is $v_s = 120$ km s^{-1} (corresponding to the post-shock temperature of 2×10^5 K). It determines the corresponding time and radius as (see also Kahn 1998, who defined this as the beginning of phase III in the evolution of a bubble),

$$t_a = 1.4 \times 10^5 \frac{E_{51}^{1/3}}{n^{1/3}} \text{ yr}, \quad R_a = 37 \frac{E_{51}^{1/3}}{n^{1/3}} \text{ pc}\,. \tag{3.2}$$

One can therefore define the coherency condition as,

$$\frac{4\pi}{3} R_a^3 t_a \nu_{SN} > 1\,, \tag{3.3}$$

which means that before a SN remnant stalls because of cooling losses, another SN explosion injects energy into the remnant and forms a single bubble. This condition determines the required SN rate

$$\nu_{SN} > 30 \times 10^{-12} \left(\frac{n}{E_{51}}\right)^{4/3} \text{ SNe yr}^{-1} \text{ pc}^{-3}\,. \tag{3.4}$$

We can estimate the surface density of SNe, by multiplying this rate density by the scale height, which is the height of a bubble at the epoch of breakout. For a scale height of $500\, z_0 = z_{0,0.5}$ pc, this corresponds to $1.5 \times 10^{-2} (n/E_{51})^{4/3}\, z_{0,0.5}$ SNe yr^{-1} kpc^{-2}. (The scale height is relevant here because, as we will see later, the maximum radius of bubbles in the plane parallel to the disk is of order πz_0.) Finally, we recall that for a Salpeter IMF, one SN corresponds to 150 M$_\odot$ of stellar mass, considering stars in the range of 1–100 M$_\odot$. Therefore the threshold condition for SFR surface density becomes $\sim 2.5 (n/E_{51})^{4/3} z_{0,0.5}$ M$_\odot$ yr^{-1} kpc^{-2}. The corresponding surface density

of energy injection is $\sim 0.05\, n^{4/3}\, E_{51}^{-1/3}\, z_{0,0.5}$ erg s^{-1} cm^{-2}. It is interesting to find that these above estimates of the threshold energy injection or SFR surface density are comparable to the observed threshold for the existence of multiphase halo gas (Tüllmann et al. 2006) and superwinds (Heckman 2002).

3.3 Kompaneets approximation

We first discuss the expansion of blastwaves in a stratified atmosphere, in the adiabatic case and then for radiative shocks. Kompaneets (1960) had first analytically worked out the case of adiabatic shocks in this case (see, e.g., Bisnovatyi-Kogan & Silich 1995). Consider an exponentially stratified medium described by $\rho(z) = \rho_0 \exp(-z/z_0)$, where ρ_0 is the midplane density and z_0 is the scale height and E_0 is the explosion energy. It is assumed that the shock pressure is uniform, and is given by,

$$P_{sh} = \frac{(\gamma - 1)\lambda E_0}{V}\,, \tag{3.5}$$

where $\lambda \sim 1$ (Kompaneets 1960) is a constant that differentiates the shock pressure from the average pressure inside the bubble; Bisnovatyi-Kogan & Silich (1995) evaluated $\lambda = 1.33$. We use $\lambda = 1$ for simplicity. We define a dimensionless time-like parameter as,

$$y = \int_0^t \sqrt{\frac{(\gamma^2 - 1)E_0}{2\rho_0 V}}dt\,. \tag{3.6}$$

Where E_{th} is the thermal energy of the interior gas, V is the volume of the bubble and t is the time. The shape of the shock front is derived as,

$$r = 2z_0 \arccos\Big\{\frac{1}{2}\exp(z/2z_0)\Big[1 - \frac{y^2}{4z_0^2} + \exp(-z/z_0)\Big]\Big\}\,. \tag{3.7}$$

The location of the top and bottom of the bubble then follows by setting $r = 0$ (with $\tilde{y} = y/z_0$),

$$z_{\pm}(\tilde{y}) = -2z_0.\ln(1 \mp \tilde{y}/2)\,, \tag{3.8}$$

which shows that the top of the bubble reaches infinity when $y \to 2z_0$ while t remains finite. This implies that the bubble accelerates in the z-direction due to stratification, after an initial deceleration phase when the bubble is small and spherical, as in the usual Sedov-Taylor solution. The maximum cylindrical radius of the bubble is also obtained from the above solution by putting $(\partial r/\partial z) = 0$,

$$r_{\rm max}(\tilde{y}) = 2z_0 \arcsin\left(\tilde{y}/2\right). \tag{3.9}$$

The z-component of the velocity of the topmost point of the bubble is given by,

$$v_z(\tilde{y}) = \frac{1}{(1-\tilde{y}/2)}\sqrt{\frac{(\gamma^2-1)}{2}\frac{E_0}{\rho_0 V(t)}}\,. \tag{3.10}$$

3.3.1 Continuous energy injection

We can extend Kompaneets approximation and radiative blastwave calculation to the case of continuous energy injection. Schiano (1985) had done a similar calculation in the case of an active galactic nucleus. Consider an association with N_{OB} stars with masses above 8 $M_\odot$, which ultimately produce supernovae. If we consider the main-sequence lifetime as $\tau_{SN} \sim 5 \times 10^7$ yr for these stars, then the total mechanical luminosity of the SN in the association can written as,

$$\mathcal{L} = 6.3 \times 10^{35} N_{OB}\, E_{51}\, (\tau_{SN}/5\times 10^7 {\rm yr})^{-1} \quad {\rm erg\,s^{-1}}\,, \tag{3.11}$$

where supernova energy is $10^{51}E_{51}$ erg. As McCray and Kafatos (1987) have argued, since the main sequence life time scales with the stellar mass as $\tau \propto M_*^{-1.6}$, and since the initial mass function (IMF) is given by, $dN_*/d(\log M_*) \propto M_*^{-1.35}$, for a Salpeter IMF, the rate of SN will scale with time as $\propto \frac{dN_*}{dM_*}\frac{dM_*}{dt} \propto t^{2.35/1.6}\, t^{-1/1.6-1} \propto t^{1.35/1.6-1}$, which is roughly constant in time. Here we have used $\frac{dM_*}{dt} \propto t^{-1/1.6-1}$, given the above mentioned dependence of stellar main sequence lifetime. Therefore we can write, for the adiabatic case, the total energy in the superbubble as $E_{th} = \mathcal{L}t$.

Instead of eqn 3.10, the $z-$velocity of the top of the bubble is then given by,

$$v_z(\tilde{y}) = \frac{1}{(1-\tilde{y}/2)}\sqrt{\frac{(\gamma^2-1)}{2}\frac{\mathcal{L}t}{\rho_0 V(t)}}\,, \tag{3.12}$$

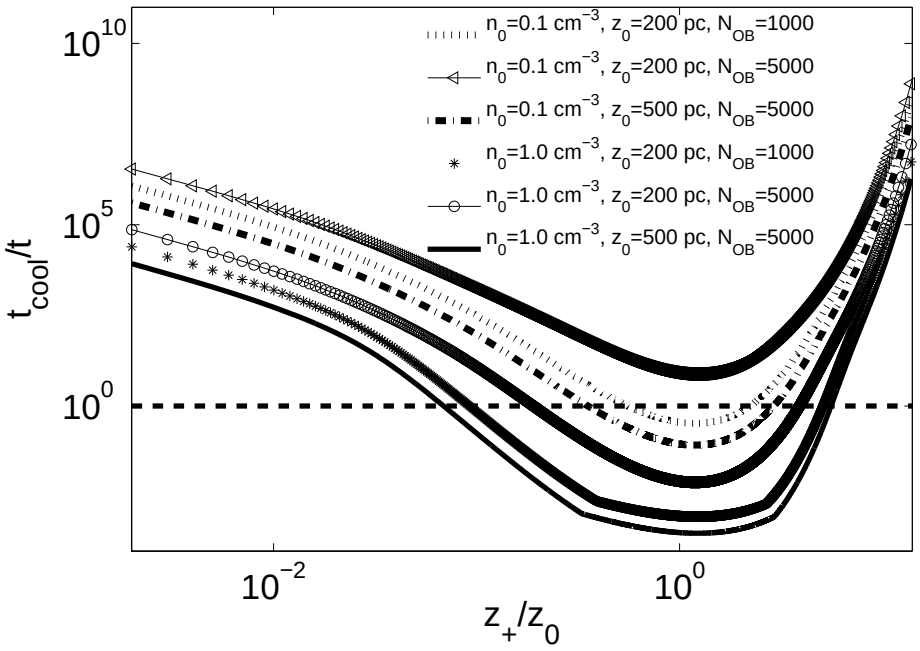

Figure 3.1: The ratio of cooling time to time ($t_{\rm cool}/t$) is plotted against the height of adiabatic superbubble with continuous energy injection, for different combinations of N_{OB}, n_0, and z_0.

and the corresponding y parameter is also written in terms of t, as

$$y = \int_0^t \sqrt{\frac{(\gamma^2-1)\mathcal{L}t'}{2\rho_0 V(t')}}\, dt' \,. \tag{3.13}$$

These equations can determine the dynamics of the superbubble in the case of continuous energy injection.

3.3.2 Radiative loss with continuous injection

Radiative losses can be important for the dynamics of both the blastwave and a superbubble with continuous energy injection. Shocks become radiative when the cooling time $t_{\rm cool} \ll t$. The cooling time behind the shell can be estimated as $t_{\rm cool} = 1.5kT/(4n\Lambda(T))$, for a strong shock with $n = n_0 \exp(-z/z_0)$, and the shock temperature being estimated from the shock speed (in the $z-$direction, say). We assume a cooling function, as given by Eqn 12 in Sharma et al. 2010, appropriate for

gas with $10^4 \leq T(\equiv 10^6 T_6) \leq 10^7$ K and given as follows:

$$\begin{aligned}
\Lambda(T) \quad &= 10^{-22}(8.6\times10^{-3}T_{keV}^{-1.7} + 5.8\times10^{-2}T_{keV}^{0.5} + \\
&\quad 6.3\times10^{-2})\ erg\,s^{-1}cm^3\,,\ T > 0.02\,keV. \\
&= 6.72\times10^{-22}(T_{keV}/0.02)^{0.6}\ erg\,s^{-1}cm^3\,, \\
&\quad T \leq 0.02\,keV,\, T \geq 0.0017235\,keV. \\
&= 1.544\times10^{-22}(T_{keV}/0.0017235)^{6.0}\ erg\,s^{-1}cm^3\,, \\
&\quad T < 0.0017235\,keV\,,
\end{aligned} \tag{3.14}$$

where T_{keV} is the temperature in keV. Figure 3.1 shows the ratio $t_{\rm cool}/t$ as a function of the bubble height z_+ for bubbles with continuous energy injection for a few cases. The curves show that the shock enters the radiative phase much before reaching the scale height unless the ambient density and scale height are very small and N_{OB} is very large (e.g., the case with $n_0 = 0.1$ cm^{-3}, $z_0 = 200$ pc, $N_{OB} = 5000$).

Radiation loss from the shocked medium can therefore be important (see also Maciejewski & Cox 1999). Kovalenko & Shchekinov (1985) had calculated the dynamics of a blastwave with radiative loss, assuming that the shock kinetic energy is converted into thermal energy of gas in a thin shell behind it, and that radiative loss from this shell keeps the shock isothermal. It can then be shown that for a strong shock the energy lost per unit mass is $\sim (1/2)u_s^2$, where u_s is the shock speed. From the Hugoniot condition for a strong shock that,

$$u_s^2 = \frac{(\gamma+1)P_s}{2\rho_0} = \frac{(\gamma^2-1)E_{th}}{2\rho_0 V(t)}\,, \tag{3.15}$$

where E_{th} is the thermal energy of the shocked gas. The structure of the shock in this case is such that the interior gas remains hot and adiabatic, whereas the shocked ambient gas that is swept into a shell loses its energy radiatively and is kept at a constant temperature (at $\sim 10^4$ K). We note that Mac Low & McCray (1988) showed that the radiative loss from the interior hot gas of the bubble does not change the dynamics of the bubble.

Following the calculation of Kovalenko & Shchekinov (1985) for a radiative blast-wave, we assume that bubbles with continuous energy injection also form an isothermal thin shell, after a certain time t_1 when it enters the radiative phase. For simplicity, we also assume a self-similar solution for a spherical shock, of the type given by Weaver et al. (1977), $r_s = A\mathcal{L}^{1/5}t^{3/5}$, where A is a constant depending on the ambient density. Furthermore, Weaver et al. (1977) have pointed out that a fraction 6/11 of the total energy is stored in the shell and the rest in the rarefied gas inside. In the spirit of Kovalenko & Shchekinov (1985) we assume the total shell energy to be thermal in nature. In other words, initially $E_{th} = (6/11)\mathcal{L}t$. We can determine the time evolution of E_{th} as follows.

Using the result derived in eqn 3.15 that the amount of energy lost per unit volume is $(1/2)\rho_0 u_s^2 = (\gamma^2-1)E_{th}/(4V(t))$, we can write for the evolution of thermal energy in this case,

$$\begin{aligned} E_{th}(r) = & \quad \frac{6}{11}\mathcal{L}t - \pi(\gamma^2-1)\int_{r_1}^{r}\frac{E_{th}(r)}{V}r^2dr\,, \\ = & \quad \frac{6}{11}\mathcal{L}^{2/3}\left(\frac{r}{A}\right)^{5/3} - \pi(\gamma^2-1)\int_{r_1}^{r}\frac{E_{th}(r)}{V}r^2dr\,. \end{aligned} \tag{3.16}$$

Here r_1 is the radius at time t_1. We can explicitly solve this equation for a spherical shock, and then use the results to estimate the $z-$ velocity of an oval shaped bubble. For a spherical shock (with volume $V = \frac{4}{3}\pi r^3$), the energy equation (no. 3.16) can be shown to yield a solution of the type $E_{th}(r) = br^{\alpha}$, where

$$b[\alpha + \frac{3}{4}(\gamma^2-1)]r^{\alpha-1} = \frac{6}{11}\frac{5}{3}\frac{\mathcal{L}^{2/3}}{A^{5/3}}\,r^{2/3}\,. \tag{3.17}$$

Comparing the powers of r from both the sides we get, $\alpha = \frac{5}{3}$. Putting this value of α in eqn 3.17 and comparing the coefficients of time on both sides we get,

$$b = \frac{30}{99}\frac{\mathcal{L}^{2/3}}{A^{5/3}}\,. \tag{3.18}$$

Therefore $E_{th}(r)$ becomes,

$$E_{th}(r) = 0.3\mathcal{L}t\,, \tag{3.19}$$

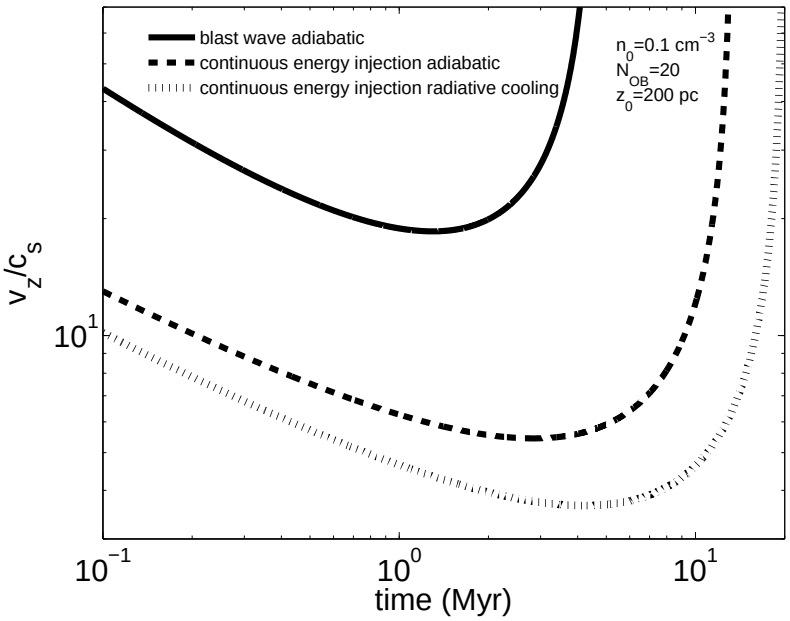

Figure 3.2: The evolution of the ratio of v_z to c_s (the sound speed for an ambient gas at 10^4 K) is plotted against time, for an adiabatic blastwave (thick solid line), adiabatic superbubble with continuous energy injection (dashed) and with radiative loss (dotted line).

showing that roughly 70% of the total energy is radiated away. Note that this is an asymptotic value of the loss in the limit $r \gg r_1$, in the regime where the approximation $E \propto r^{\alpha}$ is valid. We can therefore use equations 3.12 and 3.13, with the above value of E_{th}, and determine the dynamics of a radiative superbubble with continuous energy injection.

3.4 Analytic results

Figure 2 shows the evolution of the Mach number for a 10^4 K gas as a function of time, for an adiabatic blastwave, a superbubble with continuous energy injection with and without radiative loss. It is convenient to define a dynamical time scale for this problem (Mac Low & McCray 1988), $t_d \sim z_0^{5/3}(\rho_0/\mathcal{L})^{1/3}$, which is the expected time to reach the scale height for a self-similar evolution of superbubbles. For $z_0 = 200$pc, $\mathcal{L} \sim 1.3 \times 10^{37}$ erg s^{-1} and $\rho_o \sim 10^{-25}$ g cm^{-3} (for $\mu \sim 0.6$) , $t_d \sim 2.8$ Myr. We find that the $z-$velocity shows a minimum at $\sim 1.5t_d$, when it reaches a distance of the scale height. We denote this minimum value of $z-$velocity as $v_{z,\rm min}$, and refer to this epoch as the 'stalling epoch' in our discussion below.

Figure 3.3 shows the Mach number at stalling height, as a function of $\mathcal{L}$, the mechanical luminosity (which scales as N_{OB}). Interestingly, superbubbles with Mach number (at stalling height) of order less than unity can be triggered by even a single SN. These, in principle, can accelerate later and therefore breakout of the disk. However, as we shall see later with our simulations, there is a minimum number of SNe needed for superbubbles to breakout of the disk, particularly for high density disks. We also find from Fig 3.3 that in order to achieve a Mach number at stalling height of order ~ 5, one needs $\mathcal{L} \geq 7 \times 10^{38}$ erg s^{-1}, for $n_0 = 1$ cm^{-3} and $z_0 = 500$ pc. This is larger than the estimate of Koo & McKee (1992), and Mac Low & McCray (1988), because of the inclusion of radiative loss from the shell. If we consider $v_{z,\rm min}/c_s \geq 5$ as the breakout condition, then we find that larger densities and scale heights put

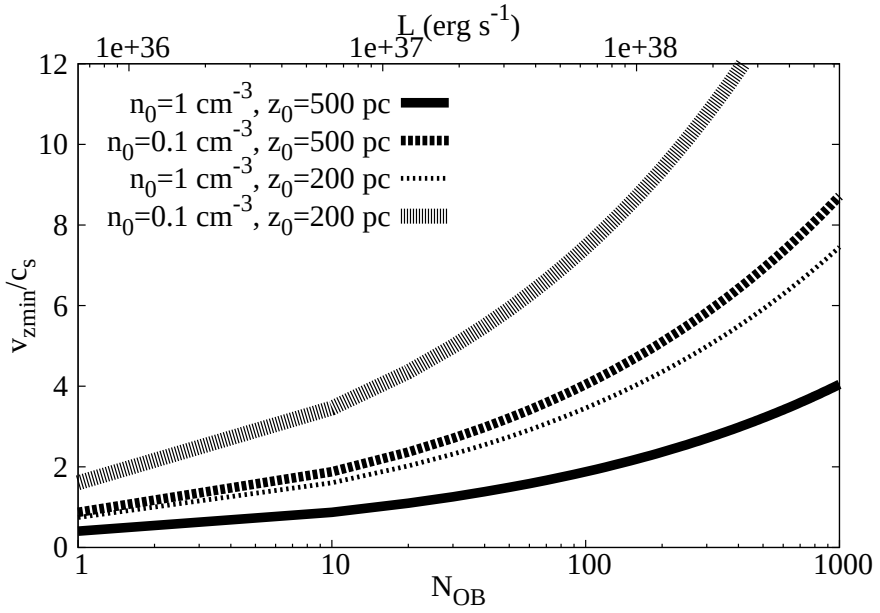

Figure 3.3: The ratio $v_{z,\min}/c_s$ of the $z-$velocity of the top of the bubble to the sound speed of the ambient gas at 10^4 K is plotted as a function of $\mathcal{L}$ the mechanical luminosity, and N_{OB}, the number of SNe responsible for the bubble. Different lines correspond to different values of mid-plane gas number density $(1, 0.1)$ cm^{-3} and scale heights $(200, 500)$ pc.

more stringent condition on the bubble to breakout.

Next we plot in Figure 3.4 the minimum Mach number as a function of the surface density of N_{OB}, considering the surface area of the bubble at the stalling height. Note that we are not concerned with the mean surface density of SFR in the disk galaxy here. The energy injection considered here is localized, but the relevant surface area as far as an emerging superbubble is concerned, is the area of the bubble in the plane of the disk at the point of breaking out. We find that for the surface density of energy deposition the analytic curves become independent of the scale height and depend only on the gas density and number of SNe. This is because the area of a superbubble in the plane parallel to the disk, scales with z_0^2, and is a constant for a given scale height. We find that for a scale height of 500 pc, the threshold surface density of SNe is $N_{OB} \sim 1000$ kpc^{-2}.

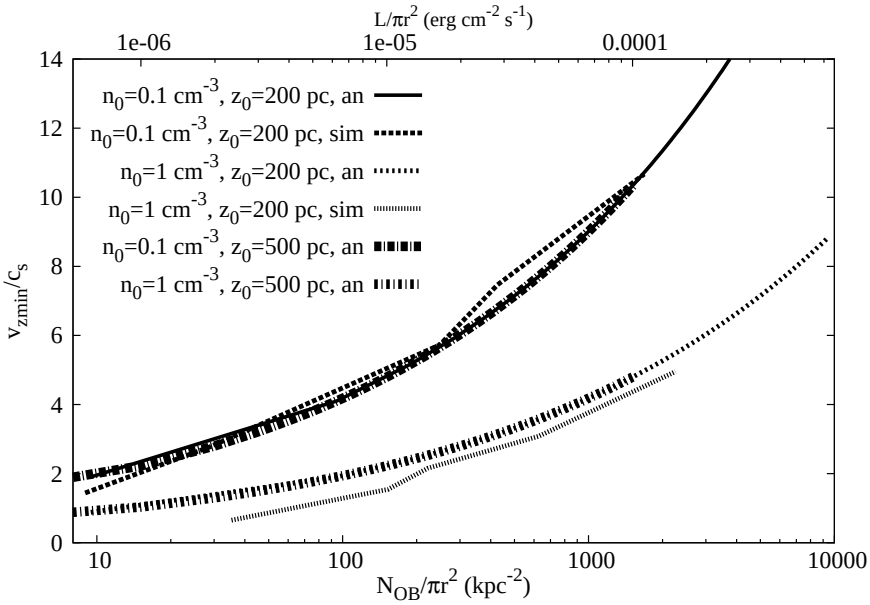

Figure 3.4: Mach number of the top of the bubble at the minimum velocity point is plotted as a function of N_{OB} divided by the cross-sectional area of the bubble at the stalling height, for analytical results and for Kompaneets simulations. Analytical results are shown for different values of mid-plane gas number densities $(1, 0.1)$ cm^{-3} and scale heights $(200, 500)$ pc, whereas simulation results for Kompaneets runs are shown for $n_0 = 0.1, 1$ cm^{-3} and scale height $z_0 = 200$ pc.

3.5 Numerical Simulations

In addition to analytic estimates and approximate calculations, we have performed 2-D axisymmetric hydrodynamic simulations of breakout using the ZEUS-MP code (Hayes et al. 2006). ZEUS-MP is a publicly available, second-order accurate Eulerian hydrodynamics code. We have carried out two sets of simulations: the first set compares numerical simulations with the analytic Kompaneets calculation of strong shocks in stratified atmospheres (hereafter these runs are referred to as 'Kompaneets runs'); and the second set of calculations use a more realistic setup, such as disk gravity, mass-loading of the ejecta, for shock (superbubble) breakbout in starforming galaxies (hereafter these runs will be called 'realistic runs').

In this section we introduce the equations that we solve numerically, the initial and boundary conditions, and the choice of setup parameters. The simulations are run using the 2-D axisymmetric, spherical polar (r, θ, ϕ) coordinates.

3.5.1 Governing Equations

We solve the following standard Euler's hydrodynamic equations including cooling, external gravity, and mass and energy loading at inner radii.

$$\frac{d\rho}{dt} = -\rho\nabla.\mathbf{v} + S_\rho(r)\,, \tag{3.20}$$

$$\rho\frac{d\mathbf{v}}{dt} = -\nabla p + \rho\mathbf{g}\,, \tag{3.21}$$

$$\frac{de}{dt} = -q^-(n,T) + S_e(r)\,, \tag{3.22}$$

where $d/dt \equiv \partial/\partial t + \mathbf{v}.\nabla$ is the Lagrangian derivative, ρ is the mass density, $\mathbf{v}$ is the fluid velocity, p is the thermal pressure, $e = p/(\gamma - 1)$ is the internal energy density (we use $\gamma = 5/3$ valid for an ideal non-relativistic gas), $\mathbf{g} = -\mathrm{sgn}(z)g\hat{\mathbf{z}}$ ($\mathrm{sgn}[z]=\pm 1$ for $z \gtrless 0$) is the constant external gravity pointing towards the $z = 0$ plane, $q^- \equiv n_e n_i \Lambda(T)$ is the cooling term due to radiation where n_e and n_i are the electron and ion number densities, $\Lambda(T)$ is the cooling function (as given in eq 3.14).

There are source terms in the mass and internal energy equations (S_ρ, S_e). These terms are non-zero and constant only within $r_{\rm in}$, a small injection radius (as discussed in chapter 2) within which supernovae pump mass and energy into the interstellar medium. Note that the mass loading (S_ρ) and external gravity ($\mathbf{g}$) terms are used only for the realistic simulations and are set to zero for the Kompaneets runs.

The energy source function is chosen to mimic the energy input by supernovae, $S_e = \mathcal{L}/[(4\pi/3)r_{\rm in}^3]$, where $\mathcal{L} = E_{SN}N_{OB}/t_* = 6.3 \times 10^{35} N_{OB}$ erg s^{-1} is the supernova heating rate, $E_{SN} = 10^{51}$ erg, $t_* = 50$ Myr is the average lifetime of main sequence OB stars, and N_{OB} is the number of OB stars. The mass-loading source function S_ρ is chosen as $S_\rho = \dot{M}/[(4\pi/3)r_{\rm in}^3]$ where $\dot{M} = \beta R_f(\mathcal{L}/4 \times 10^{41}{\rm erg\ s^{-1}}) M_\odot {\rm yr}^{-1}$; where R_f is the return-fraction ($= 0.3$) and $\beta = 3$, that includes the effect of stellar winds, as inferred by Strickland & Heckman (2009) in the case of M82. Tables 3.1 and 3.2 list the parameters for our Kompaneets and realistic simulations respectively.

We implement energy injection by assuming the deposited energy to be thermalized within a radius $r_{\rm in}$, which we determine from the condition that the corresponding analytic solution of superbubble radius enters the Sedov-Taylor (ST) phase. We note that our estimation of $r_{\rm in}$ in this method matches quite well with the analytical expression of $r_{\rm in}$ as calculated in the previous chapter (chapter 2) since the superbubble evolves in almost a uniform density ambient medium when it enters the ST phase. We assume a mass loading $(1/2)\, N_{OB}\, 10\ {\rm M}_\odot \sim 5\, N_{OB}\ {\rm M}_\odot$, for a typical mass of OB stars of order 10 M$_\odot$ and half the progenitor mass being ejected during the supernova. This is an approximation, however we found that mass loading at this level has negligible effects on the evolution of superbubbles. The superbubble enters the Sedov-Taylor phase when the ejecta mass equals the mass swept up by the shell. We choose this radius to be our $r_{\rm in}$ because before this phase, most of the energy of the superbubble is in kinetic form, and the assumption of most of the energy being thermalized is appropriate only in the Sedov-Taylor phase. Moreover, $r_{\rm in}$ should be smaller than the radius at which the shock becomes radiative. Tables 3.1 and 3.2 show the values of

$r_{\rm in}$ for different simulations.

3.5.2 Initial and Boundary conditions

We have used ZEUS-MP in spherical polar (r, θ, ϕ) coordinates. We fix the inner radial boundary (the mass and energy injection radius) at $r_{\rm min} < r_{\rm in}$, and the outer boundary at $r_{\rm max} = 3$–10 kpc, depending on the distance reached by the superbubble in 1.23×10^{15} s (39.3 Myr) , the maximum time for which we run the simulations. For $\theta - \phi$ coordinates, θ goes from 0 to π, and ϕ goes from 0 to 2π. We use a logarithmically spaced grid in the radial direction such that there are equal number of grid points in $[r_{\rm min}, (r_{\rm min} r_{\rm max})^{1/2}]$ and $[(r_{\rm min} r_{\rm max})^{1/2}, r_{\rm max}]$; the grid is uniformly spaced in the other directions. The resolution adopted for our simulation is $512 \times 256 \times 1$, in the r, θ, ϕ directions (although we have used a higher resolution of $1024 \times 1024 \times 1$ for our study of thermal instability in the relevant cases). Outflow boundary conditions are applied at the outer radial boundary. Inflow-outflow boundary condition is applied at the inner radial boundary such that mass is allowed to leave or enter the box. Reflective boundary conditions are imposed at $\theta = 0,\ \pi$, and periodic boundary conditions are applied in the ϕ direction.

The initial conditions in Kompaneets and realistic runs are different. Both set of runs have an initial temperature of 10^4 K corresponding to the stable WIM. In Kompaneets runs the density is stratified in the vertical $(z-)$ direction as $\rho(t = 0) \propto e^{-z/z_0}$, where z_0 is the scale height. Thus, the initial state is not in dynamical equilibrium. However, since the sound speed is very small, the evolution occurs because of fast energy injection in the center. We have verified that the results are the similar as for simulations with a constant initial pressure. For the Kompaneets runs, we have used a scale height of $z_0 = 200$ pc.

For realistic runs the initial ISM is symmetric with respect to the vertical direction, with $\rho(t = 0) \propto e^{-|z|/z_0}$, where the scale height is determined self-consistently for an isothermal gas in hydrostatic equilibrium; i.e., the strength of the constant gravi-

Table 3.1: Parameters for Kompaneets runs ($\mathcal{L} = 6.3 \times 10^{35}$ erg s^{-1} N_{OB})

n_0 (cm^{-3})	N_{OB}	$r_{\rm in}$ (pc)	$r_{\rm min}$ (pc)	$r_{\rm max}$ (pc)
0.1	1	10	5	2500
0.1	10	21	10	2500
0.1	100	44	30	2500
0.1	300	63	40	3000
0.1	1000	94	70	3500
1.0	1	5	3	2500
1.0	10	10	5	2500
1.0	100	20	10	2500
1.0	300	29	15	3000
1.0	1000	44	30	3000

tational acceleration is chosen to be $g = c_s^2/z_0$ where $c_s \equiv \sqrt{kT/\mu m_p}$ (k is Boltzmann constant, μ is the mean particle mass, and m_p is proton mass) is the isothermal sound speed and z_0 is the scale height.

3.5.3 Kompaneets runs

We first describe the results of our Kompaneets runs, of superbubbles in a stratified atmosphere without external gravity or mass-loading. Figure 3.4 shows the variation of the minimum Mach number of the top of the superbubble as a function of the surface density of energy injection in the disk, for a scale height of 200 pc and two values of ambient density, $n_0 = 0.1$ and 1 cm^{-3}. We find that the analytical results overestimate the Mach number of the superbubbles compared to the simulations by a factor of order ~ 1 for the case of large ambient density (1 cm^{-3}), because the analytical estimate of energy loss described in the previous section is based on sim-

plified assumptions. Note that since we determine the value of z_+ by the position of the maximum density, clumps in the shell formed due to thermal instability (see below for details) introduce some uncertainity. This manifests in the kinks seen in the simulation results in Fig. 4 and also later in Fig. 6.

3.5.4 Realistic runs

Next we describe simulations that includes vertical disk gravity and mass loading. We study the case of ambient gas at $T = 10^4$ K, with mid-plane densities $n_0 = 0.1$ and 1 cm^{-3}, and scale heights $z_0 = 100$ and 500 pc.

Our choice of parameters essentially brackets the possible range of gas density and scale height in disk galaxies. For example, the distribution of the extraplanar gas in Milky Way has two components, that of warm ionized gas and cold HI. The warm ionized gas has been observed to have an exponential profile with $n_0 \sim 0.01$–0.03 cm^{-3} and $z_0 \sim 400$–1000 pc (Reynolds 1991; Nordgren et al. 1992; Gaensler et al. 2008). For HI distribution, Dickey & Lockman (1990) found that the vertical distribution is best described by a Gaussian with FWHM of 230 pc and a central density of 0.57 cm^{-3}. The combined distribution of these two components are bracketed by exponentials with the scale heights and mid-plane densities assumed here.

We also use smaller scale heights in our simulations. The scale height near the centres of galaxies is smaller than that in the outer regions, because of deeper gravitational potentials in the central regions. Also Dalcanton, Yoachim, Bernstein (2004) found that the HI scale height of disk galaxies varies with the rotation speed (or, equivalently, the galactic mass). Dwarf spirals with rotation speed ~ 50 km s^{-1} have $z_0 \sim 200$ pc whereas larger galaxies (with rotation speed in excess of 120 km s^{-1}) have $z_0 = 500$–1000 pc. Also, as Basu et al. (1999) have found, the scale height encountered by Milky Way superbubbles such as W4 is rather small (≤ 100 pc).

We first find that unlike in the analytical case, where superbubbles ultimately break out of the disk sooner or later, irrespective of the energetics, the realistic sim-

Table 3.2: Parameters for Realistic runs

z_0 (pc)	n_0 (cm^{-3})	N_{OB}	r_{in} (pc)	r_{min} (pc)	r_{max} (pc)
100	0.1	1	10	5	1000
100	0.1	10	21	10	2500
100	0.1	100	44	10	2500
100	0.1	300	63	10	2500
100	0.1	1000	94	50	2500
100	1	100	20	10	2500
100	1	300	29	15	2500
100	1	1000	44	30	2500
100	1	2000	55	40	2500
100	1	3000	63	40	2500
500	0.1	10	21	10	2500
500	0.1	100	44	10	2500
500	0.1	300	63	30	3500
500	0.1	1000	94	50	3500
500	0.1	3000	135	110	3500
500	0.1	10000	201	160	3500
500	0.1	50000	344	300	12000
500	0.1	100000	433	400	12000
500	1	1000	44	30	2500
500	1	2000	55	40	2500
500	1	3000	63	40	2500
500	1	5000	75	50	3500
500	1	10000	94	70	3500
500	1	100000	201	150	5500

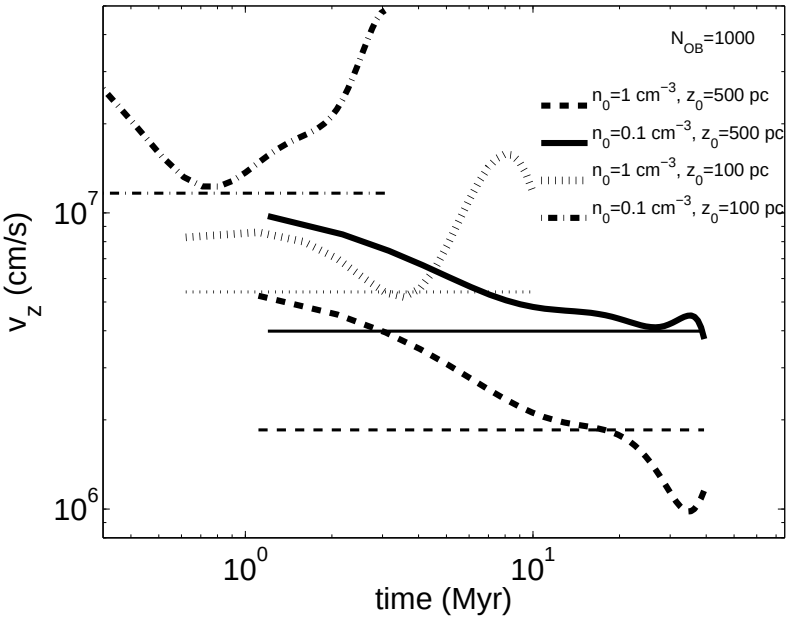

Figure 3.5: Velocity of the topmost point of the bubble is plotted against time for $N_{OB} = 1000$, but for different combinations of scale height ($z_0 = 100, 500$ pc) and mid-plane gas density ($n_0 = 0.1, 1$ cm^{-3}). The horizontal lines in each case shows $(1/5)(\mathcal{L}/\rho_0 z_0^2)^{1/3}$, the expected scaling.

ulation runs show that for high density disk material ($n_0 \geq 1$ cm^{-3}) , superbubbles keep decelerating for ever for a surface density of OB stars $\sim 100(z_0/100\,\mathrm{pc})$ kpc^{-2}. In other words superbubbles never break out of the disk in these cases. The corresponding energy injection surface density is $\sim$ 2–5 $\times\ 10^{-5}$ erg cm^{-2} s^{-1} For lower density ambient gas, $n_0 \sim 0.1$ cm^{-3}, however, even a single SN event can drive a bubble through the disk. We note that this limit is consistent with that found by Silich & Tenorio-Tagle (2001) for a Milky Way type disk.

In the case of a superbubble breaking out of the disk, there are differences in the way they evolve depending on the energy injection rate. We show the evolution of the speed of the topmost point of the bubble as a function of time for four cases in Figure 3.5, for two mid-plane densities ($n_0 = 0.1, 1$ cm^{-3}), and two scale heights ($z_0 = 100, 500$ pc), all for a surface density of OB stars of 1000 kpc^{-2}. The curves show that the bubbles show acceleration after breakout of the disk only for the case of low

density and small scale height (see the curve at the top-left corner, for $n_0 = 0.1$ cm^{-3}, $z_0 = 100$ pc). In other cases, for disk column density $\geq 3 \times 10^{19}$ cm^{-2}, the bubbles either coast along with the the speed that they reach at the breakout, or decelerate to some extent, for a considerable period of time before they start accelerating after reaching a distance of several scale heights. The curves show that the speed at the stalling height, or the minimum speed of the bubbles, is an important characteristics of the bubble dynamics. It is important because this is the characteristic speed with which the bubble sweeps most of the extra-planar region of the halo. Also, since the bubble begins to accelerate only after reaching a distance of a few times the scale height, the corresponding Rayleigh-Taylor instability should not set in at the scale height, but at a much larger distance. We shall re-visit this point in the next section on instabilities. In some cases, the curves show a deceleration at late times. This is due to the formation of clumps in the shell from radiative cooling, which often sink through the hot gas owing to gravity.

We have found that typically the minimum speed $v_{z,\rm min} \sim (1/5)(\mathcal{L}/\rho_0 z_0^2)^{1/3} \sim z_0/(5t_d)$, where t_d is the dynamical time defined earlier. These values are shown as horizontal lines in Figure 3.5 for respective cases. It is easy to see that in case of little radiation loss, the speed of the bubble at the time of reaching the scale height is $\sim (3/5)(\mathcal{L}/\rho_0 z_0^2)^{1/3}$, as expected from the self-similar evolution of a bubble ($r \sim (\mathcal{L}t^3/\rho_0)^{1/5}$). Our simulations show that the actual speed is roughly a third of this value, and therefore shows the importance of radiative loss in the dynamics of superbubbles. As analytically derived earlier, radiation losses remove as much as 70% of the total energy of the superbubbles. We recall that for an ambient medium with a given temperature, the dimensionless quantity defined by Mac Low & Norman (1988) is $D \sim (5v_{z,\rm min}/c_s)^3$, so that their condition of $D \geq 100$ for break out corresponds to a minimum Mach number of order unity.

We show the resulting value of minimum Mach number of superbubbles for different n_0 and z_0 in Figure 3.6, as a function of surface density of energy injection.

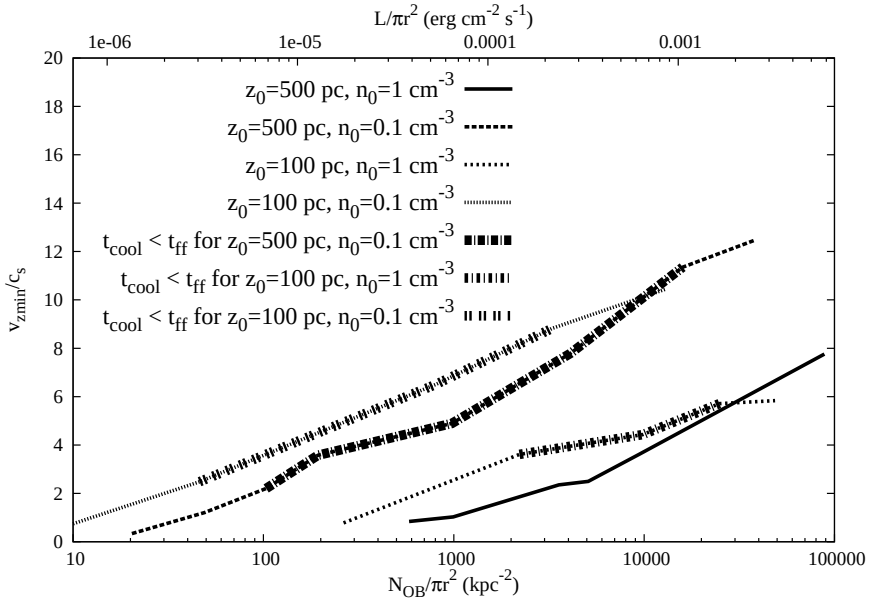

Figure 3.6: The minimum Mach number of the top of the bubble in our realistic runs are shown as a function of N_{OB} per kpc^{-2}, and $\mathcal{L}/\pi r^2$ (erg cm^{-2} s^{-1}), for $n_o = 0.1, 1$ cm^{-3} and $z_0 = 100, 500$ pc. Note that, for $n_0 = 1$ cm^{-3}, the shocks stall for a surface density of OB stars ≤ 500 kpc^{-2}. The cases for which $t_{cool} < t_{ff}$, are shown by darkened points, these cases are marked by thermal instability.

The curves show that in terms of energy injection or SNe surface density, the crucial parameter is the mid-plane gas density, which separates the curves, as was also indicated by our analytical results. Superbubbles with a given surface density of energy injection find it easier to break out of disks with lower mid-plane density. However, scale height also makes a small difference unlike in the analytical calculations; a higher energy density is required to clear a thicker disk.

The important features of our results as shown in Figure 3.6 are:

- As mentioned above, the condition for a break out from a dense ambient medium with gas density of $n_0 = 1$ cm^{-3} is an energy injection rate surface density of 2–5 $\times$ 10^{-5} erg cm^{-2} s^{-1}. For lower gas densities, the required rate density is $\sim 10^{-6}$ erg cm^{-2} s^{-1}. The corresponding Mach number for these superbubbles that can be as low as of order unity.

- Superbubbles that can break out with a larger Mach number of $\sim$ 3–5 corresponds to $\sim$ 1000 N_{OB} kpc^{-2}, or an energy injection surface density of 10^{-4} erg s^{-1} cm^{-2}, for the most realistic spiral disks, with $n_0 = 0.1$ cm^{-3}, $z_0 = 500$ pc, or $n_0 = 1$ cm^{-3}, $z_0 = 100$ pc (which for Milky Way case describes either the warm extra-planar or cold gas). We note that the largest OB associations have $\sim 10^4$ M$_\odot$ (McKee & Williams 1997), and with a cross-sectional area of order $\pi\,(\pi z_0)^2$ (since $r_{\rm max} \sim \pi z_0$ asymptotically; see equation 3.9), a superbubble blown by such a large OB association can only have $\leq 10^3$ SNe kpc^{-2}, for a Salpeter IMF. Therefore we can conclude that (a) only the largest of the OB associations can produce a bubble that can break out of Milky Way-type disks, (b) this also corresponds to the minimum energy injection rate of 10^{-4} erg s^{-1} cm^{-2} as observed by Dahlem et al. (1995) for the existence of radio emitting halo gas, and (c) larger ISM density or scale height would require more than one OB association to produce a superbubble or adjacent multiple bubbles that can coalesce and grow together. Recent simulations show that cosmic rays can stream through ISM gas to considerable heights above the disk, and break out

of superbubbles can provide such channels (Uhlig et al. (2012).

- As explained earlier, the minimum speed of 3–5 $c_s \sim 30$ km s^{-1}, for an ambient gas at 10^4 K, also corresponds to the case where the hot (and multiphase gas; see next section on instabilities and gas cooling) interior gas can sweep up to a height of ~ 1 kpc within a time period of ~ 50 Myr, the time scale over which OB stars explode and keep injecting energy in the bubble. Combined with the result mentioned above, we can conclude that an energy injection rate of 10^{-4} erg s^{-1} cm^{-2}, or $\sim 1000\ N_{OB}$ kpc^{-2} can not only produce a bubble that can break out of the disk but also fill the halo up to a height of order ~ 1 kpc.

- If we insist on a larger Mach number at stalling height, to be 5–10, then the energy injection rate becomes $\sim 10^{-3}$ erg s^{-1} cm^{-2}, with $\sim 2 \times 10^4\ N_{OB}$ kpc^{-2}. Using a time scale of ~ 50 Myr of OB stars, the corresponding SFR surface density for a Salpeter IMF is ~ 0.06 M$_\odot$ yr^{-1} kpc^{-2}. If superbubbles seed galactic outflows, then the gas speed is required to be a few hundred km s^{-1}, and the Mach number at stalling height is needed to be much larger than ten, and the corresponding requirement on SFR surface density increasing to ~ 0.1 M$_\odot$ yr^{-1} kpc^{-2}, the observed threshold. Therefore, the Heckman (2000) threshold (~ 0.1 M$_\odot$ yr^{-1} kpc^{-2}) for superwinds corresponds to a larger requirement on the part of superbubbles, of not only breaking out of disks but doing so with a large Mach number.

3.6 Thermal and Rayleigh-Taylor instability

The focus till now was on the important v_z/c_s parameter (the minimum Mach number of the shell) which determines the fate of the superbubble after it crosses the scale height. In this section we discuss the role of different instabilities, in particular Rayleigh-Taylor and thermal instabilities, in our 2-D breakout simulations. When the superbubble reaches about a scale height, the shock is generally believed to accelerate

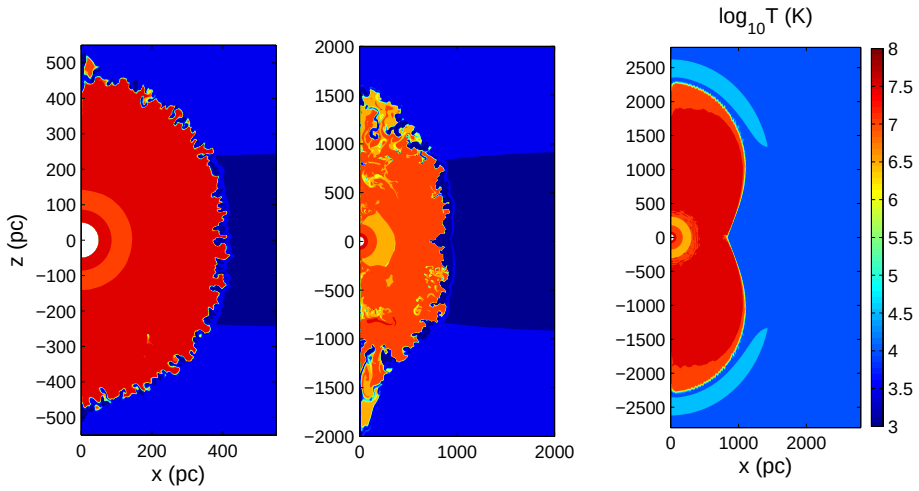

Figure 3.7: Temperature contours (colour coded) for a superbubble with $N_{OB} = 5000$, $n_0 = 1$ cm^{-3}, $z_0 = 500$ pc, at $t = 9$ Myr, when the top of the bubble has reached a distance of the scale height (left panel), at 39.3 Myr, when it has reached a distance $\sim 3z_0$ (middle panel). The rightmost panel shows the case of the same superbubble without radiative cooling at $t = 39.3$ Myr, the same evolutionary epoch as the middle panel.

owing to the decrease in pressure. This should lead to the onset of the Rayleigh-Taylor (RT) instability, as has been invoked in previous analytical works (e.g., Koo & McKee 1992) and seen in numerical simulations (e.g., Mac Low, McCray & Norman 1989). However, as mentioned earlier, our simulations show that superbubbles *do not* accelerate until after they reach a distance of several scale heights (as was also suggested by Ferrara & Tolstoy 2000 who assumed spherical bubbles). Therefore RT instability occurs at a distance *much larger* than the scale height. Also we find that before the onset of RT instability, the superbubble expanding in the disk suffers from thermal instability in the early stages of its evolution. This instability leads to clumping and fragmentation of the shell of the superbubble well in advance of the RT instability, and can therefore affect the outcome of the RT instability.

Figure 3.7 shows the 2-D snapshots of temperature at two different times for our fiducial high resolution run ($N_{OB} = 5000$, $n_0 = 1$ cm^{-3}, $z_0 = 500$ pc). Figure 3.6 indicates that the minimum Mach number for this case is ≈ 2 and the bubble is just

about able to break out within the starburst timescale. The temperature snapshot at early time (9 Myr), when the bubble has just reached the scale-height, shows that the bubble is roughly spherical. The radiative shell seems to develop corrugations where the hot bubble gas and the radiatively cooled shocked gas interpenetrate. The shell is at $\approx 10^4$ K (the same as the ambient ISM temperature), the temperature below which the cooling function drops suddenly and the gas becomes thermally stable. The dense shell is more clearly seen in the density snapshots of Figure 3.8. The corrugations are definitely driven by radiative cooling because the run without radiative cooling shows a smooth shell (the third panel in Figs. 3.7 and 3.8).

While the fragments of cold shell are confined to the bubble boundary at early times, the cold gas lags behind the hot gas at later times because the hot gas is pushed out by supernova heating. The cold blobs are only pushed out because of the drag force due to the hot gas but eventually trail behind. The cold blobs embedded in the hot gas are reminiscent of the cold multiphase filaments observed in galactic outflows, such as M82. Since in our simulations cold gas leaves the simulation box from the inner boundary, all the cold blobs embedded in the hot bubble come from the fragmenting cold shell. In reality, some cold gas from the cold star-forming regions can also be uplifted by the hot gas. At late times, in the runs with cooling, there are some signs of bubble breaking out because of RT instability close to the polar regions. All such signatures of RT instability are missing in the run without cooling (panel 3). This is mainly because RT instability in the run with cooling is seeded with large amplitude perturbations by corrugations caused by shell cooling.

In order to assess the relative importance of thermal and RT instabilities, we compare the two times scales in Figure 3.9. We note that the time scale for RT instability ($t_{RT} = \sqrt{1/(\dot{v}_z + g)k}$) is comparable to the free-fall time ($t_{\rm ff} = \sqrt{2z/(\dot{v}_z + g)}$, for the largest mode with $k \sim 2\pi/z$, where z and $\dot{v}_z$ are the height and acceleration of the shell, and g is the acceleration due to gravity. We plot this time scale with a solid line in Figure 3.9, along with the cooling time ($t_{\rm cool} = 1.5kT/n\Lambda$) of the shell as a

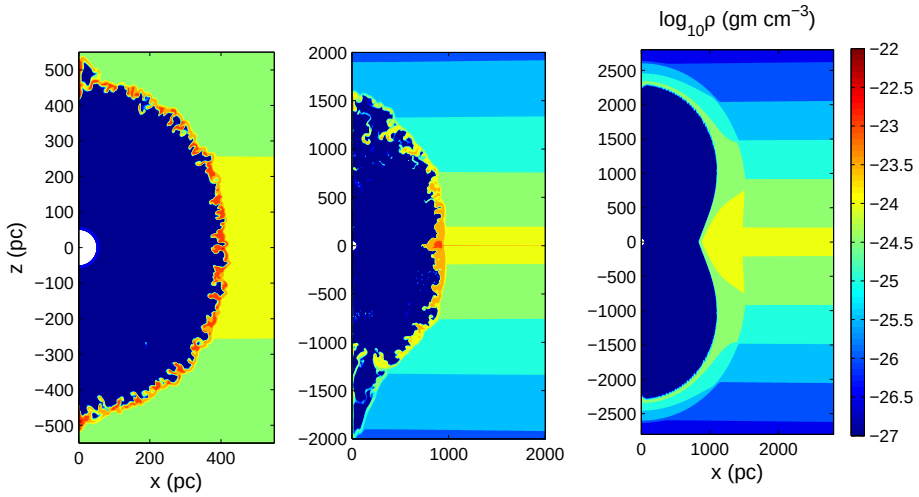

Figure 3.8: Density contours for the same cases as in Fig 3.7. Here, fragmentation of the shell is clearly seen in the run with cooling.

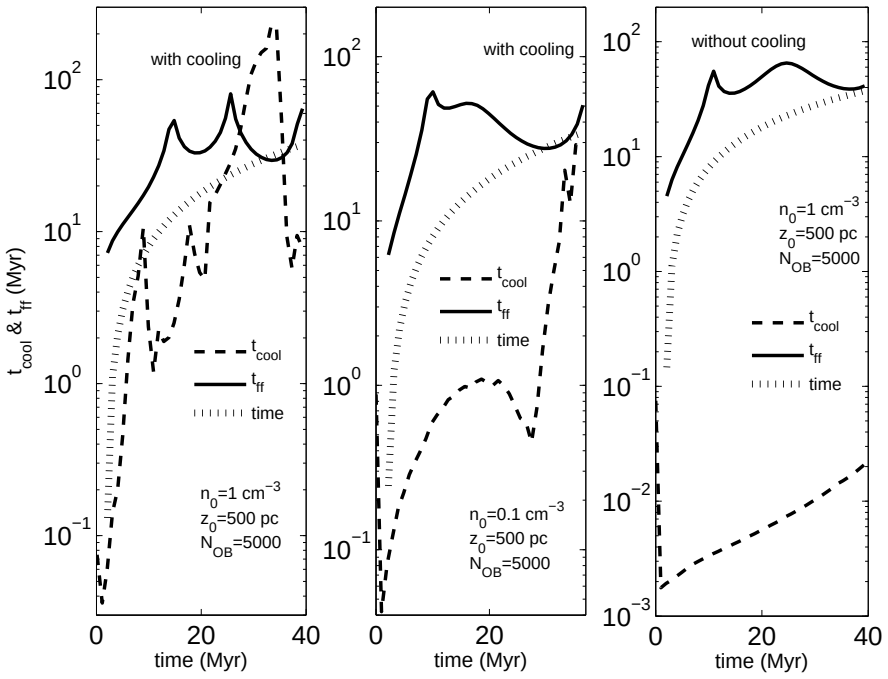

Figure 3.9: The free-fall and cooling timescales for the shell material are plotted against time, for two examples with $N_{0B} = 5000$, $z_0 = 500$ pc, and $n_0 = 1$ cm^{-3} (left panel), $n_0 = 0.1$ cm^{-3} (middle panel). The grey lines show the time elapsed in each cases for comparison. The right panel shows the case of no radiation cooling for $n_0 = 1$ cm^{-3}. The leftmost and rightmost panels correspond to the runs shown in Figs 3.7 and 3.8.

function of time for runs corresponding to Figures 3.7 & 3.8. We use the position of the outermost densest part to identify the shell position. In the left panel of Figure 3.9, we show the case of $N_{OB} = 5000$, $n_0 = 1$ cm^{-3}, $z_0 = 500$ pc. We expect the shell to cool radiatively if $t_{\rm cool}$ is shorter than time. And indeed, the radiative cooling time is shorter than time at early times. This is consistent with the cooling and fragmentation of the dense shell seen in Figs. 3.7 & 3.8. One point of caution: we should ideally plot the cooling time of the shell assuming the shell temperature and density corresponding to an adiabatic shock because cooling will happen if this timescale is short. Here we are plotting the cooling time of the shell, which for the left panel case, has already cooled to low temperatures. Since cooling time increases sharply below 10^4 K, $t_{\rm cool}$ is barely smaller than time in the left panel of Figure 3.9. At later times $t_{\rm cool}$ becomes longer than time and we do not expect the newly accumulated shell material to cool. The RT timescale ($\approx t_{\rm ff}$) is always longer than time for the fiducial run. The free-fall time increases initially as the shock slows down until a scale height. After that the shock moves at a small Mach number ~ 2. This is consistent with the fact that we do not see vigorous RT instability in Figures 3.7 & 3.8.

The middle panel of the Figure 3.9 shows various timescales for a midplane density of $n_0 = 0.1$ cm^{-3}. The cooling time for this case is shorter than the cooling time for the higher density case. This seems inconceivable given the higher density and efficient cooling for the run in the left panel. This discrepancy arises because although the density for the $n_0 = 0.1$ cm^{-3} is smaller, the temperature of the post-shock gas is 10^5 K, where the cooling function peaks. Consequently the cooling time is shorter than the higher density run. For comparison, we have also plotted the cooling and free-fall timescales for the runs without cooling in the right panel. The density and temperature snapshots for this run do not show cooling-induced fragmentation.

We have shown in Figure 3.6 by darkened points the cases in which $t_{\rm cool}$ is always less than $t_{\rm ff}$, for different values of $\mathcal{L}/\pi r^2$, z_0 and n_0. We find that these cases mostly appear for which, roughly, $10 \geq v_{z,\rm min} \geq 3$, except for the case of $z_0 = 500$ pc and

$n_0 = 1$ cm^{-3}, for which there is a cross-over point in time after $t_{\rm cool} \geq t_{\rm ff}$. We note that this range of $v_{z,\rm min}$ corresponds to a case in which the shell temperature (T_s) remains in the range of $2 \times 10^4 \leq T_s \leq 10^6$, where the cooling function peaks. This implies a range in N_{OB} for which thermal instability is imporant. In the low N_{OB} limit, the shock is not strong enough and $T_s \leq 10^4$ K, and in the high N_{OB} case, the shock is very strong ($T_s > 10^6$ K) and $t_{\rm ff}$ (RT timescale) is shorter than $t_{\rm cool}$ at late times.

We are therefore led to conclude that superbubbles are affected not only by RT instability but also by thermal instability, depending on the density and energy injection. This implies that the fragmentation of the bubble shell that releases the hot interior gas into the halo occurs under the combined effects of thermal instability at early times and RT instability at late times if the Mach number at stalling epoch is large enough.

3.7 Discussion & Summary

Superbubbles with fragmented shells are believed to ultimately form 'chimneys' (Norman & Ikeuchi (1989), which connect the halo gas to the processes in the disk in different ways. Apart from transporting hot gas to the halo, chimneys provide a natural channel for Lyman continuum photons from hot stars in the disk to reach the diffuse ionized medium of the Reynolds layer (Reynolds 1991; Dove & Shull 1994). It is however important for the superbubble shells to fragment before the main sequence life times of O stars for a substantial fraction of ionizing radiation to escape the disk (Dove, Shull, Ferrara 2000). This implies a fragmentation time scale of $\sim$ 3–5 Myr, which is comparable to the dynamical timescale ($t_d \sim z_0^{5/3}(\rho_0/\mathcal{L})^{1/3}$), for superbubbles with $\mathcal{L} \sim 10^{38}$ erg (corresponding to $N_{OB} \sim 200$), typical disk parameters. This is the energy scale for the largest of the OB associations, and as our results show superbubbles with smaller energetics find it hard to pierce through the disk, unless

the OB association is located much above the mid-plane level.

In other words, for superbubbles to act as effective conduits of ionizing radiation for the halo, or for the intergalactic medium (at high redshift, in the context of the epoch of reionization), the superbubbles need to fragment roughly around the time when they reach a scale height. This is unlikely to happen only through RT instability as superbubbles do not accelerate until reaching a distance of several scale heights. Also, as de Avillez & Breitschwerdt (2005) have discussed on the basis of simulations of a magnetized ISM, superbubble shells can stabilize against RT instability in the presence of magnetic fields. In this regard, the clumping of the shell from thermal instability at an early phase of evolution of the superbubble can be important.

We have studied the evolution of superbubbles in stratified disks analytically and with simulations. Our results can be summarised as follows:

- Our analytic calculations show that radiation losses are important for superbubble dynamics. Radiation loss is more important for superbubbles with continuous energy injection than a supernova remnant of similar total energy. We estimate almost 70% of the total energy being radiated away. We have further checked our analytical results with numerical simluations. We found that analytic results match the simulations well, differing at most by a factor of order unity for the case of large ambient density. The results obtained by the analytical means therefore provide a useful benchmark to compare with realistic simualtions. Also, for disks with large gas density, with $n_0 \geq 1$ cm^{-3}, superbubble breakouts are not possible for surface density of OB stars $\leq 100(z_0/100\,\mathrm{pc})$ kpc^{-2}, or an equivalent energy injection surface density of $\leq$ (2–5) $\times\, 10^{-5}$ erg cm^{-2} s^{-1}.

- Superbubbles that emerge from the disk with Mach number of order 2–3 require an energy injection rate of $\sim 10^{-4}$ erg cm^{-2} s^{-1}, corresponding to explosions triggered by the largest OB associations with 10^4 M$_\odot$. This energy injection scale corresponds to disk galaxies with synchrotron emitting gas in the extra-

planar regions.

- Vigorous superbubbles that break out of the disk with sufficiently large Mach number ($\geq$ 10) , correspond to an energy injection rate of $\sim 10^{-3}$ erg cm^{-2} s^{-1}, or equivalently, a SFR surface density of $\sim$ 0.1 M$_{\odot}$ yr^{-1} kpc^{-2}. These superbubbles require more than one OB associations to produce and sustain their dynamics, and this energy injection scale corresponds to (a) the existence of multiphase gas in the halo of disk galaxies, and (b) the Heckman threshold for the onset of superwinds.

- Superbubbles do not accelerate until reaching a vertical distance of a few scale heights (of order ~ 2), which implies that RT instability helps to fragment the shells not at a distance of a scale height but at a much larger height. Also, we find that for typical disk parameters, thermal instability acts on the shell at the early stages of superbubble evolution, and forms clumps and fragments in the shell, much before the shell is acted upon by RT instability. Radiative cooling therefore manifests in seeding thermal instability, which has important implications for the clumping of superbubble shell and producing channels of leakage for ultraviolet radiation into the halo.

Chapter 4

Escape fraction of LyC photons from disk galaxies

Based on : "Narrow escape: how ionizing photons escape from disc galaxies" Roy, A., Nath, B. B., Sharma, P., 2015, MNRAS, 451, 1939

Superbubbles play a role in enriching the ISM and the IGM by ejecting hot, dilute, and high metallicity gas via the shell channels (as discussed in chapter 3). These pathways also help the hydrogen ionizing photons (Lyc photons) emanating from central OB-associations to escape. Although there are various observational and theoretical estimates of the escape fraction ($f_{\rm esc}$) of Lyc photons and its evolution with redshift (z), the dependence of $f_{\rm esc}$ on the basic disc parameters (n_0, z_0) remains unexplored. In this chapter, we scan the parameter space of (n_0, z_0) in order to understand the dependence of $f_{\rm esc}$ on the disc parameters and redshift z.

Primary results

- We find that the ionizing photons escape through a narrow cone angle $\sim 40°$, which is consistent with observations.

- The escape fraction initially decreases with time as the superbubble is buried under the dense disk. After the superbubble breaks out of the disk on reaching a few scale-heights, the shell fragments into clumps and channels due to RTI. These channels are the optically thin pathways through which the Lyc photons escape.

- The average (angle averaged, time averaged, and averaged over the luminosity functions of OB associations) escape fraction is related to the disk parameters such that $f_{\rm esc}^{\alpha} n_0^2 z_0^3$ is a constant with $\alpha = 2.2$.

- We find that the value of the escape fraction for disk galaxies is $f_{\rm esc} \sim 10 \pm 5\%$, with weak variations with disk mass, and redshift if disk temperature is kept constant.

- This value of $f_{\rm esc}$ fulfils the requirements for the creation of the diffuse ionized

gas beyond the Milky-Way's HI disk (aka "Reynold's layer"). It is also sufficiently large for the universe to be reionized by stellar sources around $z \sim 6$.

4.1 Introduction

The evolution of galaxies is tuned by various regulatory mechanisms. Galaxies eject gas, radiate photons, accelerate high energy particles, thereby affecting their surroundings, which in turn influence their evolution. The leakage of ionizing photons from galaxies is one such crucial mechanism, since it produces an ultraviolet background radiation that significantly influences the evolution of galaxies in the universe. The sources of the ionizing photons determine the spectrum of the background radiation in the intergalactic medium (IGM), which has important implications, e.g., in the reionization of the universe at $z \geq 6$. However, it remains uncertain whether star forming galaxies or active galactic nuceli (AGNs) were the main contributors to the epoch of re-ionization. One of the main reasons for the uncertainty is our lack of knowledge of how the local ionizing background in individual galaxies is produced, because all extrapolations to high redshift depends on it.

The understanding of this background radiation depends on the knowledge of $f_{\rm esc}$, the fraction of ionizing photons from massive stars that can escape the galaxies. Several workers have estimated this 'escape fraction' from both theoretical considerations and observations. Since there is a wide disagreement in the value of escape fraction, we summarise below these estimates and the methods used to produce them.

Direct observations: Observational estimates of the escape fraction of ionizing photons from extragalactic objects became possible with the new generation of UV telescopes in 1990s. Leitherer et al. (1995) [116] observed the luminosity of four starburst galaxies at 900 $\AA$, and estimated $f_{\rm esc} \leq 3\%$. This estimate was revised upwards by Hurwitz et al. (1997) [91] to lie between 3–57% after taking into account a detailed model of interstellar absorption. Bland-Hawthorn & Maloney (1999) [10] used Hα measurements of the Magellanic Stream to infer $f_{\rm esc} \leq 6\%$ for our Galaxy. Observations of CII interstellar absorption line at λ1036 with *FUSE* allowed Heckman et al. (2001) [74] to estimate $f_{\rm esc} \leq 6\%$ for a set of five bright starburst galaxies. While comparing their estimate with that from starburst galaxies with outflows, Heckman et al.

(2001) [74] posed the question if the outflowing gas affect $f_{\rm esc}$ and concluded that outflows do not necessarily increase its value by creating additional channels in the ISM. However, in their later study with a bigger sample, Heckman et al. (2011) [76] concluded that outflows from starburst can significantly increase the escape fraction. They also discovered four objects, whose central regions are very compact ($\sim 10^2$ pc) and massive ($\sim 10^9$ $M_\odot$), and which had significant outflows. They have recently shown that one of these extreme objects has an escape fraction $\sim 20\%$ (Borthakur et al. (2014) 17). Working with *FUSE* archival data, Leitet et al. (2013) [115] estimated $f_{\rm esc} \leq 2.5\%$ for a local starburst. Recently, Zastrow et al. (2013) [231] obtained the emission-line ratio maps of [SIII]/[SII] for a few dwarf starbursts, and observed the ionizing photons to be confined within a cone of opening angle $\sim 40^\circ$. This means that the direct measurement of the escape fraction by modeling the absorption in UV lines depends sensitively on the orientation. They also pointed out that the escape fraction is large for galaxies older than the time needed by supernovae to create pathways for ionizing photons (~ 3 Myr), but young enough so that O stars (the main contributors to ionizing photons) are still present (main sequence life time of ~ 5 Myr).

Observational constraints on the escape of ionizing photon from high redshift galaxies are sparse. Soon after the Lyman Break Galaxies (LBG) were discovered at $z \sim 3$, the escape fraction from them were estimated to be 10–20% (Adelberger & Steidel (2000) 1; although Haehnelt et al. (2001) 72 argued that it could be as large as 50%). Recent observations by Nestor et al. (2011) [145] have yielded $f_{\rm esc} \sim 10\%$, and Cooke et al. (2014) [30] found $f_{\rm esc} \sim 16 \pm 4\%$ for LBGs. At a lower redshift, $z \sim 1$, observations of starbursts in the GOODS field have suggested $f_{\rm esc} \leq 2\%$ (Siana et al. (2010) 179).

Constraint from UV background radiation: It is possible to put constraints on $f_{\rm esc}$ from the observations of the UV background radiation and considering the possible contribution from starburst galaxies (or AGNs). Shull et al. (1999) [178] argued that

starbursts would be able to contribute as much to the UV background radiation as AGNs if $f_{\rm esc} \geq 5\%$. Inoue et al. (2006) [93] reconsidered this issue in light of more recent observations, and concluded that $f_{\rm esc} \leq 1\%$ at $z \leq 1$ and increases to $\sim 10\%$ at $z \geq 4$. Fujita et al. (2003) [58] simulated superbubbles in dwarf starburst galaxies, and argued that high redshift galaxies may make a significant contribution to the background radiation if the escape fraction is $\geq 20\%$. Recently, Kollmeier et al. (2014) [106] have suggested that the intensity of the UV background radiation at low redshift ($z < 0.4$) is likely to be higher than previously thought, which would imply a corresponding increase in the required escape fraction. However, the assumed fiducial value of escape fraction at low redshift is quite low in this calculation, the 'minimal reionization model' of $f_{\rm esc} = 1.8 \times 10^{-4}(1+z)^{3.4}$ (Haardt & Madau (2012) 71).

Constraint from the epoch of reionization: It is also possible to put constraints on the escape fraction from the requirement of explaining the observations related to reionization (the minimum redshift by which the universe is believed to have been fully ionized and the total Thomson optical depth). Madau & Shull(1996) [124] estimated the required $f_{\rm esc} \sim 50\%$ in order to keep the universe ionized at $z \sim 5$. However, this calculation depends on the assumption of luminosity function of galaxies at high redshift or, if a theoretical mass function is used, on the assumption of star formation efficiency in galaxies. Inoue et al. (2006) [93] estimated the minimum requirement for reionization, as $f_{\rm esc} = 1.8 \times 10^{-4}(1+z)^{3.4}$, which implies $f_{\rm esc} \sim 2\%$ at $z = 3$. Recently Mitra et al. (2013) [136] have used their semi-analytical model of galaxy formation to compare with the observed luminosity functions at high redshift, and then to calculate the requirement from reionization observations. They concluded that reionization requires $f_{\rm esc} \sim 7(\pm 5)\%$ at $z = 6$, and a mild (but uncertain) increase to $\sim 18^{+33}_{-13}\%$ at $z = 8$.

Theoretical calculations: Dove & Shull (1994) [44] analytically calculated the escape fraction for the Milky Way ($\sim 10\%$), considering HII regions around OB association that likely produces 'HII chimneys' for ionizing photons to escape. They argued

that this process could explain the ionizing radiation needed for the existence of the Reynolds layer of warm ionized medium. Wood & Loeb (2000) [229] estimated the escape fraction considering a disk galaxy in steady state, with sources embedded in it, using a 3-D radiation transfer code. They used a stratified disk with redshift dependent parameters, using the prescriptions of Mo, Mao & White (1998) [137]. Naturally, their disks had large density and were thin at high redshift, and their escape fraction rapidly decreased with an increasing redshift. Galaxies with mass 10^{12} $M_\odot$ at $z = 0$ have $f_{\rm esc} \sim 1\%$, whereas smaller galaxies, say with 10^9 $M_\odot$, have similar escape fraction at $z \sim 3$. On average they predicted an escape fraction $\leq 1\%$ at $z \sim 10$. A similar calculation by Benson et al. (2013) [8] took into account the effect of high energy photons in the case of sources of hard spectrum. Instead of radiation transfer through a disk, Ferrara & Loeb (2013) [55] considered the evolution of ionization fronts in dark matter halos containing gas at 10^4 K, and found the escape fraction to increase with redshift during reionization.

In contrast to these calculations, Dove et al. (2000) [45] and Clarke & Oey (2002) [28] emphasised the importance of the time evolution of superbubbles in this regard. It is clear that the structure of the ISM must be important in determining the leakage of ionizing photons. The typical HI column density in galaxies ($\geq 10^{21}$ cm^{-2}) is much larger than needed to make the ISM on average opaque to these photons, since only $N_{HI} \geq 10^{17}$ cm^{-2} is needed to shield them. Dove et al. (2000) [45] considered the OB associations in the Milky Way and propagation of ionizing photons through the superbubbles triggered by them. These superbubbles first decelerate during their early evolution, following the results of Weaver et al. (1977) [224] for the self-similar evolution of stellar wind driven bubbles. However, after they reach the scale height of the stratified disk, they accelerate (Kompaneets (1960) 107, Roy et al. (2013) 164), which can fragment the superbubble shells through Rayleigh-Taylor instability and create pathways for ionizing photons to escape. Dove et al. (2000) [45] estimated the escape fraction to be $\sim$ 6–15%, depending on the assumption of star formation

history. This idea was carried forward with the help of hydrodynamic simulations by Fujita et al. (2003) [58], who studied the time evolution of the escape fraction for OB associations of a given mass (with number of OB stars $N_O = 40000$), and stressed that superbubbles can effectively trap the ionizing photons before blowout. Their work explained the time evolution of $f_{\rm esc}$ in light of the two competing processes, between a diminishing source of ionizing photons from an evolving OB association and the increasing number of pathways created by the superbubbles. Therefore, the observed low values of $f_{\rm esc} \geq 5\%$ in local dwarf galaxies could be explained if they were young (before the feedback processes could carve out enough channels in the ISM); the time-averaged $f_{\rm esc}$ could be larger than these observational estimates. They estimated the escape fraction in high redshift disk galaxies to be $\sim 20\%$ and highly dependent on the dynamics of superbubbles in them (because at high density, escape of ionizing photons would be difficult without the aid of superbubbles).

Several authors have also used hydrodynamic simulations for galaxy formation, with star formation and their feedback processes included in them, and estimated the escape fraction. These simulations have less control on the parameters and therefore the results are often difficult to interpret. Gnedin et al. (2008) [67] found the escape fraction to decrease rapidly with a decreasing galactic mass, because of the increasing disk thickness and the paucity of young stars on the periphery of the disks. On the contrary, Razoumov & Sommer-Larsen (2010) [159] estimated the escape fraction to increase with a decreasing galactic mass and an increasing redshift (see also [226]), reaching an average of $\sim 80\%$ at $z \sim 10$. Yajima et al. (2011) [230] concluded that massive disks were more clumpy than low mass disks, and this decreased $f_{\rm esc}$ in large galaxies, since stars were embedded deep in the clumps. They estimated $f_{\rm esc} \sim 40\%$ for 10^9 $M_\odot$ galaxies and $\sim 7\%$ for 10^{11} $M_\odot$ galaxies. Paardekooper et al. (2013) [152] and Hutter et al. (2014) [92] also arrived at similar conclusions. However, this view of the effect of clumps on the escape fraction runs opposite to that of Fernandez & Shull (2011) [54], who argued that fewer, high-density clumps would lead to a greater

escape fraction than in the case of more numerous low-density clumps. Kimm & Cen (2014) [105] found from the study of a large number of galaxy halos in their simulation that on average $f_{\rm esc} \sim 10\%$ with little variation with galactic mass and redshift, although instantaneous values of the escape fraction could reach $\geq 20\%$. They also found that run away OB stars could increase the average escape fraction to $\sim 14\%$.

Our goal in this chapter is to extend the previous works on the escape fraction by focusing on the effect of superbubbles. The distinctive features of this work are: (1) controlled hydrodynamic numerical experiments on a wide range of disc parameters, with disc densities ranging between 0.5–50 cm^{-3} and scale heights between 10–600 pc; (2) the escape fraction is weighted by the luminosity function of OB associations and does not use OB associations of a particular size. Our strategy is to focus on the effect of important disc parameters on the escape fraction, rather than to explore a large number of effects at once, such as ISM clumpiness or cosmological mergers. In our simulations we use gas without any initial clumpiness, but we discuss the effect of clumpiness on the escape fraction by considering the covering fraction of the fragmented superbubbles.

This chapter is organized as follows. In section 4.2 we present the numerical set up, including the model for superbubbles and the warm disk. In section 4.3 we present the method for calculating the escape fraction, which is a function of viewing angle, time and the number of OB stars, in addition to the disk parameters (n_0, z_0). In section 4.4 we present our results on the escape fraction, including variation with redshift and the galactic mass; we also discuss the influence of clumpiness. Section 4.5 discusses and compares our results with previous works.

4.2 Numerical setup

The numerical setup in this chapter is similar to what we have discussed in section 3.5 of chapter 3 with the following differences :

- We use the Sutherland & Dopita (1993) [197] cooling function for solar metallicity in the temperature range 10^4–10^8 K; below 10^4 K $\Lambda(T)$ is set to zero. The initial isothermal gas temperature is assumed to be 10^4 K.

- We have used spherical (r, θ) coordinates for our simulations, similar to what we have used in the previous chapter. However, our radial grid extends from 1 pc ($r_{\rm min}$) to 2 kpc ($r_{\rm max}$); in some higher N_O runs ($N_O \geq 10^4$, N_O being the number of O stars) the outer boundary extends up to $r_{\rm max} = 3$ kpc. In the highest density cases ($n_0 = 50$ cm^{-3}) the inner radial boundary is $r_{\rm min} = 0.5$ pc, maintaining the strong shock condition (see eqn 4 in Sharma et al. (2014) [174]).

- Our runs with various parameters use different resolutions. Specifically, high density disks (higher n_0) with lower energy injection (smaller N_O, the number of O stars) result in extensive formation of multiphase gas, and the number of dense clumps increases with an increasing resolution (this is true in all simulations which do not resolve the transition layers between hotter and cooler phases; e.g., see Koyama & Inutsuka (2004) [112]). The low density and higher N_O runs do not show much multiphase gas and are less sensitive to resolution. Detailed resolution studies are discussed in Appendix A.1. Various parameters for our different runs, including resolution, are mentioned in Table 4.1.

- The CFL number is the standard value 0.5, but in high density ($n_0 \geq 1.5$ cm^{-3}) and low N_O cases ($N_O < 10^4$) we use the CFL number of 0.2 as it is found to be more robust.

Table 4.1: Parameters for various runs

n_0 (cm^{-3})	N_O	Resolution	$r_{\rm min}$ (pc)	$r_{\rm in}$ (pc)
0.15, 1, 1.5	100 –10^5	256×128	1	2
5, 15	100 – 300	512×512	1	2
5, 15	600 –10^5	256×128	1	2
50	100 –10^5	256×128	0.5	1

- We have carried out a large number of runs to cover a range of values in n_0, z_0 (disk scale-height) and N_O. This was necessary to obtain the key result of this chapter discussed in section 4.4.3. We have carried out 2-D axisymmetric simulations because 3-D simulations are very expensive due to a larger number of grid points and a much smaller stability time step. In Appendix A.3 we show that the results for our 2-D fiducial run are similar to the results obtained in 3-D.

4.2.1 The warm neutral disk

The vertical structure of the thin disk is determined by self-gravity and gas temperature. Hydrostatic equilibrium for the gas in z-direction is given by,

$$\frac{dp(z)}{dz} = -\rho(z)g(z) \tag{4.1}$$

where p is the thermal pressure of the gas, $\rho(z)$ is the density and $g(z)$ is the vertical disk gravity, the $z-$ component of $\mathbf{g}$. Using Poisson's equation along with eqn 4.1 leads to the vertical density distribution of the disk gas (Spitzer 1942),

$$n(z) = n_0\,\mathrm{sech}^2\Big(\frac{z}{\sqrt{2}z_0}\Big), \quad z_0 = \frac{c_s}{\sqrt{4\pi G\mu m_p n_0}}. \tag{4.2}$$

Here, n_0 is the mid-plane density of the disk ($z = 0$) and z_0 is the scale height of the gas in the disk, and $c_s = \sqrt{k_b T/\mu m_p}$ is the isothermal sound speed of the gas. The

corresponding value of $g(z)$ is,

$$g(z) = \frac{\sqrt{2}k_bT}{\mu m_p z_0} \tanh\left(\frac{z}{\sqrt{2}z_0}\right). \tag{4.3}$$

We consider only the self-gravity of the initial stratified gas, and assume it to be constant with time, which is a caveat in our calculations. Also, we assume that the initial ISM is non-clumpy.

The equilibrium value of n_0, z_0 and T are related as (eqn 4.2)

$$z_0 = 257 \text{ pc} \left(\frac{T}{10^4\text{K}}\right)^{1/2} \left(\frac{n_0}{0.5 \text{ cm}^{-3}}\right)^{-1/2}, \tag{4.4}$$

where we have used $\mu = 1.33$. Later we vary n_0 and z_0 independently to study the variation of escape fraction as a function of these disk parameters (c.f. Fig. 4.10). We note that c_s needs to be adjusted with (n_0, z_0) to obtain a self-consistent hydrostatic equilibrium (Eqs. 4.2 & 4.3). We use the initial disk temperature of 10^4 K, corresponding to the thermally stable warm neutral phase (Wolfire et al. (2003) [227]). We, therefore, keep the initial temperature fixed at 10^4 K, even when we vary n_0 and z_0 independently of each other. This means that our disks with general n_0, z_0 parameters are not in perfect hydrostatic balance, except when they satisfy eqn 4.4. However, we note that for all the cases considered here, the dynamical time scale of superbubbles breaking through the disk (eqn 4.10), which is important for the determination of escape fraction, is always shorter than the gravitational time scale (free-fall) for the disk to evolve. Therefore, the disks are stable for the time scale of importance in our calculation of escape fraction. Most of our runs highlighted in various figures correspond to a self-consistent hydrostatic equilibrium for 10^4 K (closely satisfying eqn 4.4).

We only consider a warm neutral disk at 10^4 K and do not include a cold neutral (100 K) component. This is justified because the cold neutral medium is expected to be clumpy. Moreover, even if we consider a self-consistent cold disk, the scale height z_0 should be much smaller $\propto (T/n_0)^{1/2}$ (eqn 4.2). The fraction of LyC photons

absorbed by the disk is roughly given by (c.f. eqn 4.7) $4\pi\alpha_H^{(2)} n_0^2 z_0^3/S$, which scales as $p^{1/2}T$ (p is pressure). Thus, for a warm and cold disk at pressure equilibrium the escape fraction is dominated by the hotter (10^4 K) warm disk.

4.2.2 Superbubble implementation

The mass and energy source functions in Eqs. B.1 & Euler equations (equations 3.20, 3.21, 3.22 of chapter 3) are applied in a small enough volume such that radiative losses do not quench the formation of a superbubble (Sharma et al. (2014) [174]). The mass source function $S_\rho = \dot{M}_{\rm in}/(4\pi r_{\rm in}^3)$, where $\dot{M}_{\rm in} = N_O M_{\rm ej}/t_O = 6.33\times10^{18} N_O$ g s^{-1}, $M_{\rm ej}$ is the ejected mass in a single supernova explosion (chosen as $1M_\odot$), t_O is 10 Myr (the lifetime of O stars), N_O is the number of O stars present *initially*, or equivalently, the total number of supernova explosions within time t_O. We note that the final results in our simulations are insensitive to our choice of $M_{\rm ej}$, which only affects the structure of the hot/dilute gas within the superbubble. The energy source function, which mimics the energy input by supernova explosions within $r_{\rm in}$, is given by $S_e = \mathcal{L}/(4\pi r_{\rm in}^3)$, where $\mathcal{L}$ is the mechanical luminosity of supernovae. We consider $r_{\rm in} = 2$ pc in all our simulations except for runs with $n_0 = 50$ cm^{-3}, for which we take $r_{\rm in} = 1$ pc to prevent artificial cooling losses.

We run our simulations for a period of 10 Myr, the average lifetime of O9.5 stars (Chiosi, Nasi & Sreenivasan (1978) [27], Meynet & Maeder (2003) [134], Weidner et al. (2010) [225]), the least massive O stars of mass 20.8M$_\odot$ (Vacca et al. (1996) [214]), since O stars are thought to produce most of the ionizing photons (Dove & Shull (1994) [44]). The mechanical luminosity produced by O-stars in the association is,

$$\mathcal{L} = N_O E_{\rm ej}/t_O = 3.16\times10^{36}\, N_O\, {\rm erg\,s^{-1}}\,, \tag{4.5}$$

where $E_{\rm ej} = 10^{51}$ erg is the explosion energy of one SN (10^{51} erg).

The escape fraction, which we describe shortly in the next section, depends very crucially on the structure of the ISM, in particular to the low density channels opened

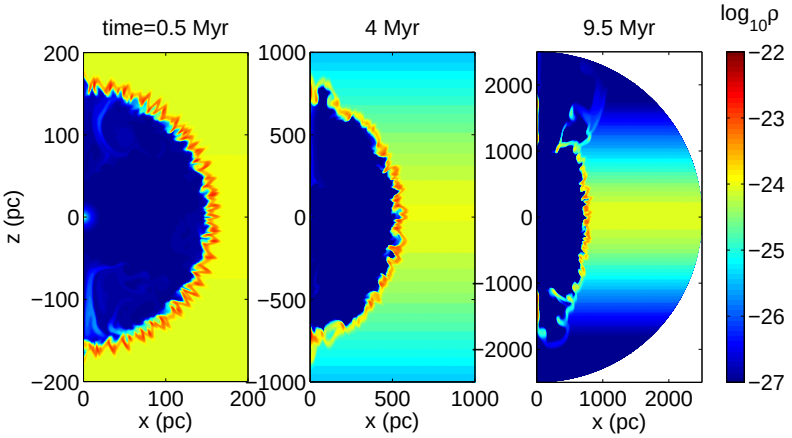

Figure 4.1: Density contour plot of the superbubble at different times (0.5, 4.0, 9.5 Myr) for $n_0 = 0.5$ cm^{-3}, $z_0 = 300$ pc and $N_O = 10^4$. Early, intermediate and late stages of superbubble evolution are shown. Notice the low density cone through which photons should escape at late times.

by the expanding superbubble. As studied in detail in Roy et al. (2013) [164], the evolution of a superbubble for a sufficiently strong starburst shows two stages: first, the Sedov-Taylor stage when the outer shock radius is smaller than the scale height; and second, the fast breakout of the superbubble due to thermal and Rayleigh-Taylor instabilities after it crosses a few scale-heights. The escape fraction for a density-bounded (Strömgren radius > disk scale height) disk is expected to decrease with time in the first stage as photons are absorbed in the dense shell. After breakout, the escape fraction increases with time because of opening of low density channels in the ISM. We see this effect in the time evolution of the escape fraction described later. Figure 4.1 shows the density contour plots of our fiducial run ($n_0 = 0.5$ cm^{-3}, $z_0 = 300$ pc, $N_O = 10^4$) at early, intermediate and late times. As the escape fraction is intimately connected to the ISM porosity, it is useful to remember these various stages of superbubble evolution in order to interpret our results.

4.3 Calculation of escape fraction

In this section we describe the formalism to calculate the escape fraction assuming photoionization equilibrium (ionization rate equals recombination rate). We can calculate the number of photons absorbed per unit time, and hence the number of photons escaping along different directions and at different times. Thus, the escape fraction is a function of angle (θ), time (t) and disk/starburst parameters (n_0, z_0, N_O). Since the distribution of OB associations is similar in different regions, we average our escape fraction in time, angle, and the number distribution of OB associations.

4.3.1 Ionization Equilibrium

In order to calculate the fraction of ionizing photons that escapes the disk, consider the ionizing photons emitted within a solid angle $d\Omega$ within angles θ and $\theta + d\theta$. First consider the case of ionization equilibrium in the disk gas, and assume that all ionizing photons are absorbed in the medium, so that the escape fraction is zero. If S denotes the time-dependent luminosity of ionizing photons (number of ionizing photons produced per unit time $\propto N_O$; discussed in section 3.2), and $\alpha_H^{(2)}$ denotes the recombination coefficient for case B ('on the spot' ionization case), then we have in the case of ionization equilibrium in a solid angle $d\Omega$,

$$S\frac{d\Omega}{4\pi} = \int \alpha_H^{(2)} n_H^2(r) r^2 dr d\Omega \,, \tag{4.6}$$

where $n_H(r)$ is the number density of hydrogen (which is equal to the electron/proton density within the ionized bubble). These considerations apply in the standard calculation of Strömgren sphere (Dyson & Williams (1997) [50]), which is ionization bounded.

In general, however, all the ionizing photons will not get absorbed; some will escape and thus eqn 4.6 will not hold. In this case the ISM is density bounded. Therefore, the escape fraction of ionizing photons in an angle between θ and $\theta + d\theta$

can then be written as,

$$f_{esc}(\theta, t, N_O; n_0, z_0) = \frac{Sd\Omega/4\pi - \int_0^\infty \alpha_H^{(2)} n_H^2(r) r^2 dr\, d\Omega}{Sd\Omega/4\pi} = 1 - \frac{4\pi\alpha_H^{(2)}}{S}\int_0^\infty n_H^2(r) r^2 dr, \quad (4.7)$$

where we have indicated the dependence of the escape fraction on various parameters in parentheses. Later we will average the escape fraction over time, angle and number of O stars. The averaged escape fraction is denoted as $\langle f_{esc}\rangle$ where the parameters over which averaging is done denoted in subscript; e.g., $\langle f_{esc}\rangle_{\theta,t}$ denotes the time- and angle-averaged escape fraction as a function of N_O for a fixed n_0 and z_0. Note that the photon luminosity ($S \propto N_O$) is time dependent, and for a given OB association S decreases abruptly after the most massive stars die off (c. f. Fig. 4.2).

The expression in eqn 4.7 is valid when the recombination time scale is shorter than other time scales in the problem, e.g., the dynamical time scale. This puts a condition on n_0 and z_0 (mid-plane density and scale height respectively) for which we can calculate the escape fraction using eqn 4.7. The recombination time scale is given by,

$$t_{\rm reco} \equiv \frac{1}{n\alpha_H^{(2)}(T)} = \frac{1}{4n_H\alpha_H^{(2)}(T)} = 0.04 n_H^{-1} T_4^{3/4} {\rm Myr}\,, \quad (4.8)$$

where we have written $n = 4n_H$, since most of the recombinations occur in the dense shell and $\alpha_H^{(2)}(T) = 2\times10^{-13} T_4^{-3/4}$ cm^{-3} s^{-1} (Dyson & Williams (1997) [50]). This means that the balance between ionization and recombination is achieved in a very short time.

The radius of a superbubble in a uniform density medium with density ρ is given by (Weaver et al. (1977) [224]),

$$r = \left(\frac{\mathcal{L}t^3}{\rho}\right)^{1/5}. \quad (4.9)$$

For a scale height z_0 of the gas distribution in the disk, the dynamical time is given

by (the time taken by the superbubble to reach the scale height),

$$t_d = \left(\frac{\rho_0 z_0^5}{\mathcal{L}}\right)^{\frac{1}{3}} = 4 n_H^{1/3}\, z_{0,100pc}^{5/3}\, N_O^{-1/3}\ \text{Myr}, \tag{4.10}$$

where $\mathcal{L}$ is the mechanical luminosity (eqn 4.5), n_H is hydrogen number density in cm^{-3} and $z_{0,100pc} = z_0/(100\,\text{pc})$, and we have assumed $\mu = 1.33$. The condition $t_{\text{reco}} < t_d$ implies,

$$\frac{n_H^4 z_{0,100pc}^5}{N_O} > 10^{-6}\,. \tag{4.11}$$

This means that the assumption of ionization equilibrium holds for the relevant ISM parameters and the use of equation 4.7 is valid. This assumption breaks down only for low mid-plane densities and small scale-heights, as discussed in section 4.4.

4.3.2 Stellar ionizing luminosity

The escape fraction of ionizing photons depends on the total ionizing luminosity S (eqn 4.7), which in turn depends on the size of the OB association, characterised by N_O, the total number of O stars. The time evolution of the ionizing luminosity depends on the initial mass function (IMF) of the OB association and how the ionizing luminosity and main sequence life time of stars depend on their masses. We use Starburst99 (Leitherer et al. (1999) [117]) to calculate the evolution of the ionizing luminosity $S(t)$ for an OB association. The time dependence of LyC luminosity, $S(t)$, is assumed to be the same for all OB associations, but $S(t)$ scales linearly with the number of O-stars (N_O). We have used the case of an instantaneous starburst and assumed Salpeter IMF between 0.1 and 100 $\text{M}_\odot$. Note that we have only considered O stars in our calculation as these stars contribute the most towards the total ionizing luminosity of an OB association. Since the least massive O stars with ~ 20 $\text{M}_\odot$ have a life time of ~ 10 Myr (see the discussion before eqn 4.5), we have used a lower mass cutoff for supernovae at 20 $\text{M}_\odot$ to calculate the value of N_O for a given cluster mass. This is also consistent with the relation of mechanical luminosity with N_O in eqn 4.5. The ionizing photon luminosity is initially constant when all the O-stars are

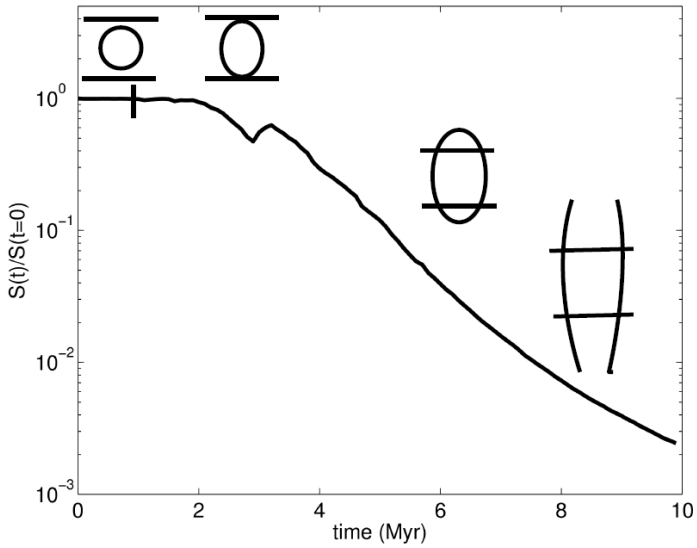

Figure 4.2: Normalized LyC photon luminosity as a function of time for a starburst calculated using Starburst 99. The dynamical time scale (of superbubble shells reaching the scale height) for $n_0 = 0.5$ cm^{-3}, $z_0 = 300$ pc ranges between 0.4–4.2 Myr for different N_O. For these values, we also sketch the superbubble shells vis-a-vis the disk, beginning from the left with a small spherical shell, then with an elliptical shell slowly breaking out and finally ending with a shell whose top has been blown off by instabilities. The short vertical line at 0.4 Myr corresponds to the dynamical time (t_d) for $N_O = 10^5$.

present in the main sequence, and it decreases abruptly after 3 Myr as the sources of ionizing photons (O-stars) start to die off. We plot a representative sketch of ionizing luminosity as a function of time in Figure 4.2. We also sketch the different evolution stages of the superbubble. Initially the superbubble shell is completely buried inside the disk, and then it takes an elliptical shape. After that, the shell breaks out of the disk, and in the final stages the superbubble ends up with a shell whose top has been blown off by thermal instabilities and RTI.

4.3.3 Escape fraction

We calculate the escape fraction along different lines of sight varying the angle from 0 to $\pi/2$ (where we measure θ from the perpendicular to the disk), using eqn 4.7 at a given time and for a particular N_O. Then we average it over 4π steradian to get the θ-averaged escape fraction as a function of time and N_O:

$$\langle f_{esc} \rangle_\theta (t, N_O) = \frac{1}{4\pi} \left[2 \int_0^{\pi/2} f_{esc}(\theta) \sin(\theta) d\theta \int_0^{2\pi} d\phi \right] . \tag{4.12}$$

The time-averaged escape fraction for a given N_O is then,

$$\langle f_{esc} \rangle_{\theta,t} (N_O) = \frac{\int_0^{t_O} \langle f_{esc} \rangle_\theta (t, N_O) S(t) dt}{\int_0^{t_O} S(t) dt} , \tag{4.13}$$

where $t_O = 10$ Myr.

We plot this $\langle f_{esc} \rangle_{\theta,t} (N_O)$ (eqn 4.13) as a function of N_O for $n_H = 0.5$ cm^{-3} and for two values of $z_0 = 10$ and 300 pc in Figure 4.3. For $z_0 = 10$ pc, the dynamical time $t_d < t_{\rm reco}$, the recombination time scale, and the escape fraction is independent of N_O (blue dashed line), whereas for $z_0 = 300$ pc, it increases with N_O (black solid line). In the first case, the superbubble reaches the scale height before substantial recombination takes place in the shell, and the escape fraction is dominated by the dynamics of the superbubble than by the recombination rate. Our formalism is not valid in the first case, as explained in section 3.1.

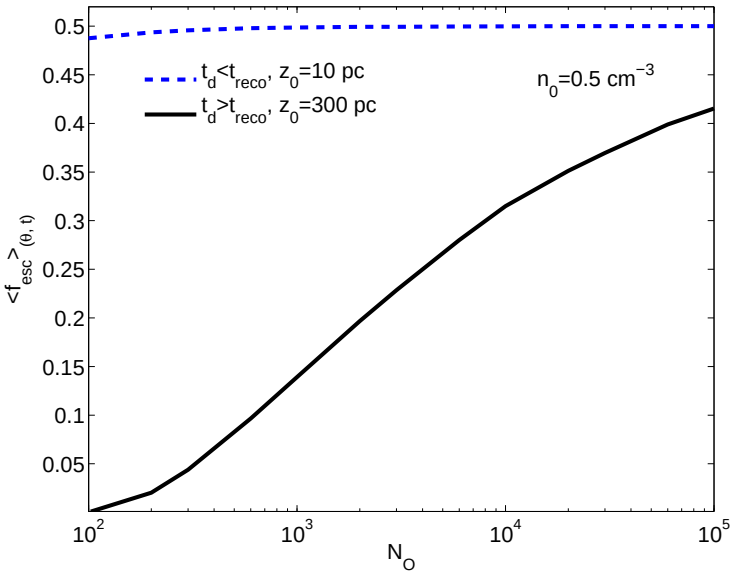

Figure 4.3: Time- and angle-averaged escape fraction as a function of the number of O stars for two scale heights, including a smaller one for which the recombination time is longer than the dynamical time.

Next we convolve $\langle f_{esc}\rangle_\theta(t, N_O)$ with the luminosity function of OB associations, as given by McKee & Williams (1997) [133],

$$\frac{dn}{dN_O}dN_O \propto \frac{1}{N_O^2}dN_O\,, \tag{4.14}$$

where the LHS denotes the number of OB associations with the initial number of O stars in the range N_O and $N_O + dN_O$. The N_O-averaged escape fraction as a function of time is defined as

$$\langle f_{esc}\rangle_{\theta,N_O}(t) = \frac{\int_{N_{O_1}}^{N_{O_2}} \langle f_{esc}\rangle_\theta(t, N_O) S(t) \frac{dn}{dN_O} dN_O}{\int_{N_{O_1}}^{N_{O_2}} S(t) \frac{dn}{dN_O} dN_O}. \tag{4.15}$$

For Salpeter IMF, the number of O stars $N_O = 0.3 N_{\rm OB}$, the total number of OB stars. We use a lower limit $N_{O_1} = 100$, corresponding to the smallest star clusters observed by Zinnecker et al. (1993) [235], and an upper limit of 10^5, for the largest clusters (Ho (1997) [85], Martin (2005) [127], Walcher et al. (2005) [220]).

The angle and time dependence of the escape fraction from all the OB associations, averaging over only the luminosity function, is another important quantity. We define the luminosity-function-averaged escape fraction as:

$$\langle f_{esc} \rangle_{N_O}(\theta, t) = \frac{\int_{N_{O_1}}^{N_{O_2}} f_{esc}(\theta, t, N_O) S(t) \frac{dn}{dN_O} dN_O}{\int_{N_{O_1}}^{N_{O_2}} S(t) \frac{dn}{dN_O} dN_O} \,. \tag{4.16}$$

We use this definition in Figure 4.5.

Finally, the average escape fraction takes the form,

$$\langle f_{esc} \rangle_{\theta,t,N_O} = \frac{\int_{N_{O_1}}^{N_{O_2}} \langle f_{esc} \rangle_{\theta,t}(N_O) \frac{dn}{dN_O} dN_O}{\int_{N_{O_1}}^{N_{O_2}} \frac{dn}{dN_O} dN_O}, \tag{4.17}$$

which is equivalent to $\int \langle f_{esc} \rangle_{\theta,N_O}(t) dt / t_O$.

4.4 Results

In this section we present our results, beginning with the angle and time dependence of the escape fraction. Then show the the escaping LyC luminosity as a function of time. Later we show the most interesting result of our study, namely, that the escape fraction increases slightly with a decreasing halo mass and a decreasing redshift. Finally we discuss the effects of clumpiness as applied to high redshift galaxies.

4.4.1 Angular dependence

We first turn our attention to the angular dependence of the escape fraction for particular values of the mid-plane density (n_0), scale height (z_0) and N_O. In Figure 4.4 we plot the escape fraction $f_{esc}(\theta)$ (eqn 4.7) as a function of θ at different epochs for $n_0 = 0.5$ cm^{-3}, $z_0 = 300$ pc, $N_O = 10^4$. The blue dotted line, black solid line, and green dashed line represent the angle dependence of the escape fraction at 0.5, 4.0, 9.5 Myr respectively (times corresponding to the snapshots in Fig. 4.1). The escape fraction at all epochs slowly decreases with θ at small angles from the poles and then

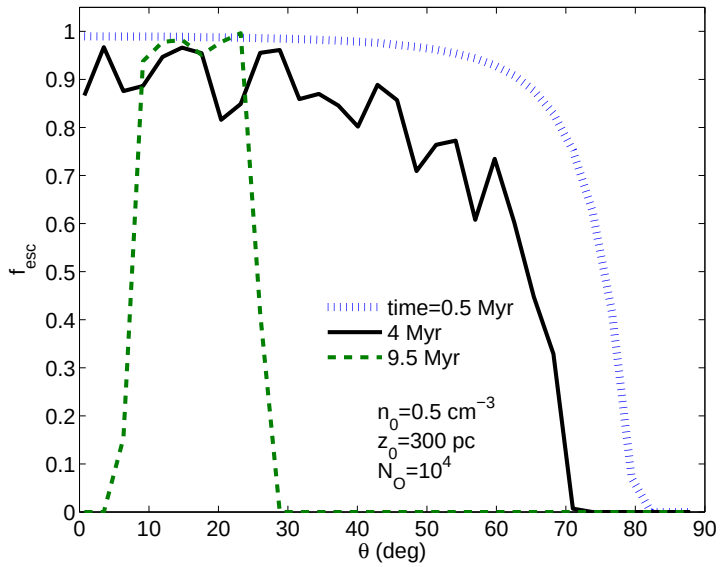

Figure 4.4: Escape fraction as a function of angle (θ) at different times (0.5, 4.0, 9.5 Myr) for $n_0 = 0.5$ cm^{-3}, $z_0 = 300$ pc, and $N_O = 10^4$. The corresponding dynamical time $t_d \sim 1$ Myr. The blue dotted line represents the escape fraction at 0.5 Myr (at $t \ll t_d$, when the superbubble is deeply buried in the disk), the black solid line at 4 Myr ($t \approx 4t_d$, when the superbubble shell begins to fragment, making the line zigzag), and the green dashed line at 9.5 Myr, when the shell opens up completely at small angles.

drops sharply at a cut-off angle. The reason for the decrease is that at larger angles (away from the poles) the line of sight encounters more of the disk/accumulated gas, and there is more recombination, making it difficult for the ionizing photons to escape. At time scales $t \ll t_d$, the superbubble is mostly spherical and buried deep in the disk, and the escape fraction decreases smoothly with angle, since all lines of sight encounter approximately the same path length through the disk, until $\theta \geq 1$ radian. At these epochs, S is large, and therefore the maximum value of the escape fraction (at small θ) is also large.

At $t \sim 2$–$3t_d$, after the superbubble breaks out from the disk, the shell begins to fragment due to radiative cooling and Rayleigh-Taylor instability (RTI; Roy et al. (2013) [164]). These clumps give rise to the zigzag nature of the angular dependence of the escape fraction. At small θ, the absorption of ionizing photons mostly occurs in the shell. At angles larger than ~ 1 rad, the escape fraction decreases rapidly, when the path of the photon begins to encounter the swept-up disk material. At later times the ionizing luminosity decreases ($S[t]$; see Fig. 4.2), and therefore the maximum value of the escape fraction (at small θ) also decreases. At a much later epoch, $t \gg t_d$, the shell opens up completely at small angles, giving a boost to the maximum value of escape fraction. However, the further decline of the ionizing luminosity also ensures a rapid decrease in the escape fraction with angle. We also notice a large drop in the escape fraction at small angles (near the θ-boundary in our numerical simulation) at 9.5 Myr. This is due to artificial accumulation of cold/dense gas near the poles, which is a feature of spherical geometry used for the simulation. Since the solid angle covered by these small angles is negligible, our results are not affected by this spurious behavior at the poles.

The opening angle of the cone can be estimated from the Kompaneets approximation of an adiabatic superbubble Kompaneets (1960) [107]. Consider cylindrical geometry with (R, z) coordinates, and consider the epoch when the superbubble has reached a height of $2z_0$ in the z-direction. The shell intersects the plane $z = z_0$ at

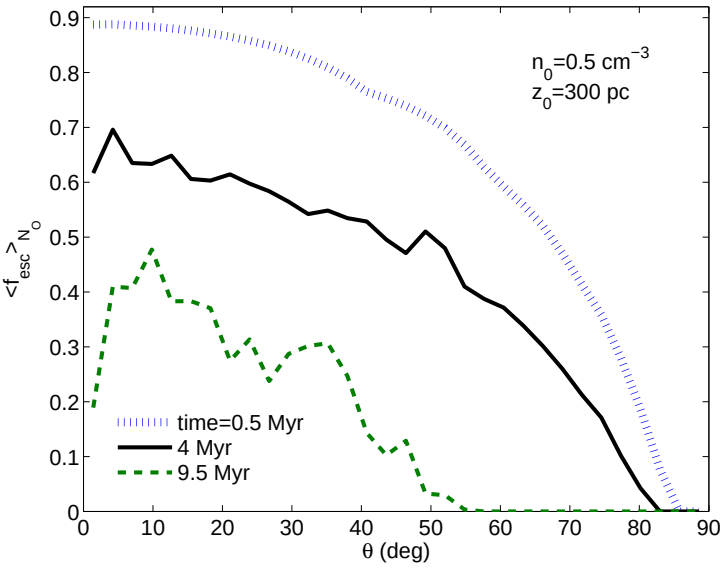

Figure 4.5: Luminosity-function-averaged escape fraction as a function of θ at different times (0.5, 4.0, 9.5 Myr) for our fiducial disk ($n_0 = 0.5$ cm^{-3}, $z_0 = 300$ pc). The blue dotted, black solid and green dashed lines represent the cases at 0.5 Myr, 4 Myr, 9.5 Myr respectively.

some distance from the axis $r = 0$. The perpendicular distance of the point of intersection of the shell with the plane $z = z_0$ is (see Eqs. 7 and 8 in Roy et al. (2013) [164]),

$$r = 2z_0 \cos^{-1}\left[\frac{\sqrt{e}}{2}[1 - (1 - 1/e)^2 + 1/e]\right]. \tag{4.18}$$

The angle that this point of intersection makes with the pole is

$$\theta = \tan^{-1}\frac{r}{z_0} = \tan^{-1}\left[2\cos^{-1}\left(\frac{\sqrt{e}}{2}\left(\frac{3}{e} - \frac{1}{e^2}\right)\right)\right] \sim 52^\circ, \tag{4.19}$$

or roughly 1 rad, as expected from simple arguments mentioned above.

Next, we calculate the angular dependence of the escape fraction after convolving with the luminosity function of OB associations (using eqn 4.16), for the same mid-plane density and scale height. Figure 4.5 shows the angular dependence at three different epochs (0.5, 4.0, 9.5 Myr, shown with blue dotted, black solid, green dashed lines). The convolution with luminosity function ensures a greater contribution from

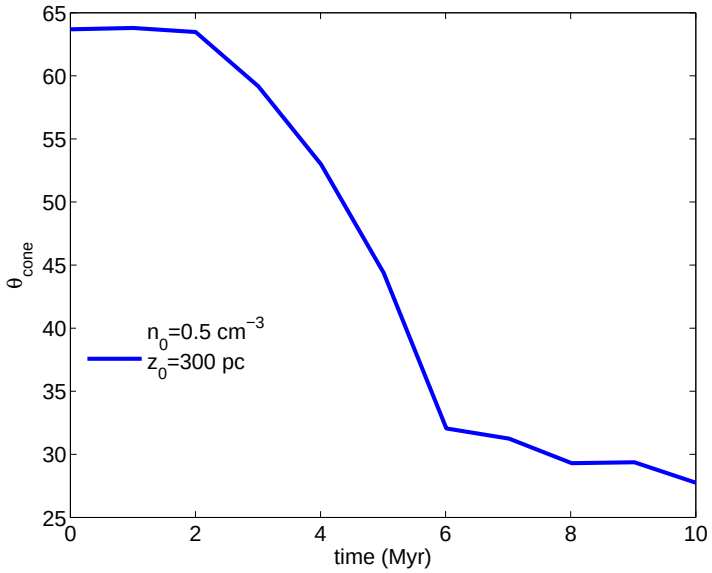

Figure 4.6: The time evolution of the ionization cone opening angle ($\theta_{\rm cone}$; where escape fraction falls by $[1 - 1/e]$ of its peak value) for our fiducial disk ($n_0 = 0.5$ cm^{-3} and $z_0 = 300$ pc).

associations with lower N_O, which leads to a marked decrease in the peak value of f_{esc} with time, compared to that seen in Figure 4.4.

For the parameters used in Figure 4.5, the dynamical time $t_d \approx 2$ Myr for the dominant $N_O = 600$ (see Appendix A.2 for the estimate of dominant N_O). The blue dotted line shows the angular dependence at $t \ll t_d$, when the shell is approximately spherical and small. The solid black line shows the case when the superbubble has broken out of the disk and has started fragmenting due to RTI. The green dashed line shows the case at a much later epoch ($t \gg t_d$) with a rapid fall with angle, as explained above.

Defining the cone angle $\theta_{\rm cone}$ as the angle at which the value of f_{esc} drops to $(1 - e^{-1})$ of its peak value, we plot $\theta_{\rm cone}$ as a function of time in Figure 4.6. We find the cone angle to be $\sim$ 55–65° (of order 1 rad) at $t \leq t_d$, as expected from the above discussion in eqn 4.19. After superbubble breakout, $\theta_{\rm cone}$ declines rapidly, and reaches an asymptotic value $\sim 40°$. This is because of opening of the top part of the

shell due to instabilities. We note that the cone angle does not represent just the opening up of the superbubble shell as it evolves (as shown in Figure 4.1); it is also affected by the decreasing ionizing luminosity with time. This is how we reconcile a decreasing $\theta_{\rm cone}$ in Figure 4.6 with an increasingly wider superbubble seen in Figure 4.1 as time progresses.

We note that our result is consistent with the results of Fujita et al. (2003) [58], who found an opening angle of 30–40° of the superbubble at $\sim$ 6 Myr (after the shell fragments due to RTI) in their simulation of dwarf galaxies. Our result is also consistent with the recent observations of Zastrow et al. (2013) [231], who found an average cone angle of $\approx 40°$ in the case of six nearby dwarf starburst galaxies. In a survey of 6 Lyman Break Galaxies and 28 Lyman-α Emitters at $z \sim 3$, Nestor et al. (2011) [145] concluded that LyC photons escape over a fraction 0.1–0.2 of the total solid angle, which implies a cone angle of 30–40°.

The fact that the opening angle is never larger than about 1 radian for a disk galaxy (eqn 4.19) also leads to an important conclusion. If we only consider the geometric effects on the escape of ionizing photons, and assume that all ionizing photons inside the cone manage to escape, and those outside of it do not, then the maximum escape fraction from a disk galaxy is $\sim (1 - \cos[1 \text{ radian}]) = 0.5$. As we have discussed in the Introduction, this inevitable limit appears to be borne out by the observations of $f_{\rm esc}$.

4.4.2 Time dependence of average escape fraction

The time-dependence of the escape fraction is governed by the competition between dynamical evolution of the superbubble which opens up an ionization cone and the lifetime of O stars. If dynamical time is short, O stars are still around at the time of opening up of the superbubble and the escape fraction can be high.

Figure 4.7 shows the luminosity function and θ-averaged escape fraction as a function of time for $z_0 = 100$ pc and for two different mid-plane densities $n_0 =$

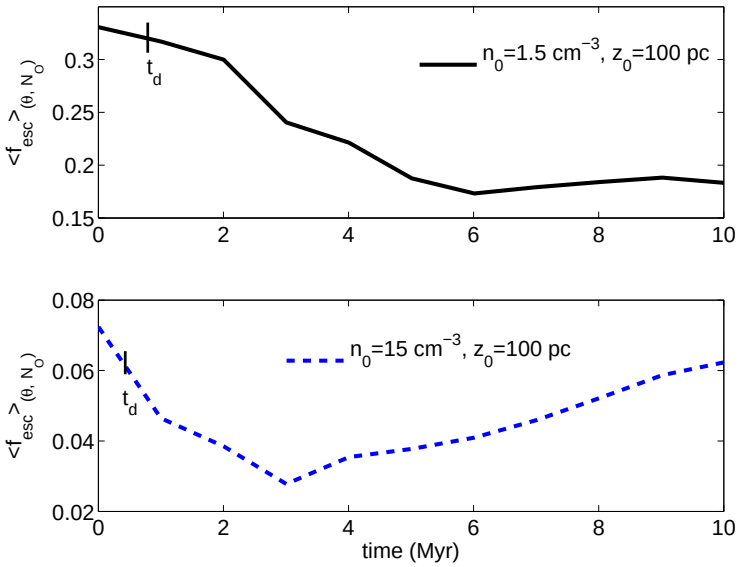

Figure 4.7: Luminosity-function-averaged θ-averaged escape fraction as a function of time for two different n_0 (1.5, 15 cm^{-3}) and a particular $z_0 = 100$ pc, to show the difference in their overall behaviour as a function time. The dynamical time (t_d) for the two cases is marked with a short vertical line.

$1.5, 15$ cm^{-3}. Initially the superbubble is small compared to the scale height, and the escape fraction depends on the magnitude of recombination in the dense shell of the superbubble (greater recombination reduces the escape fraction). As the superbubble grows in size, it sweeps up more and more of the ISM gas, the thickness of the shell increases, and the escape fraction decreases. After the superbubble breaks out of the disk, and the top of the shell opens up due to Rayleigh-Taylor instability (RTI), the escape fraction increases if the O stars are still around.

The time scale of the onset of the RTI depends on N_O, or equivalently, the mechanical luminosity driving the superbubble. For $n_0 = 1.5$ cm^{-3}, superbubbles with $N_O \approx 200$ dominate (see Appendix A.2 for a discussion of dominant N_O) the integration in eqn 4.17, for which $t_d \sim 1$ Myr (marked in the figure). The onset of RTI takes place at 4–5 times the dynamical time (Roy et al. (2013) [164]), and therefore the escape fraction keeps decreasing until (4–5) $\times\, t_d$. In the case of a denser medium,

the integration in eqn 4.17 is dominated by larger superbubbles, in this case with $N_O \approx 3 \times 10^4$, for which $t_d \approx 0.4$ Myr. Since the dynamical time is shorter in this case, the escape fraction reaches a minimum value at an earlier time, as shown in the bottom panel of Figure 4.7.

Since the life times of the most massive O stars lie in the range 2–4 Myr, if the superbubble shell breaks much later than this, the escape fraction does not increase much at later epochs (top panel of Figure 4.7). Zastrow et al. (2013) [231] found that the optimal time scale for the escape of LyC photons is 3–5 Myr, before which the superbubbles have not broken out of the disk, and after which the LyC luminosity starts declining. This is consistent with our results.

It is also important to study the final emergent ionizing luminosity ($f_{\rm esc} \times S(t)$), since this is what is observed. Figure 4.8 shows the evolution of the ionizing luminosity for $N_O = 10^4$, for the fiducial disk parameters ($n_0 = 0.5$ cm^{-3}, $z_0 = 300$ pc), and for a higher density ($n_0 = 50$ cm^{-3}) and a smaller scale-height (30 pc) case. Disk galaxies produce most of their ionizing photons in the initial ≤ 3 Myr, after which the total ionizing output decreases rapidly. Although $f_{\rm esc}$ increases at later epochs (~ 10 Myr) due to opening up of the shell, the observed ionizing luminosity is typically small because the decrease in photon luminosity (Fig. 4.2) is much more than the increase in the escape fraction (Fig. 4.7). This is also borne out in the observations of SMC and LMC by Pellegrini et al. (2012) [154] who found escape fractions from individual cluster regions to be ~ 0.4, but which had low ionizing luminosities. A comparison of the emerging photon flux for the fiducial and the higher density cases shows that the emerging flux can be larger at later times for the higher density disk, even though the time-averaged escape fraction is lower (see Fig. 4.9). This can be understood in terms of the propagation of the ionization front and the opening up of the low density cone due to supernovae. The escape fraction is initially smaller for the high density case as $n_0^2 z_0^3/S$ is larger, but the superbubble breaks out faster (see eqn 4.10) for this case because of a smaller scale height.

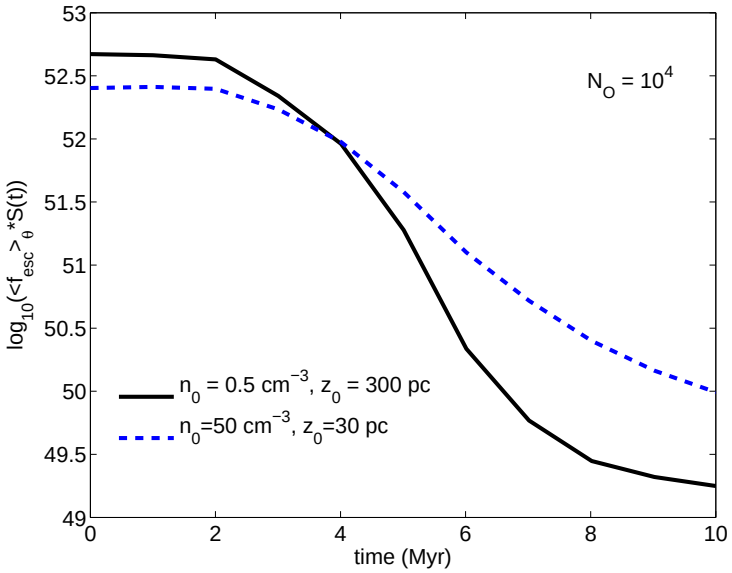

Figure 4.8: Time variation of the escaping ionizing photon luminosity from a star-cluster for two cases: $n_0 = 0.5$ cm^{-3}, $z_0 = 300$ pc, $N_O = 10^4$; and $n_0 = 50$ cm^{-3}, $z_0 = 30$ pc, $N_O = 10^4$.

4.4.3 Average escape fraction

The most important quantity for reionization and UV background is the average escape fraction, averaged over all angles, times and the OB-association number distribution. The angular and time dependence of the escape fraction is more relevant to understand the escape of UV photons in a particular system.

Figure 4.9 shows the average escape fraction as a function of z_0 for different n_0. The curves show that with an increase in gas density, the decrease of the escape fraction with scale height becomes sharper. For disks with small density and scale height, the average escape fraction can be as larger as ~ 0.5, while for $n_0 = 0.5$ cm^{-3} and $z_0 = 300$–500 pc, similar to the Milky Way disk, the escape fraction is ~ 0.05. However, the cases with small densities and small scale heights need to be considered with caution, as explained below.

Figure 4.10 is a contour plot of the average escape fraction as a function of logarithmic n_0 and z_0. The colour bar represents the value of the escape fraction. As is

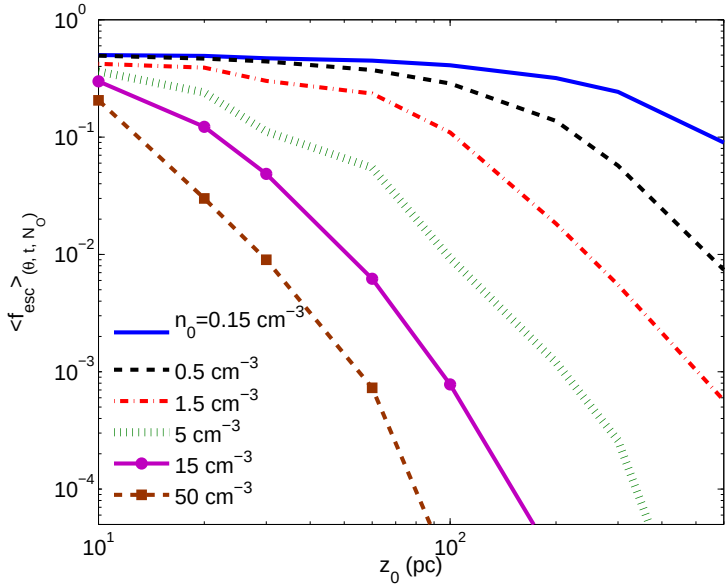

Figure 4.9: Time-averaged, luminosity-function-averaged and θ-averaged escape fraction as a function of z_0 for different n_0. Notice the sharp fall in the escape fraction with an increase in z_0.

evident in Figure 4.9, the regions in the parameter space of n_0–z_0 with small density and small scale height show larger values of the escape fraction than at high density and large scale height.

A note on the dominant N_O that contributes the most to the value of the escape fraction is in order here. For small n_0 and z_0, near the bottom-left corner of Figure 4.10, the dominant value of N_O is $\approx$ 100, and superbubbles with larger N_O start dominating as one goes towards the top-right corner (large n_0 and z_0). For $n_0 = 5$ cm^{-3} and $z_0 = 100$ pc, the dominant $N_O = 4000$ (see Appendix A.2 for a discussion of the dominant N_O as a function of the disk parameters n_0 and z_0). The dominant N_O corresponds to the value for which the integrand in the numerator of eqn 4.17 peaks.

Recall the discussion on the validity of the assumption of ionization balance in §3.1. Our formalism is not valid if $t_{\rm reco} > t_{\rm d}$, and this inequality depends on N_O for a given combination of disk density and scale height. We have found that this problem

arises for small values of N_O, especially at the bottom-left corner of Figure 4.10 for small n_0 and z_0. In this region, the dominant $N_O = 100$ and $t_{\rm reco} > t_{\rm d}$. We show with a black dashed-dotted line the locus of points with $t_{\rm reco} = t_{\rm d}$ for $N_O = 100$. The results for escape fraction for the region on the left of this line are not strictly valid. On the right hand side of this line, the dominant N_O is such that $t_{\rm reco} < t_{\rm d}$, and our results are valid. We note that photoionization/recombination equilibrium holds for most n_0 and z_0 considered here. Also, equilibrium disks with these combinations of density and scale height correspond to very low ISM temperatures (in the range of 150–4000 K, see eqn 4.2), and should not be considered realistic.

The grey dashed thick, thinner and thinnest lines in Figure 4.10 represent constant column densities of 10^{22}, 10^{21} and 5×10^{20} cm^{-2}, respectively, for a vertical line-of-sight. The column density is given by,

$$N_H \;\; = \;\; n_0 \int_{-\infty}^{\infty} \mathrm{sech}^2\big(\frac{z}{\sqrt{2}z_0}\big) dz = 2\sqrt{2} n_0 z_0. \tag{4.20}$$

We note that at redshift $z \sim 0$, disks with $N_{\rm HI} \sim 10^{21}$ cm^{-2} dominate the mass density of HI (Zwaan et al. (2005) [238]), and possibly also at high redshifts. Prochaska et al. (2005) [157] however suggests that disks with $N_{\rm HI} \sim 10^{20.3}$ and $10^{21.3}$ contribute more or less similarly in the overall mass-density of HI. It has been pointed out by several authors (Cen (2012) [22], Hirashita & Ferrara (2005) [84], Schaye (2001) [171], Zwaan & Prochaska (2006) [237]) that at $z \sim 0$ the systems above $N_{\rm HI} \sim 10^{22}$ are very difficult to find due to HI-H2 coversion. In general, the escape fraction is lower for low column density systems, as expected.

The magenta solid thick and thin lines in Figure 4.10 correspond to the ISM temperatures of 10^4 K and 8000 K respectively. Wolfire et al. (2003) [227] considered the thermal and ionization balance in the Milky Way ISM, and inferred a range in the disk temperature in which two phases can coexist to be $T \sim$ 7000–8500 K. We show the lines for disks with ISM temperatures of 8000 K and 10^4 K according to eqn 4.4 The escape fraction from disks at higher temperature ($T \sim 10^4$ K) is lower

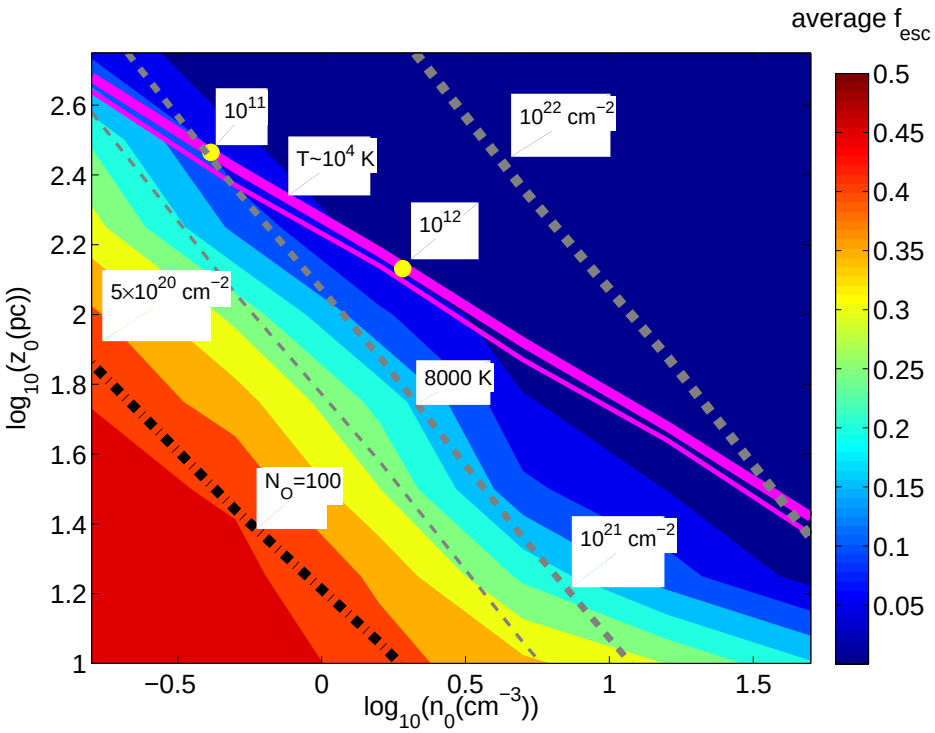

Figure 4.10: Contour plot of time-averaged luminosity-function-averaged and θ-averaged escape fraction as a function of n_0 and z_0. The regions below the black dashed-dotted line is for $t_d < t_{\rm reco}$ for $N_O = 100$. The magenta solid thick and thin lines represent the n_0, z_0 values for two different ISM temperatures 10^4K, 8000 K respectively of the warm neutral medium (WNM). The yellow circular scatterers represent the n_0–z_0 values corresponding to the density and scale height calculated from Wood & Loeb (2000) for the halo masses of $M_h \sim 10^{12} M_\odot$ (the lower circle) and $M_h \sim 10^{11} M_\odot$ (the upper circle) respectively at present redshift ($z = 0$). The grey dashed thick, thinner and thinnest lines represent constant HI-column density of $N_{\rm HI} \sim 10^{22}$ cm^{-2}, 10^{21} cm^{-2} and 5×10^{20} respectively.

than that at lower temperature (8000 K). As we see from eqn 4.4, higher temperature corresponds to a larger scale height (for a given density) due to the puffing up of the disk. In that case, it becomes difficult for ionizing photons to escape the disk, and thus explains the behaviour of $f_{\rm esc}$ with the disk temperature.

It is important to note that this density-height relation is roughly independent of the disk (galaxy) mass and redshift. The WNM disk column increases with the galaxy mass and redshift, but the relation between the mid-plane density and the scale height satisfies eqn 4.4, as long as the disk temperature remains the same and the disk is in hydrostatic equilibrium.

Finally we come to the main result of this chapter. *The contours of equal values of escape fraction roughly obey the relation* $n_0^2 \propto z_0^{-3}$. In other words, disks in which the mid-plane density and scale height are related such that $n_0^2 z_0^3$ is constant, would have similar escape fractions. Note that in the case of a constant ionizing luminosity, the Strömgren sphere has a radius $R_s \propto n_0^{-2/3}$. This means that, the disks in which the Strömgren radius for a constant ionizing luminosity is a fixed ratio of the scale height, would have similar values of escape fraction. In hindsight, one could argue that this is expected from a simple theoretical argument, because the escape fraction must depend on the amount of ionizing photons absorbed by the disk gas, and so the ratio of the Strömgren radius to the scale height must be a relevant parameter. But without the aid of detailed calculation such as presented here, one could not have drawn such a conclusion with confidence, since there are a large number of competing factors (such as opening up of low density channels) at play.

Note that lines of isothermal disks ($n_0 \propto z_0^{-2}$; eqn 4.4) and those of constant column density ($n_0 \propto z_0^{-1}$; eqn 4.20) straddle the iso-$f_{\rm esc}$ contours from two sides in Figure 4.10. In other words, $f_{\rm esc}$ of disks with constant WNM temperatures or disks with a given column densities would differ slightly. Consider disks with similar WNM temperatures that lie on the solid thick line in Figure 4.10. Disks of galaxies with different masses would be separated on this line, given by eqn 4.23 (explained later

in §4.5). We show two such points corresponding to halo masses 10^{11} and 10^{12} $M_\odot$ at the present epoch. The escape fraction for the disk of the less massive galaxy is slightly larger than that of the more massive one (by a factor ~ 1.4).

Roughly one can fit the values of the escape fraction to the mid-plane disk density and the scale height as,

$$f_{\rm esc} \sim 0.1 \Big(\frac{n_0}{1\,{\rm cm}^{-3}}\Big)^{-2/2.2} \Big(\frac{z_0}{135\,{\rm pc}}\Big)^{-3/2.2}. \tag{4.21}$$

This fit is reasonably good for values of n_0 and z_0 for which $0.133 \leq \Big(\frac{n_0}{1\,{\rm cm}^{-3}}\Big)^2 \Big(\frac{z_0}{135\,{\rm pc}}\Big)^3 \leq 7.5$ and $n_0 \leq 15$ cm^{-3}. Since gas density and scale height depend on the WNM temperature (eqn 4.4) and the galactic mass (eqn 4.23), we can use this fit to determine the dependence of $f_{\rm esc}$ on galactic mass and the WNM temperature. Equation 4.23 states that $n_0 \propto M^2/(c_s^2 R_d^4)$. Since R_d, the scale length, scales as the virial radius, which scales as $M^{1/3}$, we have $n_0 \propto M^{2/3} c_s^{-2}$. Combining with the above fit and the relation $n_0 z_0^2 \propto c_s^2$, we finally have

$$f_{\rm esc} \propto M^{-0.15} c_s^{-0.9}\,. \tag{4.22}$$

Therefore, decreasing the mass of a galaxy by a factor of 10 increases the escape fraction by a factor ~ 1.4 (as also seen from the two marked points in Figure 4.10).

Present day disks occupy the upper-left corner of the parameter space in Figure 4.10, shown by the marked points for two halos. Disk galaxies therefore have an escape fraction of $f_{\rm esc} \sim 0.05$–0.15, with a weak variation with galactic mass.

This result admittedly pertains to discs that are not clumpy and we have not evolved the discs in a cosmological setting. However, our result does reveal an interesting connection between disc parameters and the escape fraction. This interesting result could be obtained only after scanning a large parameter space of n_0–z_0 that we have done here for the first time. In order to scan the parameter space, we used 48 different combinations of disc density and height, and each combination had 13 runs with different N_O for the averaging over OB associations. Our aim was to explore

the effect of disc parameters in a simple case before introducing other effects such as clumpiness or cosmological and galactic evolutionary effects.

Another word of caution is in order here. Although we have drawn the points in Figure 4.10 for two halo masses, guided by the eqn 4.23, they may not represent real disk galaxies with those halo masses. For one reason, the column densities in the prescription of Mo, Mao & White (1998) [137] are an overestimate. For example, the disk of our Milky Way (corresponding to a halo mass of $\sim 10^{12}$ M$\odot$) has a WNM column density of $\sim 2 \times (1.6 \times 10^{20})$ cm^{-2} at high latitudes (implying a face-on geometry; Table 1 in Kanekar et al. (2011) [98]), almost an order of magnitude smaller than that predicted by Wood & Loeb (2000) [229] and two orders of magnitude smaller than in the prescription of Mo, Mao & White (1998) [137]. Therefore, the marked points in the figure should be used with caution, and we use them here to demonstrate that low mass disks would in general occupy the upper-left corner of the $n_0 - z_0$ space.

4.4.4 Effect of clumping in the shell

Clumpiness in the ISM can strongly affect the escape routes of ionizing photons in more than one way. Ionising photons escape easily through the low density channels in the ISM. On the other hand, recombination rate is high in denser regions but the escape fraction also depends on the photon luminosity. Therefore it is not entirely clear how clumpiness should affect the angle-averaged, time-averaged and OB association luminosity-function-averaged escape fraction. Although there may not be a one-to-one correspondence between clumpiness (for a given definition) and the escape fraction, it is expected that $f_{\rm esc}$ increases with an increasing clumpiness (a higher clumpiness corresponds to the availability of low density escape paths for photons). Wood & Loeb (2000) [229] considered distributed sources in a disc and found that increasing the volume filling factor of clumps decreased the escape fraction. They found that the escape fraction is larger than 1% only if the filling factor is ≤ 0.2, or

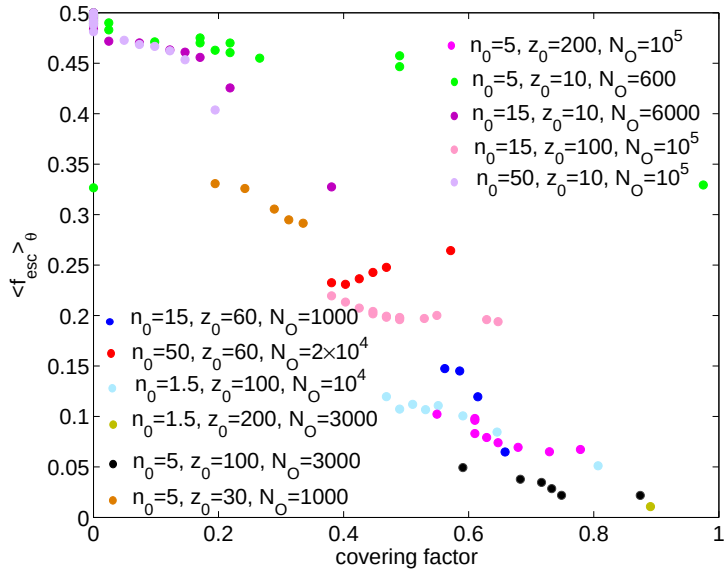

Figure 4.11: Escape fraction for a few cases (different n_0, z_0, N_O) are shown against the corresponding covering fraction (see text for details). All the densities are in cm^{-3} and all the scale heights are in pc. Different points in the plot correspond to the values of θ-averaged f_{esc} and covering factor at different epochs of the superbubble evolution.

if the interclump (empty) regions filled up more than 80% of the ISM volume.

Thermal and Rayleigh-Taylor instabilities give rise to clumps and channels in superbubble shell. These channels help the ionizing photons to escape and can increase the value of the escape fraction. Although we have not taken into account the clumpy nature of the ISM, the clumps in the superbubble shell mimic the clumpiness in the ISM. In this section we discuss how a clumpy ISM can affect the escape fraction, by studying the effect of the clumps in the shell on the escape fraction. We show that an increased clumpiness in the medium (in the shell, and therefore, by extrapolation, in the ISM) decreases the escape fraction.

Instead of the volume filling factors of clumps, which is difficult to infer in projected images of galaxies, we study the effect of surface covering factor on the escape fraction in our simulations. We define the covering factor as the fraction of the total surface area around the central source along which the line-of-sight column density

is ≥ 10 % of the initial value. We calculate the covering factor from the epoch when the escape fraction increases after reaching a minimum, when the shells are clumpy enough so that one can distinguish between clumps and channels in the shell. The column density along polar regions deceases as the superbubble evolves with time, since most of the volume is filled with the low density gas. We have also checked the density contours at different snapshots visually, and found that our definition of the covering factor matches well the surface covering fraction estimated by considering dense clumps along different lines of sight.

We show a plot of the escape fraction in a few cases (gas density, scale height and N_O) as a function of the covering fraction in Figure 4.11. One can notice that there is a rough trend that as the covering factor decreases, the value of the escape fraction increases. It is clear that the escape of ionizing photons is facilitated by the opening up of pathways, which corresponds to a small covering fraction. For the escape fraction to be larger than 10%, the covering fraction needs to be less than $\sim 70\%$.

While we have used a particular definition of the covering factor (or clumpiness), in general we expect the escape fraction to rise with a decreasing covering factor. An exception is when the UV sources are embedded inside the high density massive clumps (which is not the case, at least in our simulations).

4.4.5 Variation with redshift

One can use the prescription of Mo, Mao & White (1998) [137] to estimate the disk gas density for different galaxies at various redshifts (see also Wood & Loeb (2000) [229]). Assume that the disk mass M_d is a fraction m_d of the halo mass. Then, assuming a stratified disk with a (vertical) density profile given by eqn 4.2, we have (eqn 8 of Wood & Loeb (2000) [229])

$$n_0 = \frac{GM_d^2}{128\pi\mu m_p c_s^2 R^4}\,, \tag{4.23}$$

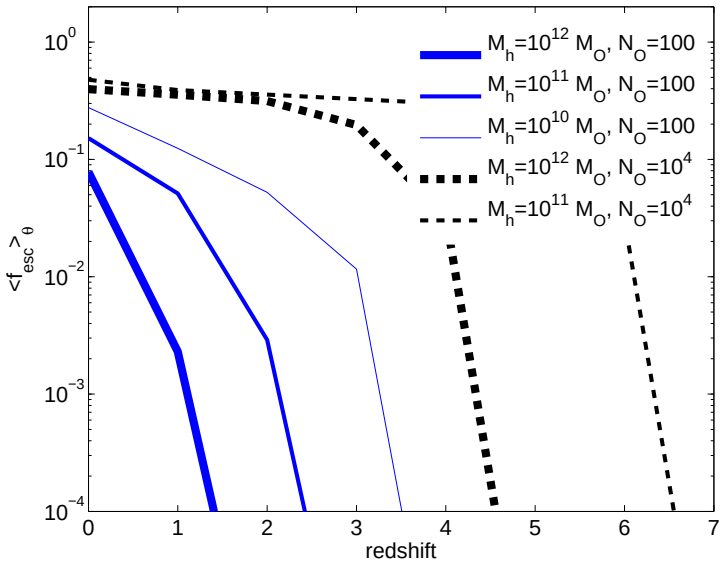

Figure 4.12: Escape fraction for the initial disk (without superbubbles) as a function of redshift, for a few halo masses and $N_O = 100, 10^4$. The purpose of this figure is to compare with the results of Wood & Loeb (2000) [229].

where R is the scale radius of the mid-plane disk density (this is half of the scale radius corresponding to the surface density, which is used in Mo, Mao & White (1998) [137]; this factor of two can make a factor of 16 difference in n_0 if one is not careful). The redshift factor enters into this relation through the scale radius R, which is related to the virial radius r_{vir}, which depends on the redshift (see eqn 5 of Wood & Loeb (2000) [229]). One therefore obtains n_0 (and therefore z_0) for the disk of given halo mass at a certain redshift. At high redshifts, disks with the same WNM temperature would slide down the solid lines in Figure 4.10 towards higher density and smaller scale height. Therefore in principle, one predicts smaller $f_{\rm esc}$ for disks with a given mass and temperature at higher redshifts. However, this weak trend is likely to be mitigated by the stronger effect of clumpiness on the scape fraction, as described below.

We note that instead of the mid-plane density and scale height, another set of

parameters that can describe a disk are the disk mass and its spin. The mid-plane density (n_0) is connected to the disk mass (M_d) and scale radius (R) via equation 4.23. In the scenario of dark matter haloes gaining angular momentum through tidal torque, it is conventional to use a dimensionless spin parameter λ as,

$$\lambda = J_h |E_h|^{1/2} G^{-1} M_h^{-5/2}\,, \tag{4.24}$$

where the angular momentum of the halo is J_h and its total energy it E_h, with a total mass M_h. The fraction of the halo angular momentum transferred to the disk is parameterised by $j_d = J_d/J_h$, where J_d is the disk angular momentum. Thus the scale radius (R) is connected to the spin parameter via the following equation (Mo, Mao & White (1998) [137]),

$$R = \Big(\frac{j_d}{\sqrt{2} m_d}\Big) \lambda r_{vir} \tag{4.25}$$

The scale height is also connected to the mid-plane density via equation 4.2. Therefore, n_0 and z_0 are related to the disk mass and the spin parameter.

We recall that Wood & Loeb (2000) [229] considered discs with distributed sources, without any dynamical movement of the gas in the disc. For such discs, the escape fraction depends only on radiation transfer aspects (and not on opening up of the superbubble), and depend on the redshift because of the n^2 dependence of the recombination rate. High redshift discs with large gas density would have small escape fraction. Wood & Loeb (2000) [229] showed that the escape fraction drops sharply with an increasing redshift because of this. In Figure 4.12 we show the variation of $f_{\rm esc}$ with the halo mass and redshift for $N_O = 100$ and 10^4, but without considering the dynamical effects of superbubbles. The case with large N_O has large values of $f_{\rm esc}$ and falls less sharply with redshift because of a higher ionizing luminosity (see eqn 4.7). However, when the luminosity function of OB association is taken into account, the low N_O associations dominate, and therefore the discs in our calculation also show rapid decline of $f_{\rm esc}$ with z as in Wood & Loeb (2000) [229].

We do not expect the Wood & Loeb (2000) [229] prescription for the structure of smooth disks to apply at high redshifts because it predicts extremely large densities

and tiny scale heights for even moderate redshifts. For example, for $M_h = 10^{12} M_\odot$ at $z = 3$, the density $n_0 \sim 200$ cm^{-3} and a scale height $z_0 \sim 13$ pc. These disks are likely to cool quickly ($t_{\rm cool} \sim 3.3 \times 10^{-6}$ Myr), form stars and puff up from feedback effects. These disks will therefore not be able to sustain their high density and small scale heights for long time. Moreover, frequent mergers at high redshifts make it difficult for smooth equilibrium discs to survive.

Observationally, one does not find disc-like structures at redshifts beyond ~ 2, and high redshift disc galaxies are likely to be clumpy (Conselice (2014) [29]). Drawing from our discussion on clumping in the previous section, it is then likely that $f_{\rm esc}$ increases with redshift due to increasing clumpiness in discs. Such an increase is consistent with the requirements of reionization (Mitra et al. (2013) [136]).

Figure 4.13 shows a schematic representation of a clumpy ISM expected in a high redshift galaxy. We expect the escape fraction to be higher for such a case for several reasons: clumps are more spherical (the difference between z_0 and the scale radius is not as large as in disks) and photon escape both due to radiative effects and due to gas dispersal via supernovae can lead to photon escape in all directions (unlike in disks in which photons moving along the disk plane are always absorbed); the clumps are themselves more perforated because of higher star-formation and merger rates at higher redshifts; if most of the clumps are molecular (as is likely in at least in star-forming galaxies at high redshifts; Tacconi et al. (2010) [198]) then the escape fraction is higher (as the temperature is much lower and since $n_0^2 z_0^3 \propto T$; see eqn 4.7). A self-consistent numerical calculation is required to calculate the escape fraction in disturbed galaxies at high redshifts because of several complexities, but the escape fraction is likely to be larger than in static equilibrium disks.

Based on the discussion above, it is then likely that disks at high redshifts did not have extremely large density (or very small scale heights) as expected from simple extrapolations of scaling relations. If disks at high redshifts had gas density in the range $n_0 \leq 10$ cm^{-3} and scale height ≥ 100 pc, then our results imply that those

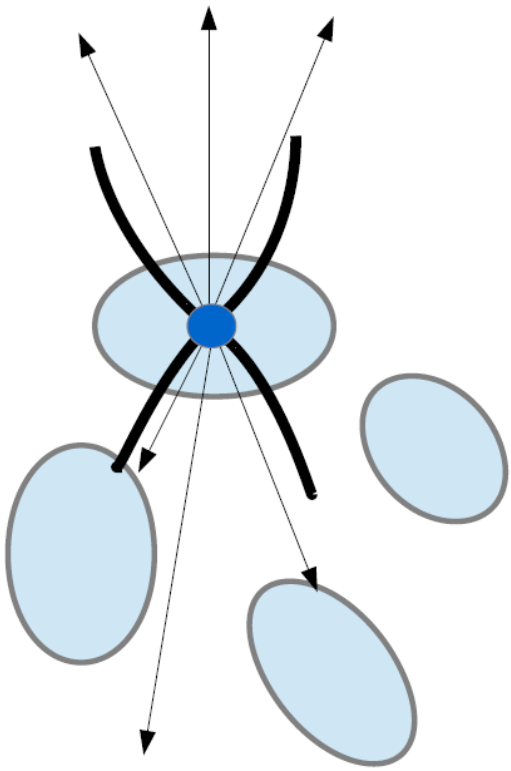

Figure 4.13: Schematic diagram of a clumpy ISM at high redshift. The ellipses represent ISM clumps in which star formation occurs; one of them has a starburst at its center which opens up a superbubble. The thin rays with arrows show LyC photon trajectories through the ISM.

disks also had an escape fraction $f_{\rm esc} \sim 10(\pm 5)\%$, similar to present day disks. The presence of clumpiness at high redshift would introduce an additional uncertainty, and is likely to increase the value of the escape fraction.

4.5 Discussion

Our main result is that the escape fraction of ionizing photons depends on the combination of disk gas density and scale height, in particular, on the combination of $n_0^2 z_0^3$. The relation between gas density and scale height in turn depends on the disk gas (WNM) temperature. The dependence of the escape fraction on other galactic parameters (such as mass and redshift) will be determined by how the WNM temper-

ature and the disk structure depend on these parameters. The WNM temperature in our Milky Way is known to be $\sim$ 8000 K (Wolfire et al. (2003) [227]). It is believed that the WNM temperature increases with decreasing metallicity, because of lack of cooling routes in a low metallicity gas. It is therefore generally thought that the WNM temperature is higher at high redshift, because of metallicity evolution in galaxies. Recent observations of damped Lyman-α systems at $z \sim 3$ support this idea and have found a WNM temperature of $\sim 10^4$ K (Cooke et al. (2015) [31]). The fact that the spin temperature for 21 cm radiation tends to increase with redshift also supports this (Kanekar et al. (2014) [99]). Therefore disk galaxies at $z \sim 3$ will have similar escape fractions as in the Milky Way, since the escape fraction does not change substantially for WNM temperature in the range of 8000–10^4 K, as seen in Figure 4.10. At higher redshifts, however, the disk column density is higher and the escape fraction is expected to be smaller (see section 4.5 for details).

Our result of an increasing escape fraction with a decreasing galactic mass can be compared with previous results. Razoumov & Sommer-Larsen (2010) [159], Yajima et al. (2011) [230] have found a decreasing trend of escape fraction with an increasing galactic mass, although Gnedin et al. (2008) [67] found an opposite trend. However, these results stem from the dependence of clumpiness on disk mass (disks in Yajima et al. (2011) [230]'s simulation became more clumpy with increasing mass), or the dependence of disk thickness with galactic mass (in the case of Gnedin et al. (2008) [67]). In contrast, our results pertain to smooth disks, and relate the escape fraction in terms of fundamental disk parameters instead of explicitly coupling it to the galactic mass. We have separately discussed the effect of clumpiness on the escape fraction, which can be used in conjunction with our basic result.

Figure 4.10 shows that present day disks likely occupy a region of the parameter space of density and scale height such that $f_{\rm esc} \sim 10(\pm 5)\%$ (upper left corner of the solid line for isothermal disks). This matches with the requirements for the presence of the Ultraviolet (UV) background radiation in the galaxies (Heckman et al. (2001)

[74], Hurwitz et al. (1997) [91], Leitherer et al. (1995) [116]), as well as with direct estimates of escape fraction of Milky Way and present day disc galaxies (Bland-Hawthorn & Maloney (1999) [10], Zastrow et al. (2013) [231]). However, one must bear in mind that, $f_{\rm esc}$ strongly depends on the orientation of the object in the plane of the sky, as previously shown (Dove et al. (2000) [45], Fujita et al. (2003) [58]) and as our calculations confirm. Therefore, the observational estimates may be lower than the angle-averaged values presented in this chapter.

If high redshift disks have disk gas density ≤ 10 cm^{-3} and scale heights ≥ 100 pc, then our results imply that those disks would also have $f_{\rm esc} \sim 10(\pm 5)\%$, modulo the effect of clumping. This is consistent with requirements from models that explain the epoch of reionization with stellar sources (Barkana & Loeb (2001) [6], Fujita et al. (2003) [58], Gnedin (2000) [66], Inoue et al. (2006) [93], Madau & Shull(1996) [124], Miralda-Escudé et al. (2000) [135], Mitra et al. (2013) [136], Paardekooper et al. (2013) [152], Razoumov & Sommer-Larsen (2010) [159], Robertson et al. (2013) [162], Sommerville et al. (2003) [184], Yajima et al. (2011) [230]). Recent numerical simulations by Kimm & Cen (2014) [105] have found an average value of $f_{esc} \sim 10$ % ($\sim 15\%$ including the effect of runaway OB stars) in galaxies with mass 10^8–$10^{10.5}$ M$_\odot$, and also found this average value to be constant over redshift. Our calculations put these results in the perspective of the underlying connection between disk parameters and the escape fraction.

4.6 Summary & Conclusions

We summarise our conclusions below:

- Ionizing photons escape from disc galaxies within a cone of angle $\sim 55°$, before the superbubble breaks out of the disc, and within $\sim 40°$ towards the end of the lifetime of OB stars.

- The ionization cone is unlikely to be larger than an opening angle of 1 radian for

disk galaxies. This puts an upper limit on the escape fraction for disk galaxies of 0.5 from geometric considerations.

- The escape fraction initially decreases, when the superbubble is buried within the disc. It reaches a minimum at the breakout epoch and slowly increases with the opening of the shell and the formation of clumps and pathways for ionizing photons.

- The time-averaged, angle-averaged and OB association luminosity-function-averaged escape fraction for non-clumpy discs depends mostly on the WNM temperature and the column density. For typical parameters, we estimate an escape fraction of disk galaxies to be $\sim 10(\pm 5)\%$.

- Escape fraction decreases with the increase of surface covering fraction, although there is no one-to-one correspondence, because the escape fraction depends on several factors (such as the gas density, scale height, OB association mass, and time). Therefore, the escape fraction for high redshift discs is likely to be higher due to the clumpy nature of ISM at those epochs.

- A non-negligible escape fraction, especially at high redshifts relevant for reionization, is possible only if superbubbles open up a low density ionization cone through which ionizing photons leak into the IGM. The clumpiness of the ISM and the distribution of massive stars (which produce most UV photons) play an important role in determining the escape fraction.

Chapter 5

Molecule formation in violent environment : starburst nuclei

Based on : "Molecular outflows in starburst nuclei"

Roy, A., Nath, B. B., Sharma, P., Shchekinov, Y., 2016, submitted to MNRAS, arXiv:1607.04328

Apart from the escape of ionizing photons (discussed in chapter 4), the evolution of superbubble shells in a dense ambient medium can also give rise to molecular ouflows in the central region of a star-burst galaxy. There are a few observations of nuclear molecular outflows in the local universe, and it is surprising that all of them have similar molecular masses, sizes, and expansion velocities. Striking similarities pose some obvious questions : (i) Do all of these molecular outflows have similar origins? (ii) Do all of them have similar molecule formation and destruction mechanisms? In this chapter, we address these questions and model the molecular outflows theoretically.

Primary results

- We find that molecules can form in expanding shells in the central region of star-burst galaxies with SFR$\geq$ 1 $M_\odot$ yr^{-1}, equivalently the number of O, B stars in the OB association corresponds to $N_{\rm OB} \geq 10^5$ in the nuclear region with the mid-plane density $n_0 \sim$ 200–1000 cm^{-3} and scale-height $z_0 \geq 200(n_0/100{\rm cm}^{-3})^{-3/5}$ pc. This threshold condition of (n_0, z_0) implies that molecules form in environment where the threshold gas surface density is $\geq$ 2000 $M_\odot$ pc^{-2}.

- Molecule formation is favoured by the SFR surface density of $10 \leq \Sigma_{SFR} \leq 50$ $M_\odot$ yr^{-1} kpc^{-2}, matching well with observations.

- The estimated molecular mass of the outflow comes out to be $\sim 10^6$–10^7 $M_\odot$ at a distance of $\sim$ a few 100 pc from the centre of the discs with an expansion speed of $\sim$ 30–40 km s^{-1}, consistent with observations.

5.1 Introduction

Observations show that outflows from starburst galaxies contain gas in different phases, which manifest with different emission mechanisms and are probed in different wavelengths. The fully ionised component usually show up through free-free emission and is probed by X-ray observations (Strickland et al. (2004) [192], Heckman et. al. (1990) [79]). Partially ionized/atomic component are more clumpy than the fully ionised gas, and are probed by line emission from various ions, e.g. NaI, MgII etc Heckman et al. (2000) [75]. Outflows from some nearby starburst galaxies have also been observed to contain a molecular component. Understanding the dynamics of this molecular component has become an important issue, in light of recent observations with *ALMA* and further observations in the future.

Bolatto et al. (2013) [13] observed a molecular outflow in the central region of NGC 253 with a rate of ≥ 3 $M_\odot$ yr^{-1} (likely as large as 9 $M_\odot$ yr^{-1}), with a mass loading factor 1–3. Four expanding shells with radii 60–90 pc have velocities of $\simeq$ 23–42 km s^{-1}, suggesting a dynamical age of $\sim$ 1.4–4 Myr. The inferred molecular mass is $(0.3-1)\times 10^7$ $M_\odot$, and energy $\sim (2-20)\times 10^{52}$ erg. These shells likely outline a larger shell around the central starburst region.

Tsai et al. (2012) [210] observed a molecular outflow in NGC 3628 with the CO (J=1-0) line. The outflow shows almost a structureless morphology with a very weak bubble breaking through in the north part of the central outflow. Its size of $\sim$ 370–450 pc, inferred molecular mass of $\sim 2.8\times 10^7$ $M_\odot$, and outflow speed $\sim 90\pm 10$ km s^{-1}, suggest a total kinetic energy of molecular gas of $\sim 3\times 10^{54}$ erg.

More recently Salak et al. (2016) [167] observed dust lanes above the galactic plane in NGC 1808 along with NaI, NII, CO(1-0) emission lines tracing extraplanar gas close (within 2 kpc) to the galactic centre with a mass of 10^8 $M_\odot$, and a nuclear star formation rate of $\sim$ 1 $M_\odot$ yr^{-1}. The velocity along the minor axes varies in the range 48–128 km s^{-1} and most likely indicates a gas outflow off the disk with an estimated mass loss rate of (1–10) $M_\odot$ yr^{-1}.

The molecular outflow observed in M82 has a complex morphology. The part of it outlined by CO emission is at a larger radii than the part seen with HCN and HCO^+ lines. The CO (J=1-0) observations show diffuse molecular gas in a nearly spherical region of radius ~ 0.75 kpc, with a total molecular mass 3.3×10^8 $M_\odot$, with an average outflow velocity of ~ 100 km s^{-1} Walter et al. (2002) [222]. The corresponding kinetic energy of the CO-outflow is of $\sim 3\times10^{55}$ erg. More recently Salak et al. (2014) [166] re-estimated the mass and kinetic energy of CO gas to be larger by factors of 3 and 3-10 respectively. Notably, the molecular outflow morphology is similar to that of the dust halo described by Alton, Davies & Bianchi (1999) [4].

The morphology of the region of the outflow observed in HCN/HCO^+ is similar to that of the CO outflow – it is amorphous and nearly spherical with slightly smaller length scale: the radius of the HCN region is of 400–450 pc, and around 600 pc for HCO^+; both HCN and HCO^+ emissions show clumpy structure with characteristic size of 100 pc Salas et al. (2014) [168]. The kinematics and the energetics differ slightly from those inferred for the CO-outflow: the mean de-projected outflow velocity for HCO^+ is 64 km s^{-1}, while for HCN it is 43 km s^{-1}. The total molecular mass contained into the HCN (HCO^+) outflows is $\geq 7(21)\times10^6$ $M_\odot$, which in total is an order of magnitude lower for molecular outflows associated with CO Walter et al. (2002) [222]. The kinetic energy of the outflow associated with HCN/HCO^+ emission ranges between 5–30 $\times10^{52}$ erg. The molecular outflow rate is ≥ 0.3 $M_\odot$ yr^{-1}. They also inferred a SFR of $\sim$ 4–7 $M_\odot$ yr^{-1} from free-free emission.

These observations pose a number of questions that we address in this chapter: are the molecules formed *in situ* in the flow or are they entrained the flow, or are the residues of the parent molecular cloud (in which the superbubble has gone off)? What are the typical length scales, time scales, molecular mass and speed? How are these related to the SFR, or disk parameters (e.g., gas density, scale height)?

In this chapter we outline a model which includes the basic physical processes for producing a molecular outflow in starburst nuclei, and addresses some of these

issues. We have kept our model simple enough to be general, but it has the essential ingredients in order to explain some of the observed parameters mentioned above, namely the length scales and velocities, as well as an estimate of the molecular mass. Our results can become the base models of more sophisticated numerical simulations which would be able to address finer details of this complex phenomenon.

We use a model of a shell propagating in a stratified ISM in our calculation. Such an outflow is inherently 2-dimensional, with the dense shell pushed out to a roughly constant stand-off radius in the plane of the disk, while the top of the bubble is blown of by Rayleigh-Taylor instability. In steady state, a dense shell (in which molecules can form) exists in a dynamically young ($r/v \sim$ few Myr) conical shell confined within a few times the scale-height (see Figure 5.2 for a cartoon; for numerical simulations, see Figs 2, 3 of Sarkar et al. (2015) [169]). For analytical tractability, we consider the formation and survival of molecules in the dense shell expanding in a stratified disk. All starburst nuclei discussed in the chapter show a CO disk and biconical outflows emanating from them. We expect our simple estimates to apply, at least to an order of magnitude, for the realistic scenario.

We begin with a discussion of the phase space of molecular and ionic components of outflows from starbursts, and after eliminating various possibilities we arrive at a basic scenario (§2). In the later part of this section, we study various physical constraints on the parameters of the starburst and the disk galaxy for producing molecular outflows. Next we discuss the physical processes involved in the formation and destruction of molecules in these outflows (§3) and present our results in §4.

5.2 Arriving at a physical model

5.2.1 Radius-velocity space of molecular and atomic components

The phase space of the outflows with molecular and ionic components that we introduce below can be instructive in order to arrive at a physical model. Consider the case of a dense shell of a superbubble triggered by an OB association. In the case of a uniform ambient medium density ρ, the position and velocity of the shell are given by,

$$r \sim \Big(\frac{\mathcal{L}t^3}{\rho}\Big)^{1/5}; \quad v \sim \frac{3}{5}\Big(\frac{\mathcal{L}}{\rho}\Big)^{1/5} t^{-2/5} \approx \frac{3}{5}\Big(\frac{\mathcal{L}}{\rho}\Big)^{1/3} r^{-2/3}\,, \tag{5.1}$$

where $\mathcal{L}$ is the mechanical luminosity driving the superbubble. In other words, the position and velocity of the shell are related as $r \propto v^{-3/2}$. We can first compare this with observational data. However, in order to make a meaningful comparison between galaxies with different SFR, one can take out the dependence on SFR, by plotting $v/(\mathrm{SFR})^{1/5}$ against $r/(\mathrm{SFR})^{1/5}$, since both r and v depend on $\mathcal{L}$ (and consequently, the SFR)

We show in Figure 5.1 data from observations of molecular components from NGC 253 and NGC 3828 (black points), and M82 (HCN component in magenta, and the warm component in cyan). The length scales and velocities of this component are known from imaging and spectroscopic observations. It is not easy to determine the distances of atomic clouds that are usually probed by absorption lines. However there are a handful of cases of outflows from edge-on galaxies where one has reliable information on the position and speed of the atomic clouds (M82, NGC 3079, 5253, 1482, 4666, 1808). These are shown as olive green points in the same figure. We also show the data of atomic components in outflows from ULIRG as red points (from Martin (2005) [127]).

We also show as brown slanted lines the simple scaling of $v \propto r^{-2/3}$, for different uniform ambient densities ρ, with the density being the largest in the bottom-left

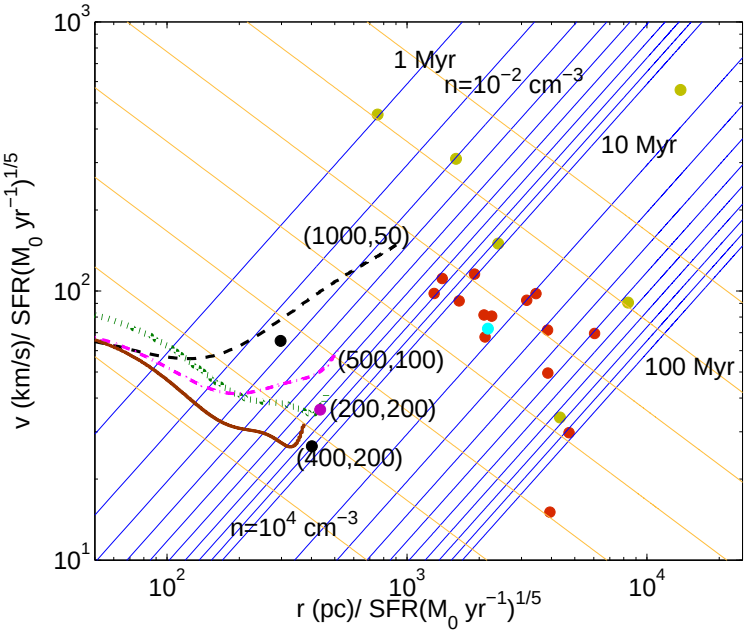

Figure 5.1: Phase space of molecular and atomic outflows, with points representing different observations of molecular (black and magenta points) and atomic outflows (olive green points), as well as atomic outflows from ULIRGs (red points). The cyan point represent the warm (2000 K) molecular outflow of M82. The black-dashed, green-dotted, magenta-dashed-dotted and the brown solid lines show the simulation results for superbubble evolution with radiative cooling for different combinations of mid-plane density and scale height (as labelled, with the first number of the pair being density in cm^{-3} and the second being the scale height in pc). Orange solid lines represent the v–r lines for different fixed hydrogen particle densities (of the ambient medium) ranging from 0.01 cm^{-3} (top) to 10^4 cm^{-3} (bottom), and for a given mechanical luminosity injection. The density increases from top to bottom with the increment by a factor of 10 between two consecutive lines. The blue solid lines are for different epochs in the logarithmic scale. The first ten lines are separated by 1 Myr starting from 1 Myr to 10 Myr, and the rest of the ten lines have a separation of 10 Myr between two consecutive lines ranging from 10 Myr to 100 Myr.

corner ($n_0 = 10^4$ cm^{-3}) and the smallest ($n_0 = 10^{-2}$ cm^{-3}) in the top-right corner of the diagram. The blue lines are the iso-chrones at different times, starting with 1 Myr from the top and each line separated by 1 Myr from the next, and separated by 10 Myr after the 10 Myr mark.

It is interesting that the molecular and atomic components separate out into different regions in the phase-space. (One cyan point among the olive green and red points for atomic component refers to the case of warm (2000 K) molecules in M82.) They also separate out with regard to the constant density lines although there are some exceptions. In other words, molecules appear to probe small scale outflows and high ambient density regions, whereas the atomic components probe large scale outflows ($\geq$ 1 kpc) and low ambient density. However, we note that here the length scales and velocities are normalized by SFR$^{1/5}$ and so the diagram may not allow such a neat interpretation in terms of length scales and velocities.

The molecular and atomic components may not appear to be parts of an evolutionary sequence in the context of a uniform ambient medium, but they may be related if the density is not uniform as in the case of a stratified disk gas. We show the evolution of the vertical heights of superbubbles triggered by an association of 10^5 OB stars (the reasons for this choice of parameter will be explained later), in an exponentially stratified medium characterised by mid-plane density n_0 and scale height z_0. The dashed, dot-dashed, dotted and solid lines show the cases for different combinations of mid-plane density and scale heights (labelled by these parameters, n_0 in units of cm^{-3}, and z_0 in pc). The evolutionary tracks are different from slanted lines because of stratification and radiative cooling in the simulations. However, the point to be noted is that the atomic/ionic outflow data points may be connected to the molecular outflow data points through such evolutionary curves of superbubbles in a stratified medium, connecting these two apparently disparate phenomena with an evolutionary sequence.

5.2.2 Preliminary estimates

These observations lead to a few preliminary estimates. For example, from typical sizes and velocities in observed outflows in NGC 253 and NGC 3068 one infers a dynamical age of $r/v \sim 2$–4 Myr. Assuming that the age of the star cluster associated with the outflow is longer than the main sequence lifetime of the least massive OB star, *i.e.* 30 Myr, and with a constant SFR of a few $M_\odot$ yr^{-1}, the total number of SNe exploded during the dynamical time scale is $\sim 10^5$, and a total SNe energy of $\sim 10^{56}$ erg. The total kinetic energy deposited by these SNe is $\sim 7 \times 10^{55}$ erg. However, when a SN remnant enters the radiative phase, its energy (both kinetic and thermal) is lost and a small fraction remains in the form of kinetic energy. Smith (1993) [182] have shown that the energy of SN remnants decrease as $\propto R^{-2}$ in the radiative phase. Assuming that SN remnants merge with each other earlier than when their radii grow 3 times since the onset of radiative phase Nath & Shchekinov (2013) [139], we arrive at the estimate of kinetic energy available for molecular outflow as $\simeq 7 \times 10^{54}$ erg. Therefore the observed kinetic energy of the molecular outflow ($< 10^{53}$ erg s^{-1}) is much smaller than the mechanical energy deposited by stars. This is even smaller than the mechanical energy retained by the superbubble, assuming that 90% of the mechanical energy is lost via radiative cooling Gupta et al. (2016) [70], Sharma et al. (2014) [174], Vasiliev et al. (2015) [215].

These considerations point towards the following scenario. Suppose that the central starburst drives a shell by multiple SNe explosions. A quasi-spherical expanding shock wave from an OB-association becomes unstable against Rayleigh-Taylor and Kelvin-Helmholtz instabilities (the latter begins to be operative when the shock front expands into the halo where the front goes up faster due to decreasing density and a tangential component emerges) Mac-Low et al (1998) [120]. In the next stage the uppermost part of the front breaks and forms an outflow in the vertical direction, while the rest of the shell fragments and forms multiple clouds and clumps moving pervasively within the expanding shell. The expanding molecular gas can be swept

up at the observed distance $D \sim 500$ pc by the quasi-spherical shock wave propagating in an exponentially stratified gas layer with the scale height $z_0 = 100$ pc and the mid-plane density $n_0 = 3 \times 10^2$ cm^{-3}, such that characteristic cooling time at $T \sim 10^6$ K is only 100 yr, and the current observed state of molecular outflow is consistent with the fact the majority of energy has been lost.

We elaborate on this model in the rest of the chapter. However, let us consider here briefly the possibility that the molecular clumps are pushed by radiation pressure. Molecular clumps are dense enough to ensure tight collisional coupling between dust and gas particles. In such conditions the radiation force acting on the clump, and the resulting acceleration, are

$$F_R \sim \frac{\pi R^2}{c}\Phi, \qquad\qquad a_R \sim \frac{3}{8}\frac{\Phi}{m_{\rm H} N_{\rm H} c}, \tag{5.2}$$

where R is the clump radius, Φ is radiation energy flux, $N_{\rm H}$ is the column density of the clump, where we explicitly assumed $N_{\rm H_2} = 2N_{\rm H}$. The energy flux can be estimated as $\Phi \sim 300 N_* L_\odot / 4\pi D^2$, for a Kroupa IMF with N_* being total number of stars in the underlying central stellar association, D is the distance of clumps from the galactic centre. For the same IMF one can assume $N_* \simeq 100 N_{OB}$, N_{OB} being the number of OB stars in the association. For $D \sim 500$ pc, $N_{\rm H} \gtrsim 10^{22}$ cm^{-3} for a typical molecular cloud, one obtains

$$v \sim \sqrt{2 \int a_R dr} \sim 30 \text{ km s}^{-1} \times (N_{OB}/10^5)^{1/2}\,. \tag{5.3}$$

Therefore radiation pressure alone cannot possibly explain the typical length scale and velocities of the observed outflows. Moreover, although the molecular outflow is dynamically young, the nuclear starburst may be old enough such that most luminous O-stars (producing radiative acceleration) are absent. 1-D numerical simulations show that radiative acceleration plays a subdominant role after a few Myr Gupta et al. (2016) [70].

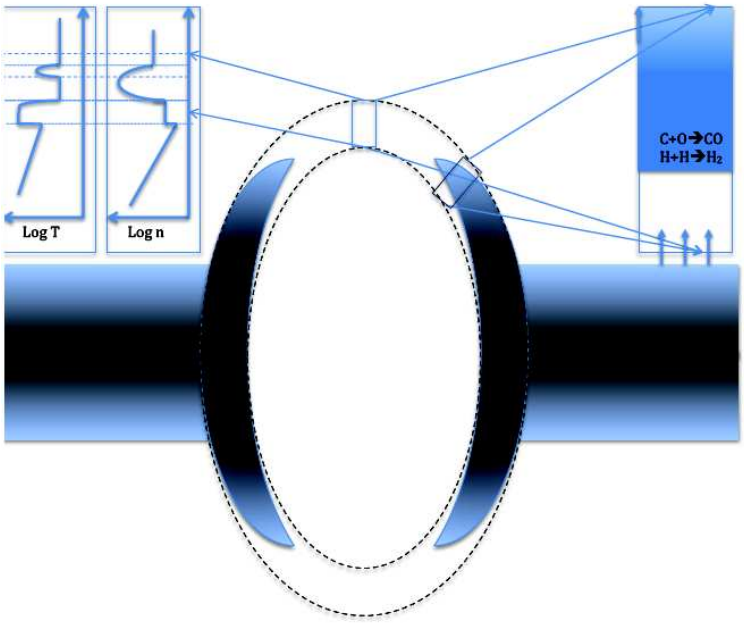

Figure 5.2: Schematic diagram for the model of outflow used in this chapter, with a superbubble shell ploughing through a stratified disk. The observed morphology is shown in grey tones, and the idealised superbubble shell is shown with dashed lines. A zoomed version of the shell is shown on the right, highlighting the region where CO forms (for details, see §4.2). The arrows at the bottom of the zoomed shell denote photons incident on the shell. Another zoomed version of the shell is shown on the left, that portrays the density and temperature profile in and around the shell. See §4.1 for an explanation of this aspect.

5.3 Physical model

Consider a central OB association embedded in a dense stratified disk. The stratification in the disk is assumed to be exponential, with a scale height of z_0 and a mid-plane particle density n_0. The ambient temperature is assumed to be in the range of few tens of K, appropriate for a dense region, with densities in the range of 100–1000 cm^{-3}. The mechanical luminosity arising from stellar processes in the OB association drives a shock through the ambient medium, and this superbubble sweeps up ambient matter, which cools and forms a dense shell. The morphology of the observed molecular outflows (mentioned in §1) suggests an epoch when the shell has broken out of the disk, as shown in the schematic diagram in Figure 5.2. The observed morphology is shown in grey tones whereas the idealised scenario of a superbubble adopted in this chapter is shown with dashed lines. Mac-Low et al (1998) [120] have shown that most of the mass in the superbubble is confined to regions near the disk. However, for analytical simplicity of a 1-dimensional calculation, we assume a quasi-spherical shell, and consider its height as the indicator of its distance. The diagram also shows a zoomed version of the shell, and highlights the region of CO formation which will be our region of interest for the calculation of molecule formation/destruction (§4.2). Another schematic zoomed view of the shell is shown on the left that shows the density and temperature profiles in and around the shell. We will describe this structure in detail in §4.1.

The parameters used for the stratified disk (the midplane density from 100 to 10^3 cm^{-3}, and the scale height 50 to 200 pc) correspond roughly to a molecular cloud with the surface gas density of $\Sigma_g \simeq (10^3 - 10^4) M_\odot$ pc^{-2} (equivalent to typical column densities of molecular clouds $N(\mathrm{H}) = 10^{23}$–10^{24} cm^{-2}), or the total mass of molecular cloud with size $D = 1$ kpc of $M \sim 2 \times 10^8 - 10^{10} M_\odot$ (for $\mu = 2$, where μ is the mean molecular weight).

Consider the minimum size of the OB association needed to explain the observations which show outflowing shell at $\sim$ 500 pc with a speed $\sim$ 50 km/s. The

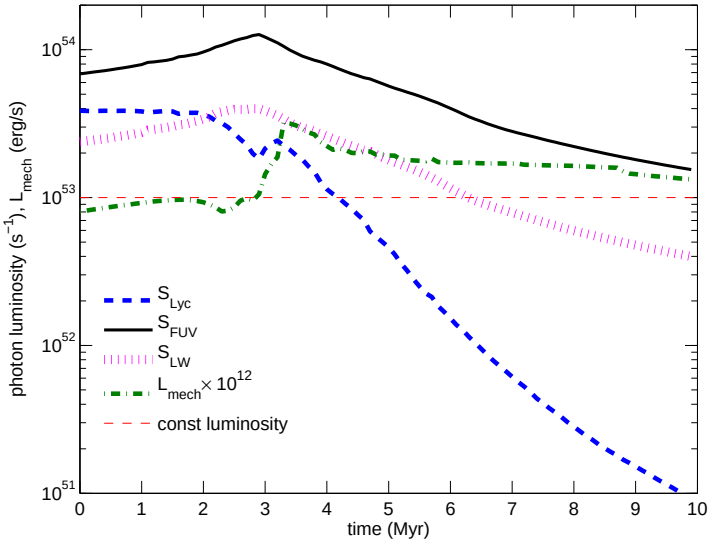

Figure 5.3: The evolution of mechanical luminosity (L_{mech}), Lyman continuum photon luminosity and luminosity in the FUV ($S_{\rm FUV}$), and Lyman-Werner band for $N_{OB} = 10^5$ ($S_{\rm LW}$), calculated using Starburst99. In this figure, we have plotted $L_{mech} \times 10^{12}$ to accommodate the mechanical luminosity curve along with the other luminosity plots. The slowly growing part on mechanical luminosity on initial stages ($t < 2$ Myr) is due to active stellar wind from massive stars; at $t > 3$ Myr SNe explosions become dominant.

observations of a molecular mass of $\geq 10^7$ M$_\odot$ implies a minimum gas density of ~ 100 cm^{-3}. For a superbubble expanding in a uniform medium of density ρ, the required mechanical luminosity $\mathcal{L}$ for an outflow to have a speed v at distance r, is given by $\mathcal{L} \approx (5/3)^3 \rho\, v^3 r^2$. The above mentioned observed parameters of speed, distance and density, therefore implies a minimum mechanical luminosity of $\geq 10^{41}$ erg s^{-1}, which corresponds to $\geq 10^5$ OB stars (which we refer to as N_{OB}) Roy et al. (2013) [164]. We will use this value of N_{OB} as a fiducial number in our work here.

The evolution of the Lyman continuum luminosity of the central source is calculated with Starburst99 code for instantaneous star formation. We also show the evolution of Lyc and Lyman-Werner band photon luminosities in Figure 5.3 for $N_{\rm OB} = 10^5$. Although the mechanical luminosity varies with time, for simplicity we use a constant

value (10^{41} erg s^{-1}) as shown by a red dashed horizontal line, and which is a reasonable approximation within the time scale of 10 Myr considered here. Note the initial rise and subsequent decline in the FUV luminosity (solid line) with time. This behaviour of the FUV luminosity will be important in understanding the evolution of the thermodynamics of the shell, as will be described later in this chapter.

5.3.1 A flow-chart of our calculation strategy

We first describe the formalism of our calculation before discussing the details.

- *Dynamics* :–We first study the dynamics of a superbubble in a stratified medium. Since the density is large, cooling is important, and therefore the standard solution of Weaver et al. (1977) [224] for uniform media, or the Kompaneets approximation Kompaneets (1960) [107] for an adiabatic shock wave from a point explosion in a stratified atmosphere, is not adequate. We use hydrodynamical simulations with gas cooling in order to obtain the evolution of the shell. However, in order to focus on the essential physical processes, we only use the vertical height of the shell (denoted here by z_+), and ignore the effects of deviations from sphericity of the shell. We describe the numerical set up in §B.1, and use the results of $z_+(t)$ and the corresponding superbubble velocity in our calculation.

- *Thermodynamics*:– Given the knowledge of the dynamics of the superbubble, we then discuss the (density and temperature) structure of the shocked gas in §5.4.1. We focus on thermodynamics of the the cool, dense shell that forms behind the shock. We assume the density jump between the shell density and the stratified ISM density to be constant in time, for simplicity. Although not precise, this assumption allows us to glean qualitative trends. The estimates of the density jumps are given in 5.4.1 in the presence of the ISM magnetic field. Then we describe the dominant heating processes (photo-electric heating)

and gas cooling (§5.4.2). The photo-electric (PE) heating rate is calculated for the FUV photon luminosity (S_{FUV}) with dust extinction (see Appendix B.4 for details). One also needs to have an estimate of the electron density (n_e) to calculate the PE-heating rate. The diffuse ISM UV photon luminosity is responsible for ionization of the ambient gas, that lies outside the Strömgren sphere for the central source. We calculate n_e assuming ionization equilibrium. We solve two coupled equations using thermal equilibrium (equating PE-heating with cooling) and ionization equilibrium to obtain the equilibrium shell temperature ($T_{shell}(t)$), and n_e. We also demonstrate that the heating and cooling time scales are much shorter than the dynamical time scale, and thus thermal equilibrium in the shell is a good approximation (§B.5).

- *Molecule formation:*–Equipped with the knowledge of the density and temperature of the dense shell, we discuss the processes of molecule formation and destruction (using H_2 as a proxy for all molecules) in §5.5, and calculate the amount of molecules formed in the shell in different cases (§5.5.1). The Lyman-Werner band photon luminosity (S_{LW}) is used to calculate the photo-dissociation of the molecules, after taking into account the effect of dust extinction.

A schematic diagram of the flowchart of the calculation strategy is shown in figure 5.4.

However, the formation of molecules requires some basic conditions to be met. In section 5.3.2, we discuss the threshold conditions for molecule formation in the outflowing shell, determined by the ionization due to the OB association.

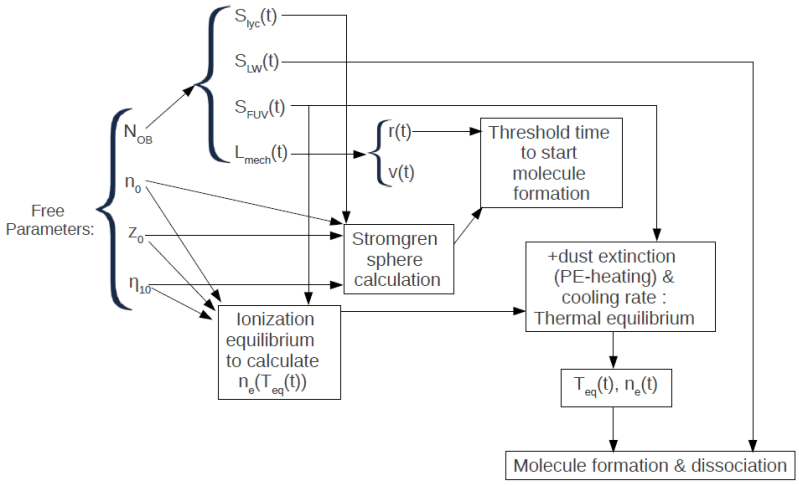

Figure 5.4: The schematic diagram of the flowchart of the calculation

5.3.2 Threshold conditions for molecule formation in outflows

When the OB association is born, the initial spurt of ionizing photons will send an ionisation front propagating through the surrounding medium, asymptotically forming an ionized zone (Strömgren sphere). The gas will be largely swept-up in a shell such that the remaining gas becomes as dilute as having 2 to 2.5 orders of magnitude lower density than in the host cloud Dale et al. (2014) [38], Freyer, Hensler & Yorke (2003) [57], García, et al. (2013) [61]. At the same time the supernovae and stellar winds arising in the OB association trigger an expanding superbubble that ploughs through the surrounding medium. Conditions inside the ionisation front will not support the formation any molecules, and any existing molecule (entrained from the parent molecular cloud) will likely get photo-dissociated. Therefore, as long as the superbubble shell is inside the ionisation front, its shell will propagate in a low-density environment and will not show any molecules. Initially, the ionization front would always move faster than the superbubble, and molecules cannot form in the shell until it has overtaken the ionization front.

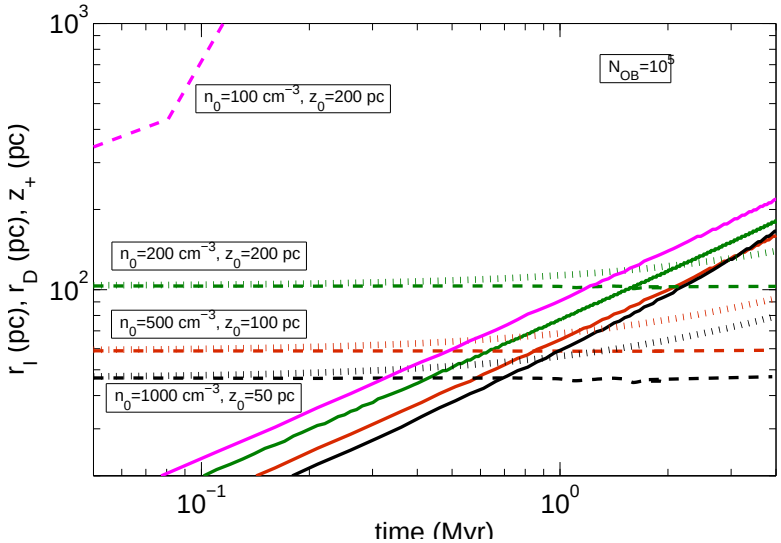

Figure 5.5: The evolution of the ionisation front (the dotted and dashed lines) and the superbubble shell (solid lines), for $N_{OB} = 10^5$ for four sets of n_0-z_0. The black lines represent the maximum density case ($n_0 = 1000$ cm^{-3}, $z_0 = 50$ pc), the red, and the green lines represent $n_0 = 500$ cm^{-3}, $z_0 = 100$ pc, and $n_0 = 200$ cm^{-3}, $z_0 = 200$ pc respectively. The magenta curve refers to the case of $n_0 = 100$ cm^{-3}, $z_0 = 200$ pc. The dashed lines represent the Strömgren radii for the ambient medium with exponential density stratification, and time varying LyC photon luminosity for the corresponding sets of n_0–z_0. The dotted lines represent the D-type ionisation front for the corresponding n_0–z_0 cases.

We use hydrodynamical simulation (described in detail in Appendix A) in order to calculate the evolution of the superbubble. The mechanical luminosity driving the superbubble is assumed to be constant in time, $\mathcal{L} \approx 10^{41}$ erg s^{-1} $\times$ $(N_{OB}/10^5)$ as obtained from Starburst99. In order to focus our attention to the basic physical processes, we consider the evolution of the vertical height (z_+) of bubble and compare with the ionization front in that direction.

The evolution of the ionization front r_I is obtained by integrating,

$$\frac{dr_I}{dt} = \frac{(S_{Lyc}(t) - 4\pi r_I^3 \alpha_H n^2/3)}{4\pi r_I^2 n}\,, \tag{5.4}$$

where α_H is the case B recombination coefficient of hydrogen. We have calculated r_I for the Lyc photon luminosity profile ($S_{Lyc}(t)$) as obtained from Starburst99, and for an exponentially stratified density structure. As the ionisation front propagates, it gives rise to a D-type front, whose distance can be estimated by eqn 37.26 of Draine (2011b) [48]. The epoch of conversion in to a D-type front can be estimated by eqn 37.15 of Draine (2011b) [48].

For simplicity, we have calculated the evolution of the ionization front and the superbubble shell independently. In other words, the shell is assumed to move in a neutral medium, and the ionization front is assumed to move in a uniform density medium. For most cases, except for $n_0 = 100$ cm^{-3}, $z_0 = 200$ pc, the corresponding error is small, because the gas mass within the Strömgren sphere is not large enough to considerably change the dynamics of the shell.

Figure 5.5 shows the evolution of the ionization front, and the vertical location of the superbubble shell for four sets of n_0–z_0 values and for $N_{OB} = 10^5$. The figure shows that the Stömgren sphere radius in the different cases is of order $\sim$ 50–100 pc (shown by the black, red and green dashed lines). The ionization fronts transform to D-type fronts (prior to 0.1 Myr) and expand slowly beyond the Strömgren radii, to reach heights of order $\sim$ 80–140 pc in $\sim$ 4 Myr. At the same time, the corresponding superbubble shells overtake the ionization fronts at heights of order $\sim$ 60–120 pc.

Figure 5.5 also shows that there are two different regimes: at low column densities

of the layer $N(\mathrm{H}) = n_0 z_0$ the ionization front moves ahead so quickly such that the superbubble shell can never catch up with, and the shell propagates in a low-density ionized gas (as shown by magenta lines). At high column density limit, the shell can overtake the ionization front, as shown by black, red and green solid lines.

It is reasonable to contend that molecular outflows can form behind the supernova-driven shock wave only in the latter case. These considerations lead us to determine the locus of the threshold combination of n_0 and z_0 for the formation of molecules in outflowing shell. We show the result with the thin blue solid line in Figure 5.6. The curve can be approximated by a fit,

$$z_0 \geq 200\,\mathrm{pc}\left(\frac{n_0}{10^2\,\mathrm{cm}^{-3}}\right)^{-3/5} \tag{5.5}$$

Note that for a uniform ambient medium of density n_0, and a constant Lyc luminosity of 4×10^{53} photons s^{-1}, the Strömgren radius is given by $\sim 116\,\mathrm{pc}(n_0/10^2\,\mathrm{cm}^{-3})^{-2/3}$. The difference between this estimate and the above fit is due to (a) density stratification and (b) variation of Lyc luminosity with time.

In Figure 5.6 we also show lines of constant surface density, marked in the units of $\mathrm{M}_\odot\ \mathrm{pc}^{-2}$. We find that molecular outflow is possible in a starburst nuclei region with surface density roughly $\geq 1500\mu\,(\mathrm{SFR}/\mathrm{M}_\odot\,\mathrm{yr}^{-1})\ \mathrm{M}_\odot\ \mathrm{pc}^{-2}$.

It is interesting that Nath & Shchekinov (2013) [139] derived a lower limit on the molecular surface density of order 1000 $\mathrm{M}_\odot\ \mathrm{pc}^{-2}$ in starburst nuclei for producing outflows. A surface gas density of $\Sigma \sim 1.5 \times 10^3\,\mu\ \mathrm{M}_\odot\ \mathrm{pc}^{-2}$ with $\mu = 1.33$ implies a SFR surface density of $\sim 10\ \mathrm{M}_\odot\ \mathrm{yr}^{-1}\ \mathrm{kpc}^{-2}$ from Kennicutt-Schmidt law Kennicutt (1998) [102]. This is incidentally ~ 100 times larger than the threshold SFR surface density for galactic superwinds Heckman et. al. (2015) [78]. Considering a nucleus region of radius ~ 300 pc, this translates to a SFR of $\geq 3\ \mathrm{M}_\odot\ \mathrm{yr}^{-1}$.

At the same time, our threshold relation also puts an upper limit on the SFR that can produce molecular outflows. Recall that the size of the Strömgren sphere depends on the ratio of $(L_{\mathrm{LyC}}/n^2)^{1/3}$. Since the density stratification has rendered a scaling of $z_0 \propto n^{-3/5}$, therefore our threshold condition on the scale height likely scales as

$N_{\rm OB}^{3/10}$, or $({\rm SFR})^{3/10}$. Recalling that $N_{\rm OB} = 10^5$ corresponds to a SFR of ~ 0.3 M$_\odot$ yr^{-1}, we can re-write our threshold condition as,

$$z_0 \geq 200\,{\rm pc}\left(\frac{n_0}{10^2\,{\rm cm}^{-3}}\right)^{-3/5}\left(\frac{\rm SFR}{0.3\,M_\odot\,{\rm yr}^{-1}}\right)^{3/10} \tag{5.6}$$

Considering the size of the central starburst nuclei region to be ~ 300 pc, we can transform this relation to one involving surface densities. We have,

$$\begin{aligned}\Sigma_{\rm SFR} \quad &\leq 50\,M_\odot\,{\rm yr}^{-1}\,{\rm kpc}^{-2} \\ &\times\left(\frac{\Sigma}{1.5\times10^3\,\mu\,M_\odot\,{\rm pc}^{-2}}\right)^{10/3}\left(\frac{n_0}{10^2\,{\rm cm}^{-3}}\right)^{-4/3}\end{aligned} \tag{5.7}$$

This essentially implies that the SFR has to be lower than a certain value for a given column density of the starburst nucleus; a larger SFR than the above inequality would inhibit the formation of molecules by ionizing the gas in the superbubble shell.

We then have three relevant scales for SFR surface density. A lower limit of $\Sigma_{SFR} \geq 0.1$ M$_\odot$ yr^{-1} kpc^{-2} ensures a galactic wind. However, the production of molecular outflows is limited to SFR surface densities $10 \leq \Sigma_{SFR} \leq 50$ M$_\odot$ yr^{-1} kpc^{-2}. It is interesting to note that the SFR surface densities of galaxies observed to host molecular outflows fall in this range. Therefore our threshold condition for disk parameters for hosting molecular outflows is consistent with observations. We should, however, emphasize that galaxies show a considerable variation around the Kennicutt-Schmidt law and the above constraint on SFR surface density may not be a strong one.

5.4 Shell density and temperature

Given the knowledge of the threshold density and scale height for molecule formation, the next important issues for molecules to form are the heating and cooling in the superbubble shell. In this section, we discuss the heating and cooling processes that play an important role in determining the shell temperature.

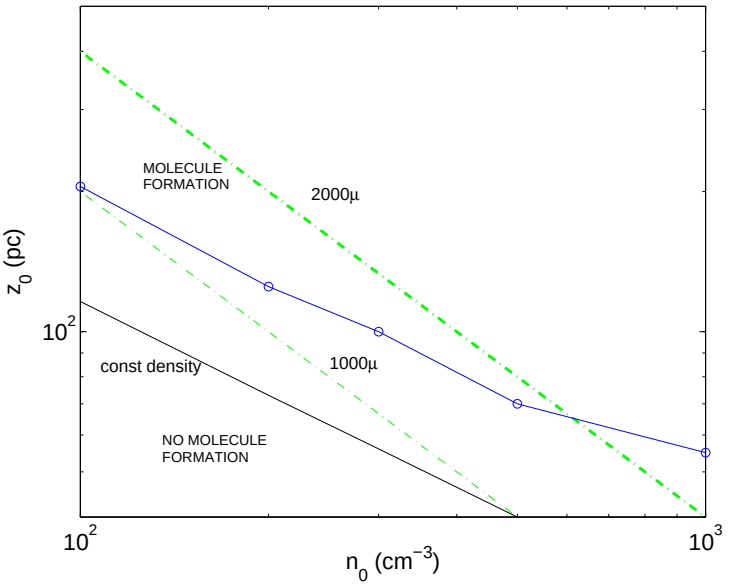

Figure 5.6: The threshold combination of mid-plane density and scale height for the formation of molecules in an outflowing shell triggered by an OB association with $N_{OB} = 10^5$. The blue-solid line represent the cut-off n_0–z_0 condition below which molecules can not form. The green dashed-dotted lines correspond to two values of constant surface densities in units of $M_\odot/\mathrm{pc}^2$, where μ is the mean molecular weight. The black line plots the Strömgren radii for ambient medium with uniform densities for comparison.

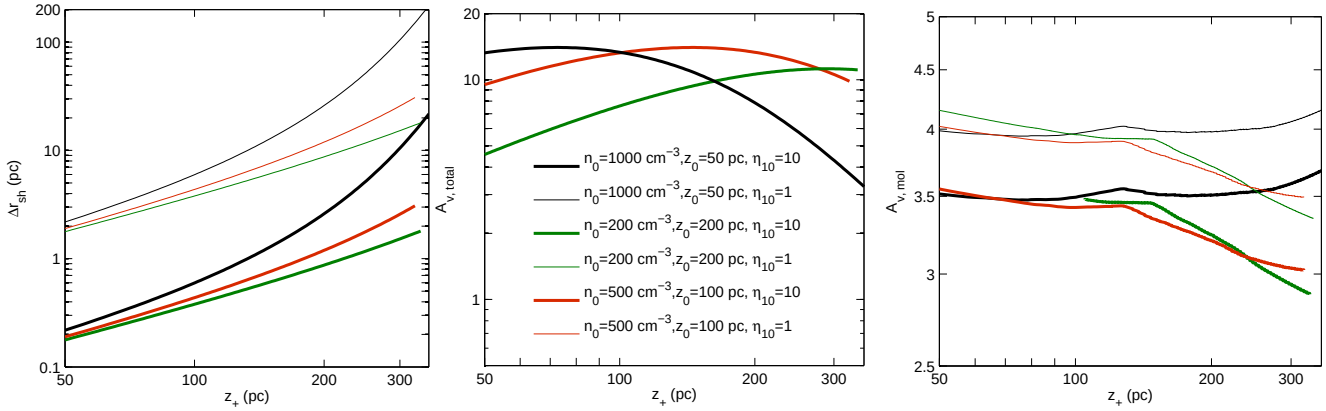

Figure 5.7: The evolution of the shell thickness and A_v for three mid-plane density and scale height combinations for $N_{OB} = 10^5$, and for for three different n_0, z_0 cases ($n_0 = 1000$ cm^{-3}, $z_0 = 50$ pc; $n_0 = 200$ cm^{-3}, $z_0 = 200$ pc, and $n_0 = 500$ cm^{-3}, $z_0 = 100$ pc), for two η_{10} cases and for $N_{OB} = 10^5$. The thick, and thin solid lines correspond to $\eta_{10} = 10$, 1 respectively. The black, green, and the red lines represent $n_0 = 1000$ cm^{-3}, $z_0 = 50$ pc; $n_0 = 200$ cm^{-3}, $z_0 = 200$ pc, and $n_0 = 500$ cm^{-3}, $z_0 = 100$ pc cases respectively. All the plots hereafter follow the same colour and line-styles for the corresponding n_0, z_0, and η_{10} values. The left-most panel shows the shell thickness as a function of the vertical position of superbubble shell, and the middle panel represents the evolution of total A_v (which does not depend on the value of η_{10}, or in other words, the thin lines coincide with the thick ones). The right panel shows the values of A_v(mol) for the region where molecules form in substantial quantity, and which is the region of our concern.

5.4.1 Four-zone structure

From the point of view of the presence of molecular gas in the expanding shell associated with the wind outflow it is convenient to separate the whole post-shock flow on to four distinct zones, which are schematically shown on the left in Fig 5.2 (see also Figure 5 of Sharma et al. (2014) [174]). The zones described below are shown in the schematic diagram as being separated by dotted lines, from top to bottom: *i)* the viscous layer where kinetic energy of the inflowing gas is transformed partly in to thermal energy, and the entropy grows to the post-shock value Zeldovich & Raizer (1966) [232], *ii)* the radiative relaxation layer (RRL) where radiative losses lead to the formation of a dense shell, *iii)* thin dense shell restricted from the bottom by *iv)* the still hot low-density gas formed by the termination shock. Dissipation due to viscous forces brings the gas into a new high-temperature state and vanishes beyond the viscous layer. The thickness of this layer is determined by the viscosity, but for strong shock it can be as thin as a few free-path length of gas particles Zeldovich & Raizer (1966) [232]. In numerical models its thickness is always unresolved as this thickness is equivalent to a few times the mean-free path. The rate of energy loss due to radiation losses in the second zone depends on post-shock temperature and density and becomes important when the dynamical time becomes comparable to the cooling time.

We show in Appendix C that the density in the cool/dense shell (region *iii*) can be larger than the ambient density by a factor of a few to ~ 100. Magnetic field in the ISM prevents the shell density from becoming exceedingly large. We characterise the density in the shell as,

$$n_{sh} = 10\,\eta_{10}\,n_{amb}\,, \tag{5.8}$$

where $n_{amb} = n_0 e^{-z_+/z_0}$. Given this density jump, the shell thickness ($\triangle \mathrm{r_{sh}}$) can be found by equating the total swept up mass to the shell mass,

$$\int_0^{z_+} 4\pi z^2 n_0 e^{-z/z_0} dz \approx 4\pi z_+^2 \triangle \mathrm{r_{sh}} n_{sh}\,, \tag{5.9}$$

which gives the value of $\triangle r_{sh}$. Here we have assumed the shell to be spherical, which is a reasonable approximation since the spherical shape of superbubble shell is roughly maintained until it reaches a few times (2–3) the scale height. The shell thickness is shown in the left-most panel of Figure 5.7 for different cases. The lower set of curves are for $\eta_{10} = 10$ and the upper set of curves, for $\eta_{10} = 1$.

Although the radius and thickness increases with time, since the density in a stratified medium decreases with height, the total column density in the shell does not increase monotonically. It rises until the shell reaches the scale height and then decreases. We show the evolution of the total opacity in the shell (proportional to the column density) in the middle panel of Figure 5.7. The visual extinction is related to the column density as $A_v \approx (N_H/1.9 \times 10^{21}\,\mathrm{cm}^{-2})$ Bohlin et al. (1978) [12]. We find that the maximum visual extinction A_v lies in the range of 10–20, which is attained at roughly the scale height. Note that the value of A_v does not depend on the value of density jump.

The temperature in the shell is determined by the balance of heating and cooling processes, which we consider next.

5.4.2 Heating and cooling processes in the shell

The physical state and ionization structure of the shell resembles the so-called photo-dissociation region (PDR) considered in the literature Hollenbach & Tielens (1997) [87]. Going outward from the central region, beyond the ionized gas, one first encounters a region of neutral atoms, after which there are regions whose ionization structure is dominated by the influence of FUV photons on different trace elements, beginning with carbon. Here we focus on the region where CO/H_2 are produced in significant quantity. According to Wolfire et. al. (2010) [228] (their eqn 21), the visual extinction A_v corresponding to CO and H_2 are comparable, and is given by,

$$A_v(\mathrm{mol}) \approx 0.1 \ln\left[3.3 \times 10^7 (G_0/1.7n)^2 + 1\right], \tag{5.10}$$

where G_0 is the FUV photon density (number of photons per unit volume) obtained from Starburst99 code.

The rightmost panel of Figure 5.7 shows the value of A_v(mol) corresponding to the molecular region that we will focus on, calculated with eqn 5.10. Recall the rise and decline in the FUV luminosity of the central OB association (see Fig 5.3). This evolution in the FUV luminosity makes the value of A_v(mol) also rise and then decline (through the term G_0), as seen Fig 5.7. For the cases of small scale height (solid lines), the shell density decreases rapidly with height, increasing the value of A_v(mol).

The corresponding ionization fraction of the free carbon ions $x_{C^+} \equiv n_{C^+}/n_C$ in the carbon dominated region is given by Tielens (2005) [205]

$$\frac{1 - x_{C^+}}{x_{C^+}^2} \approx 3.3 \times 10^{-6} \left(\frac{n}{10^4\,\mathrm{cm}^{-3}}\right) \left(\frac{T}{300\,K}\right)^{-0.6} \times \left(\frac{G_0}{10^4}\right)^{-1} \exp[2.6 A_v]\,. \tag{5.11}$$

The ionization fraction therefore is given by $x_e = A_C x_{C^+}$, where $A_C = 1.4 \times 10^{-4}$ is the carbon abundance for solar metallicity. The ionization fraction depends on temperature weakly, and is roughly given by $x_e \approx A_C$, since $x_{C^+} \approx 1$, from eqn 5.11.

The dominant heating process in this region of the shell is photoelectric (PE) heating, and it cools through radiation. Given the large density of this region, the temperature is likely to be in the range of $\sim$ 10–20 K. We show in Appendix D and E with detailed calculation the values of the ionization fraction and the equilibrium temperature, for different shell densities, and for different cases of n_0 and z_0. The results of the calculation confirms that the ionization fraction $x_e \approx 1.4 \times 10^{-4}$ and that the equilibrium temperature is of order $\sim$ 10–20 K (which, to be specific, we approximate as 15 K). We assume thermal equilibrium to calculate the shell temperature and x_e, as heating and cooling time scales of the shell are much shorter than the dynamical time throughout the evolution of the shell. In the following calculations for molecule formation we adopt these values of x_e and T.

5.5 Molecule formation and dissociation

While the observations of molecular outflows have shown that the velocity and the momentum of the molecular component is in rough agreement with the expectations from a star formation driven outflow, the existence of molecules in the outflowing gas is not trivially explained, for the following reasons. The molecular component that is seen at a few hundred pc can either be formed in the outflowing gas, or can be a residue of the molecules entrained from the parent molecular clouds, whatever has survived the destruction process while the shell has evolved and has been shocked. In this section, we study the molecule formation and destruction processes in detail. The two important mechanism for the dissociation of molecules are the photo-dissociation and the collisional dissociation.

5.5.1 Formation and destruction of molecules in the shell

Consider the case of a shell propagating outward, and being irradiated by Lyman-Werner band photons from the OB stars responsible for the outflow in the first place. We consider the formation and dissociation of molecular hydrogen as hydrogen is the most abundant element. Photons in the Lyman-Werner band (11.2–13.6 eV) are responsible for the dissociation of hydrogen molecule. The net rate of formation of molecular hydrogen, for a gas density n, is given by,

$$\begin{aligned} \frac{dn_{H_2}}{dt} &= \mathcal{R}_f\, n\, n_{HI} - \mathcal{R}_{d,thin} f_{\rm dust,H_2}\, f_{\rm shield,H_2}\, n_{H_2} \\ &\quad -k_D\, n\, n_{H_2}\,, \end{aligned} \tag{5.12}$$

where n_{H_2} is the number density of H_2 molecules. As mentioned above, $\mathcal{R}_{d,thin}$ depends on the radiation field, and therefore on the distance of the shell from the centre and the Luminosity in the Lyman-Werner band. The formation rate $\mathcal{R}_f \approx 3 \times 10^{-18} T^{1/2}$ cm^3 s^{-1}, for solar metallicity Hollenbach & McKee (1979) [86]. The density and temperature refers to the shell density and equilibrium temperature calculated in Appendix B.5.

$\mathcal{R}_{d,thin} = 3.3 \times 10^{-11}\, G_{LW}$ s^{-1} is the photo-dissociation rate in optically thin gas Draine & Bertoldi (1996) [46], G_{LW} being the strength of the radiation field in units of Habing field. The factor $f_{\rm dust,H_2}$ takes into account the effects of dust extinction and $f_{\rm shield,H_2}$, that of H_2 self-shielding. We calculate G_{LW} similar to the equation B.7 with the replacement of S_{FUV} by S_{LW}, albeit without the extinction factor.

For the shielding due to dust, we have,

$$f_{\rm dust,H_2} = \exp(-3.5 A_v({\rm mol}))\,. \tag{5.13}$$

For the self-shielding due to molecules, we use the fit given by Draine & Bertoldi (1996):

$$f_{\rm shield,H_2} = \frac{0.965}{(1+x/b_5)^2} + \frac{0.035}{\sqrt{1+x}} \exp\left(-8.5\times10^{-4}\sqrt{1+x}\right), \tag{5.14}$$

where $x = N_{H_2}/(5\times10^{14}\ {\rm cm}^{-2})$, $b_5 = b/(10^5\ {\rm cm\ s}^{-1})$, $b^2 = kT/m_H$, being the Doppler broadening parameter.

The collisional dissociation is another important dissociation process for destruction of molecules. This process crucially depends on the shell temperature and density. The dissociation rate coefficient ($k_D(n,T)$) is given by Lepp & Shull (1983) [118],

$$\log k_D(n,T) = \log k_H - \log(k_H/k_L)/(1+n/n_{cr})\,, \tag{5.15}$$

where $k_H(T)$, and $k_L(T)$ are the dissociation rate coefficients for the high, and low density limits respectively given in Table 1 of Lepp & Shull (1983) [118]. The critical density n_{cr} depends on temperature and is calculated using equation 6 of Lepp & Shull (1983) [118]).

The formation time scale of molecules is given by,

$$t_{\rm form} \approx (\mathcal{R}_f\, n)^{-1} \approx 10^{-2}\,{\rm Myr}\left(\frac{n}{10^3\,{\rm cm}^{-3}}\right)^{-1}\left(\frac{T}{100\,{\rm K}}\right)^{-1/2}, \tag{5.16}$$

The photo-dissociation time scale of molecules is given by,

$$\begin{aligned} t_{\rm dest} \;\approx\; & 7\times10^{-7}\,{\rm Myr}\left(\frac{S_{LW}}{10^{53}\,s^{-1}}\right)^{-1}\left(\frac{r}{100\,{\rm pc}}\right)^{2} \\ & \times(f_{\rm dust,H_2}\, f_{\rm shield,H_2})^{-1}\,. \end{aligned} \tag{5.17}$$

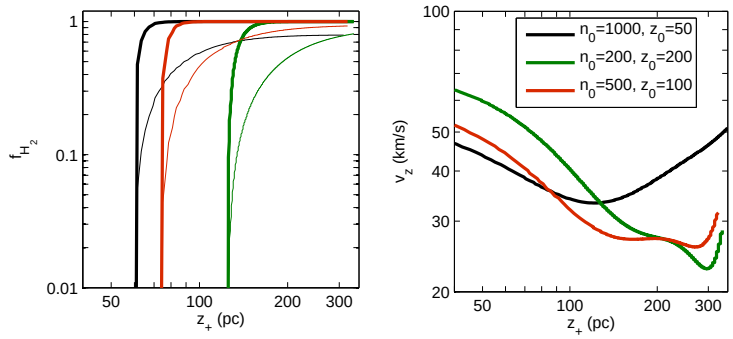

Figure 5.8: Evolution of molecular fraction (left), and the bubble shell velocity (right) with the size of the superbubble shell, for $N_{OB} = 10^5$, for different n_0, z_0, and η_{10} cases. The thick, and thin lines correspond to $\eta_{10} = 10$, 1 respectively. All the calculations of molecule formation and dissociation are performed in the dense superbubble shell after it crosses the D-type ionisation front.

In general, the collisional dissociation time scale is much longer than the photo-dissociation time scale, given the low temperature of the dense shell.

These time scales should be compared with the dynamical time scale of the dense shell. We found that the formation time scale becomes comparable to or shorter than the dynamical time scales, when the shell size exceeds $\sim$ 200 pc, signalling the onset of molecule formation.

5.5.2 Results

Figure 5.8 (left panel) shows the resulting molecular fraction as a function of shell distance for $N_{OB} = 10^5$, for the fiducial cases. The right panel shows the corresponding velocity of the shell.

There is an abrupt jump in the value of the molecular fraction ($f_{\rm H_2}$) from a small value of 10^{-6} to a maximum value of 1 for large value of η_{10} (=10) whereas for the case of small η_{10}(=1), $f_{\rm H_2}$ increases slowly to a maximum value of 0.8–0.9 for all the n_0–z_0 cases. The sharp rise in the molecular fraction corresponds to the epoch of the shell crossing the ionization front, as discussed in §5.3.2.

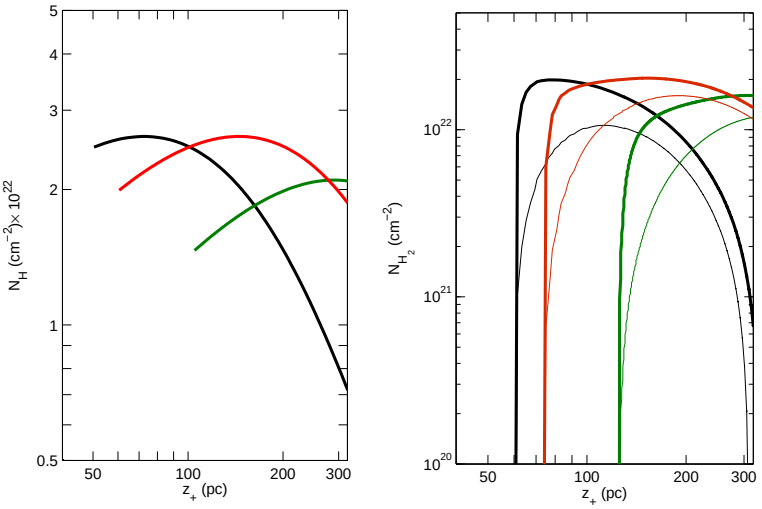

Figure 5.9: Evolution of the total hydrogen column density (left) and molecular column density (right), with the size of the superbubble shell, for $N_{OB} = 10^5$, for different n_0, z_0, and η_{10} cases. The details of the line-styles, and line-colours for different parameters are mentioned in the caption of the figure 5.7.

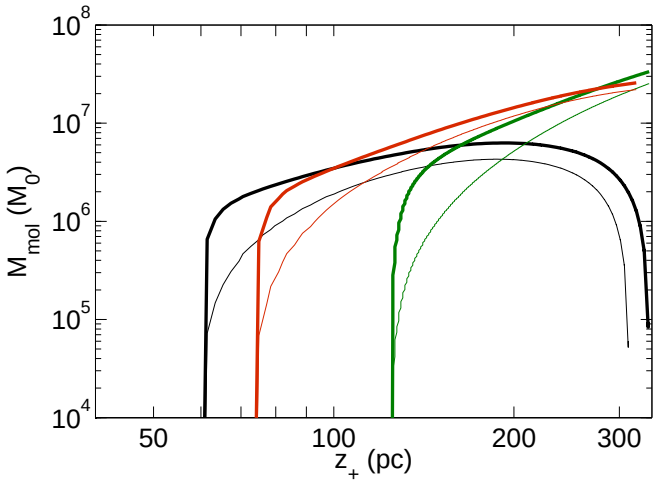

Figure 5.10: The evolution of molecular mass with the size of the superbubble shell, for $N_{OB} = 10^5$, for three different n_0–z_0 cases, and for the two different values of η_{10} (1, 10). Refer to figure 5.7 for the details of the different line-styles, and line-colours. The molecular mass is the integrated mass over the molecular region of the shell.

The velocity of the superbubble shell for all the n_0–z_0 cases at $\sim$ 100–300 pc is $\sim 10 - 40$ km/s, which matches with the velocities of the molecular outflows as seen in observations, particularly of NGC 253 Bolatto et al. (2013) [13].

Figure 5.9 shows the total hydrogen column density and the corresponding molecular column densities, in the left and right panels respectively. The total column density plots have been explained earlier in the context of total visual extinction in Figure 5.7. The H_2 column density first rises and then falls due to decreasing shell density and column density. It falls more rapidly in the case of small scale height when the gas density rapidly decreases with height.

Figure 5.10 shows the evolution of the total molecular mass (integrated over the shell) for different parameters. The molecular mass is found to be in the range of $\sim$ 10^7–10^8 $M_\odot$) at $\geq$ 200 pc, in the three fiducial cases, consistent with observations. As both the dissociation rates (photo-dissociation, and collisional dissociation) are much smaller compared to the formation rate of molecules, for most cases the molecular

mass does not decrease as the radius of the superbubble shell increases– rather its rate of increase may slow down, particularly in the case of disks with small scale heights. For the cases of large mid-plane density and small scale height, the molecular mass decreases, as the column density of the shell decreases with increasing height. We note that at larger radii, when the shell crosses a few scale heights, the shock-heating can be an important mechanism (as the velocity goes up till $\sim$ 50–100 km/s, and also the density of the shell reduces) to destroy the molecules in the dense shell, and thus reducing the molecular mass integrated over the shell. This aspect is beyond the scope of the present work.

The important parameters that can be used to compare with observations are the molecular mass and the length scale of the molecular shell (as well as its speed). We wish to determine the ranges in the combination of gas density and scale height (for the given $N_{OB} = 10^5$) that can give rise to molecular outflows with a certain molecular mass and radius of the shell. We consider the molecular mass attained at the time of crossing the disk scale height. We show in Figure 5.11 the regions in the parameter space of n_0 and z_0 that correspond to molecular masses (calculated at the scale height) of different ranges. The lower blank portion corresponds to the lower limit of Figure 5.6.

5.6 Discussion

5.6.1 Previous studies

Despite a rather long history of numerical simulations of galactic winds (see the seminal papers Suchkov et al. (1994) [193], Suchkov et al.(1996) [194]), only one paper with theoretical analysis of galactic winds published to date appears to be relevant for the formation of molecular outflows. Thompson et al. (2016) [208] described a *steady-state* model of a galactic wind with a detailed description of the thermal processes, such as radiative cooling and thermal conduction, along with a qualitative analysis

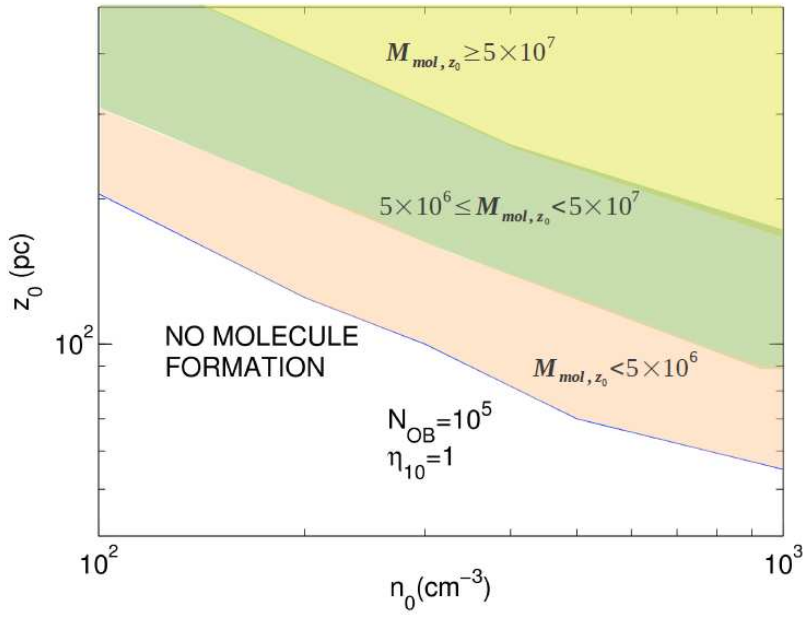

Figure 5.11: Regions in the parameter space of n_0 and z_0 that can give rise to molecular mass of different ranges in shells triggered by star formation activity, with $N_{\rm OB} = 10^5$, and with $\eta_{10} = 1$. Corresponding CO luminosities are also indicated.

of thermal instability and convection in the expanding gas. Their study focuses, however, on generic features of such a flow, connecting the central energy and mass source and a distant circumgalactic gas. The inner boundary conditions here are set at $R = 0.3$ kpc from a central energy and mass injection source as described by Chevalier & Clegg (1985) [25], which is actually comparable to the sizes of regions where molecules are already seen in galactic winds. Moreover, gas density ($n \leq 1$ cm^{-3}) and temperature ($T \geq 2 \times 10^3$ K) in the outflow always remain in the range that is unsuitable for the formation of molecules.

A more plausible scenario for the observed molecular outflows, and the one that we favour, is the cooling of the shocked gas in the radiative outer shock. Thompson et al. (2016) [208] (see also Sarkar et al. (2016) [170]) only consider multiphase cooling in the mass-loaded galactic outflow and not the dense shell. Thompson et al. (2016) [208]). In our *non-steady* outflow, the formation of a shock in the very beginning

(at scales of a few pc) is an essential event which makes the gas cool down quickly to $T \lesssim 100$ K within a few Myr or less. At this stage, the ambient gas density is quite high and therefore the post-shock density and temperature are in the range $n > 10^3$ cm^{-3} and $T \lesssim 10 - 30$ K where molecules can efficiently form. Moreover, these conditions are suitable for line emission of CO and HCN/HCO$^+$.

Girichidis et al. (2016) [64] simulated the effect of SNe driven outflows and studied the effects of clustering and frequency of SNe. Their simulations showed that molecules formed at vertical distances less than the disc scale height (their Figure 2). However, their focus was on the velocity dispersion of different phases of gas in a typical disc galaxy, and not on the dynamics and chemistry of expanding shells triggered by large OB associations, as have been observed in starburst nuclei.

We also note that Zubovas & King (2014) [236] considered the formation of molecules in AGN driven outflows. However, their model is more relevant for the formation of molecules in outflows with speed ~ 1000 km s^{-1} and with mass outflow rates of ~ 1000 M$_\odot$ yr^{-1}, and is different in scope and nature than the small scale outflows in starburst nuclei with smaller speeds.

5.6.2 Comparison with observations

It is readily seen from Figure 5.10 that in a wide range of parameter space (n_0, z_0), the model predictions are consistent with the observed molecular outflows. Moreover, numerical models reveal the range of physical parameters under which starbursts generate powerful high-mass molecular outflows. In particular, it is clear from Figure 5.10 that for small gas scale heights z_0 the expanding molecular layers widen, thereby decreasing the column density due to mass conservation $N_{\rm H_2} \propto (z_0/z)^2$ with nearly constant molecular fraction. The decrease in $N_{\rm H_2}$ is faster in models with smaller z_0. As a result, the maximum molecular mass in such models remains relatively low $M_{\rm mol} \sim 10^6\ M_\odot$, while larger scale heights can give rise to increasing molecular mass beyond ~ 300 pc. Unfortunately, observations of molecular w inds are yet too

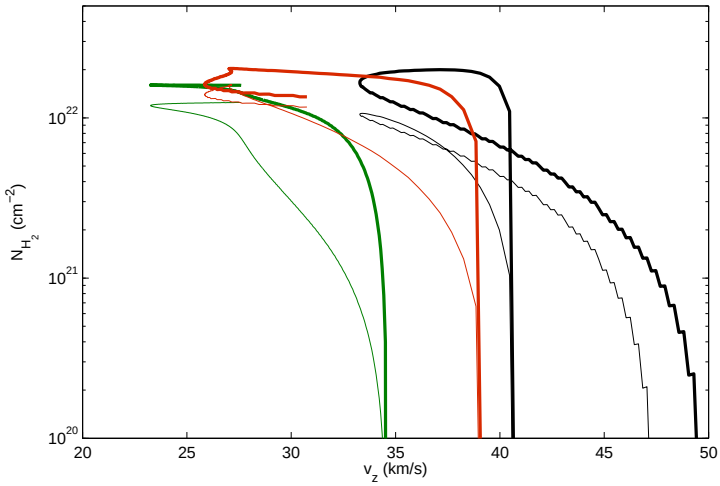

Figure 5.12: Molecular column density is plotted against the expansion velocity. The line styles correspond to the same cases as in Figure 5.7.

few, and such an interrelation between density profiles in gas preceding the starburst cannot be inferred from the available observational data.

In general, our calculations show that competitive processes governing the thermodynamics and chemical kinetics of the shell, *viz*, the heating and ionization by Lyman continuum from the underlying nuclear stellar cluster on one side, and from the shock front on the other, and an additional effect from magnetic pressure – determine the possibility to form and expel high velocity molecular gas into the outflow. It is seen from Figure 5.8 and 5.9 that in general for a given n_0-z_0 pair, the molecular outflow may show distinct paths on the $N_{\rm H_2} - v$ plane, as shown separately in Figure 5.12.

We find that the H_2 column density grows steeply at a nearly constant velocity when the outflowing shell is small. Then, at higher z the expansion velocity decreases while the H_2 column density continues to grow. At a certain point close to the breakout level, the column density starts to decrease and the velocity increases – this path is clearly seen for the case of small scale height of $z_0 = 50$ pc (black solid line). For larger values of z_0, the curve $N_{\rm H_2}(v)$ shifts left (decreasing velocity), and the loop

occurs at a lower velocity, $v_{\rm min} \propto \rho_0^{-1/3} z_0^{-2/3}$. Even though we show results for a fixed numbers of massive stars $N_{\rm OB}$ in the cluster, this relation allows to predict that in general the scaling would be $v_{\rm min} \propto N_{\rm OB}^{1/3} \rho_0^{-1/3} z_0^{-2/3}$, as follows from a simple wind model in an exponential density p rofile.

It is worth noting that in realistic conditions the molecular layer is expected to disintegrate due to Rayleigh-Taylor instability with fragments moving outwards nearly ballistically, with the velocity close to the minimum velocity at the loop. In general, the velocity range spanned by the paths agrees with observations. One can therefore expect that the range of observed velocities in molecular outflows relates to the central gas density, its scale height and likely the number of massive stars, and may help to constrain them.

5.6.3 Off-centered shells

We have considered the OB associations that trigger the expanding shells to be located at the mid-plane for simplicity of calculations. However, in reality it could be situated at some height $z\prime \leq z_0$, the scale height. Below, we briefly consider the case of off-centered expanding shells. As an extreme case, we show in Figure 5.13 the case of a superbubble triggered by an association at a height $z\prime = z_0$, and compare the molecular fraction and molecular mass with those of a superbubble located at mid-plane.

In the case of an off-center location of stellar cluster, there are two competing factors: (1) the decreasing column density of the shell and (2) the large distance traversed by the ionization front, because of density stratification. The column density of the shell roughly decreases as (since the accumulated mass is being distributed over the expanding shell),

$$N_H \approx \frac{n_0 z_0}{3} \Big(\frac{z_0}{z_+ - z\prime} \Big)^2 . \tag{5.18}$$

When the shell crosses the ionization front at z_I, the visual extinction should exceed a critical value (~ 3) in order to form a substantial amount of molecules. In other

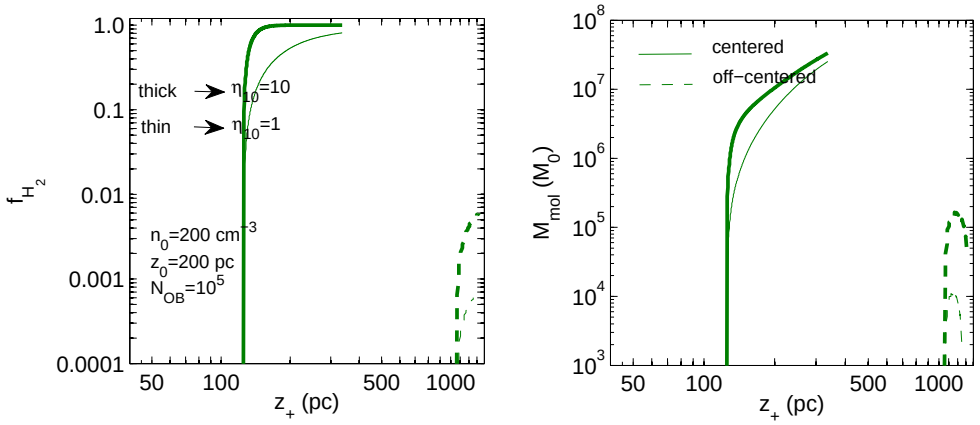

Figure 5.13: Molecular fraction and molecular mass for an off-centered superbubble (centered at $z' = z_0$) are compared with the case of superbubbles located at the mid-plane, for $n_0 = 200$ cm^{-3} and $z_0 = 200$ pc.

words,

$$\frac{n_0 z_0}{3 \times 1.9 \times 10^{21}\,\mathrm{cm}^{-2}} \left(\frac{z_0}{z_I - z'}\right)^2 \geq 3\,. \tag{5.19}$$

In this case illustrated above, for $n_0 = 200$ cm^{-3}, $z_0 = 200$ pc, and $z' = z_0$, the ionization front quickly reaches $z_I \sim 1$ kpc. Therefore the above condition is not satisfied and molecules do not form in substantial quantity. This estimate could, in principle, put constraints on the height z'/z_0 of the stellar cluster that can trigger a molecular outflow. However, one could argue that such a large OB association (with $N_{\rm OB} = 10^5$) is likely to be located close to the mid-plane, where the density is highest, rather than being far above the disk. Another point to note is that the expansion speed of an off-centered expanding shell will increase monotonically, if $z/z_0 \sim 1$, and will not have any loops as shown in Figure 5.12.

5.6.4 Caveats

We had set out to understand the dynamical parameters of observed molecular outflows in nearby starburst galaxies, namely, the length scales and velocities, as well as

the corresponding molecular masses. We also sought to understand the possible range of parameters for producing molecular outflows in highly energetic winds. Our 1-D calculations, with simplified assumptions of molecule formation in a spherical shell, show that it is possible to understand the observed outflow sizes ($\geq$ 50 pc) and velocities ($\sim$ 30–100 km s^{-1}) in the context of superbubbles triggered by starburst activity. The corresponding predicted molecular masses are of order several times 10^6–10^7 $M_\odot$, also consistent with observations of NGC 253 and NGC 3628. The morphology, dynamics and molecular masses of M82 are admittedly not explained by our simplified model, and therefore we wish to point out various caveats in our calculations.

To begin with, it is not possible to discuss the morphologies of observed molecular outflows with a 1-D calculation, and as a first step towards understanding this phenomenon our strategy has been to assume a spherical shell. In reality, this shell is likely to fragment, especially after the shell has broken out of the disk, due to thermal and Rayleigh-Taylor instabilities Roy et al. (2013) [164]. Therefore the covering factor of the shell is likely to be much smaller than unity, allowing radiation and gas to leak through. This is consistent with the observation of Hα radiation from gas far beyond the molecular outflow in M82, for example. These considerations imply that our estimate of molecular mass is at best approximate, and should be viewed/used with caution. As we mentioned in the introduction that the morphology and dynamics of molecular outflows are diverse, and therefore a better estimate would have to consider the details of the PDR region in the shell, and possible clumping in it, as well as the differences in the formation/destruction processes for different molecules, which are beyond the scope of the present work in this chapter.

5.7 Summary & Conclusions

We summarise our main findings as follows:

- We have considered a simple 1-D model of molecule formation in expanding

superbubble shells triggered by star formation activity in the nuclei of starburst galaxies. We have determined a threshold condition (eqn 5) for disk parameters (gas density and scale height) for the formation of molecules in superbubble shells breaking out of disk galaxies. This threshold condition implies a gas surface density of $\geq$ 2000 $M_\odot$ pc^{-2}, which translates to a SFR of $\geq$ 3 $M_\odot$ yr^{-1} within the nucleus region of radius $\sim$ 300 pc, consistent with observed SFR of galaxies hosting molecular outflows. We also show that there is a range in the surface density of SFR that is most conducive for the formation of molecular outflows, given by $10 \leq \Sigma_{SFR} \leq 50$ $M_\odot$ yr^{-1} kpc^{-2}, consistent with observations.

- Consideration of molecule formation in these expanding superbubble shells predicts molecular outflows with velocities $\sim$ 30–40 km s^{-1} at distances $\sim$ 100–200 pc with a molecular mass $\sim$ 10^6–10^7 $M_\odot$, which tally with the recent ALMA observations of NGC 253.

- We have considered different combinations of disk parameters and the predicted velocities of molecule bearing shells in the range of $\sim$ 30–100 km s^{-1} with length scales of $\geq$ 100 pc are in rough agreement with the observations of molecules in NGC 3628 and M82.

Chapter 6

Conclusions & future directions

In this thesis, we have studied the overall aspects of superbubble evolution, and its implications for galactic feedback and evolution. In this chapter we highlight a few important outcomes of the thesis in order to obtain a comprehensive understanding and importance of it in the context of the problems that initially motivated us to study them in detail. We also discuss the relevance of these results in galaxy formation and evolution. We end with some future projects.

6.1 Conclusions

Supernova feedback in the ISM is an important feedback mechanism among various other complicated physical processes governing galaxy evolution. However realistic implementation of SNe feedback in numerical simulations has always been a challenging issue. In various cosmological simulations of galaxy evolution, the lack of resolution makes the heating due to SNe ineffective, and thus earlier simulations suffered from numerical overcooling. This problem prompted us to study SNe feedback realistically and to estimate the radius within which SNe energy needs to be deposited for it to effectively couple to the ISM. This problem has been addressed in chapter 2. In chapter 2, we have also compared the various existing SNe feedback recipes, and derived the analytic expression for the injection radius ($r_{\rm in}$).

For effective feedback due to SNe, the heating rate has to be larger than the cooling rate. In other words, the heating time-scale has to be shorter than the cooling time-scale. We found that different existing numerical models such as the luminosity driven (LD) model, the thermal energy addition (TEa) model, and the most realistic kinetic explosion (KE) model produce similar results when the energy is deposited within a small volume. We also discussed that to create a strong shock, one requires multiple SNe to evolve coherently in space and time. Bubble created by a single SN fizzles out within a few dynamical time-scales, and therefore loses almost all the input energy by the end of a star cluster lifetime. However superbubble created by multiple SNe

can retain $\sim$ 35% of the injected energy in the form of bubble thermal and shell kinetic energy. These multiple SNe go off within a hot, dilute bubble carved by the initial SNe and stellar winds, and do not suffer extensive radiative losses as isolated SN explosions.

In chapter 3, we studied a few outflow problems in detail applying SN feedback mechanism to realistic galactic disks. Tüllmann et al. (2006) [211] studied multiphase halos in edge-on galaxies, and determined the cut-off surface density of energy injection rate for the creation and existence of multiphase halos. Dahlem et al. (1995) [40] studied synchrotron radio emission from five edge-on galaxies. They concluded that for the creation of radio halos, the threshold surface density of energy injection rate has to be $\sim 10^{-4}$ erg cm^{-2} s^{-1}, which is an order of magnitude lower than the threshold condition for a multiphase halo. For galactic "superwinds", Heckman (2002) [77] estimated the threshold SFR surface density, which implies an equivalent surface density of energy injection rate, similar to the requirement for multiphase halo. The *mismatch between energy scales* for the aforementioned different outflow observations motivated us to study each of these individual phenomena in detail in chapter 3.

Our analytic estimates of superbubble energetics show that almost 70% of the total input energy is radiated away towards the end of the superbubble evolution, similar to what we obtained in numerical simulations (as discussed earlier, and also in chapter 2). We found a clear demarcation between the two energy input rates : (i) a milder explosion (corresponding Mach number of order 2–3), triggered by the largest OB-association with 10^4 M$_\odot$, can only produce radio-synchrotron halos which requires an energy injection rate of $\sim 10^{-4}$ erg cm^{-2} s^{-1}, whereas (ii) a multiphase halo (and galactic superwinds of Heckman) requires a larger energy input rate of $\sim 10^{-3}$ erg cm^{-2} s^{-1} with an equivalent SFR surface density of $\sim$ 0.1 M$_\odot$ yr^{-1} kpc^{-2}), which can be produced by the spatially and temporally coherent evolution of multiple OB-associations. In this work, we also found that superbubbles do not

accelerate before they reach the vertical heights of a few times the scale-heights, and thus the Rayleigh-Taylor instability (RTI) plays an important role in corrugating superbubble shells only at that height. Before RTI fragments the shell into clumps and channels, thermal instability corrugates the shell and seeds the RTI. These optically thin channels in superbubble shells create pathways for the hydrogen ionizing photons emanating from the central O, B stars in the OB associations to escape.

The effect of superbubble evolution on the escape of Lyc photons is an important aspect that we study in detail. There are various observational and theoretical studies in the literature that estimates the escape fraction ($f_{\rm esc}$). However the *dependence of $f_{\rm esc}$ on the disk parameters* has not been explored and understood. In order to understand the aforementioned connection between $f_{\rm esc}$ and disk parameters, we have studied superbubble evolution using two-dimensional hydrodynamic (ZEUS-MP) simulation with the assumption that the disc is in ionization equilibrium. This problem has been addressed in chapter 4.

We found that ionizing photons do not escape through all solid angles, instead they have a preferred cone angle of $\sim 40^\circ$ at the end of the lifetime of OB stars. $f_{\rm esc}$ initially decreases with time as the superbubble is buried in the disc, and therefore most of the ionizing photons get absorbed by the dense shell, and the disc. After the bubble crosses a few scale-heights, the clumping in the shell due to thermal instabilities and RTI creates optically thin channels (discussed earlier). These "chimneys" help $f_{\rm esc}$ to increase with time at later epochs. The time-averaged, angle-averaged $f_{\rm esc}$, when convolved with the luminosity-function of OB associations gives the averaged $f_{\rm esc}$ from a disk galaxy. We found that this averaged escape fraction is connected to the disk parameters such that $f_{\rm esc}^{\alpha} n_0^2 z_0^3$ is a constant, where $\alpha = 2.2$. We estimated the averaged escape fraction for non-clumpy discs for typical disc parameters to be $\sim 10(\pm 5)\%$, which is roughly constant for all the real discs if the disc temperature is fixed. However, $f_{\rm esc}$ weakly varies with the disk mass and redshift. This value of $f_{\rm esc}$ is sufficient for only stars to reionize the universe at high redshifts.

Apart from $f_{\rm esc}$, the dense superbubble shells in starburst nuclei can be important sites for molecule formation. Several observations (discussed in detail in chapter 5) of starburst nuclei in the local universe show molecular outflows within a central region of $\sim$ 100–200 pc with expansion velocities of a few 10s of km s^{-1} to $\sim$ 100 km s^{-1} and a total molecular mass of $\sim 10^7$–10^8 M$_\odot$. These *striking similarities in masses, radii, and velocities* of molecular outflows have inspired us to study molecule formation and dissociation mechanisms in expanding superbubble shells. We have performed a one-dimensional equilibrium (ionization, thermal, and chemical) calculation to study molecule formation and dissociation in these outflows in chapter 5.

We found that molecules can form in the expanding superbubble shells in the nuclear region of starburst galaxies for a gas surface density of ≥ 2000 M$_\odot$ pc^{-2}. This value of gas surface density implies to a SFR of ≥ 3 M$_\odot$ yr^{-1} within the nucleus region of radius $\sim$ 300 pc, consistent with the observed SFR of the host galaxies of molecular outflows. Our analytic calculation also determines the range of surface density of SFR to be $\simeq 10 \leq \Sigma_{SFR} \leq 50$ M$_\odot$ yr^{-1} kpc^{-2}, for which molecule formation is favoured. This range of SFR surface density is consistent with observations. If $\Sigma_{SFR} \geq 50$ M$_\odot$ yr^{-1} kpc^{-2}, then the SFR would be higher, and thus the ionizing and dissociating photon luminosities would also be higher. The higher ionizing photon luminosity would increase the ionizing radius, and therefore molecules would form at a larger radius and at a later epoch. The higher luminosity of dissociating photons and low density at large radii would resist the *in-situ* molecule formation. We also explained the observed parameters (mass, size, and expansion velocity) in the expanding, dense superbubble shells in central regions of starburst galaxies via *in-situ* molecule formation and dissociation mechanisms.

6.2 Future directions

We have so far summarised the brief motivations and important results of the thesis. Some aspects of superbubble evolution can be studied further.

While discussing "molecular outflows" in starburst nuclei in chapter 5, we briefly mentioned the evolutionary scenario of molecules (molecule-atom-ion). However, a more detailed study is required to understand : (i) whether the molecules dissociate at larger radii, and give rise to atomic outflows, (ii) what is the transition radius for molecular outflows to become atomic, and (iii) the metallicity environment in which one might expect to observe molecules. In order to answer these questions, one needs to perform detailed numerical hydrodynamic simulations with high resolution (almost a tenth of a pc) with a more realistic supernova feedback model, magnetic fields, turbulent interstellar medium (ISM), and accurate cooling tracing the metals in the post shock dense material. In order to get a complete picture of the effect of clumping on molecule formation (as clumps are the denser regions where molecule formation is more probable) and dissociation (as turbulence might prevent molecule formation), one needs to perform two-dimensional simulations in a clumpy ISM. The realistic model should also cover a wide range of length-scales starting from a few 10s of pc to a few kpc to follow the entire evolutionary track of molecule-atom-ion conversion.

The evolution of $f_{\rm esc}$ at high redshifts is another important and interesting aspect to study in detail. At high redshifts (z), the ISM is more clumpy than the ISM at $z = 0$ as shown in figure 4.13 in chapter 4. Also at high redshifts, the dense superbubble shells will be optically thick, and thus one can not perform the ionization equilibrium calculation to determine $f_{\rm esc}$. In the calculation of $f_{\rm esc}$ in chapter 4, SFR is kept constant although we varied the column densities of galactic disks, and this is a caveat in our model. However for a realistic estimation of $f_{\rm esc}$, the SFR should be varied with the column density following the Kennicutt-Schmidt law. Therefore to determine $f_{\rm esc}$ at high redshifts, one needs to perform radiation transfer calculation

with the realistic size and mass distributions of the clumps, and with realistic star-formation rates. The model should also include an effective SNe feedback prescription at high redshifts. It is also interesting to estimate the AGN-contribution to $f_{\rm esc}$, as compared to the stellar contribution.

There are also various other aspects of outflows which are not yet completely understood, such as : (i) the creation and existence of multi-phase halos, (ii) the metal enrichment of the IGM, and metallicity mixing in the ISM via superbubbles. These problems require large scale simulations upto few 10s of kpc away from the disks, tracing metals to evaluate accurate cooling as mentioned earlier and superbubble evolution till few 100s of Myr (longer than the life-time of OB-associations) after the driving sources (wind + SNe) vanish within a few 10s of Myr.

Appendix A

Escape fraction

A.1 Convergence test

We compare the resolutions of 256×128, 512×256, and 512×512 for the time and angle dependence of the escape fraction. In Figure A.1 the upper panel shows the time dependence of the θ-averaged escape fraction. Both the subplots are for $n_0 = 0.5$ cm^{-3}, $z_0 = 300$ pc and $N_O = 1000$. We notice that initially the escape fraction with low resolution is slightly higher than with high resolutions. However, after 2-3 $t_{\rm d}$ ($t_{\rm d} = 2$ Myr), the escape fraction for all resolutions are similar.

The bottom panel of Figure A.1 shows the angular dependence of the escape fraction for the three resolutions at 4 Myr for the same parameters, after the shell fragments due to RTI. One can see the zigzag nature in the high resolution curve, whereas the low resolution curve is comparatively smooth. At higher resolutions, there are more high density clumps and it results in absorption over many angles.

In Figure A.2, we show the time dependence of the escape fraction for 256×128, 512×256 and 512×512 resolution runs for $n_0 = 15$ cm^{-3}, $z_0 = 30$ pc, and for two different N_O. The upper and lower panels represent the cases for $N_O = 300$ and $N_O = 10^5$ respectively. The density considered is high, and consequently there is more clumping at $t < t_d$ for higher resolution. This leads to a high escape fraction in

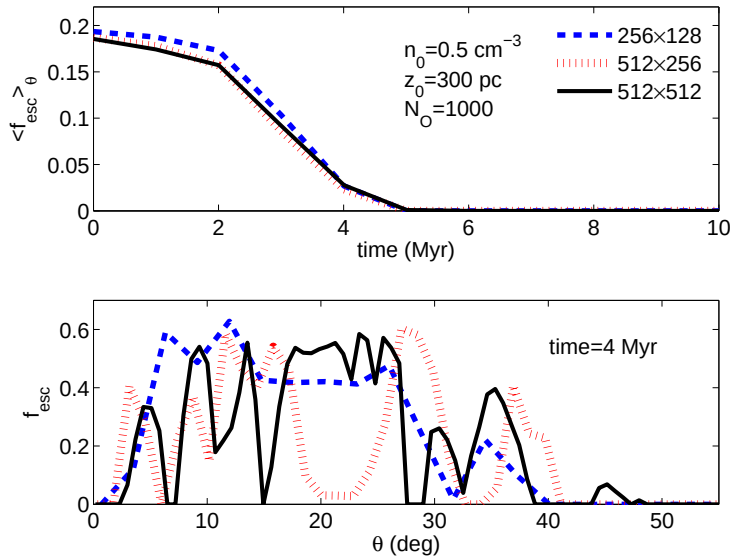

Figure A.1: Comparison between the resolutions of 256×128, 512×256 and 512×512 for the angle and time dependence of the escape fraction for $n_0 = 0.5$ cm^{-3}, $z_0 = 300$ pc, $N_O = 1000$. The upper panel shows the time dependence and the bottom panel represents the angle dependence at 4 Myr, when the fragmentation of the shell becomes important due to RTI. All $\langle f_{esc} \rangle_\theta$ values in the top panel are zero after 5 Myr.

high resolutions than that in the low resolution case initially. After the superbubble crosses 2–3 scale heights, the different resolution cases start behaving differently due to the different widths of the clumps and channels in them. The bottom panel shows the time dependence of the escape fraction for the same n_0 and z_0 but for $N_O = 10^5$. One can notice that the escape fraction at any epoch for all the resolutions are roughly the same and the small changes arise from the detailed structure of the shell at a given epoch.

In Figure A.1, the time-averaged and θ-averaged escape fraction for the resolutions of 256×128, 512×256 and 512×512 are 0.1392, 0.1274 and 0.1278 respectively. The percentage change in escape fractions is thus $\leq$ 8%. One can also easily notice that at both the high resolution (512×256 and 512×512) cases the percentage difference of escape fraction is 0.3%. In our simulations N_O ranges from 100 [235] to 10^5 ([85, 127, 220]) and z_0 ranges from 10 pc to 600 pc. The maximum difference in the average escape fraction between low (256×128) and high resolutions (512×256 and 512×512) for the whole range of N_O and z_0 used in our simulations for the low n_0 ($n_0 < 5$ cm^{-3}) runs is $\approx$ 10%.

In Figure A.2 we notice that for low N_O ($N_O = 300$), the average escape fraction for three resolutions (256×128, 512×256 and 512×512) are 0.023, 0.07 and 0.05 respectively. Thus the percentage change in average escape fraction is 68% between resolutions of 256×128 and 512×256 but it is 28% between 512×256 and 512×512. For high N_O case the average escape fraction for low and high resolutions are 0.4165, 0.4243 and 0.4060 respectively, giving a maximum percentage change in escape fraction of $\sim$ 4%. We also find that the difference in the average escape fraction between resolutions of 256×128 and 512×256 for large n_0 (5 cm$^{-3} \leq n_0 <$ 50 cm^{-3}) cases comes within 10% for $N_O \geq 1000$ for all the values of z_0. The high density simulations with $n_0 = 50$ cm^{-3} are numerically very expensive and we have to use a relatively low resolution (256×128) for these runs.

Table 4.1 shows the resolution for our different runs using different n_0, z_0 and N_O.

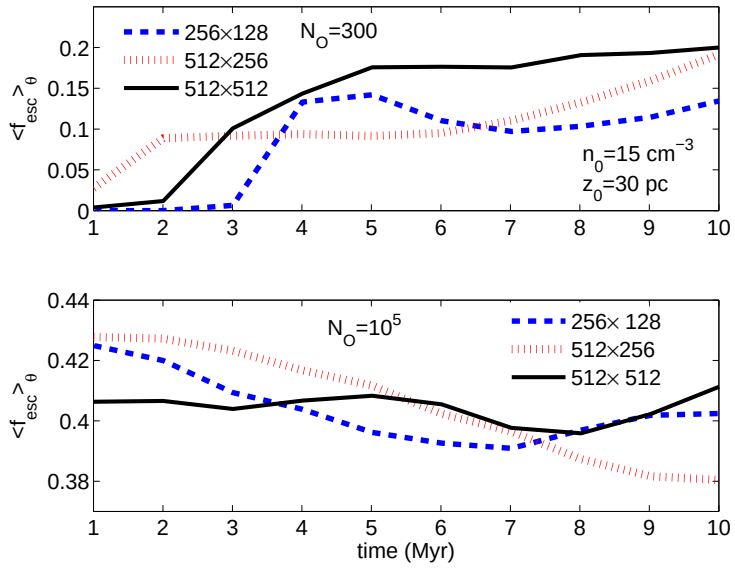

Figure A.2: Comparison between low and high N_O ($N_O = 300$, 10^5 respectively) cases for the resolutions of 256×128, 512×256 and 512×512 for the time dependence of escape fraction for $n_0 = 15$ cm^{-3}, $z_0 = 30$ pc.

We have chosen a high enough resolution in each case such that the time- and angle-average escape fraction does not change by more than 20% for a higher resolution run.

A.2 Convolution of escape fraction with OB-association

It is of interest to estimate the value of N_O that dominates the process of averaging $f_{\rm esc}$ over the luminosity function of OB associations. In eqn 4.17 we have convolved time-averaged and θ-averaged escape fraction with the luminosity function of OB-association. On one hand the luminosity function scales as N_O^{-2}, on the other hand $f_{\rm esc}$ increases with the number of OB stars. Therefore the integrand (of the numerator) in eqn 4.17 peaks at a certain value of N_O.

Figure A.3 plots the integrand as a function of N_O for $n_0 = 1.5$ cm^{-3} for two different z_0 (60 pc (the black solid line), 300 pc (the red dashed-dotted line)) and

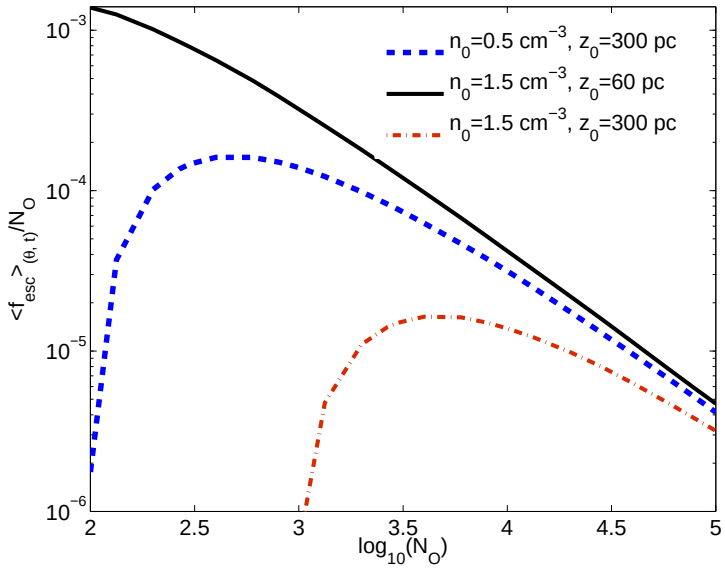

Figure A.3: The integrand of the numerator of eqn 4.17 as a function of N_O for different n_0 and z_0. The blue dashed line represents $n_0 = 0.5$ cm^{-3}, $z_0 = 300$ pc; the black solid line and the red dashed-dotted lines represent $n_0 = 1.5$ cm^{-3} cases ($z_0 = 60$ and 300 pc respectively).

$n_0 = 0.5$ cm^{-3}, $z_0 = 300$ pc (the blue dashed line). For $n_0 = 1.5$ cm^{-3} and for large scale heights (300 pc), the escape fraction decreases to zero for small N_O (≤ 1000) and thus the integrand peaks at higher value of N_O ($N_O = 4000$). The integrand decreases with N_O for small z_0 ($z_0 = 60$ pc) in the case of $n_0 = 1.5$ cm^{-3}. Thus for the small scale heights, the averaging process is dominated by the lowest value of N_O ($N_O = 100$). In general, the average escape fraction is dominated by larger N_O for higher n_0 and z_0.

A.3 Comparison between 2D and 3D numerical simulations

In this section we show the angle and time variation of the escape fraction for 2D (256×128) and 3D ($256 \times 128 \times 32$) simulations for the fiducial case ($n_0 = 0.5$ cm^{-3},

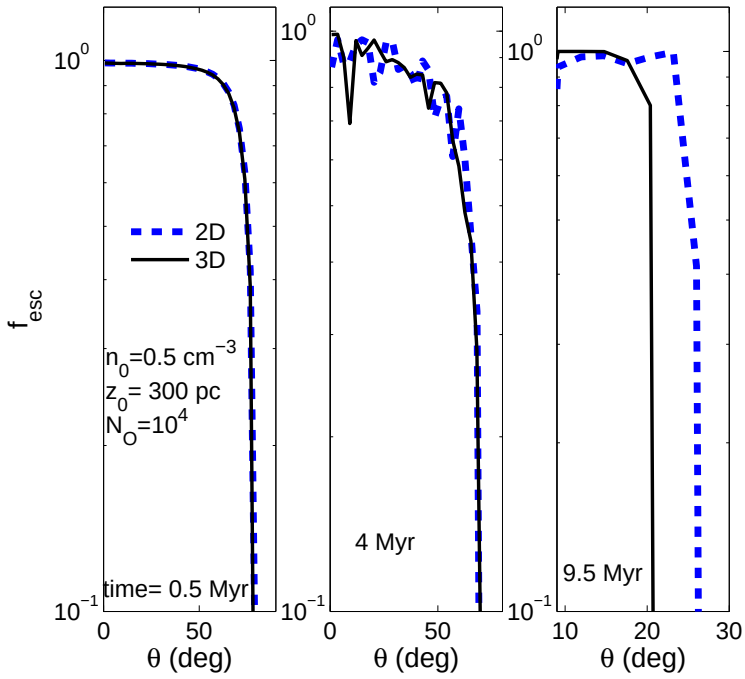

Figure A.4: The comparison of angular variation of the escape fraction between 2D and 3D numerical runs. The blue-dashed and black solid lines represent the 2D and 3D runs respectively. The plot is for the fiducial case ($n_0 = 0.5$ cm^{-3}, $z_0 = 300$ pc, $N_O = 10^4$).

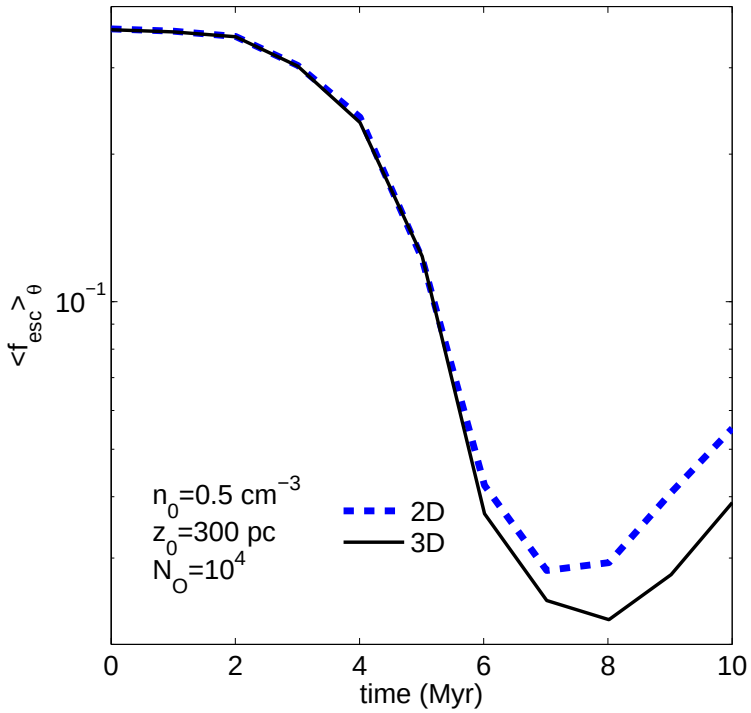

Figure A.5: The comparison of time variation of the escape fraction between 2D and 3D numerical runs. The blue-dashed and black solid lines represent the 2D and 3D runs respectively. This plot is also for the fiducial case ($n_0 = 0.5$ cm^{-3}, $z_0 = 300$ pc, $N_O = 10^4$).

$z_0 = 300$ pc, $N_O = 10^4$). In 3D simulation we have uniformly spaced grid points in the ϕ-direction.

Figure A.4 shows the angular variation of the escape fraction for the 2D and 3D runs at three different times. The angular variation of the escape fraction in 2D and 3D matches at early times (0.5 Myr). At a later epoch (4.0 Myr), when RTI starts playing a crucial role for the detailed structure of the shell, the angular variations show some differences. The differences are small enough to have a negligible effect on the final $< f_{esc} >_\theta$ (refer to the figure A.5). At very late times the escape cone is slightly larger in 2D compared to 3D, which makes $< f_{esc} >_\theta$ a bit higher in 2D. The time-averaged theta-averaged escape fraction in 2D and 3D (0.315 and 0.3137, respectively) are very similar. Thus, the use of the faster 2D simulations to calculate the escape fraction is justified.

Appendix B

Molecular Outflow

B.1 Numerical Setup

In this section, we describe our simulation set up. Our simulation set up is similar to the ones described in chapter 4 except a few following differences,

- We extend the cooling function below 10^4 K for molecular cooling for an electron fraction ($x_e = n_e/n_H$) of $\sim 10^{-3}$, guided by the observed ionization fraction for CNM (cold neutral medium), $\sim 10^{-3}$–10^{-4}[48]. The cooling function is also independent of x_e, for $10^{-4} < x_e < 10^{-2}$, between 10 K to 10^4 K. We have assumed the initial isothermal ambient medium temperature to be 10 K.

- We use the exponential density stratification ($n = n_0 \exp(-|z|/z_0)$, where n_0, and z_0 are the mid-plane density, and the scale-height of the disc respectively) for the ambient ISM gas.

- We implement continuous mechanical luminosity till the life-time of OB association (10 Myr), $\mathcal{L} = 10^{37} N_{OB}$ erg s^{-1} (mechanical luminosities from stellar winds and supernova explosions) as obtained from Starburst99.

- In the r–direction, we use 512 grid points to calculate the evolution of superbubble shell. We show that the time evolution of superbubble shell position is

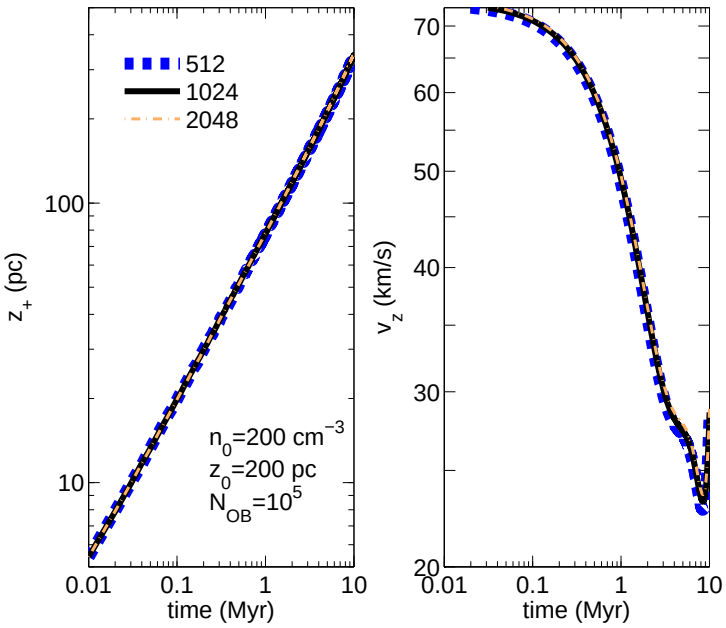

Figure B.1: The time evolution of superbubble shell position and velocity for $n_0 = 200$ cm^{-3}, $z_0 = 200$ pc, and for $N_{OB} = 10^5$. The left panel shows the shell position, and the right panel represents the shell velocity. The blue-dashed, the black-solid, and the light brown dashed-dotted lines are for 512, 1024, 2048 grid points respectively.

similar for different resolutions with a maximum percentage change of 10% (see B.2). We also show that the velocity evolution for different resolutions are also similar (B.2). We adopt $n_0 = 200$ cm^{-3}, and $z_0 = 200$ pc to be the fiducial case.

B.2 Convergence test of superbubble shell position & velocity

We show the time evolution of the shell position and velocity for three resolutions (512, 1024, 2048 grid points), and for $n_0 = 200$ cm^{-3}, $z_0 = 200$ pc, $N_{OB} = 10^5$. The left panel shows the time evolution of the shell position, and the right panel represents the shell velocity.

One can notice that superbubble shell positions for the three resolution are comparable. The low resolution runs (512, 1024 grid points) show a similar evolution, whereas the high resolution case (2048 grid points) varies slightly from the low resolution cases with a maximum percentage change being of order $\sim 10\%$. One can also notice that the velocity evolutions show similar results as in the case of the evolution of the shell positions (showing that the low resolution runs are similar, and a maximum percentage change of 10% for the case of 2048 grid points). Therefore, we run all our numerical simulation with 512 grid points with an error of ~ 10 % in both the cases of the shell position, and velocity evolution.

B.3 Density jump in the superbubble shell

Since the formation of molecules takes place in the cool/dense shell (region *iii*), it is important to estimate its density. Let $(\rho_1,\ u_1)$ and $\rho_3,\ u_3$ be the density and velocity of the ISM (region *i*) and the shell (region *iii*), respectively, in the shock rest frame. The conservation of mass, momentum, and magnetic flux gives

$$\rho_1 u_1 = \rho_3 u_3; \tag{B.1}$$

$$\rho_1 u_1^2 + p_1 + p_{\rm mag,1} = \rho_3 u_3^2 + p_3 + p_{\rm mag,3}; \tag{B.2}$$

$$B_1 u_1 = B_3 u_3; \tag{B.3}$$

where $p_{1,3}$ ($p_{\rm mag1,3} \equiv B_{1,3}^2/[8\pi]$) is the gas (magnetic) pressure in region *i,iii*, and $B_{1,3}$ is the field strength in region *i,iii*. We assume the field lines to be in the shock-plane (this component is important in preventing the shell to be compressed to very high densities). All the cooling is concentrated in region *ii*, and the temperatures T_1 and T_3 correspond to the stable thermal equilibrium temperatures in regions *i* and *iii* (this replaces the energy equation, required to solve for downstream quantities in region *iii*; see Fig. 5 in [**?**]). Lets define the compression ratio $r = \rho_3/\rho_1 = u_1/u_3 = B_3/B_1$.

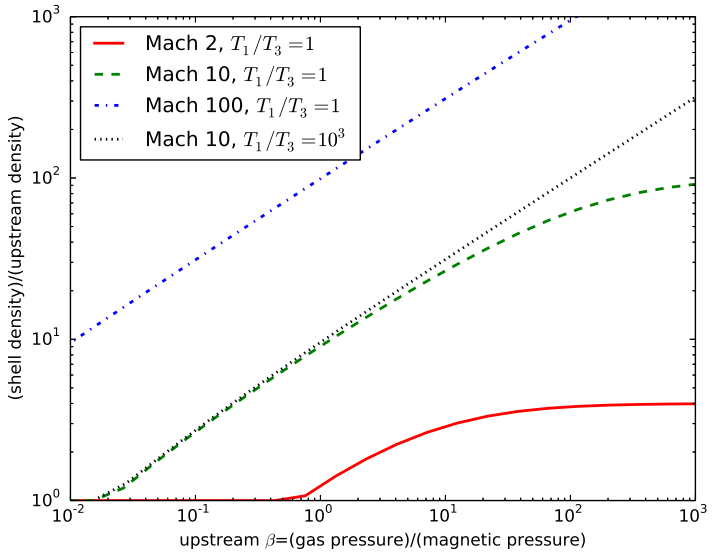

Figure B.2: Compression factor (numerical solution of Eq. B.4) as a function of upstream β_1 for various values of the upstream Mach number. The influence of the ratio of the temperatures in regions *1* and *iii* is small in the relevant β_1 regime.

Then, Eqs. B.1-B.3, and the temperature information gives,

$$\frac{r^3}{\beta_1} + \left(\frac{c_3}{c_1}\right)^2 r^2 - \left(1 + \mathcal{M}_1^2 + \frac{1}{\beta_1}\right) r + \mathcal{M}_1^2 = 0, \tag{B.4}$$

where $c_{1,3}^2 \equiv \gamma_{1,3} k_B T_{1,3}/(\mu_{1,3} m_p)$ is the sound speed, $\mathcal{M}_1 \equiv u_1/c_1$ is the upstream Mach number, and $\beta_1 \equiv 8\pi p_1/B_1^2$ is the upstream plasma β. Eq. B.4 can be solved numerically for various parameters (β_1, $\mathcal{M}_1$, c_3/c_1).

Figure B.2 shows the compression factor as a function of a reasonable range in upstream plasma β for three different Mach numbers, assuming the same temperature in regions *i* and *iii* ($c_1 = c_3$). As expected, the compression factor is larger for a higher Mach number. The compression factors with a reasonable upstream magnetic field $\beta \sim 1$ is much smaller than the hydrodynamic limit ($r \sim \mathcal{M}_1^2$ as $\beta \to \infty$). A reasonable value for ρ_3/ρ_1 for typical ISM β is in the range few to 100 (see also [182]).

B.4 Heating and cooling in the shell

The dominant heating process in the molecular region of the shell is photoelectric (PE) heating. We use the PE heating rate given by [227], in which they take into account the electron-PAH collisions by the term ϕ_{PAH} (which takes into account the fraction of PAH). At a given density, the heating rate depends on the electron abundance, the diffuse incident UV radiation, temperature of the medium, and ϕ_{PAH}. Therefore, the heating rate per unit volume is given by,

$$n\Gamma_{pe} = 1.3 \times 10^{-24} n\epsilon G_{FUV} \,\mathrm{ergs\,cm^{-3}\,s^{-1}}\,, \tag{B.5}$$

where n is the density of the hydrogen nucleus, G_{FUV} is the incident UV radiation field with the dust-extinction (see equation B.7) in terms of the Habing radiation, and ϵ is the heating efficiency given by,

$$\begin{aligned}\epsilon &= \frac{4.9 \times 10^{-2}}{1 + 4.0 \times 10^{-3}(G_{FUV}T^{1/2}/n_e\phi_{PAH})^{0.73}} \\ &\quad + \frac{3.7 \times 10^{-2}(T/10^4)^{0.7}}{1 + 2.0 \times 10^{-4}(G_{FUV}T^{1/2}/n_e\phi_{PAH})}\,,\end{aligned} \tag{B.6}$$

[47], where T is temperature of the medium, n_e is the electron density. The heating rate weakly depends on ϕ_{PAH} value varying from 0.25 to 1 [227]. In our calculation, we have assumed the value of $\phi_{PAH} \sim 0.5$.

We assume a central OB association at the centre of the galactic disk. We use the Starburst99 code to calculate the FUV (5.4–13.6eV) photon luminosity (S_{FUV}) (see figure 5.3 in section 5.3) to obtain G_{FUV} as a function of z_+ as,

$$\begin{aligned}G_{FUV}(z_+) &= \frac{\left(S_{FUV}\exp(-\tau_{FUV})/4\pi z_+^2\right)}{\left(4 \times 10^{-14} c/h\nu_{1000A^\circ}\right)} \\ &= \frac{(S_{FUV}\exp(-\tau_{FUV})/4\pi z_+^2)}{6 \times 10^7}\,,\end{aligned} \tag{B.7}$$

where c is the speed of light, $\tau_{FUV}(= \sigma_d A_v(\mathrm{mol}) \times 1.87 \times 10^{21})$ is the optical depth of the shell for the FUV photons for the dust extinction cross-section of σ_d. We have considered σ_d at 1000Åto be $\sim 6 \times 10^{-22}$ cm^2 for dense clouds with reddening

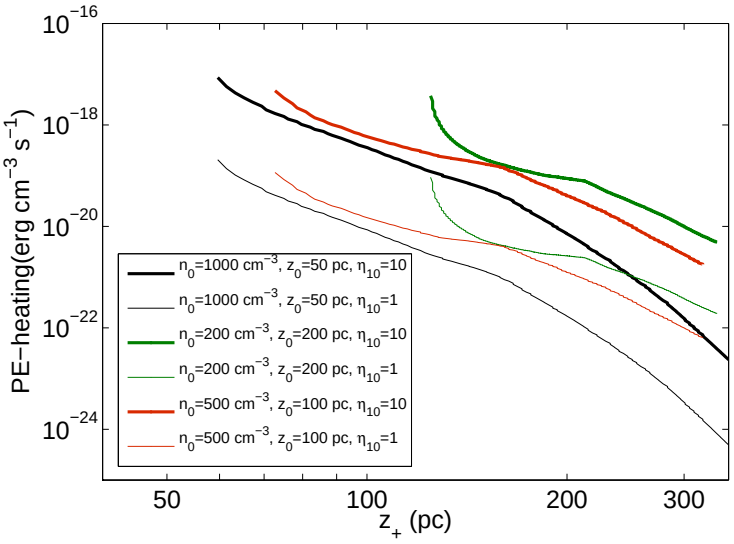

Figure B.3: The time evolution of the heating rate in superbubble shell at the time when its uppermost position is z_+ , for three different n_0, z_0 cases ($n_0 = 1000$ cm^{-3}, $z_0 = 50$ pc; $n_0 = 200$ cm^{-3}, $z_0 = 200$ pc, and $n_0 = 500$ cm^{-3}, $z_0 = 100$ pc), for two η_{10} cases and for $N_{OB} = 10^5$. The thick, and thin solid lines correspond to $\eta_{10} = 10$, 1 respectively. The black, green, and the red lines represent $n_0 = 1000$ cm^{-3}, $z_0 = 50$ pc; $n_0 = 200$ cm^{-3}, $z_0 = 200$ pc, and $n_0 = 500$ cm^{-3}, $z_0 = 100$ pc cases respectively.

parameter of $R_v = 5.5$ [46]. We have used the fact that Habing field has an energy density of 4×10^{-14} erg cm^{-3} at 1000 A° [46].

We show the PE heating in Figure B.3 for the two fiducial cases. We calculate the PE-heating rate once the shell crosses the Strömgren sphere radius for all the three combinations of n_0, z_0. We notice that PE-heating depends on electron density, and FUV luminosity, and the equilibrium shell temperature. On the other hand, the electron density depends on the shell density and temperature (as recombination is temperature dependant) which in turn is determined by the heating (PE-heating) and cooling balance. Thus one needs to solve the equations of ionization and thermal equilibrium simultaneously to obtain n_e, and T_{shell}, and to understand their effect on PE-heating rate. The electron density (n_e) has a strong dependence on the shell density, thus n_e decreases as the shell density decreases. Therefore, the PE-heating rate also drops initially. In all these three n_0– z_0 combinations the shell radius reaches at $\sim$ 200 pc in 2–3 Myr, when the FUV photon luminosity starts dropping drastically, and thus we notice kinks in the curves of PE-heating rates at $\sim$ 200 pc, and PE-heating rate drops after 200 pc due to the drop in S_{FUV}.

We use the same cooling function as in our simulation for the dynamics of the superbubbles, the details of which are described in §B.1.

B.5 Density and temperature in the dense shell

The heating and cooling time scales in the shell are shorter than the dynamical time scale (z_+/t) at all times. Thus one can assume thermal equilibrium to calculate the shell temperature.

First we show the ionization fraction, total gas density and electron density in the shell in Figure B.4. The nature of the curve for n_e mimics that of the curve for the total shell density, n_{sh}, albeit with small differences which show clearly in the plot for x_e, the ionization fraction. Here again there are kinks in the curves at $\sim$ 200 pc,

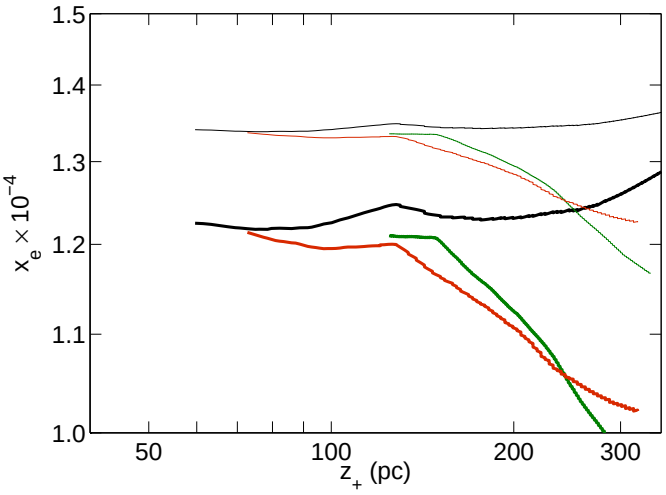

Figure B.4: The evolution of the ionisation fraction as a function of the vertical height of the superbubble. All the line styles, and line-colours representing different n_0, z_0, and η_{10} are mentioned in the caption of figure B.3.

and they arise because of the change in the FUV luminosity as mentioned earlier.

Next we show the equilibrium shell temperature as a function of the position of the shell in Figure B.5, for three different combinations of n_0, z_0 and for $N_{OB} = 10^5$. In the case of larger scale height (200 pc), the shell temperature initially is $\sim$ 10–20 K, and it falls to $\sim$ 10 K at larger radii. This is owing to the high density in the shell, and consequently, greater cooling. In the case of smaller scale height, the low density at large heights, the ionization fraction increases and so does PE heating, and thus the shell temperature increases with radius. Again, kinks arise due to the nature of FUV luminosity evolution.

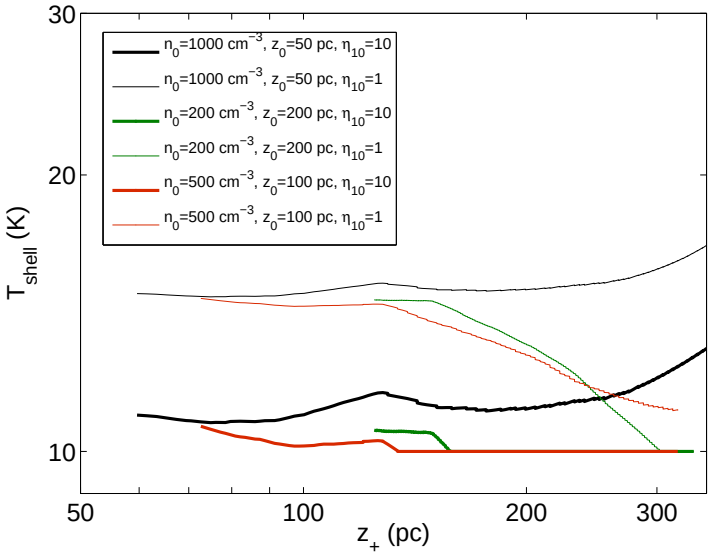

Figure B.5: The equilibrium temperature of the shell is plotted as a function of the shell-radius for three difefrent n_0, z_0 cases for $N_{OB} = 10^5$, and for $\eta_{10} = 1$, 10.

Bibliography

[1] Adelberger, K. L., Steidel, C. C. 2000, ApJ, 544, 218

[2] Agertz, O., Teyssier, R., & Moore, B. 2011, MNRAS, 410, 1391

[3] Altay, G., Theuns, T., Schaye, J., Vrighton, N. H. M., Dalla Vecchia, C. 2011, ApJ, 737, L37

[4] Alton, P. B., Davies, J. I., & Bianchi, S., 1999, A&A, 343, 51

[5] Bagetakos, I., Brinks, E., Walter, F., de Blok, W. J. G., Usero, A., Leroy, A. K., Rich, J. W., Kennicutt, Jr. R. C., 2010, arXiv:1008.1845v1

[6] Barkana, R., Loeb, A. 2001, Phys. Rep., 349, 125

[7] Basu, S., Johnstone, D., Martin, P. G., 1999, ApJ, 516, 843

[8] Benson, A., Venkatesan, A. Shull, J. M. 2013, ApJ, 770, 76

[9] Bisnovatyi-Kogan, G. S., Silich, S. A. 1995, Rev Mod Phys, 67, 661

[10] Bland-Hawthorn, J., Maloney, P. R. 1999, ApJL, 510, 33

[11] Bland-Hawthorn, J., Cohen, M., 2003, ApJ, 582, 246

[12] Bohlin, R. C., Savage, B. D., Drake, J. F., 1978, ApJ, 224, 132

[13] Bolatto, A. D. et al. 2013, Nature, 499, 450

[14] Bolatto, A. D., Wolfire, M., Leroy, A. K., 2013, Annu. Rev. Astron Astrophys., 51, 207

[15] Boomsma, R., Oosterloo, T. A., Fraternali, F., van der Hulst, J. M., Sancisi, R., 2005, A&A, 431, 65

[16] Boomsma, R., Oosterloo, T. A., Fraternali, F., van der Hulst, J. M., Sancisi, R., 2008, A&A, 490, 555

[17] Borthakur, S., Heckman, T. M., Leitherer, C., Overzier, R. A. 2014, Science, 346, 216

[18] Bregman, J. N., 1980, ApJ, 236, 577

[19] Brinks, E., Bajaja, E., 1986, A&A, 169, 14

[20] Cecil, G., Bland-Hawthorn, J., Veilleux, S. 2002, ApJ, 576, 745

[21] Cecil, G., Bland-Hawthorn, J., Veilleux, S., Filippenko, A. V. 2001, ApJ, 555, 338

[22] Cen, R. 2012, ApJ, 748, 121

[23] Chevalier, R. 1974, MNRAS, 169, 229

[24] Chevalier, R. 1977, Ann. Rev. Astr. Astr., 15, 175

[25] Chevalier, R. A. & Clegg, A. W. 1985, Nature, 317, 44

[26] Chevalier, R. A. & Blondin, J. M. 1995, ApJ, 444, 312

[27] Chiosi, C., Nasi, E., Sreenivasan, S. P. 1978, Astr. Ap., 63, 103

[28] Clarke, C., Oey, M. S. 2002, MNRAS, 337, 1299

[29] Conselice, C. 2014, ARAA

[30] Cooke, J., Ryan-Weber, E. V., Garel, T., Díaz, C. G. 2014, MNRAS, 441, 837

[31] Cooke, R. J., Pettini, M., Jorgenson, R. A., 2015, ApJ, 800, 12

[32] Cooper, J. L., Bicknell, G. V., Sutherland, R. S., & Bland-Hawthorn, J. 2008, ApJ, 674, 157

[33] Cox, D. P. 1972, ApJ, 178, 159

[34] Cox, D. P. 1974, ApJL, 189, 105

[35] Cox, D. P. 2005, Ann. Rev. Astr. Astr., 43, 337

[36] Creasey P., Theuns, T., Bower, R. G., & Lacey, C. G. 2011, MNRAS, 415, 3706

[37] Creasey, P., Theuns, T., & Bower, R. G. 2013, MNRAS, 429, 1922

[38] Dale, J. E., Ngoumou, J., Ercolano, B., Bonnel, I. A., 2014, MNRAS, 442, 694

[39] Dalla Vecchia, C. & Schaye, J. 2012, MNRAS, 426, 1401

[40] Dahlem, M., Lisenfeld, U., Golla, G. , 1995, ApJ, 444, 119

[41] Dalcanton, J., Yoachim, P., Bernstein, R. 2004, ApJ, 608, 189

[42] de Avillez, M. A., Breitscshwerdt, D. 2005, A&A, 436, 585

[43] Dickey, J. M., Lockman, F. J. 1990, ARAA, 28, 215

[44] Dove, J. B., Shull, J. M. 1994, ApJ, 430, 222

[45] Dove, J. B., Shull, J. M., Ferrara, A. 2000, ApJ, 531, 846

[46] Draine, B. T., Bertoldi, F., 1996, ApJ, 468, 269

[47] Draine, B. T., 2011a, ApJ, 732, 100

[48] Draine, B. T., 2011b, Physics of the Interstellar and Intergalactic Medium, Princeton University Press

[49] Dubois, Y., Teyssier, R. 2008, A&A, 477, 79

[50] Dyson, J. E., Williams, D. A. 1997, The Physics of the Interstellar Medium, Second Edition

[51] Ehlerová, S., Palouš, J., 2005, A&A, 437, 101

[52] Erkal, D., Gnedin, N. Y. , Kravtsov, A. V. 2012, ApJ, 761, 54

[53] Fenech, D., et al., 2010, MNRAS, 408, 607

[54] Fernandez, E. R., Shull, J. M. 2011, ApJ, 731, 20

[55] Ferrara, A., Loeb, A. 2013, MNRAS, 431, 2826

[56] Ferrara, A., Tolstoy, E. 2000, MNRAS, 313, 291

[57] Freyer, T., Hensler, G. & Yorker, H. W., 2003, ApJ., 594, 888

[58] Fujita, A., Martin, C., MacLow, M., Abel, T. 2003, ApJ, 599, 50

[59] Fumagalli, M., Prochaska, J. X., Kasen, D., Dekel, A., Ceverino, D., Primack, J. R. 2011, MNRAS, 418, 1796

[60] Gaensler, B. M., Madsen, G. J., Chatterjee, S., Mao, S. A. 2008, PASA, 25, 184

[61] García, J., Elhoussieny, E. E., Bautista, M. A., Kallman, T. R., 2013, ApJ, 775, 8

[62] Geach, J. E., Hickox, R. C., Diamond-Stanic, A. M., Krips, M., Rudnick, G. H., Tremonti, C. A., Sell, P. H., Coil, A. L., Moustakas, J., 2014, Nature, 516, 68

[63] Gerritsen, J. P. E. 1997, PhD Thesis, University of Groningen

[64] Girichidis, P. et al. 2016, MNRAS, 456, 3432

[65] Gnedin, N. Y. 1998, MNRAS, 297, 407

[66] Gnedin, N. 2000, ApJ, 535, 530

[67] Gnedin, N. Y., Kravtsov, A. V., Chen, H.-W. 2008, ApJ, 672, 765

[68] Gould, R. J., Salpeter, E. E., 1963, ApJ, 138, 393

[69] Guedes, J., Callegari, S., Madau, P., & Mayer, L. 2011, 742, 76

[70] Gupta, S., Nath, B. B., Sharma, P., Shchekinov, Y. 2016, arxiv: 1606.09127

[71] Haardt, F., Madau, P. 2012, ApJ, 746, 125

[72] Haehnelt, M. G., Madau, P., Kudritzki, R., Haardt, F. 2001, ApJ, 549, 151

[73] Hayes, J. C., Norman, M. L., Fiedler, R. A., Bordner, J. O., Li, P. S., Clark, S. E., ud-Doula, A., Mac Low, M-M 2006, ApJS, 165, 188

[74] Heckman, T., Sembach, K., Meurer, G., Leithere, C., Calzetti, D., Martin, C. 2001, ApJ, 558, 56

[75] Heckman, T. M., Lehnert, M. D., Strickland, D. K., Armus, L. 2000, ApJ, 129, 493

[76] Heckman, T., Borthakur, S., Overzier, R. et al. 2011, ApJ, 730, 5

[77] Heckman, T. M. 2002, in ASP Conf. Ser. 254, Extragalactic Gas at Low Redshift, ed. L. S. Mulchaey & J. Stocke (San Fransisco, CA: ASP), 292

[78] Heckman, T. M., Alexandroff, R. M., Borthakur, S., Overzier, R., Leitherer, C. 2015, ApJ, 809, 147

[79] Heckman, T. M., Armus, L., George, K. M. 1990, ApJS, 74, 833

[80] Heiles, C. 1990, ApJ, 354, 483

[81] Heiles, C. 1979, ApJ, 229, 533

[82] Heiles, C. 1984, ApJS, 55, 585

[83] Martín-Hernández, N. L., Schaerer, D., Sauvage, M. 2005, A&A, 429, 449

[84] Hirashita, H., Ferrara, A. 2005, MNRAS, 356, 1529

[85] Ho, P. 1997, Rev. Mex AA Conference Ser., 6, 5

[86] Hollenbach, D., McKee, C. F. 1979, ApJS, 41, 555

[87] Hollenbach, D., Tielens, A. G. G. M. 1997, ARAA, 35, 197

[88] Hopkins, P. F., Quataert, E., & Murray, N. 2011, MNRAS, 417, 950

[89] Hopkins, P. F., Quataert, E., & Murray, N. 2012, MNRAS, 421, 3522

[90] Hu, E. M., 1981, ApJ, 248, 119

[91] Hurwitz, M., Jelinsky, P., Dixon, W. V. 1997, ApJ, 481, L31

[92] Hutter, A., Dayal, P., Partl, A. M., Müller, V. 2014, MNRAS, 441, 2861

[93] Inoue, A. K., Iwata, I., Deharveng, J.-M., 2006, MNRAS, 371, L1

[94] Jenkins, E. B., Meloy, D. A. 1974, ApJ, 193, L121

[95] Joung, M. K. R. & Mac Low, M. 2006, ApJ, 653, 1266

[96] Kahn, F. D. 1998, in "Lecture Notes in Physics, vol.506: The Local Bubble and Beyond. Lyman-Spitzer Colloquium", Proceedings of the IAU Colluquium No. 166, eds. D. Breitschwerdt, M. J. Freyberg, J.Truemper (Springer-Verlag: Berlin), p. 483

[97] Kamphuis, J., Sancisi, R., 1993, Astron. Astrophys., 273, L31

[98] Kanekar, N., Braun, R., Roy, N. 2011, ApJ, 737, L33

[99] Kanekar, N., Prochaska, J. X., Smette, A. et al. 2014, MNRAS, 438, 2131

[100] Katz, N. 1992, 391, 502

[101] Kay, S. T., Pearce, F. R., Frenk, C. S., & Jenkins, A. 2002, MNRAS, 330, 113

[102] Kennicutt, R, C. Jr. 1998, ApJ, 498, 541

[103] Kennicutt, Jr. R. C., Edgar, B. K., Hodge, P. W., 1989, ApJ, 337, 761

[104] Kim, S., et al. , 1999, AJ, 118, 2797

[105] Kimm, T. & Cen, R. 2014, ApJ, 788, 121

[106] Kollmeier, J. A., Weinberg, D. H., Oppenheimer, B. D. et al. 2014, ApJL, 789, L32

[107] Kompaneets, A. S. 1960, Soviet Phys Dokl., 5. 46

[108] Koo, B-C., McKee, C. F. 1992, ApJ, 388, 93

[109] Korolev, V., Vasiliev E. O., Kovalenko, I. G., Shchekinov, Yu. A., 2015, ARep, 59, 690

[110] Kovalenko, I. G., Shchekinov, Y. A. 1985, Astrophysics, 23, 578

[111] Kovalenko, I.G., Shchekinov, Y. A., 1985, Astrophysics, 23, 578

[112] Koyama, H. & Inutsuka, S. 2004, ApJ, 602, L25

[113] Larsen, S. S. 1999, A&A Supp. Ser., 139, 393

[114] Leisawitz, D., Bash, F. N., & Thaddeus, P. 1989, ApJS, 70, 731

[115] Leitet, E., Bergvall, N., Hayes, M., Linné, Zackrisson, E. 2013, A&A, 553, 106L

[116] Leitherer, C., Ferguson, H. C., Heckman, T. M, Lowenthal, J. D. 1995, ApJ, 454, L19

[117] Leitherer C. et al. , 1999, ApJS, 123, 3

[118] Lepp, S., Shull, J. M., 1983, ApJ, 270, 578

[119] Maciejewski, W., Cox, D. P. 1999, ApJ, 511, 792

[120] Mac-Low M.-M., Norman, M. 1998, ApJ,

[121] Mac Low, M-M., McCray, R. 1988, ApJ, 324, 776

[122] Mac Low, M-M., McCray, R., Norman, M. L. 1989, ApJ, 337, 141

[123] Mac Low, M. & Ferrara, A. 1999, ApJ, 513, 142

[124] Madau, P., Shull, J. M., 1996, ApJ, 457, 551

[125] Madau, P., Haardt, F. & Rees, M. J., 1999, ApJ, 514, 648

[127] Martín-Hernández, N. L., Schaerer, D., Sauvage, M. 2005, A&A, 429, 449

[127] Martin, C. 2005, ApJ, 621, 227

[128] Martin P. G., Keogh W. J. & Mandy M. E., 1998, ApJ, 499, 793

[129] McClure-Griffiths, N. M., Dickey, J. M., Gaensler, B. M., Green, A. J., 2002, ApJ, 578, 176

[130] McCray, R. & Kafatos, M. 1987, ApJ, 317, 190

[131] McCray, R. & Kafatos, M. 1987, ApJ, 317, 190

[132] McKee, C. F., Ostriker, J. P. 1977, ApJ, 218, 148

[133] McKee, C. F., Williams, J. P. 1997, ApJ, 476, 144

[134] Meynet, G., Maeder, A. 2003, A&A, 404, 975

[135] Miralda-Escudé, J., Haehnelt, M., Rees, M. J. 2000, ApJ, 530, 1

[136] Mitra, S., Ferara, A., Choudhury, T. R., 2013, MNRAS, 428, L1

[137] Mo H. J., Mao S., White S. D. M., 1998, MNRAS, 295, 319

[138] Murray, N., Ménard, B. & Thompson, T. A. 2011, ApJ, 735, 66

[139] Nath, B. B. & Shchekinov, Y. 2013, ApJL, 777, 12

[140] Navarro, F. F. & White, S. D. M. 1993, MNRAS, 265, 271

[141] Navarro J. F., Frenk C. S., White S. D. M., 1997, ApJ, 490, 493

[142] Navarro, J. F., White, S. D. M., 1994, MNRAS, 267, 401

[143] Navarro, J. F., Steinmetz, M., 1997, ApJ, 478, 13

[144] Navarro, J. F., Steinmetz, M., 2000, ApJ, 538, 477

[145] Nestor, D. B., Shapley, A. E., Steidel, C. C., Siana, B. 2011, ApJ, 736, 18

[146] Nordgren, T. E., Cordes, J. M., Terzian, Y. 1992, AJ, 104, 1465

[147] Norman, C., A., Ikeuchi, S. 1989, ApJ, 345, 372

[148] O'Connell, R. W., Gallagher, J. S., Hunter, D. A., & Colley, W. N. 1995, ApJ, 446, L1

[149] Oey, M. S. 2009, AIP Conf. Proc., 1156, 295 (2009)

[150] Oey, M. S., & Clarke, C. J., 1997, MNRAS, 289, 570

[151] Oey, M. S., et al. , 2005, ApJ, 129, 393

[152] Paardekooper, J.-P., Khochfar, S., Dalla Vecchia, C. 2013, MNRAS, 429, L94

[153] Palouš, J., Wünsch, R., Martínez-González, S., Hueyotl-Zahuantitla, F., Silich, S., & Tenorio-Tagle, G. 2013, ApJ, 772, 128

[154] Pellegrini, E. W., Oey, M. S., Winkler, P. F., Points, S. D., Smith, R. C., Jaskot, A. E., Zastrow, J. 2012, ApJ, 755, 40

[155] Pidopryhora, Y., Lockman, F. J., Shields, J. C., 2007, ApJ, 656, 928

[156] Portegies Zwart, S. F., McMillan, S. L., & Gieles, M. 2010, Ann. Rev. Astr. Astr., 2010, 48, 431

[157] Prochaska, J. X., Herbert-Fort, S., Wolfe, A. M. 2005, ApJ, 635, 123

[158] Radhakrishnan, V., Goss, W. M., Murray, J. D., Brooks, J. W. 1972, ApJS, 24, 49

[159] Razoumov, A. O, Sommer-Larsen, J. 2010, ApJ, 710, 1239

[160] Recchi, S. & Hensler, G. 2013, A&A, 551, 41

[161] Reynolds, R. J. 1991, ApJ, 372, L17

[162] Robertson, B. E., Furlanetto, S. R., Schneider, E. et al. 2013, ApJ, 768, 71

[163] Rosen, A., et al., 2014, MNRAS, 442, 2701

[164] Roy A., Nath B. B., Sharma P., Shchekinov Y., 2013, MNRAS, 434, 3572

[165] Roy A., Nath B. B., Sharma P., 2015, MNRAS, 451, 1939

[166] Salak, D., Nakai, N., Miyamoto, Y., Yamauchi, A., Tsuru, T. G., 2013, PASJ, 65, 66

[167] Salak, D., etal 2016, ApJ, 823, 68

[168] Salas, P., Galaz, G., Salter, D. Herrera-Camus, R., Bollatto, A. D., Kepley, A. 2014, ApJ, 797, 134

[169] Sarkar, K. C., Nath, B. B., Sharma, P., Shchekinov, Y. 2015, MNRAS, 448, 328

[170] Sarkar, K. C., Nath, B. B., Sharma, P., Shchekinov, Y. 2016, ApJL, 818, L1

[171] Schaye, J. 2001, ApJ, 562, L95

[172] Schiano, A. V. R. 1985, ApJ, 299, 24

[173] Shapiro, P. R., Field, G. B., 1976, ApJ, 205, 762

[174] Sharma, P., Roy, A., Nath, B. B., Shchekinov Y., 2014, MNRAS, 443, 3463

[175] Sharma, M., Nath. B. B. 2012, ApJ, 750, 55

[176] Sharma, P., Parrish, I. J., & Quataert, E. 2010, ApJ, 720, 652

[177] Shu, F. H., The Physics of Astrophysics, vol. II, Gas Dynamics, University Science Books, 1992

[178] Shull, J. M., Roberts, D., Giroux, M. L., Penton, S. V., Fardal, M. A. 1999, AJ, 118, 1450

[179] Siana, B., Teplitz, H. I., Ferguson, H. C. 2010, ApJ, 723, 241

[180] Silich, S. A., Tenorio-Tagle, G. 2001, ApJ, 552, 91

[181] Silich, S., Tenorio-Tagle, G., Torres-Campos, A., Munõz-Tuñòn, Monreal-Ibero, A., & Melo, V. 2009, ApJ, 700, 931

[182] Smith, M. D., 1993, A&A, 272, 571

[183] Smith, N., 2014, ARA& A, 52, 487

[184] Sommerville, R. S., Bullock, J. S., Livio, M. 2003, ApJ, 593, 616

[185] Springel, V. & Hernquist, L. 2003, MNRAS, 339, 289

[186] Springel, V. et al. 2005, Nature, 435, 629

[187] Staveley-Smith et al. , 1997, MNRAS, 289, 225

[188] Stinson, G., Seth, A., Katz, N., Wadsley, J., Governato, F., & Quinn, T. 2006, MNRAS, 373, 1074

[189] Stone, J. M. & Norman, M. L. 1992, ApJS, 80, 753

[190] Strickland, D. K. & Stevens, I. R. 2000, MNRAS, 314, 511

[191] Strickland, D. K. & Heckman, T. M. 2009, ApJ, 697, 2030

[192] Strickland, D. K, Heckman, T. M., Colbert, E. J. M., Hoopes, C. G., Weaver, K. A., 2004, ApJ, 606, 829

[193] Suchkov, A. A., Balsara, D. S., Heckman, T. M., & Leitherer, C. 1994, ApJ, 430, 511

[194] Suchkov, A. A., Berman, V. G., Heckman, T. M., Balsara, D. S. 1996, ApJ, 463, 518

[195] Suchkov, A. A., Shchekinov, Y. A., 1974, Astrophysics, 10, 159

[196] Sunyaev, R. A., Strelnitsky, V. S., Astron. Rept.

[197] Sutherland, R. S., Dopita, M. A. 1993, ApJS, 88, 253

[198] Tacconi, L. J. et al. 2010, Nature, 463, 781

[199] Tang, S. & Wang, Q. D. 2005, ApJ, 628, 205

[200] Tasker, E. J. & Bryan, G. L. 2006, ApJ, 641, 878

[201] Tenorio-Tagle, G., Rozyczka, M., Bodenheimer, P. 1990, A&A, 237, 207

[202] Tenorio-Tagle, G., Silich, S., & Muñoz-Tuñón, C. 2003, ApJ, 597, 279

[203] Thacker, R. J. & Couchman, H. M. P. 2000, ApJ, 545, 728

[204] Thornton, K., Gaudlitz, M., Janka, H., & Steinmetz, M. 1998, ApJ, 500, 95

[205] Tielens, A. G. G. M. 2005, *The physics and chemistry of interstellar medium*, Cambridge University Press.

[206] Tomisaka, K., Ikeuchi, S. 1986, PASJ, 38, 697

[207] Tomisaka, K., Ikeuchi, S. 1988, ApJ, 330, 695

[208] Thompson, T. A., Quataert, E., Zhang, D., Weinberg, D. H. 2016, MNRAS, 455, 1830

[209] Truelove, J. K. & McKee, C. F. 1999, ApJS, 120, 299

[210] Tsai, A.-L., Matsushita, S., Kong, K. H., Matsumoto, H., Kohno, K. 2012, ApJ, 752, 38

[211] Tüllmann, R, Breitschwerdt, D., Rossa, J., Pietsch, W., Dettmar, R. J. 2006, A&A, 457, 779

[212] Tumlinson, J., Thom, C., Werk, J. K, Prochaska, J. X., Tripp, T. M., Weinberg, D. H., Peeples, M. S., OMeara, J. M., Oppenheimer, B. D., Meiring, J. D., Katz, N. S., Davé, R., Ford, A. B., & Sembach, K. R. 2011, Science, 2011, 334, 948

[213] Uhlig, M., Pfrommer, C., Sharma, M., Nath, B. B., Ensslin, T. A., Springel, V. 2012, MNRAS, 423, 237

[214] Vacca, W. D., Garmany, C. D., Shull, J. M., 1996, ApJ, 460, 914

[215] Vasiliev, E. O., Nath, B. B., Bondarev, R., & Shchekinov, Y. 2015, MNRAS, 446, 1703

[216] Veilleux, S., Rupke, D. S. N., Swaters, R., 2009, ApJ, 700, L149

[217] Wakker, B. P., 2001, ApJS, 136, 463

[218] Wakker, B. P., York, D.G., Howk, J. C., et al. , 2007, ApJ, 670, L113

[219] Wakker, B. P., York, D.G., Wilhelm, R., et al. 2008, ApJ, 672, 298

[220] Walcher, C. J., et al. 2005, ApJ, 618, 237

[221] Walter, F., & Brinks, E., 1999, AJ, 118, 273

[222] Walter, F., Weiss, A., Scoville, N. 2002, ApJL, 580, 21

[223] Walter, F., Brinks, E., de Blok, W. J. G., Bigiel, F., Kennicutt, Jr. R. C., Thornley, M. D., Leroy, A. K., 2008, arXiv:0810.2125v1

[224] Weaver R., McCray R., Castor J., Shapiro P., Moore R., 1977, ApJ, 218, 377

[225] Weidner C., Vink J. S. 2010, A&A, WVostars Rev.

[226] Wise, J. H., Demchenko, V. G., Halicek, M. T., Norman, M. L., Turk, M. J.,Abel, T., Smith, B. D. 2014, MNRAS, 442, 2560

[227] Wolfire, M. G., McKee, C. F., Hollenbach, D., Tielens, A. G. G. M. 2003, ApJ, 587, 278

[228] Wolfire, M. G., Hollenbach, D. McKee, C. F. 2010, ApJ, 716, 1191

[229] Wood, K., Loeb, A. 2000, ApJ, 545, 86

[230] Yajima, H., Choi J.-H., Nagamine, K. 2011, MNRAS, 412, 411

[231] Zastrow, J., Oey, M. S., Veilleux, S., McDonald, M. 2013, ApJ, 779, 76

[232] Zeldovich, Ya. B., Raizer, Yu. P., Physics of Shock Waves and High-Temperature Hydrodynamic Phenomena, Academic Press, Vol. I, 1966

[233] Zhang, Q., Fall, S. M., & Whitmore, B. C. 2001, ApJ, 561, 727

[234] Zhao, J.-H., Anantharamaiah, K. R., Goss, W. M., Viallefond, F. 1997, ApJ, 482, 186

[235] Zinnecker, H., McCaughrean, M. J., Wilking, B. A. 1993, in Protostars and Planets III, ed. E. H. Levy & J. I. Lunine (Univ. of Arizona Press), 429

[236] Zubovas, K., King, A. R. 2014, MNRAS, 439, 400

[237] Zwaan, M. A., Prochaska, J. X. 2006, ApJ, 643, 675

[238] Zwaan, M. A., van der Hulst, J. M., Briggs, F. H., Verheijen, M. A. W. 2005, MNRAS, 364, 1467

List of Publications

1. A. Roy, B. B. Nath, P. Sharma, Y. Shchekinov, "Molecular outflows in starburst nuclei", 2016, submitted to MNRAS, arXiv:1607.04328

2. A. Roy, B. B. Nath, P. Sharma, "Narrow escape: how ionizing photons escape from disc galaxies", 2015, MNRAS, 451, 1939

3. P. Sharma, A. Roy, B. B. Nath, Y. Shchekinov, "In a hot bubble: why does superbubble feedback work, but isolated supernovae do not?", 2014, MNRAS, 443, 3463

4. A. Roy, B. B. Nath, P. Sharma, Y. Shchekinov, "Superbubble breakout and galactic winds from disc galaxies", 2013, MNRAS, 434, 3572